

Megacrysts in Volcanic Rocks of the Cameroon Volcanic Line - Constraints on Magma Genesis and Contamination

Dissertation
zur Erlangung des Doktorgrades
der Naturwissenschaften

vorgelegt beim
Fachbereich Geowissenschaften/Geographie
der Johann-Wolfgang-Goethe-Universität
in Frankfurt am Main

von
Kai Rankenburg
aus Frankfurt am Main

Frankfurt (2002)

vom Fachbereich Geowissenschaften/Geographie der Johann Wolfgang Goethe - Universität
als Dissertation angenommen.

Dekan: Professor Dr. Wolfgang Oschmann, Universität Frankfurt

Erstgutachter: Professor Dr. Gerhard Brey, Universität Frankfurt

Zweitgutachter: Professor Dr. Albrecht W. Hofmann, Max-Planck-Institut für Chemie, Ab-
teilung Geochemie, Mainz

Datum der Disputation: 29.11.2002

Erklärung

Ich versichere hiermit, die vorliegende Arbeit selbständig verfasst zu haben und alle benutzten Hilfsmittel und Quellen in der Arbeit angegeben zu haben. Diese Arbeit wurde an keiner anderen Fakultät als Dissertation eingereicht.

Mainz, den 12. September 2002

Zusammenfassung

1. Primäre Magmen als Mantelsonden

'Primäre' Magmen sind solche, die durch partielles Aufschmelzen des oberen Erdmantels generiert werden und deren Zusammensetzungen nicht durch sekundäre Prozesse (wie z.B. Kristallisation, Kontamination, Magmen-Mischung, -Entmischung, oder -Entgasung) modifiziert sind. Primäre Magmen sind für den Geochemiker von besonderem Interesse, da sie als Sonden in den tiefen Erdmantel dienen und damit zur Kartierung von Größe und Charakter von Mantelheterogenitäten herangezogen werden können. Der Nachweis des 'primären' Charakters eines Magmas ist jedoch nicht immer eindeutig, da Magmen auf ihrem Weg von der Mantelquelle zur Erdoberfläche modifiziert werden können (z.B. O'Hara (1968), Thirlwall, (1997)). Studien an Ozeaninselbasalten haben dennoch den Vorteil, dass die Schmelzen eine vergleichsweise dünne, hochschmelzende, und kompositionell ähnliche Kruste passieren, und damit die Ausmaße einer möglichen Kontamination geringer sind. Unser heutiges Bild der Zusammensetzung, Größe und Verteilung von Mantelheterogenitäten basiert deshalb weitgehend auf den Studien an primitiven Ozeaninselbasalten. Die Untersuchung langlebiger radioaktiver Nuklide wie z.B. ^{87}Rb , ^{147}Sm , ^{238}U , ^{235}U , ^{232}Th und ^{187}Re ist dabei von besonderem Vorteil, da die Tochterisotope dieser Nuklide bei Schmelz- oder Kristallisationsprozessen nicht signifikant fraktioniert werden. Der isotopische 'Fingerabdruck' der Quellregion im Erdmantel wird somit während einer Schmelzbildung auf das Magma übertragen und bleibt während folgender Kristallisationsprozesse unverändert. Um oberflächlich eruptierte Basalte als Mantelsonden zu verwenden, muss man allerdings sichergestellt werden, dass das Magma nicht durch andere Magmen (oder Nebengesteine) verschiedener isotopischer Zusammensetzung kontaminiert wurde.

Schon die ersten Bestandsaufnahmen radiogener Isotope an Ozeaninselbasalten zeigten die langzeitliche Heterogenität des Erdmantels auf (z.B. Faure & Hurley (1963), Hedge & Walhall (1963), Gast *et al.* (1964)). Nachfolgende detaillierte Studien von z.B. Hart *et al.* (1973), Schilling (1973), Zindler *et al.* (1979) und Poreda *et al.* (1986) belegten den fundamentalen geochemischen Unterschied zwischen Mantelschmelzen, die an den mittelozeanischen Rücken zu Tage treten (mid-ocean-ridge basalts: MORB), gegenüber solchen, die von sogenannten 'hot spots' oder Manteldiapiren stammen. Der 'verarmte' Charakter der Mantelquelle von MORB-Schmelzen wurde auf ein einfaches Modell zurückgeführt, in welchem die Mantelquelle eine frühere Schmelzextraktion erfuhr, die zur Bildung der kontinentalen Kruste führte

(z.B. Hofmann (1988)). Da während einer Schmelzbildung die in den Mantelphasen inkompatiblen Elemente bevorzugt in die Schmelze partitionieren, wird der Mantel an inkompatiblen Spurenelemente abgereichert, was langfristig auch zu 'verarmten' isotopischen Signaturen führt. Die variable geochemische Signatur von Ozeaninselbasalten wurde demgegenüber durch Mischung von verarmtem oberem Mantel mit 'primitivem' Mantel erklärt (DePaolo & Wasserburg, 1976), (O'Nions *et al.*, 1979), (Allègre *et al.*, 1979). Weitere Studien zeigten aber, dass auch andere Mantelkomponenten an der Bildung von Ozeaninselbasalten beteiligt sein müssen, die gegenüber dem 'primitiven' Mantel angereichert sind (z.B. O'Nions *et al.* (1977), Richardson *et al.* (1982), White & Hofmann (1982), Stille *et al.* (1983), Roden *et al.* (1984), Roden *et al.* (1994), Woodhead & McCulloch (1989), White & Hofmann (1982), Palacz & Saunders (1986), Wright & White (1987), Farley *et al.* (1992), Palacz & Saunders (1986), Nakamura & Tatsumoto (1988), Woodhead (1996)). Zindler & Hart (1986) zeigten, dass sich die gesamten Isotopensignaturen des ozeanischen Mantels auf die Mischung von vier prinzipiellen Endgliedern zurückführen lassen: Verarmter MORB-Mantel (DMM), sowie drei angereicherte Endglieder EM1, EM2 und HIMU. Die Interpretation der angereicherten Endglieder basiert auf der Idee, dass subduziertes Material regeneriert und in die Quellregionen (Manteldiapire) der Ozeanbasalte inkorporiert wird (Hofmann & White, 1982).

Wie oben beschrieben, beruht die Systematik der Mantelheterogenitäten auf der Voraussetzung, dass die den Studien zugrunde liegenden Laven 'primär' sind, d.h. unkontaminierte Mantelschmelzen repräsentieren. Demgegenüber haben Studien an kontinentalen Intraplattenvulkaniten immer mit isotopisch und an inkompatiblen Spurenelementen angereicherten Komponenten zu rechnen, wie sie zweifellos im subkontinentalen lithosphärischen Mantel (SCLM) als auch in der kontinentalen Kruste zu finden sind. So führten z.B. Halliday *et al.* (1988) und Halliday *et al.* (1990) eine positive $^{206}\text{Pb}/^{204}\text{Pb}$ -Anomalie in Gesteinen der Cameron Volcanic Line (CVL) auf die Interaktion primärer Magmen mit einer metasomatisch überprägten Lithosphäre zurück. Lee *et al.* (1996) erbrachten in einer Studie von Mantelxenolithen der CVL eindeutige Belege für deren langfristig angereicherten Charakter. Überdies belegen Daten von Marzoli *et al.* (1999) die Interaktion einiger kontinentaler CVL-Magmen mit kontinentaler Kruste.

2. Ziel dieser Arbeit

Die in dieser Studie analysierten Laven und Megakristalle des Biu und Jos Plateaus (nördliche CVL, Abb. 1.2) überdecken einen großen Teil der isotopischen Heterogenität der CVL (Abb. 1.1). Die Bestimmung der Ursachen der Heterogenität der Magmen des Biu und Jos Plateaus sollte also Rückschlüsse auf die Genese der gesamten CVL erlauben. Eine Möglichkeit zur Identifikation oberflächennaher Kontamination einer Suite von Laven bietet der Vergleich der isotopischen Zusammensetzung der Laven mit kogenetischen phenokristischen oder xenokristischen Phasen, die im Mantel kristallisierten. Die Laven des Biu und Jos Plateaus enthalten zahlreiche 'Megakristalle' homogener Zusammensetzung bis ~5 cm Größe. Als Mineralphasen treten Klinopyroxen (cpx), Granat (gnt), Ilmenit, Plagioklas, sowie untergeordnet Amphibol, Spinell, Phlogopit, Olivin, Zirkon und Korund auf. Die Untersuchungen der Genese von Megakristallen und die sich daraus ergebenden Aussagen über die Beschaffenheit des Erdmantels ist Gegenstand der vorliegenden Arbeit. In Kapitel zwei wird zunächst die genetische Relation der Megakristalle mit ihren Wirtsmagmen aufgezeigt, während sich Kapitel drei mit der Isotopensystematik von Megakristallen und Laven des Biu und Jos Plateaus befasst. Als Ergebnis der Studie ist festzuhalten, dass die kontinentale Signatur in Laven des ozeanischen Sektors der CVL, vormals als EM1-Quellkomponente (Lee *et al.*, 1994), oder LOMU-Komponente interpretiert (Douglass *et al.*, 1999) (LOMU: low μ = niedriges $^{238}\text{U}/^{204}\text{Pb}$, das langfristig zu niedrigen $^{206}\text{Pb}/^{204}\text{Pb}$ -Verhältnissen führt; im Gegensatz zu HIMU), auch durch oberflächennahe Assimilation krustalen Materials erklärt werden kann. Möglicherweise geschah dies durch Assimilation kontinentaler Sedimente, oder Assimilation von Blöcken kontinentalen Materials, die in der ozeanischen Lithosphäre während des kontinentalen Bruchs im Mesozoikum als 'Treibgut' zurückblieben.

3. Methodik

Um die Megakristalle als Sonde zur Wirtsmagmenchemie im oberen Mantel zu verwenden, muss zunächst deren Verwandtschaft im Erdmantel aufgezeigt werden. In der Literatur wurden verschiedene Modelle zur Genese der Megakristall diskutiert. Einerseits kommen die Mineralphasen der Megakristalle auch in assoziierten ultramafischen Mantelxenolithen vor und könnten damit von disaggregierten Peridotiten abstammen (Irving, 1974), (Righter & Carmichael, 1993). Sie könnten ebenso einer früheren magmatischen Phase entstammen, die älter ist als der Vulkanismus, der sie schließlich an die Erdoberfläche transportierte (Liotard *et al.*, 1988), (Capedri *et al.*, 1989), (Davies *et al.*, 2001). Der überwiegende Teil der Autoren

schlägt jedoch eine kogenetische Relation zwischen Megakristallen und Wirtsmagma vor (Green & Ringwood, 1967), (Binns, 1969), (Binns *et al.*, 1970), (Frisch & Wright, 1971), (Wilkinson, 1975), (Irving & Frey, 1984), (Jones, 1987), (Moore, 1987), (Geist *et al.*, 1988), (Wilkinson & Hensel, 1991), (Hops *et al.*, 1992), (Liu *et al.*, 1992a), (Liu *et al.*, 1992b), (Nasir, 1995), (Schulze *et al.*, 2001). Die oben genannte Kontroverse basiert dabei zumeist auf dem Vergleich von Spurenelementkonzentrationen und/oder der isotopischen Zusammensetzung von Megakristallen und ihrem Wirtsmagma. Eine Interpretation basierend auf petrologischen und petrographischen Indizien erscheint jedoch erfolgversprechender, da Magmen nach Kristallisation der Megakristalle kontaminiert werden können.

4. Diskussion – Herkunft der Megakristalle

Die Laven des Biu und Jos Plateaus enthalten zahlreiche Mantelxenolithe. Es besteht daher die Möglichkeit, dass die Megakristalle disaggregierte Phasen solcher Gesteine sind. Die Hauptelementchemie der Megakristalle, sowie deren systematische Kovariation (Abb. 2.4-2.7) sind in Übereinstimmung mit der Kristallisation der Megakristalle aus einem sich entwickelnden Magma (Putirka *et al.*, 1996), (Bultitude & Green, 1971), (Putirka, 1998), (Johnson, 1998), (Hart & Dunn, 1993), (Green *et al.*, 2000), (Rocholl *et al.*, 1996), (Hauri *et al.*, 1994), (Dunn, 1987), (Skulski *et al.*, 1994). Abschätzung der Kristallisationsbedingungen der Megakristalle aufgrund von Phasenbeziehungen, thermodynamischer und geothermobarometrischer Modelle (Bultitude & Green, 1971), (Krogh, 1988), (Putirka, 1997), (Hirschmann *et al.*, 1998) ergeben Drücke von 17-23 kbar und Temperaturen von ca. 1400°C, die deutlich über den Temperaturen typischer Mantelxenolithe liegen (Nixon, 1987). Darüber hinaus zeigen die Spurenelementmuster von Klinopyroxenen aus Pyroxeniten oder Peridotiten des Biu Plateaus signifikante Unterschiede zu Klinopyroxen-Megakristallen (Abb. 2.8). Die magmatischen Temperaturen und kompositionellen Unterschiede zwischen Megakristallen und pyroxenitischen/peridotitischen Phasen schließen eine Herkunft der Megakristalle von disaggregierten Xenolithen aus.

Die Megakristalle des Biu und Jos Plateaus könnten auch einer früheren Phase magmatischer Aktivität entstammen und mechanisch in ihr Wirtsmagma inkorporiert worden sein. Dies setzt jedoch eine Speicherung der Megakristalle in kühlerem Lithosphärenmaterial voraus. Verwachsungen von cpx- und gnt-Megakristallen zeigen jedoch magmatische Texturen und Temperaturen. Anzeichen einer thermischen Reequilibration, wie sie in Pyroxenitxenolithen oft beobachtet werden (in Form von z.B. Rekristallisation, chemischer Zonierung oder Entmi-

schungslamellen in Klinopyroxen (Sautter & Harte, 1988), (Sautter & Harte, 1990), (Sen & Jones, 1988), (Wilkinson & Stolz, 1997)), fehlen in den Megakristallen. Nimmt man für die Temperatur der umgebenden Lithosphäre eine durchschnittliche Temperatur von $\sim 1000^\circ\text{C}$ an (Lee *et al.*, 1996), so ergibt die Modellierung der Diffusionsprofile an cpx/gnt-Kontakten (Abb. 2.11) eine Abkühlzeit der Megakristalle von nur ~ 500 Jahren. Somit lassen sich die Megakristalle eindeutig der magmatischen Aktivität des Biu und Jos Plateaus (< 5.35 Ma (Grant *et al.*, 1972), (Fitton & Dunlop, 1985)) zuordnen.

Da die krustale Mächtigkeit in den untersuchten Gebieten nur etwa 30 km (oder ca. 9 kbar) beträgt (Poudjom-Djomani *et al.*, 1995), die primitiven Megakristalle aber Drücke von 17-23 kbar anzeigen, fand die Kristallisation der Megakristalle im subkontinentalen lithosphärischen Erdmantel statt. Die Größe und chemische Homogenität der Megakristalle legen eine Entstehungsgeschichte in relativ großen, langsam abkühlenden Magmenkammern nahe. Die rasche Verarmung der kompatiblen Spurenelemente in cpx lässt sich mittels fraktionierender Kristallisation aus dem Magma erklären (Abb. 2.13a). Die Laven selbst zeigen jedoch nicht das erwartete Muster einer fraktionierenden Kristallisation. Die relativ geraden Mischungslinien (Abb. 2.15) sind eher durch Mischung von primären Schmelzen mit ihren fraktionierten Derivaten zu erklären. Ein integriertes Modell der Megakristallgenese wird vorgeschlagen, in dem ein primäres Magma in die subkontinentale Lithosphäre intrudierte und dabei die Megakristalle kristallisierte. Die Mischung von primären Schmelzen mit den fraktionierten, megakristall-führenden Derivaten und der Aufstieg zur Erdoberfläche erfolgte durch einen erneuten Puls von Magma aus der tiefgelegenen Magmenquelle. Da die Granat- und Plagioklasme-gakristalle schnell von einem primitiveren Magma resorbiert werden (Brearley & Scarfe, 1986), (Canil & Fedortchouk, 1999), (Donaldson, 1985), fand die Mischung der primärer Schmelzen mit ihren entwickelten Derivaten kurz vor der Eruption statt.

5. Aussagen über lithosphärische Kontamination in der Genese von CVL-Lavas anhand von Strontium-, Neodym-, Blei- und Osmiumisotopen

Die Strontium- und Neodym-Isotopensystematik der Laven und Megakristalle in Abb. 3.1 erlaubt keine Unterscheidung der zwei möglichen Kontaminanten kontinentale Kruste (CC) und angereicherter Mantel (EM), da die jeweiligen Mischungstrajektorien in die gleiche Richtung weisen. Die Basalte des Biu und Jos Plateaus können jedoch aufgrund ihrer kombinierten Sr, Nd und Pb-Isotopenvariation in zwei verschiedene Mischreihen aufgeteilt werden, wobei das gemeinsame Endglied (Komponente A) durch $^{206}\text{Pb}/^{204}\text{Pb} \sim 19.82$, $^{207}\text{Pb}/^{204}\text{Pb} \sim 15.64$,

$^{208}\text{Pb}/^{204}\text{Pb} \sim 39.53$, $\epsilon_{\text{Nd}} \sim 7.0$ und $^{87}\text{Sr}/^{86}\text{Sr} \sim 0.70290$ charakterisiert ist (Abb. 3.3). Das zweite Endglied (Komponente B) wird am besten durch den isotopisch angereichtesten cpx-Megakristall repräsentiert, wobei die Megakristalle den Trend der Laven ($^{206}\text{Pb}/^{204}\text{Pb}$ bis 20.33, $^{207}\text{Pb}/^{204}\text{Pb}$ bis 15.69, $^{208}\text{Pb}/^{204}\text{Pb}$ bis 40.35, ϵ_{Nd} bis 6.0 und $^{87}\text{Sr}/^{86}\text{Sr}$ bis 0.70310) überlappen und ausdehnen. Megakristalle des Jos Plateaus definieren dabei andere Mischungsvektoren als solche des Biu Plateaus. Alle Laven mit $^{206}\text{Pb}/^{204}\text{Pb} < 19.82$ lassen sich als Mischung von Komponente A mit maximal $\sim 7\%$ lokaler Pan-Afrikanischer kontinentaler Kruste modellieren (Abb. 3.6 und 3.7).

Zur Klärung der Herkunft der Komponente B sollte insbesondere das Rhenium-Osmium-System aufgrund des isotopischen Kontrastes zwischen radiogener Kruste und unradiogenem Mantel hilfreich sein. Da für die Magmen mit $^{206}\text{Pb}/^{204}\text{Pb} > 19.82$ kein korrelierter Anstieg der $^{187}\text{Os}/^{188}\text{Os}$ -Verhältnisse zu erkennen ist (Abb. 3.2b), kann die Beteiligung kontinentaler Kruste an den Trends zu radiogenen $^{206}\text{Pb}/^{204}\text{Pb}$ -Verhältnissen ausgeschlossen werden. Dies ist in Übereinstimmung mit den Ergebnissen der Thermobarometrie, die zeigen, dass die Megakristalle im Mantel kristallisierten. Ein HIMU-artiges Mischungsendglied kann ebenfalls aufgrund divergierender isotopischer Zusammensetzung ausgeschlossen werden (Abb. 3.3). Alternativ dazu wird vorgeschlagen, dass die Komponente B eine lithosphärische Mantelschmelze repräsentiert. Dies wird unterstützt durch \pm konstante $^{187}\text{Os}/^{188}\text{Os}$ -Verhältnissen in Magmen mit $^{206}\text{Pb}/^{204}\text{Pb} > 19.82$ (Abb. 3.2b), sowie durch direkte Hinweise auf isotopisch angereicherte Lithosphäre unterhalb des Biu Plateaus (Lee *et al.*, 1996).

Die systematische Variation der Isotopendaten lässt weiterhin vermuten, dass kontinentales Krustenmaterial auch in der Genese von einigen Ozeaninseln der CVL von Bedeutung gewesen ist (Abb. 3.3). Ausgehend von der These, dass die CVL als Ganzes eine gleichförmige, homogene Quellregion besitzt, legt diese Studie eine gleichermaßen oberflächennahe Kontamination der ozeanischen Laven nahe. Andere publizierte Befunde für oberflächennahe Kontamination von Ozeaninselbasalten, wie z.B. paläozoische bis proterozoische Zirkone in Gabbro-Bohrkernen des mittelatlantischen Rückens (Pilot *et al.*, 1998), bzw. Funde von präkambrischem Gneiss (Belyatsky *et al.*, 1997), sowie unterkretazischer Sedimente in der Nähe des Rückens (Bonatti *et al.*, 1996) unterstützen diese These. Douglass *et al.* (1999) schlugen delaminierten SCLM als Ursache für niedrige $^{206}\text{Pb}/^{204}\text{Pb}$ -Verhältnisse in mittelatlantischen Basalten vor. Da die isotopische Zusammensetzung dieser hypothetischen LOMU-Komponente in der Verlängerung einer Mischungslinie von Komponente A durch die Zusammensetzung von kontinentaler Kruste zu liegen kommt, könnte die LOMU-Signatur prin-

ziell auch durch Assimilation kontinentalen Materials begründet werden. Vorläufige Ergebnisse aus der Osmiumisotopie von Gesteinen der ozeanischen CVL (Gannoun *et al.*, 2001) lassen jedoch noch keine eindeutige Zuordnung zu. Die von Lee *et al.* (1994) vorgeschlagene EM1-Komponente in der Genese ozeanischer CVL-Basalte kann ebenfalls als Assimilation oberflächennaher Sedimente oder Assimilation von krustalen Blöcken interpretiert werden, die während des kontinentalen Bruchs im Mesozoikum in der ozeanischen Lithosphäre als 'Treibgut' zurückblieben.

Abstract

Lavas of the Biu and Jos Plateau, northern Cameroon Volcanic Line (CVL), contain abundant genetically related megacrysts of clinopyroxene, garnet, plagioclase, ilmenite and subordinately amphibole, spinel and apatite. P, T-estimates of crystallization for the primitive group of clinopyroxene and garnet megacrysts are 17-23 kbar and $\sim 1400^{\circ}\text{C}$. Because crustal thickness in these areas is only ~ 30 km (or ~ 9 kbar), megacrysts formed within the subcontinental lithospheric mantle. Lavas of Biu and Jos Plateau do not reflect simple fractionation or equilibrium crystallization products, but instead reflect mixing between primary melts and their fractionated derivatives shortly before eruption. Because megacrysts grew within the lithospheric mantle and are unaffected by crustal contamination, study of the isotopic characteristics of megacrysts and host lavas provides insights into processes that affected the magma composition after formation of the megacrysts. Strontium, neodymium, lead and osmium isotope systematics of lavas and megacrysts allows to distinguish between two contamination paths of the primary magmas. The first is characterized by both increasing $^{206}\text{Pb}/^{204}\text{Pb}$ (19.82 to 20.33) and $^{87}\text{Sr}/^{86}\text{Sr}$ (0.70290 to 0.70310) and decreasing ϵ_{Nd} (7.0 to 6.0), and involves addition of an enriched SCLM-derived liquid. The second contamination path is characterized by decreasing $^{206}\text{Pb}/^{204}\text{Pb}$ (19.82 to 19.03), but also increasing $^{87}\text{Sr}/^{86}\text{Sr}$ (0.70290 to 0.70359) and decreasing ϵ_{Nd} (7.0 to 4.6), and involves addition of up to 7% bulk continental crust. Isotope systematics suggest that continental crust also was involved in formation of some lavas from the oceanic sector of the CVL. Assuming that the line as a whole shares a common source, this study proposes that the continental signature seen in the oceanic sector of the CVL is also caused by shallow contamination, either by continent-derived sediments or by rafted crustal blocks that became trapped in the oceanic lithosphere during continental breakup in the Mesozoic.

Zusammenfassung	I
Abstract	VIII
Contents	IX

CHAPTER 1: INTRODUCTION

1.1. 'Primary' magmas as probes to the mantle	1
1.2. Aims and approach of this work	1
1.3. Geologic setting	
1.3.1. <i>The Cameroon Volcanic Line (CVL): Hot spot track or 'hot line'?</i>	3
1.3.2. <i>The source of CVL magmatism</i>	7
1.3.3. <i>Geologic setting: The Benue Trough</i>	8
1.3.4. <i>The Biu and Jos Plateaus</i>	9
1.3.5. <i>The basement</i>	10
1.4. Appendix: Glossary of mantle components	10
1.5. References	13

CHAPTER 2: ORIGIN OF MEGACRYSTS IN VOLCANIC ROCKS OF THE CVL

2.1. Introduction	22
2.2. Results	
2.2.1. <i>Volcanic rocks of Biu and Jos Plateau</i>	22
2.2.2. <i>Megacrysts – major element systematics</i>	26
2.2.3. <i>Megacrysts – trace element systematics</i>	29
2.2.4. <i>Megacrysts – moessbauer spectroscopy</i>	31
2.3. Discussion	
2.3.1. <i>Fe³⁺ and calculation of temperatures</i>	32
2.3.2. <i>Origin of megacrysts – cogenetic or exotic to their host magma?</i>	32
2.3.3. <i>Where did the megacrysts grow – pressure estimates</i>	36
2.3.4. <i>Further constraints on megacryst growth</i>	41
2.3.5. <i>Contrasting crystallization/magma mixing histories deduced from megacrysts and lavas</i>	42
2.3.6. <i>Constraints on the timing of magma mixing processes</i>	44
2.3.7. <i>Constraints on garnet/melt distribution coefficients</i>	45
2.4. Conclusions	49
2.5. References	50

CHAPTER 3: CONSTRAINTS ON MAGMA CONTAMINATION

3.1. Introduction	57
3.2. Results	59
3.2.1. <i>Sr, Nd, Pb and Os isotopes of lavas and megacrysts</i>	59
3.3. Discussion	65
3.3.1. <i>Data arrays in Sr-Nd-Pb isotope space</i>	65
3.3.2. <i>Evidence for SCLM involvement in the genesis of Biu and Jos Plateau lavas</i>	65
3.3.3. <i>Evidence for enriched lithosphere beneath the CVL</i>	68
3.3.4. <i>Models for the origin of enriched SCLM</i>	69
3.3.5. <i>Constraints on mixing relations from isotope systematics</i>	70
3.3.6. <i>A quantitative model of SCLM assimilation?</i>	71
3.3.7. <i>Evidence for crustal contamination of Biu and Jos Plateau lavas</i>	72
3.3.8. <i>Implications for crustal contamination in the oceanic CVL</i>	75
3.4. Conclusions	77
3.5. Outlook.....	77
3.6. References	79

CHAPTER 4: APPENDICES

Appendix A: Sampling and analytical techniques

<i>Appendix A.1.: Sampling locations</i>	83
<i>Appendix A.2.: Major and trace element analyses of volcanic rocks</i>	85
<i>Appendix A.3.: Major and trace element analyses of megacrysts</i>	87
<i>Appendix A.4.: Isotope (Sr, Nd, Pb, Os) analyses of volcanic rocks</i>	88
<i>Appendix A.5.: Isotope analyses of megacrysts</i>	92
<i>Appendix A.6.: Data analysis</i>	94
<i>Appendix A.7.: References</i>	97
Appendix B: Data tables	100
Appendix C: Picture tables.....	140
Curriculum Vitae.....	143

CHAPTER 1: INTRODUCTION

1.1. 'Primary' magmas as probes to the mantle

'Primary' magmas are those formed by partial melting of the upper mantle, the composition of which have not been modified subsequently by differentiation processes. Clearly, it is of great petrogenetic significance to be able to recognize primary magma compositions as these may be useful as probes to the mantle to learn about mantle heterogeneity. However, it may be difficult to prove the primary character of erupted intraplate lavas, because primary magmas may be modified by e.g. fractional crystallization, crustal contamination, magma mixing, liquid immiscibility and volatile loss on their way to the surface (e.g. O'Hara, 1968). Studies of oceanic intraplate volcanoes often neglect lithospheric contamination based upon three reasons: the lithospheric cover on which they erupt is much thinner, the crust has a higher solidus, and it is compositionally similar to melts of the mantle. Our present picture of the composition, size and distribution of mantle heterogeneities therefore is mainly based upon the study of primitive OIBs. The importance of radiogenic isotopic variations in that picture is that they frequently survive the chemical fractionation events which accompany the formation and evolution of magmas. Thus, during partial melting, the magma will inherit the isotopic composition of its source, and this will remain constant during subsequent fractional crystallization processes, provided that the magma does not become contaminated by interaction with isotopically distinct wall rocks or other batches of magma.

1.2. Aims and approach of this work

Petrogenetic modeling of continental intraplate magmas bears the additional problem of distinguishing between enriched mantle source components derived from mantle plumes as opposed to those which undoubtedly exist within the subcontinental lithosphere. For example, Lee *et al.* (1996) provided evidence that portions of the lithosphere beneath the Cameroon Volcanic Line (CVL) are isotopically enriched. Moreover, there is also clear isotopic evidence for interaction with the continental crust in some CVL lavas of the continental sector (Marzoli *et al.*, 1999). Figure 1.1 shows a collection of published Sr-Nd isotopic compositions of the more primitive rocks of the CVL along with our own analyses of rocks from Biu and Jos Plateau, northern Nigeria.

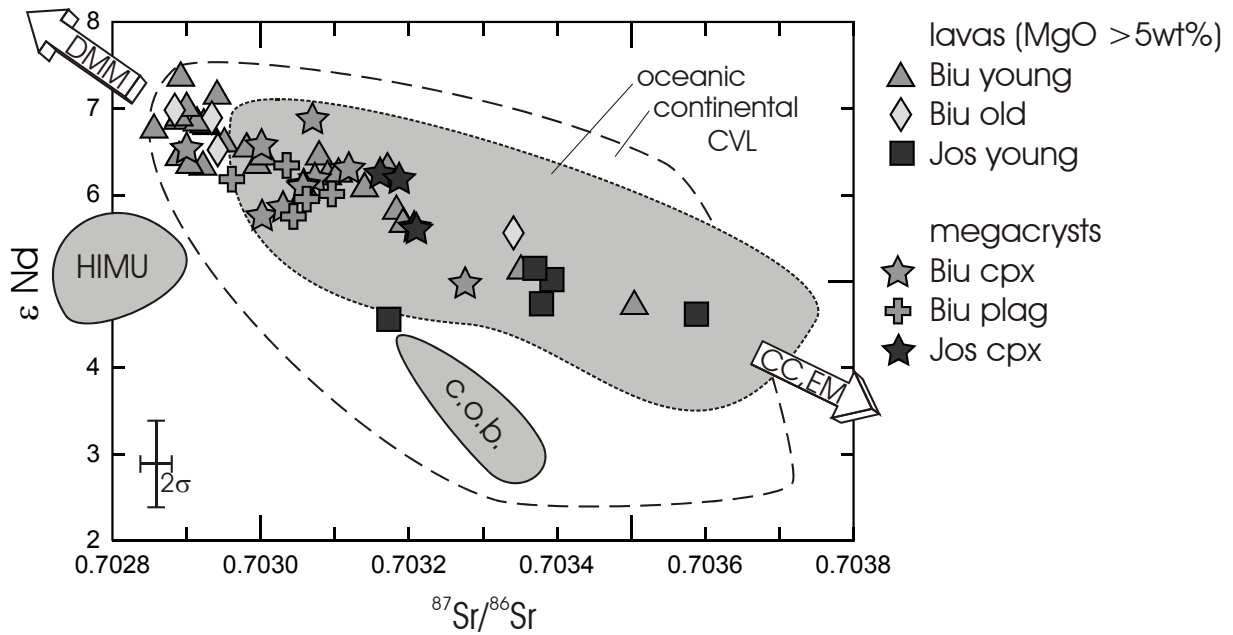


Fig. 1.1: Collection of Sr-Nd isotopic compositions of the more primitive rocks ($\text{MgO} > 5 \text{ wt}\%$) from the oceanic and continental CVL along with data for megacrysts. Data compiled from Halliday *et al.* (1988), Halliday *et al.* (1990), Lee *et al.* (1994), Marzoli *et al.* (1999), Marzoli *et al.* (2000) and this work. Rocks from the Biu and Jos Plateau span much of the range of CVL lavas as a whole. Isotope systematics may be explained by mixing between a DMM (depleted MORB mantle) component and a CC (continental crust) and/or EM (enriched mantle) component.

CVL magmas are isotopically heterogeneous in Sr-Nd isotope space. Evidently, there is considerable overlap between compositions of continental and oceanic sector lavas, although the continental sector extends to somewhat lower ϵ_{Nd} . It is unclear whether the heterogeneity observed in the more primitive magmas is related primarily to heterogeneity in the asthenospheric source region of the lavas and represents mixing of a depleted and a more enriched endmember, or if part of this heterogeneity is due to melt interaction with continental lithospheric mantle, or melt interaction with continental crust.

Lavas from Biu and Jos Plateau analyzed in this work span much of the isotopic heterogeneity found in CVL magmas as a whole. Therefore, determining the source of isotopic heterogeneity in the Biu and Jos Plateau lavas should provide insight into processes affecting CVL magmas as a whole. One way of constraining the role of shallow contamination in a suite of lavas is to compare the isotopic composition of the lavas with cogenetic phenocrystic or xenocrystic phases that precipitated within the mantle. Lavas from Biu and Jos Plateau contain abundant megacrysts of clinopyroxene (cpx), garnet (gnt), plagioclase (plag) and il-

menite (ilm), and subordinate megacrysts of amphibole (amph), spinel (sp), zircon (zr), corundum (cor), phlogopite (phlo) and olivine (ol). In the following chapter, petrologic and petrographic evidence is presented, which shows that at least cpx and gnt megacrysts precipitated from recent CVL magmas within the lithospheric mantle. In chapter three, the isotopic compositions of the host lavas and the megacrysts are compared to constrain the role of magma contamination within the SCLM, crustal contamination and magma mixing in the genesis of Biu and Jos Plateau lavas, and by inference, in the CVL as a whole. The main conclusion drawn from this work is that the continental signature seen in the oceanic sector of the CVL, which was previously interpreted as an EM1 source component (Lee *et al.*, 1994), or 'LOMU' component (Douglass *et al.*, 1999), may also be caused by shallow contamination, either by continent-derived sediments or by rafted crustal blocks that became trapped in the oceanic lithosphere during continental breakup in the Mesozoic.

1.3. Geologic setting

1.3.1. The Cameroon Volcanic Line (CVL): Hot spot track or 'hot line'?

Although ~90% of present-day volcanic activity is concentrated within or adjacent to zones of plate divergence or convergence, volcanism also occurs at locations far from plate boundaries. The 'hot spot' or 'mantle plume' model for oceanic intraplate volcanism, first proposed by Wilson (1963) and developed by e.g. Morgan (1971), Hofmann & White (1982), Zindler & Hart (1986), Molnar & Stock (1987) and Wolfe *et al.* (1997), involves a relatively stationary magma source in the mantle over which the oceanic plate moves. Ultimately, this creates a chain of volcanoes moving away from the hot spot in the direction of seafloor spreading. Such an age progression is clearly documented for e.g. the Hawaiian chain. To date, an increasing number of intraplate volcanic centers have been ascribed to hot spots. Burke & Wilson (1976) identified a global pattern of not less than 122 hot spots, active during the past 10 Ma, within both the oceanic and continental plates.

The Cameroon Volcanic Line (CVL) is the only known intraplate alkaline province which straddles a continental margin. The CVL comprises a genetically related series of Cenozoic intraplate volcanoes that extends for 1600 km from the island of Pagalu in the South Atlantic Ocean to the continental interior of West Africa (fig. 1.2). There are 12 main volcanic centers which range in age from 30 Ma to present (Fitton & Dunlop, 1985) and 17 anorogenic ring complexes in the continental sector with ages ranging from 66 to 30 Ma (Fitton,

1987), (Kraml *et al.*, 2001). The northern end of the continental part of the CVL is marked by the Cenozoic volcanics of the Biu Plateau, Nigeria.

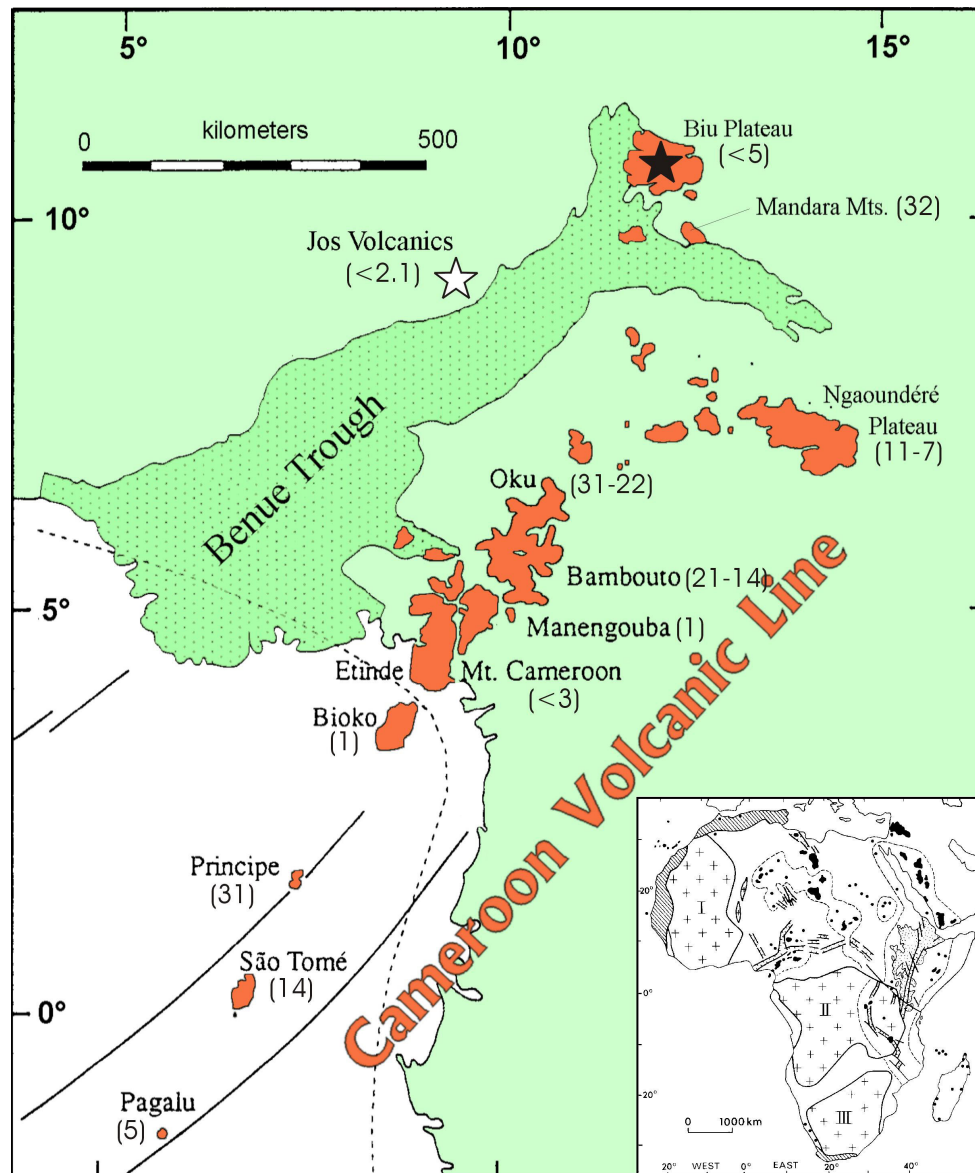


Fig. 1.2: Geological map showing the eruption ages of the major volcanic centers of the Cameroon Volcanic Line and the Gulf of Guinea (adapted from Fitton & Dunlop (1985) and Dautria & Girod (1987)). Ages compiled from Fitton & Dunlop (1985), Halliday *et al.* (1990), Lee *et al.* (1994) and Ngounouno *et al.* (1997). The Jos volcanics are shifted ~400 km to the NW of the line axis and are usually not included in CVL magmatism. However, no occurrence of continental Cenozoic volcanism (black areas in lower right insertion) has been recorded west of the Jos Plateau. Sample locations are indicated as black (Biu Plateau) and white star (Jos Plateau).

Magmatism of the CVL cannot be a simple expression of the African plate sliding over a fixed mantle hotspot because there has been no systematic change in the focus of magmatism for 30 Ma and plio/pleistocene volcanism younger than 5 Ma is dispersed all along the line (e.g. Pagalu, Bioko, Mt. Cameroon, Jos and Biu Plateau). Fitton (1980) showed that basaltic rocks in the oceanic and continental sectors are geochemically and isotopically (Sr, Nd) similar and suggested that a line or zone of hot asthenospheric mantle is upwelling underneath the CVL, forming the source magmas without any substantial involvement of the overlying lithosphere. Given that the CVL deep mantle source is of elongated rather than punctual shape, the occurrence of contemporaneous oceanic and continental alkaline volcanism within a single province makes the CVL a unique area in which to study the differences, if any, between the suboceanic and subcontinental mantle sources for alkali basalt.

In a combined Nd, Sr, Pb and O isotopic study, however, Halliday *et al.* (1988) found a distinctive $^{206}\text{Pb}/^{204}\text{Pb}$ -anomaly focused at the CVL continent/ocean boundary (c.o.b.), which diminishes over a distance of 400 km to either side (fig. 1.3).

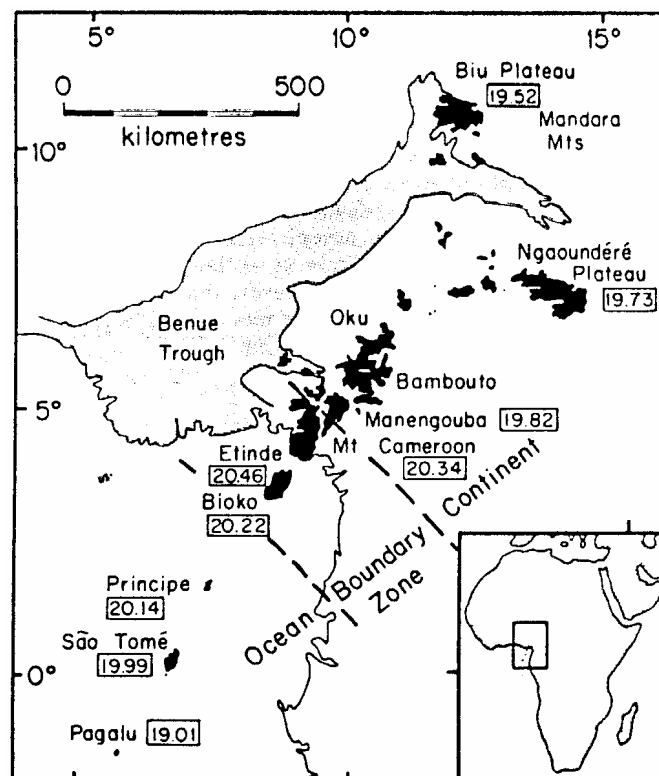


Fig. 1.3: Map showing the definition of the continent/ocean boundary region. The mean $^{206}\text{Pb}/^{204}\text{Pb}$ of the <10 Ma lavas is given for each locality (taken from Halliday *et al.*, 1990).

Halliday *et al.* (1990) attributed this HIMU-signature (high $\mu \equiv$ high $^{238}\text{U}/^{204}\text{Pb}$, leading to time-integrated high $^{206}\text{Pb}/^{204}\text{Pb}$) to be inherited from relatively recent U/Pb-fractionation during impregnation of the uppermost mantle by the St. Helena hot spot, because a) the authors did not find significant differences in the range of $^{207}\text{Pb}/^{204}\text{Pb}$ between individual CVL volcanic centers, suggesting a 'young' fractionation and b) the c.o.b., as inferred from plate reconstructions (Fitton, 1980), was directly underlain by the St. Helena plume at ~ 125 Ma when the Equatorial Atlantic opened. To account for the increase in U/Pb and Ce/Pb, while maintaining uniform Ba/Ce and Ce/U ratios in the mesozoic CVL lithosphere, Halliday *et al.* (1995) proposed a source region of the metasomatic agent that contains small amounts of residual sulfide (plus amphibole and phlogopite). Sulfide is thus far the only mantle phase known with high partition coefficients for lead (Shimazaki & Maclean, 1976), and therefore may fractionate U/Pb ratios, if sulfide remains in the melt residuum (for sulfide capacity of silicate melts see e.g. Wendlandt (1982), Mavrogenes & O'Neill (1999) and O'Neill & Mavrogenes (2002)). In summary, the observed Pb-isotope heterogeneities of CVL magmas were proposed to be derived from remelting of variably metasomatized lithosphere rather than reflecting primary asthenospheric source heterogeneities.

In a study of three islands of the oceanic sector of the CVL (Principe, São Tomé and Pagalu) Lee *et al.* (1994) found evidence for an age progression of the oldest lavas erupted on each island, consistent with the motion of the African Plate. Lee *et al.* (1994) explained the observed space-time variations in isotopic ratios by the gradual incorporation of a HIMU component into a common source, which was suggested to be best represented by the island of Pagalu. Because the inferred DMM/EM1 components were interpreted to be homogenized differently in different islands, Lee *et al.* (1994) suggested that each island is supplied by individual plumes sharing a common origin, and proposed a new model where the CVL originates from a sublithospheric enriched 'hot zone', periodically fed and melted by deep mantle plumes. Hafnium isotope data of Ballentine *et al.* (1997) suggests that the CVL basalts were derived from a mantle source that was basically uniform over its whole length based on their isotopic homogeneity, but upon which a symmetrical pattern of enrichment has been superimposed. The authors argued that the heterogeneity in Pb isotopic composition was not the result of variable incorporation of HIMU components in the mantle source, therefore contradicting the model of Lee *et al.* (1994). Whatever the role of the lithospheric mantle in the genesis of CVL magmas may be, there is clear isotopic evidence for interaction with the con-

tinental crust in some CVL lavas of the continental sector (Marzoli *et al.*, 1999), and it is not clear if and to what extent primitive magmas are also affected by lithospheric processes.

1.3.2. The source of CVL magmatism

Recent investigations connect the upsurge in hotspot volcanism on the African plate with its significant deceleration to 20 ± 1 mm/a since 19-30 Ma (O'Connor *et al.*, 1999) which may be due to the beginning collision with the Eurasian continent at 38 Ma (Silver *et al.*, 1998). According to England & Houseman (1984), this is approximately the critical speed at which a transition from heat transfer via large scale circulation to heat transfer via thermal plumes rising from the lower boundary layer occurs (cf. fig. 1.4), therefore giving an explanation for the onset of CVL activity at that time.

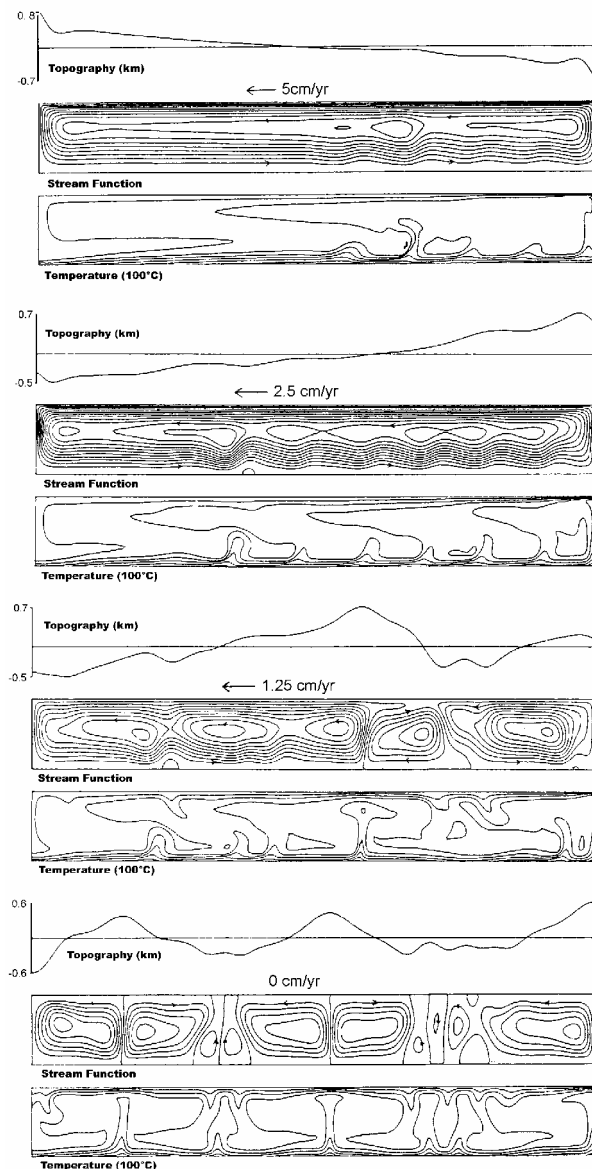


Fig. 1.4: Cross sections illustrating the topography of a plate surface above a convecting shallow mantle. There is little relief on the surface when the plate is moving fast. At slower speeds of 1.25 cm/a 'plumes' occur. A basin and swell pattern comparable to that of the African plate may be established when the plate is at rest. Simplified from the results of numerical experiments reported by England & Houseman (1984).

Burke (2001) proposed a plate-wide shallow mantle convection system to account for the regular spacing of CVL 'swells', which presumes complete arrest of the African plate. However, the difficulty in constraining African plate motions is the precise dating of the onset of volcanism in a particular magmatic province, which may or may not be in accordance with a migrating plate (Marzoli *et al.*, 2000). Ebinger & Sleep (1998) proposed a single plume impact beneath the Ethiopian plateau and subsequent sublithospheric 'channeling' of plume material as explanation for the onset of Cenozoic magmatism throughout central Africa. In summary, however, all previous work suggests that the whole CVL shares a common deep source, variably modified by shallow sublithospheric and/or lithospheric processes.

1.3.3. The Benue Trough

The Benue Trough forms the major part of a NE-SW trending sedimentary basin, 50-150 km wide, which extends for over 1000 km from the Niger delta to Lake Chad (cf. table 2.1). Its northern end is y-shaped, formed by the E-W trending Yola rift and the north trending Gongola rift. It is part of the West and Central African Rift System (Fairhead, 1988), (Popoff, 1988), whose origin is linked to the opening of the Equatorial Atlantic, which in turn was initiated in the latest Jurassic (Nürnberg & Müller, 1991). The Benue trough has been interpreted as a failed arm of a RRR triple junction (Burke & Dewey, 1974), or the faulted arm of a RRF system (Popoff, 1988). More recent data suggest a more complicated origin where transtensional tectonics appear to have dominated the evolution of the trough from the Aptian to present, except for major compressional episodes of short duration in the Santonian and at the end of the Cretaceous (Benkhelil, 1989).

The main features of the Benue trough are a thick layer up to 6500 m of cretaceous sediments, a broad positive gravity anomaly attributable to Moho uplift, and associated Mesozoic to early Cenozoic magmatism, which can be divided into two principal domains. In the Northern Benue, magmatism is characterized by transitional alkaline and tholeiitic basalts and some dispersed peralkaline acidic rocks with ages ranging from 147-106 Ma (Maluski *et al.*, 1995). The Southern Benue shows two additional episodes with alkaline intrusive rocks of 97-81 Ma age, and alkaline intrusions followed by tholeiitic subvolcanoes of 68-49 Ma age (Maluski *et al.*, 1995). Maluski *et al.* (1995) suggest that the Mesozoic to Cenozoic magmatism of the Benue Trough constitutes a step in a general N to S direction from the Mesozoic alkali ring complexes of the Jos Plateau which were emplaced at ~170 Ma (Dickin *et al.*, 1991), to the Cenozoic volcanism of the CVL. In a subsequent paper of Coulon *et al.* (1996), the isotope systematics of Benue trough

basalts were explained by mixing of EM1, DMM and HIMU components, similar to the work of Lee *et al.* (1994) and thus linked to the genesis of the CVL, whereas involvement of continental crust in the genesis of the lavas was considered insignificant. In the Northern Benue magmatism restarted in the Miocene with intrusion of trachyte-phonolite plugs which have been dated by Grant *et al.* (1972) between 22-11 Ma and proceeded with the magmatic province of the Biu Plateau.

1.3.4. The Biu and Jos Plateaus

Samples of basalts and megacrysts were collected from the Biu and Jos Plateau in Nigeria (cf. symbols in fig. 1.2). The Biu Plateau defines the end of the NNW branch of the continental CVL and is also situated at the structural and topographic divide between the Benue and Chad basins. Although the Jos Plateau is usually not assigned to CVL volcanism because of its offset to the line axis, it has a similar volcanic history and geochemistry.

According to Turner (1978), the Biu Plateau mainly overlies basement rocks (see chapter 2.1.4), whereas to the W and N, basalts of the Biu Plateau have spread over cretaceous sediments, mainly arkosic Bima sandstone. The Biu Plateau was constructed in three stages during two periods of volcanism: 1) An early fissure type eruption and 2) formation of relatively large tephra ring volcanoes and building up of localized thick lava piles (up to 250 m) in the southern part of the plateau. Lavas of this plateau building stage range in composition from hypersthene-normative basalt to basanite and K/Ar-ages range from 5.35 to 0.84 Ma (Grant *et al.*, 1972), (Fitton & Dunlop, 1985). Extensive weathering and laterite formation suggests a break period after this episode. 3) Resumption of igneous activity with formation of over 80 NNW-SSE aligned cinder cones with similar chemistry to earlier basalts. A rough estimate of the age of the last magmatic period is <50,000 years based on diffusional constraints of He in mantle xenoliths of the CVL (Barfod *et al.*, 1999) and >25,000 years based on pollen dating of maar sediments from the Biu Plateau (Salzmann, 2000). Although the younger volcanoes of the Biu Plateau are prominent landscape features, individually they are only small volcanic structures. Many of them are quite typical cinder cones, examples include some of the most prominent peaks: Pelamabelu and Ga Tila. Others are broader and lower with wide flat crater floors corresponding more closely to tuff cones and rings (e.g. Miringa), or cut into country rock below general ground level (maars, see pic. 1-3).

As with the Biu Plateau, volcanic activity of Jos Plateau (located approximately 400 km to the NW of the central CVL axis, cf. fig. 1.2) occurred during two periods and thus the

basalts have been divided into an earlier and more recent group (McLeod *et al.*, 1971). There are no isotopic age determinations available for the older basalts, however, Wright (1976) suggests a palaeocene age, roughly synchronous with the Benue Trough folding and uplift. The more recent activity formed a group of 22 cinder cones. Radiometric K-Ar ages (Grant *et al.*, 1972) suggest, unlike on the Biu Plateau, continuous volcanism between 2.1 - 0.9 Ma.

1.3.5. The basement

The Biu Plateau lies mainly on granite, gneisses and charnockitic rocks of the Pan-African basement complex of Nigeria, and on the cretaceous Bima sandstones of the Benue trough in the north and west. Radiometric ages of Nigerian basement rocks have been presented by e.g. Dickin *et al.* (1991), Dada (1998), Van Breemen *et al.* (1977) and Kröner *et al.* (2001). They cluster around 3.5, 3.1-3.0, 2.7-2.5, 2.1-1.8 Ga and a main tectonometamorphic imprint on most crystalline rocks of the Nigerian basement in Pan-African (~600 Ma) times. Protolith Nd model ages may reflect mean crust residence ages with contributions from juvenile material and reworked older Archaean crustal components when there is no independent indicator of a major crustal formation event at that time.

The Jos Plateau is underlain by anorogenic ring complexes with peralkaline to subalkaline granites of Mesozoic ages (~170 Ma, Dickin *et al.* (1991)). Average crustal residence times of these rocks based on Sm/Nd isotope analyses yield ~1.8 Ga, consistent with other basement model ages. Two granulite enclaves from the CVL analyzed by Halliday *et al.* (1988) yield model ages of 1.47 and 2.09 Ga, which are within the same range as the Jos Plateau samples and therefore suggest a similar basement. However, the Sr isotope composition of the inclusions is less radiogenic, possibly because they represent Rb-depleted lower crust (Dickin *et al.*, 1991).

1.4. Appendix: Glossary of mantle components

The long-term chemical heterogeneity of the Earth's mantle was demonstrated by the earliest surveys of radiogenic isotopes in oceanic basalts (Faure & Hurley, 1963), (Hedge & Walthall, 1963), (Gast *et al.*, 1964). Subsequent detailed studies revealed several fundamental geochemical differences between mantle-derived magmas erupting at ridges and hot spots (e.g. Hart *et al.* (1973), Schilling (1973), Zindler *et al.* (1979), Poreda *et al.* (1986)). These

differences were consistent with a fairly simple model, in which the source of mid-oceanic ridge basalts (MORBs) had a prior history of melt extraction to form the continental crust (CC), whereas the variable geochemistry of ocean-island basalts (OIBs) was explained by mixing of the depleted upper mantle (DMM) with 'primitive' mantle (DePaolo & Wasserburg, 1976), (O'Nions *et al.*, 1979), (Allègre *et al.*, 1979). This conceptual model essentially defines three different reservoirs. Primitive mantle is identical to the bulk silicate Earth (BSE), which is the bulk Earth composition minus the core. Continental crust is the product of melt extraction from a portion of the original primitive upper mantle, which left the depleted upper mantle as the third reservoir.

However, further survey work on hot spots revealed a large number of distinct hot spot components, which could be circumscribed by a small number of mantle end-members with enriched geochemical signatures (e.g. White (1985), Zindler & Hart (1986), Allègre *et al.* (1987)). Zindler & Hart (1986) showed that the entire isotopic database for the oceanic mantle could be described by the DMM and three enriched components (EM1, EM2, HIMU), with all other compositions created by mixing. Hart (1988) reviewed the possible mixing relationships between these various components. The interpretation of the isotope and trace element character of the enriched mantle components is centered around the hypothesis that subducted material is recycled and incorporated into the sources of ocean island basalts (mantle plumes), as proposed by Hofmann & White (1982). The heterogeneities in OIBs may thus originate from different types of recycled materials in their sources. For example HIMU (HIMU: high μ = high $^{238}\text{U}/^{204}\text{Pb}$, leading over time to high $^{206}\text{Pb}/^{204}\text{Pb}$ ratios) is often attributed to recycled oceanic crust. Pelagic and/or terrigenous sediment appears often to be subducted along with the oceanic crust, supposedly giving rise to the enriched 'flavors' EM1/EM2. Varying amounts, types, and ages of subducted sediment may be responsible for some of the geochemical variety displayed by plumes. A compilation of the trace element compositions of mantle components and average continental crust, along with their composition in Sr-Nd-Pb isotope space is given in fig. 1.5 (taken from Hofmann (1997)).

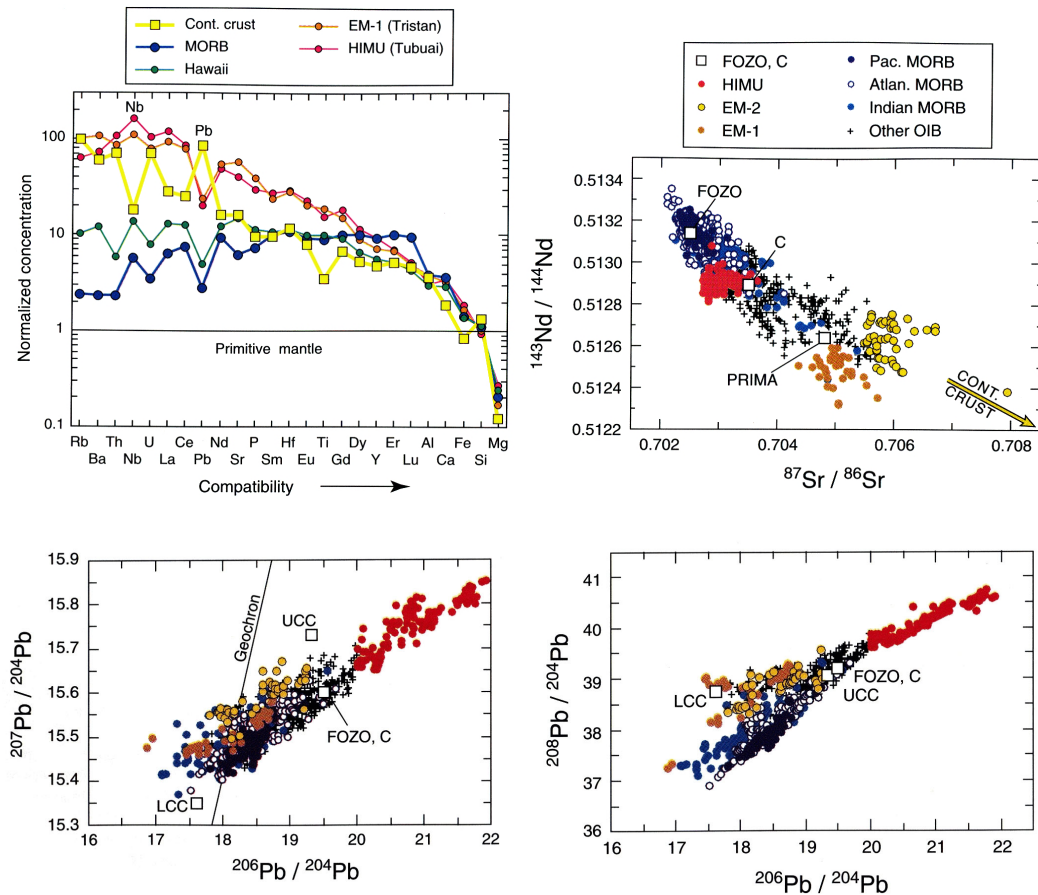


Fig. 1.5: **a)** Concentrations of selected trace and major elements, arranged in the order of ascending compatibility and normalized to primitive-mantle concentrations, in average continental crust, average MORB, and three types of OIB: average Mauna Loa (Hawaii), average Tristan and Inaccessible Island representing EM1, and Tubuai representing HIMU islands. **b-d)** Isotopic compositions of MORB and OIB, with extreme HIMU, EM1 and EM2 samples marked in red, brown and yellow colors, respectively. HIMU samples are arbitrarily defined by having $^{206}\text{Pb}/^{204}\text{Pb} \geq 20$. Also marked are the compositions of the 'primitive mantle' (PRIMA) and the proposed common mantle components of most plumes 'FOZO' and 'C'. The solid line labeled 'geochron' marks the locus of possible primitive mantle values assuming an overall age of the mantle of 4.50 Ga. UCC and LCC mark average compositions of upper and lower continental crust, respectively (taken from Hofmann (1997) and references therein).

Work on mantle xenoliths and peridotite massifs from the continental lithosphere revealed an alternative origin for enriched components. Melt-fluid-rock interactions (so-called mantle metasomatism) can create enriched compositions whose current (or time-evolved) isotopic compositions resemble many of the enriched mantle end-members (cf. Morris & Pasteris (1987), Menzies & Hawkesworth (1987), Nixon (1987) and references therein). However, recent studies have shown that the osmium isotope composition of the SCLM is quite differ-

ent from that of mantle plumes (for a recent review of the Re-Os isotope system, see Shirey & Walker (1998)). Because mantle plumes come in several geochemical varieties, it is possible that both mechanisms operate. Indeed, other as yet unknown processes may be involved as well.

1.5. References

- Allègre, C. J., Hamelin, B., Provost, A. & Dupre, B. (1987). Topology in Isotopic Multispace and Origin of Mantle Chemical Heterogeneities. *Earth and Planetary Science Letters* **81** (4), 319-337.
- Allègre, C. J., Othman, D. B., Polve, M. & Richard, P. (1979). The Nd-Sr isotopic correlation in mantle materials and geodynamic consequences. *Physics of the Earth and Planetary Interiors* **19** (4), 293-306.
- Ballentine, C. J., Lee, D. C. & Halliday, A. N. (1997). Hafnium isotopic studies of the Cameroon line and new HIMU paradoxes. *Chemical Geology* **139** (1-4), 111-124.
- Barfod, D. N., Ballentine, C. J., Halliday, A. N. & Fitton, J. G. (1999). Noble gases in the Cameroon line and the He, Ne, and Ar isotopic compositions of high μ (HIMU) mantle. *Journal of Geophysical Research-Solid Earth* **104** (B12), 29509-29527.
- Belyatsky, B. V., Levsky, L. K., Trukhalev, A. I., Pogrebitsky, Y. E., et al. (1997). Precambrian granite-gneiss from the Mid-Atlantic Ridge (26°N): a U-Pb and Sm-Nd isotopic study. *Geochemistry International* **35** (8), 770-773.
- Benkhelil, J. (1989). The Origin and Evolution of the Cretaceous Benue Trough (Nigeria). *Journal of African Earth Sciences* **8** (2-4), 251-282.
- Binns, R. A. (1969). High-Pressure Megacrysts in Basanitic Lavas near Armidale New South Wales. *American Journal of Science* **267**, 33-49.
- Binns, R. A., Duggan, M. B. & Wilkinson, J. F. G. (1970). High Pressure Megacrysts in Alkaline Lavas from Northeastern New-South-Wales. *American Journal of Science* **269** (2), 132-168.
- Bonatti, E., Ligi, M., Borsetti, A. M., Gasperini, L., et al. (1996). Lower Cretaceous deposits trapped near the equatorial Mid-Atlantic Ridge. *Nature* **380** (6574), 518-520.
- Brearley, M. & Scarfe, C. M. (1986). Dissolution rates of upper mantle minerals in an alkali basalt melt at high-pressure: an experimental study and implications for ultramafic xenolith survival. *Journal of Petrology* **27** (5), 1157-1182.
- Bultitude, R. J. & Green, D. H. (1971). Experimental Study of Crystal-Liquid Relationships at High Pressures in Olivine Nephelinite and Basanite Compositions. *Journal of Petrology* **12** (1), 121-147.
- Burke, K. (2001). Origin of the Cameroon line of volcano-capped swells. *Journal of Geology* **109** (3), 349-362.
- Burke, K. & Dewey, J. F. (1974). Two plates in Africa during the Cretaceous? *Nature* **249**, 313-316.

- Burke, K. & Wilson, J. T. (1976). Hot spots on the Earth's surface. In: Decker, R. & Decker, B. (eds) *Volcanoes and the Earth's interior*. New York: W.H. Freeman (1982), 31-42.
- Canil, D. & Fedortchouk, Y. (1999). Garnet dissolution and the emplacement of kimberlites. *Earth and Planetary Science Letters* **167** (3-4), 227-237.
- Capedri, S., Venturelli, G., Salviolimarani, E., Crawford, A. J., et al. (1989). Upper-Mantle Xenoliths and Megacrysts in an Alkali Basalt from Tallante, Southeastern Spain. *European Journal of Mineralogy* **1** (5), 685-699.
- Coulon, C., Vidal, P., Dupuy, C., Baudin, P., et al. (1996). The Mesozoic to Early Cenozoic magmatism of the Benue Trough (Nigeria): Geochemical evidence for the involvement of the St Helena plume. *Journal of Petrology* **37** (6), 1341-1358.
- Dada, S. S. (1998). Crust-forming ages and Proterozoic crustal evolution in Nigeria: a reappraisal of current interpretations. *Precambrian Research* **87** (1-2), 65-74.
- Dautria, J. M. & Girod, M. (1987). Cenozoic volcanism associated with swells and rifts. In: Nixon, P. H. (ed) *Mantle Xenoliths*. Chichester: John Wiley and Sons Ltd., 195-214.
- Davies, G. R., Spriggs, A. J. & Nixon, P. H. (2001). A non-cognate origin for the Gibeon kimberlite megacryst suite, Namibia: Implications for the origin of Namibian kimberlites. *Journal of Petrology* **42** (1), 159-172.
- DePaolo, D. J. & Wasserburg, G. J. (1976). Inferences about magma sources and mantle structure from variations of $^{143}\text{Nd}/^{144}\text{Nd}$. *Geophysical Research Letters* **3** (12), 743-746.
- Dickin, A. P., Halliday, A. N. & Bowden, P. (1991). A Pb, Sr and Nd Isotope Study of the Basement and Mesozoic Ring Complexes of the Jos Plateau, Nigeria. *Chemical Geology* **94** (1), 23-32.
- Donaldson, C. H. (1985). The Rates of Dissolution of Olivine, Plagioclase, and Quartz in a Basalt Melt. *Mineralogical Magazine* **49** (354), 683-693.
- Dougllass, J., Schilling, J. G. & Fontignie, D. (1999). Plume-ridge interactions of the Discovery and Shona mantle plumes with the southern mid-Atlantic ridge (40 degrees-55 degrees S). *Journal of Geophysical Research-Solid Earth* **104** (B2), 2941-2962.
- Dunn, T. (1987). Partitioning of Hf, Lu, Ti, and Mn between Olivine, Clinopyroxene and Basaltic Liquid. *Contributions to Mineralogy and Petrology* **96** (4), 476-484.
- Ebinger, C. J. & Sleep, N. H. (1998). Cenozoic magmatism throughout east Africa resulting from impact of a single plume. *Nature* **395**, 788-791.
- England, P. & Houseman, G. (1984). On the Geodynamic Setting of Kimberlite Genesis. *Earth and Planetary Science Letters* **67** (1), 109-122.
- Fairhead, J. D. (1988). Mesozoic Plate Tectonic Reconstructions of the Central South-Atlantic Ocean: the Role of the West and Central African Rift System. *Tectonophysics* **155** (1-4), 181-191.
- Farley, K. A., Natland, J. H. & Craig, H. (1992). Binary mixing of enriched and undegassed (primitive?) mantle components (He, Sr, Nd, Pb) in Samoan lavas. *Earth and Planetary Science Letters* **111** (1), 183-199.

- Faure, G. & Hurley, P. M. (1963). The Isotopic Composition of Strontium in Oceanic and Continental Basalts - Application to the Origin of Igneous Rocks. *Journal of Petrology* **4** (1), 31-50.
- Fitton, J. G. (1980). The Benue through and Cameroon Line - a Migrating Rift System in West-Africa. *Earth and Planetary Science Letters* **51** (1), 132-138.
- Fitton, J. G. (1987). The Cameroon Line, West-Africa: a comparison between oceanic and continental alkaline volcanism. In: Fitton, J. G. & Upton, B. G. J. (eds) *Alkaline Igneous Rocks* Geological Society Special Publication, 273-291.
- Fitton, J. G. & Dunlop, H. M. (1985). The Cameroon Line, West-Africa, and Its Bearing on the Origin of Oceanic and Continental Alkali Basalt. *Earth and Planetary Science Letters* **72** (1), 23-38.
- Frisch, T. & Wright, J. B. (1971). Chemical composition of high-pressure megacrysts from Nigerian Cenozoic lavas. *Neues Jahrbuch für Mineralogie-Monatshefte* **7**, 289-304.
- Gannoun, A., Burton, K. W., Barfod, D. N. & Halliday, A. (2001). Osmium-Isotope Variations in Cameroon Line Basalts: HIMU Mantle Versus Crustal Contamination. *Eos Trans. AGU*, 82(47), Fall Meet. Suppl., Abstract V21D-07
- Gast, P. W., Hedge, C. E. & Tilton, G. R. (1964). Isotopic composition of lead and strontium from Ascension and Gough Islands. *Science* **145** (363), 1181-85.
- Geist, D. J., Myers, J. D. & Frost, C. D. (1988). Megacryst-Bulk Rock Isotopic Disequilibrium as an Indicator of Contamination Processes - the Edgecumbe Volcanic Field, Se Alaska. *Contributions to Mineralogy and Petrology* **99** (1), 105-112.
- Grant, N. K., Rex, D. C. & Freeth, S. J. (1972). Potassium-Argon Ages and Strontium Isotope Ratio Measurements from Volcanic-Rocks in Northeastern Nigeria. *Contributions to Mineralogy and Petrology* **35** (4), 277-292.
- Green, D. H. & Ringwood, A. E. (1967). The genesis of basaltic magmas. *Contributions to Mineralogy and Petrology* **15**, 103-190.
- Green, T. H., Blundy, J. D., Adam, J. & Yaxley, G. M. (2000). SIMS determination of trace element partition coefficients between garnet, clinopyroxene and hydrous basaltic liquids at 2-7.5 GPa and 1080-1200 degrees C. *Lithos* **53** (3-4), 165-187.
- Halliday, A. N., Davidson, J. P., Holden, P., Dewolf, C., et al. (1990). Trace-Element Fractionation in Plumes and the Origin of HIMU Mantle beneath the Cameroon Line. *Nature* **347** (6293), 523-528.
- Halliday, A. N., Dickin, A. P., Fallick, A. E. & Fitton, J. G. (1988). Mantle Dynamics - a Nd, Sr, Pb and O Isotopic Study of the Cameroon Line Volcanic Chain. *Journal of Petrology* **29** (1), 181-211.
- Halliday, A. N., Lee, D. C., Tommasini, S., Davies, G. R., et al. (1995). Incompatible Trace-Elements in OIB and MORB and Source Enrichment in the Sub-Oceanic Mantle. *Earth and Planetary Science Letters* **133** (3-4), 379-395.
- Hart, S. R. (1988). Heterogeneous Mantle Domains - Signatures, Genesis and Mixing Chronologies. *Earth and Planetary Science Letters* **90** (3), 273-296.

- Hart, S. R. & Dunn, T. (1993). Experimental Cpx/Melt Partitioning of 24 Trace-Elements. *Contributions to Mineralogy and Petrology* **113** (1), 1-8.
- Hart, S. R., Schilling, J. G. & Powell, J. L. (1973). Basalts from Iceland and along the Reykjanes Ridge: Sr isotopic geochemistry. *Nature* **246** (155), 104-107.
- Hauri, E. H., Wagner, T. P. & Grove, T. L. (1994). Experimental and Natural Partitioning of Th, U, Pb and Other Trace-Elements between Garnet, Clinopyroxene and Basaltic Melts. *Chemical Geology* **117** (1-4), 149-166.
- Hedge, C. E. & Walthall, F. G. (1963). Radiogenic Strontium-87 as an Index of Geologic Processes. *Science* **140** (357), 1214-17.
- Hirschmann, M. M., Ghiorso, M. S., Wasylenki, L. E., Asimow, P. D., et al. (1998). Calculation of peridotite partial melting from thermodynamic models of minerals and melts I. Review of methods and comparison with experiments. *Journal of Petrology* **39** (6), 1091-1115.
- Hofmann, A. W. (1988). Chemical Differentiation of the Earth - the Relationship between Mantle, Continental Crust, and Oceanic Crust. *Earth and Planetary Science Letters* **90** (3), 297-314.
- Hofmann, A. W. (1997). Mantle geochemistry: the message from oceanic volcanism. *Nature* **385**, 219-229.
- Hofmann, A. W. & White, W. M. (1982). Mantle Plumes from Ancient Oceanic Crust. *Earth and Planetary Science Letters* **57** (2), 421-436.
- Hops, J. J., Gurney, J. J. & Harte, B. (1992). The Jagersfontein Cr-Poor Megacryst Suite - Towards a Model for Megacryst Petrogenesis. *Journal of Volcanology and Geothermal Research* **50** (1-2), 143-160.
- Irving, A. J. (1974). Megacrysts from Newer Basalts and Other Basaltic Rocks of Southeastern Australia. *Geological Society of America Bulletin* **85** (10), 1503-1514.
- Irving, A. J. & Frey, F. A. (1984). Trace-Element Abundances in Megacrysts and Their Host Basalts - Constraints on Partition Coefficients and Megacryst Genesis. *Geochimica Et Cosmochimica Acta* **48** (6), 1201-1221.
- Johnson, K. T. M. (1998). Experimental determination of partition coefficients for rare earth and high-field-strength elements between clinopyroxene, garnet, and basaltic melt at high pressures. *Contributions to Mineralogy and Petrology* **133** (1-2), 60-68.
- Jones, R. A. (1987). Strontium and neodymium isotopic and rare earth element evidence for the genesis of megacrysts in kimberlites of southern Africa. In: Nixon, P. H. (ed) *Mantle Xenoliths*. Chichester: John Wiley and Sons Ltd, 711-724.
- Kraml, M., Kamdem, J. B., Keller, J. & Henjes-Kunst, F. (2001). Time Constraints for Cameroon Line Magmatism from Single Crystal Laser $^{40}\text{Ar}/^{39}\text{Ar}$ Dating of the Hossere Ngo Anorogenic Plutonic Complex. *EUG XI* 596.
- Krogh, E. J. (1988). The garnet-clinopyroxene Fe-Mg geothermometer: a reinterpretation of existing experimental data. *Contributions to Mineralogy and Petrology* **99** (1), 44-48.

- Kröner, A., Ekwueme, B. N. & Pidgeon, R. T. (2001). The oldest rocks in West Africa: SHRIMP zircon age for Early Archean migmatitic orthogneiss at Kaduna, northern Nigeria. *Journal of Geology* **109** (3), 399-406.
- Lee, D. C., Halliday, A. N., Davies, G. R., Essene, E. J., et al. (1996). Melt enrichment of shallow depleted mantle: A detailed petrological, trace element and isotopic study of mantle-derived xenoliths and megacrysts from the Cameroon line. *Journal of Petrology* **37** (2), 415-441.
- Lee, D. C., Halliday, A. N., Fitton, J. G. & Poli, G. (1994). Isotopic Variations with Distance and Time in the Volcanic Islands of the Cameroon Line - Evidence for a Mantle Plume Origin. *Earth and Planetary Science Letters* **123** (1-4), 119-138.
- Liotard, J. M., Briot, D. & Boivin, P. (1988). Petrological and Geochemical Relationships between Pyroxene Megacrysts and Associated Alkali-Basalts from Massif Central (France). *Contributions to Mineralogy and Petrology* **98** (1), 81-90.
- Liu, C. Q., Masuda, A., Shimizu, H., Takahashi, K., et al. (1992a). Evidence for Pressure-Dependence of the Peak Position in the REE Mineral-Melt Partition Patterns of Clinopyroxene. *Geochimica Et Cosmochimica Acta* **56** (4), 1523-1530.
- Liu, C. Q., Masuda, A. & Xie, G. H. (1992b). Isotope and Trace-Element Geochemistry of Alkali Basalts and Associated Megacrysts from the Huangyishan Volcano, Kuandian, Liaoning, NE China. *Chemical Geology* **97** (3-4), 219-231.
- Maluski, H., Coulon, C., Popoff, M. & Baudin, P. (1995). Ar-40/Ar-39 Chronology, Petrology and Geodynamic Setting of Mesozoic to Early Cenozoic Magmatism from the Benue Trough, Nigeria. *Journal of the Geological Society* **152**, 311-326.
- Marzoli, A., Piccirillo, E. M., Renne, P. R., Bellieni, G., et al. (2000). The Cameroon Volcanic Line revisited: Petrogenesis of continental basaltic magmas from lithospheric and asthenospheric mantle sources. *Journal of Petrology* **41** (1), 87-109.
- Marzoli, A., Renne, P. R., Piccirillo, E. M., Francesca, C., et al. (1999). Silicic magmas from the continental Cameroon Volcanic Line (Oku, Bambouto and Ngaoundere): $^{40}\text{Ar}/^{39}\text{Ar}$ dates, petrology, Sr-Nd-O isotopes and their petrogenetic significance. *Contributions to Mineralogy and Petrology* **135** (2-3), 133-150.
- Mavrogenes, J. A. & O'Neill, H. S. C. (1999). The relative effects of pressure, temperature and oxygen fugacity on the solubility of sulfide in mafic magmas. *Geochimica Et Cosmochimica Acta* **63** (7-8), 1173-1180.
- McLeod, W. N., Turner, D. C. & Wright, E. P. (1971). The geology of the Jos Plateau. *Bulletin of the Geological Survey of Nigeria* **32** (1), 17-23.
- Menzies, M. A. & Hawkesworth, C. J. (1987). *Mantle Metasomatism*, Academic Press, Inc., pp. 472.
- Molnar, P. & Stock, J. (1987). Relative Motions of Hotspots in the Pacific, Atlantic and Indian Oceans since Late Cretaceous Time. *Nature* **327** (6123), 587-591.
- Moore, A. E. (1987). A model for the origin of ilmenite in kimberlite and diamond: implications for the genesis of the discrete nodule (megacryst) suite. *Contributions to Mineralogy and Petrology* **95** (2), 245-253.
- Morgan, J. W. (1971). Convection plumes in the lower mantle. *Nature* **230**, 42-43.

- Morris, E. M. & Pasteris, J. D. (1987). Mantle Metasomatism and Alkaline Magmatism, Special Paper 215, The Geological Society of America, Inc., Boulder, pp. 392.
- Nakamura, Y. & Tatsumoto, M. (1988). Pb, Nd, and Sr Isotopic Evidence for a Multicomponent Source for Rocks of Cook-Austral Islands and Heterogeneities of Mantle Plumes. *Geochimica Et Cosmochimica Acta* **52** (12), 2909-2924.
- Nasir, S. (1995). Cr-Poor Megacrysts from the Shamah Volcanic Field, Northwestern Part of the Arabian Plate. *Journal of African Earth Sciences* **21** (3), 349-357.
- Ngounouno, I., Deruelle, B., Demaiffe, D. & Montigny, R. (1997). New data on the Cenozoic volcanism of the Garoua valley (Upper Benue trough, northern Cameroon). *Comptes Rendus De L Academie Des Sciences Serie Ii Fascicule a- Sciences De La Terre Et Des Planetes* **325** (2), 87-94.
- Nixon, P. H. (1987). Mantle Xenoliths, John Wiley and Sons Ltd, Chichester, pp. 864.
- Nürnberg, D. & Müller, R. D. (1991). The Tectonic Evolution of the South-Atlantic from Late Jurassic to Present. *Tectonophysics* **191** (1-2), 27-53.
- O'Connor, J. M., Stoffers, P., van den Bogaard, P. & McWilliams, M. (1999). First seamount age evidence for significantly slower African plate motion since 19 to 30 Ma. *Earth and Planetary Science Letters* **171** (4), 575-589.
- O'Hara, M. J. (1968). Are ocean floor basalts primary magmas? *Nature* **220**, 683-686.
- O'Neill, H. S. C. & Mavrogenes, J. A. (2002). The sulfide capacity and the sulfur content at sulfide saturation of silicate melts at 1400°C and 1 bar. *Journal of Petrology* **43** (6), 1049-1087.
- O'Nions, R. K., Evensen, N. M. & Hamilton, P. J. (1979). Geochemical modeling of mantle differentiation and crustal growth. *Journal of Geophysical Research* **84**, 6091-6101.
- O'Nions, R. K., Hamilton, P. J. & Evensen, N. M. (1977). Variations in $^{143}\text{Nd}/^{144}\text{Nd}$ and $^{87}\text{Sr}/^{86}\text{Sr}$ ratios in oceanic basalts. *Earth and Planetary Science Letters* **34** (1), 13-22.
- Palacz, Z. A. & Saunders, A. D. (1986). Coupled Trace-Element and Isotope Enrichment in the Cook-Austral-Samoa Islands, Southwest Pacific. *Earth and Planetary Science Letters* **79** (3-4), 270-280.
- Pilot, J., Werner, C. D., Haubrich, F. & Baumann, N. (1998). Palaeozoic and Proterozoic zircons from the Mid-Atlantic Ridge. *Nature* **393** (6686), 676-679.
- Popoff, M. (1988). From Gondwana to the South-Atlantic - Connections between the Benue Trough and the Basins of Northeastern Brazil from the Precambrian to the Opening of the Gulf of Guinea in the Early Cretaceous. *Journal of African Earth Sciences* **7** (2), 409-431.
- Poreda, R., Schilling, J. G. & Craig, H. (1986). Helium and Hydrogen Isotopes in Ocean-Ridge Basalts North and South of Iceland. *Earth and Planetary Science Letters* **78** (1), 1-17.
- Poudjom-Djomani, Y. H., Nnange, J. M., Diament, M., Ebinger, C. J., et al. (1995). Effective Elastic Thickness and Crustal Thickness Variations in West Central-Africa Inferred from Gravity Data. *Journal of Geophysical Research-Solid Earth* **100** (B11), 22047-22070.

- Putirka, K. (1997). Magma transport at Hawaii: Inferences based on igneous thermobarometry. *Geology* **25** (1), 69-72.
- Putirka, K. (1998). Garnet plus liquid equilibrium. *Contributions to Mineralogy and Petrology* **131** (2-3), 273-288.
- Putirka, K., Johnson, M., Kinzler, R., Longhi, J., et al. (1996). Thermobarometry of mafic igneous rocks based on clinopyroxene-liquid equilibria, 0-30 kbar. *Contributions to Mineralogy and Petrology* **123** (1), 92-108.
- Richardson, S. H., Erlank, A. J., Duncan, A. R. & Reid, D. L. (1982). Correlated Nd, Sr and Pb Isotope Variation in Walvis Ridge Basalts and Implications for the Evolution of Their Mantle Source. *Earth and Planetary Science Letters* **59** (2), 327-342.
- Righter, K. & Carmichael, I. S. E. (1993). Mega-Xenocrysts in Alkali Olivine Basalts - Fragments of Disrupted Mantle Assemblages. *American Mineralogist* **78** (11-12), 1230-1245.
- Rocholl, A., Ludwig, T., Altherr, R., Meyer, H.-P., et al. (1996). Experimental partitioning of trace elements between clinopyroxene, garnet and basaltic melt studied by ion microprobe. *Journal of Conference Abstracts* **1**, 517-518.
- Roden, M. F., Frey, F. A. & Clague, D. A. (1984). Geochemistry of Tholeiitic and Alkalic Lavas from the Koolau Range, Oahu, Hawaii - Implications for Hawaiian Volcanism. *Earth and Planetary Science Letters* **69** (1), 141-158.
- Roden, M. F., Trull, T., Hart, S. R. & Frey, F. A. (1994). New He, Nd, Pb, and Sr Isotopic Constraints on the Constitution of the Hawaiian Plume - Results from Koolau Volcano, Oahu, Hawaii, USA. *Geochimica Et Cosmochimica Acta* **58** (5), 1431-1440.
- Salzmann, U. (2000). Are modern savannas degraded forests? - A Holocene pollen record from the Sudanian vegetation zone of NE Nigeria. *Vegetation History and Archaeobotany* **9** (1), 1-15.
- Sautter, V. & Harte, B. (1988). Diffusion Gradients in an Eclogite Xenolith from the Roberts Victor Kimberlite Pipe - 1. Mechanism and Evolution of Garnet Exsolution in Al₂O₃-Rich Clinopyroxene. *Journal of Petrology* **29** (6), 1325-1352.
- Sautter, V. & Harte, B. (1990). Diffusion Gradients in an Eclogite Xenolith from the Roberts Victor Kimberlite Pipe - 2. Kinetics and Implications for Petrogenesis. *Contributions to Mineralogy and Petrology* **105** (6), 637-649.
- Schilling, J. G. (1973). Icelandic mantle plume: geochemical evidence along the Reykjanes Ridge. *Nature* **242** (5400), 565-571.
- Schulze, D. J., Valley, J. R., Bell, D. R. & Spicuzza, M. J. (2001). Oxygen isotope variations in Cr-poor megacrysts from kimberlite. *Geochimica Et Cosmochimica Acta* **65** (23), 4375-4384.
- Sen, G. & Jones, R. E. (1988). Exsolved Silicate and Oxide Phases from Clinopyroxenes in a Single Hawaiian Xenolith - Implications for Oxidation-State of the Hawaiian Upper Mantle. *Geology* **16** (1), 69-72.
- Shimazaki, H. & Maclean, W. H. (1976). Experimental-Study on Partition of Zinc and Lead between Silicate and Sulfide Liquids. *Mineralium Deposita* **11** (2), 125-132.

- Shirey, S. B. & Walker, R. J. (1998). The Re-Os isotope system in cosmochemistry and high-temperature geochemistry. *Annual Review of Earth and Planetary Sciences* **26**, 423-500.
- Silver, P. G., Russo, R. M. & Lithgow-Bertelloni, C. (1998). Coupling of South American and African Plate motion and Plate deformation. *Science* **279** (5347), 60-63.
- Skulski, T., Minarik, W. & Watson, E. B. (1994). High-Pressure Experimental Trace-Element Partitioning between Clinopyroxene and Basaltic Melts. *Chemical Geology* **117** (1-4), 127-147.
- Stille, P., Unruh, D. M. & Tatsumoto, M. (1983). Pb, Sr, Nd and Hf Isotopic Evidence of Multiple Sources for Oahu, Hawaii Basalts. *Nature* **304** (5921), 25-29.
- Thirlwall, M. F. (1997). Pb isotopic and elemental evidence for OIB derivation from young HIMU mantle. *Chemical Geology* **139** (1-4), 51-74.
- Turner, D. C. (1978). Volcanoes of the Biu Basalt Plateau, Northeastern Nigeria. *Journal of Mining and Geology* **15** (2), 49-63.
- Van Breemen, O., Pidgeon, R. T. & Bowden, P. (1977). Age and Isotopic Studies of Some Pan-African Granites from North-Central Nigeria. *Precambrian Research* **4**, 307-319.
- Wendlandt, R. F. (1982). Sulfide Saturation of Basalt and Andesite Melts at High-Pressures and Temperatures. *American Mineralogist* **67** (9-10), 877-885.
- White, W. M. (1985). Sources of Oceanic Basalts - Radiogenic Isotopic Evidence. *Geology* **13** (2), 115-118.
- White, W. M. & Hofmann, A. W. (1982). Sr and Nd Isotope Geochemistry of Oceanic Basalts and Mantle Evolution. *Nature* **296** (5860), 821-825.
- Wilkinson, J. F. G. (1975). Ultramafic Inclusions and High-Pressure Megacrysts from a Nephelinite Sill, Nandewar Mountains, Northeastern New-South- Wales, and Their Bearing on Origin of Certain Ultramafic Inclusions in Alkaline Volcanic Rocks. *Contributions to Mineralogy and Petrology* **51** (4), 235-262.
- Wilkinson, J. F. G. & Hensel, H. D. (1991). An Analcime Mugarite - Megacryst Association from North-Eastern New-South-Wales: Implications for High-Pressure Amphibole-Dominated Fractionation of Alkaline Magmas. *Contributions to Mineralogy and Petrology* **109** (2), 240-251.
- Wilkinson, J. F. G. & Stolz, A. J. (1997). Subcalcic clinopyroxenites and associated ultramafic xenoliths in alkali basalt near Glen Innes, northeastern New South Wales, Australia. *Contributions to Mineralogy and Petrology* **127** (3), 272-290.
- Wilson, J. T. (1963). A Possible Origin of Hawaiian Islands. *Canadian Journal of Physics* **41** (6), 863-870.
- Wolfe, C. J., Bjarnason, I. T., VanDecar, J. C. & Solomon, S. C. (1997). Seismic structure of the Iceland mantle plume. *Nature* **385** (6613), 245-247.
- Woodhead, J. D. (1996). Extreme HIMU in an oceanic setting: the geochemistry of Mangaia Island (Polynesia), and temporal evolution of the Cook-Austral hotspot. *Journal of Volcanology and Geothermal Research* **72** (1-2), 1-19.

-
- Woodhead, J. D. & McCulloch, M. T. (1989). Ancient Seafloor Signals in Pitcairn-Island Lavas and Evidence for Large-Amplitude, Small Length-Scale Mantle Heterogeneities. *Earth and Planetary Science Letters* **94** (3-4), 257-273.
- Wright, E. & White, W. M. (1987). The Origin of Samoa - New Evidence from Sr, Nd, and Pb Isotopes. *Earth and Planetary Science Letters* **81** (2-3), 151-162.
- Wright, J. B. (1976). Volcanic rocks in Nigeria. In: Kogbe, C. A. (ed) *Geology of Nigeria*. Lagos: Elizabethan Publishing Co., 125-173.
- Zindler, A. & Hart, S. (1986). Chemical Geodynamics. *Annual Review of Earth and Planetary Sciences* **14**, 493-571.
- Zindler, A., Hart, S. R., Frey, F. A. & Jakobsson, S. P. (1979). Nd and Sr isotope ratios and rare earth element abundances in Reykjanes Peninsula basalts: evidence for mantle heterogeneity beneath Iceland. *Earth and Planetary Science Letters* **45** (2), 249-262.

CHAPTER 2: ORIGIN OF MEGACRYSTS IN VOLCANIC ROCKS OF THE CVL

2.1. Introduction

One way of constraining the role of shallow contamination in a suite of lavas is to compare the isotopic composition of the lavas with cogenetic phenocrystic or xenocrystic phases that precipitated within the mantle. Lavas from Biu and Jos Plateau, northern CVL, contain abundant megacrysts of clinopyroxene (cpx), garnet (gnt), plagioclase (plag) and ilmenite (ilm), and subordinate megacrysts of amphibole (amph), spinel (sp), zircon (zr), corundum (cor), phlogopite (phlo) and olivine (ol). In this chapter, petrologic and petrographic evidence is presented, which shows that at least cpx and gnt megacrysts precipitated from recent CVL magmas within the lithospheric mantle, and constrains the role of magma mixing in the genesis of lavas from the Biu and Jos Plateau.

2.2. Results

2.2.1. Volcanic rocks of Biu and Jos Plateau

Major element, trace element and isotope data were obtained for 27 volcanic rocks from the younger Biu Plateau suite, 4 rocks from the older, plateau-building suite of the Biu Plateau, and 5 rocks from the younger Jos Plateau suites (see tables B.7. and B.19.). Analytical accuracy and precision is reported in tables B.8., B.18., B.20. and B.21. Only the younger suites of the Biu and Jos Plateau contain xenoliths (peridotites, pyroxenites and crustal rocks, see pic. 4-6) and megacrysts.

In the discrimination diagram of Le Bas *et al.* (1986), most Biu and Jos Plateau rocks are classified as basalts and include both nepheline- and hypersthene-normative compositions (fig. 2.1). The older plateau-building rocks of the Biu Plateau range from basanites to trachybasalts. In contrast, the younger volcanics have more variable chemistry ranging from basanites to phonolites. Figure 2.2 shows covariations of the major elements plotted versus MgO.

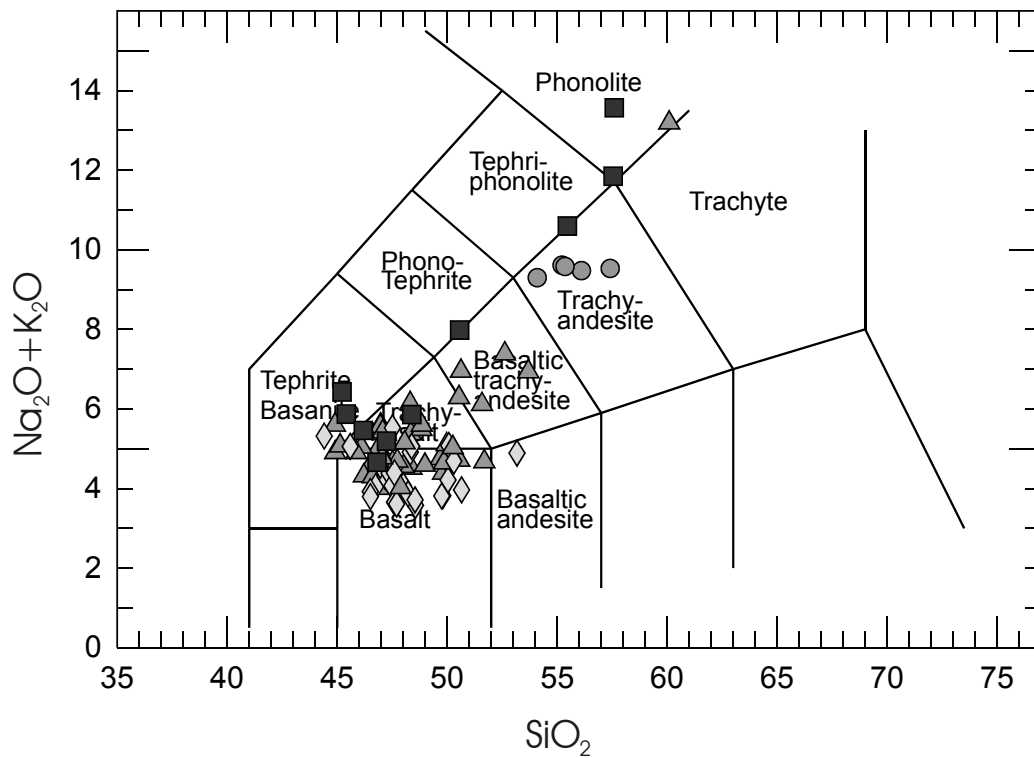


Fig. 2.1.: Total alkali versus silica discrimination diagram of Le Bas *et al.* (1986). Triangles: Biu young lavas, diamonds: Biu old lavas, squares: Jos lavas, grey dots: melt inclusions found in Biu ilmenite megacrysts. Most rock samples (literature and own data) are alkaline basalts. Both younger Biu and Jos Plateau lavas show fractionation paths towards phonolite. Phonolites carry inclusions of mantle xenoliths, suggesting phonolite evolution within in the mantle (Irving & Price, 1981).

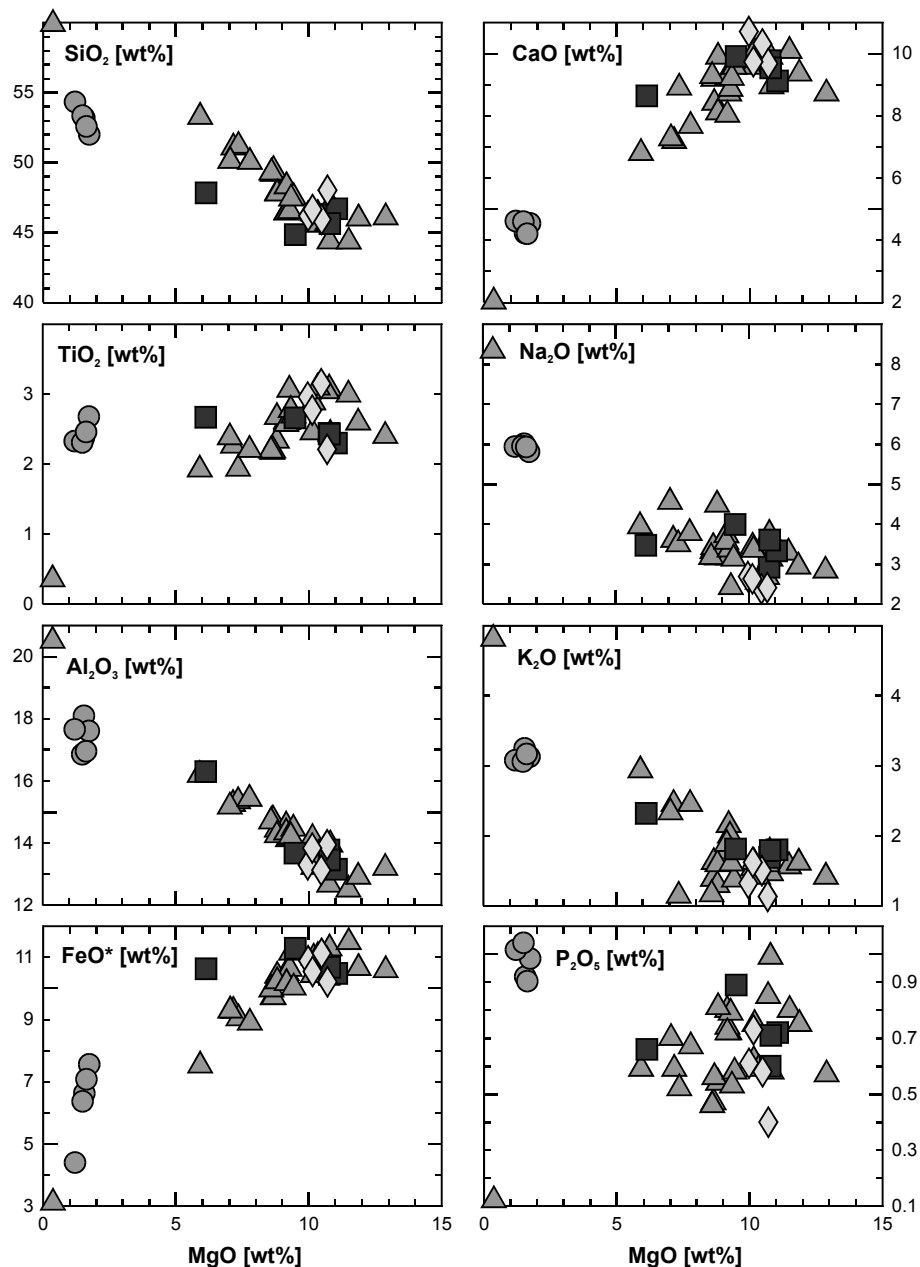


Fig. 2.2: Covariation of major elements of Biu and Jos Plateau rocks plotted vs. MgO. Coding as in fig. 2.1. FeO* = total Fe as FeO. Progressive fractionation is proceeding from right to left.

Although the cinder cones are only small volcanic structures that produced $<2 \text{ km}^3$ lava (Turner, 1978), rock samples from a single location can be chemically heterogeneous. For example, two samples from a single cone (Dam) are basanite and trachybasalt, respectively. Ilmenite megacrysts from a rock of basaltic trachyandesitic composition (Miringa) contain melt inclusions of a more evolved trachyandesitic composition. This highlights the importance of magma mixing processes in the genesis of the younger rocks.

Typical primitive mantle (McDonough & Sun, 1995) normalized trace element patterns for Biu and Jos Plateau samples are shown in fig. 2.3. Although all Biu and Jos rocks (except the phonolite) have trace element patterns similar to typical ocean island basalt patterns (cf. St. Helena basalt SH68 (Thirlwall, 1997) in fig. 2.3) with positive Nb and negative Pb anomalies, they are overall more enriched in incompatible elements than typical OIB. The melt inclusions found in ilmenite megacrysts are highly enriched in incompatible trace elements but depleted in the heavy rare earth elements, possibly indicating garnet fractionation in the genesis of the melts. The phonolite pattern is most enriched, but shows large negative troughs in phosphorus and titanium, pointing to fractionation of apatite and Fe-Ti-oxides. It lacks, however, a negative europium anomaly, indicating that plagioclase was not a major fractionating phase in phonolite genesis.

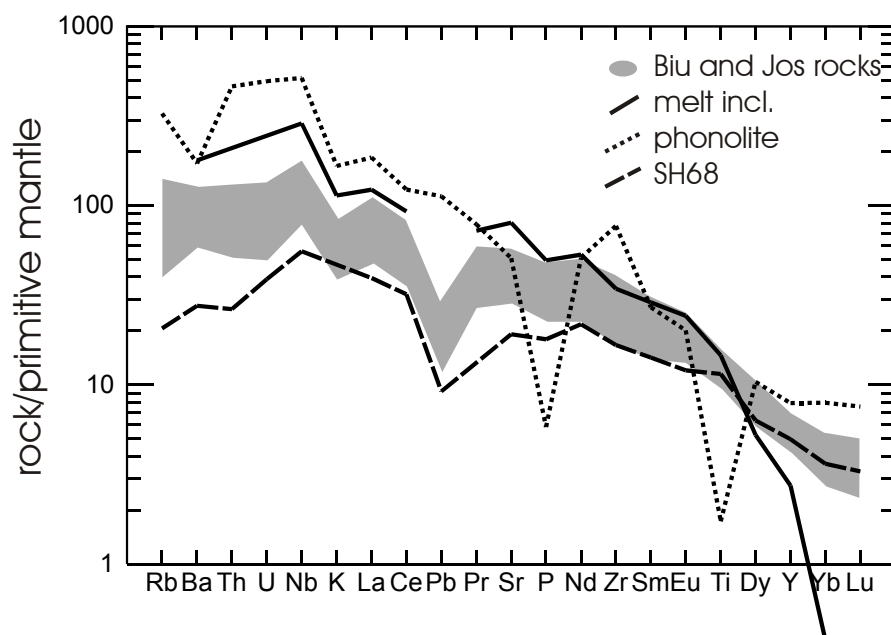


Fig. 2.3: Primitive mantle normalized trace element patterns for rock samples of Biu and Jos Plateau, along with a basalt pattern from St. Helena (Thirlwall, 1997), and the HREE depleted pattern of mean melt inclusions found in Biu ilmenite megacrysts (solid line, no Rb and Pb determinations available).

Two samples seem to be affected by late-stage alteration because of their unusual low U/Nb (Hilia 2), or low K/Rb (Hizshi), respectively. Excluding the two altered samples and the phonolite, La/Yb, Zr/Nb, Ce/Pb and K/U ratios are similar for Biu and Jos lavas and range from 17.6 – 63.8, 2.8 – 4.1, 23.5 – 38.8 and 6060 – 12200, respectively. While La/Yb and Zr/Nb ratios are comparable to ratios reported for HIMU-type ocean island basalts worldwide

(e.g. Sun & McDonough (1989), Weaver (1991), Thirlwall (1997)), Ce/Pb and K/U ratios are highly variable and cover the full range from MORB to HIMU.

2.2.2. Megacrysts – major element systematics

Detailed chemical analyses of megacrysts from Biu and Jos Plateau are presented in tables B.9.-B.17 and B.22. The megacryst-suite of Biu and Jos Plateau was described in detail by Wright (1970) and Frisch & Wright (1971) and comprises chemically homogeneous crystals of clinopyroxene (cpx), garnet (gnt), plagioclase (plag) and ilmenite (ilm) with diameters of up to several cm, while crystals of olivine (ol), amphibole (amph), spinel (sp), apatite (apa), zircon (zr) and blue corundum (cor) are extremely rare. Only ilmenite, spinel, zircon, corundum and evolved compositions of cpx occasionally show planar faces.

The most abundant phase is a subcalcic titaniferous aluminous augite with poor cleavage, conchoidal fracture and a glassy appearance on freshly broken surfaces (pic. 7). Megacrysts as a whole define smooth trends in major element variation diagrams (fig. 2.4). In thin section cpx megacrysts occasionally show signs of deformation and frequently channels of fluid inclusions (pic. 8, 9). Furthermore, some contain small drop-shaped polyphase assemblages of Fe-Cu-Ni-sulfides (pic. 10, 11), which may or may not be orientated along crystallographic planes. A preliminary EDS study revealed three different S-bearing phases, namely pyrite, pyrrhotite and chalcopyrite. The sulfide grains are similar to the pyroxenite-hosted sulfide suite described by e.g. Guo *et al.* (1999) and are consistently interpreted as exsolution from monosulfide solid solution that was initially present as an immiscible sulfide liquid during growth of the megacrysts. Frequently observed are intergrowths between cpx and garnet in a magmatic cumulus texture (pic. 12, 13), whereas the range of chemical compositions of cpx and gnt in the intergrowths overlaps the range of compositions of cpx and gnt found as solitary crystals (fig. 2.4). Only most evolved cpx compositions are sometimes intergrown with plagioclase and apatite (pic. 14). When in contact with the host melt, evolved cpx compositions show breakdown reactions (pic. 15).

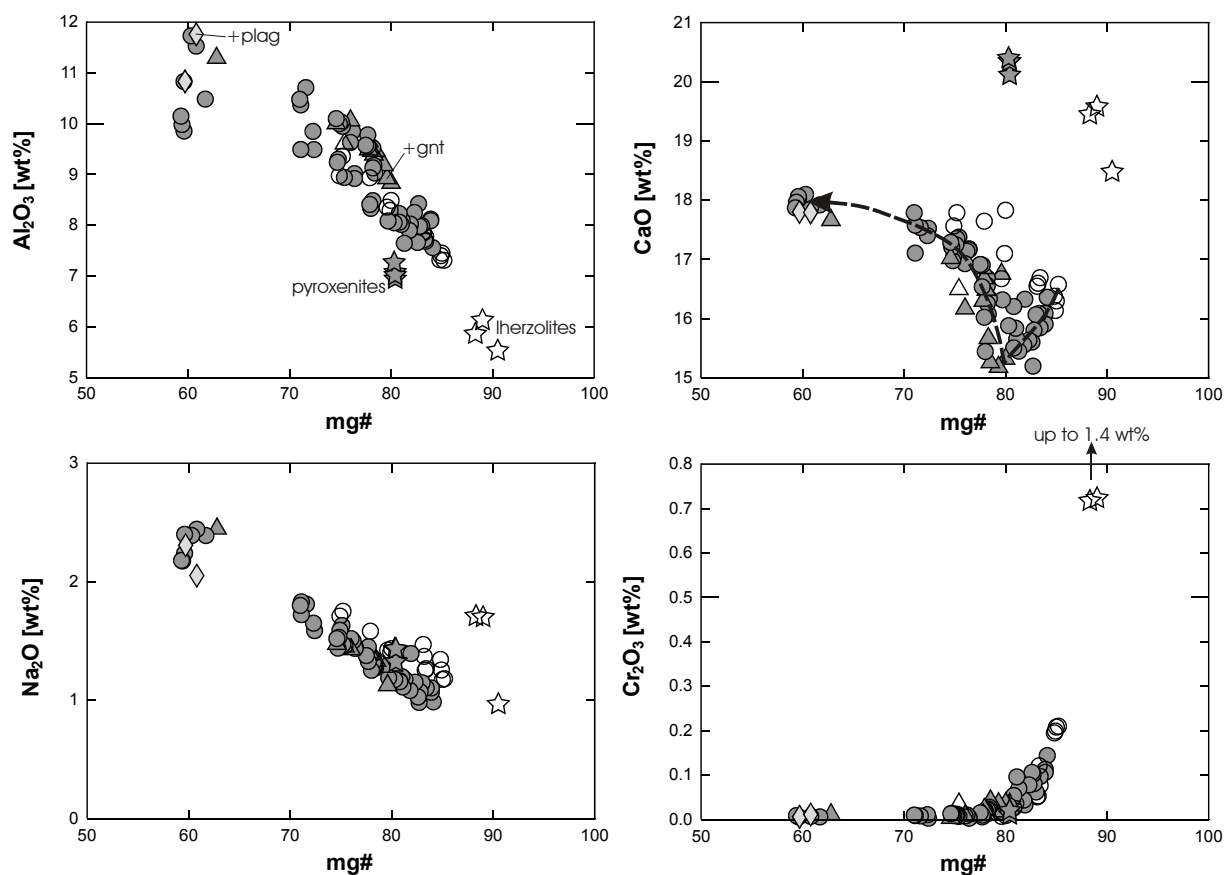


Fig. 2.4: Covariation of Al_2O_3 (a), CaO (b), Na_2O (c) and Cr_2O_3 (d) with mg# of cpx megacrysts (mg# = molar $\text{MgO}/(\text{MgO}+\text{FeO})$). Filled circles: Biu Plateau, open circles: Jos Plateau, triangles: cpx intergrown with garnet, diamonds: cpx intergrown with plagioclase and apatite. Filled stars mark cpx from pyroxenite xenoliths, open stars cpx from sp-lherzolite xenoliths. Megacrysts as a whole define smooth trends consistent with fractional crystallization from an evolving magma. Individual grains, however, are chemically unzoned. In terms of their major element chemistry, cpx derived from lherzolite xenoliths are different from megacryst cpx in their overall higher mg#, and lower Al_2O_3 and higher CaO . There is a compositional gap between cpx with mg# 85-70 and a group of evolved cpx with mg# of ~60, which are sometimes intergrown with plagioclase and apatite. Only cpx with mg# lower than ~80 are sometimes intergrown with garnet, suggesting a kink in the CaO trend (stippled line in b). Cpx from the Jos Plateau comprise the most primitive compositions and have somewhat higher Na_2O for a given mg# than Biu cpx.

Solitary crystals of garnet are solid solutions of pyrope (61-73 wt%), almandine (14-23 wt%), grossular (5-10 wt%) and andradite (see chapter 2.2.4 for analyses of Fe^{3+}). The crystals display the same homogeneous nature as cpx, some of them have an identical sulfide inclusion suite as cpx. Larger unfragmented pieces of several centimeters diameter are well rounded by magmatic resorption and show reaction rims of usually $<100 \mu\text{m}$, which extend into the crystal along cracks (pic. 16, 17).

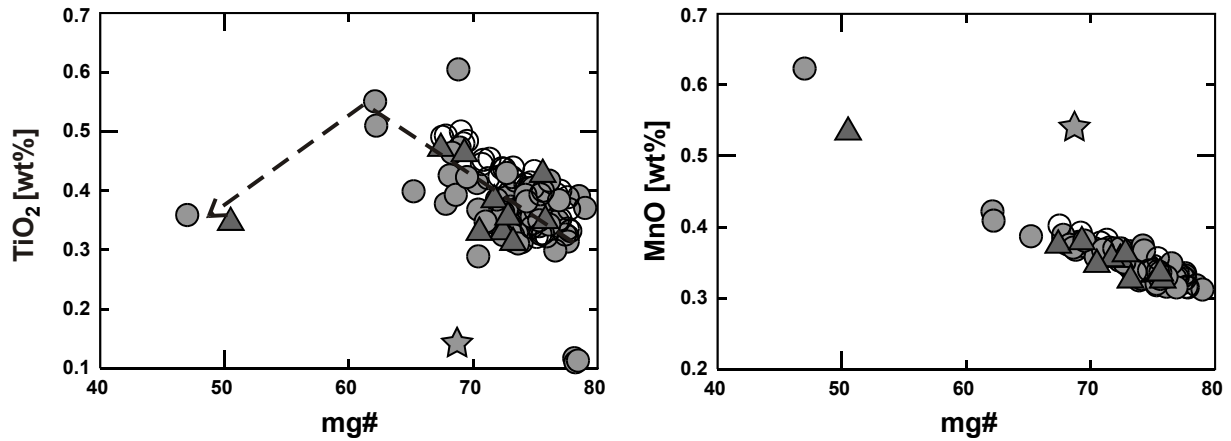


Fig. 2.5: Covariation of TiO_2 (a) and MnO (b) with $\text{mg}\#$ of garnet megacrysts. Coding as before. Garnet that formed as exsolution in the pyroxenite has lower TiO_2 and higher MnO for a given $\text{mg}\#$. The kink in TiO_2 concentrations may be due to the onset of additional ilmenite fractionation. Few solitary grains of gnt with $\text{mg}\# \sim 78$ also show low TiO_2 , but their origin as exsolution cannot be proved.

Abundant ilmenite megacrysts are solid solutions of FeTiO_3 (54-65 wt%), MgTiO_3 (6-15 wt%) and Fe_2O_3 (20-40 wt%) and often show planar faces (pic. 18). Ilmenite that formed as exsolution from cpx differs from megacrysts in its higher MgTiO_3 (24-34 wt%) contents. Ilmenite is the only phase in which melt inclusions (evolved benmoreitic compositions) were observed (pic. 19).

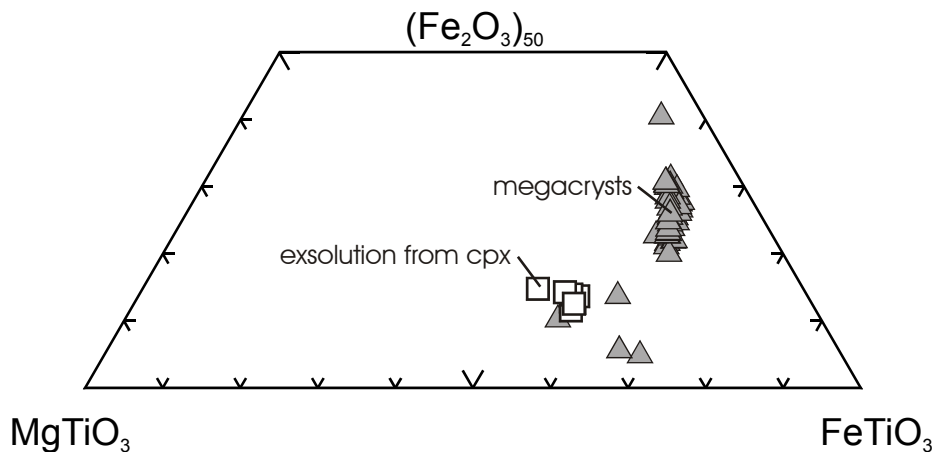


Fig. 2.6: Ilmenite megacrysts in the ternary system hematite – geikielite – ilmenite.

Plagioclase megacrysts are clear crystals of oligoclase to andesine with a mean of an_{25} (pic. 20). They often are rounded by magmatic resorption. Plagioclase intergrown with evolved cpx defines the most calcic compositions, but is indistinguishable from larger solitary crystals of up to several centimeters in size.

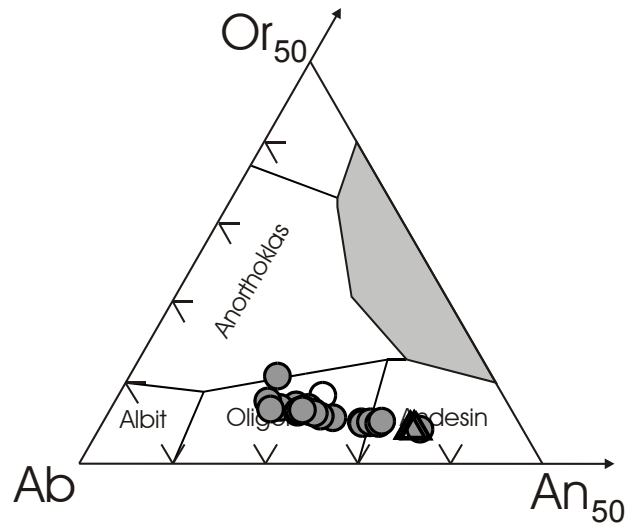


Fig. 2.7: Plagioclase megacryst compositions in the high temperature system orthoclase (or) – albite (ab) – anorthite (an). Triangles mark intergrowths with cpx.

2.2.3. Megacrysts – trace element systematics

Figure 2.8 shows the chondrite-normalized trace element concentrations for cpx and gnt megacrysts. All of them were found to be chemically unzoned within error of trace element analysis. The most primitive cpx compositions of Biu and Jos Plateau with $mg\#$ of 84-75 are similar. Decreasing $mg\#$ of cpx is correlated with enrichment of the highly incompatible elements, but heavy rare earth elements (HREE) show progressively fractionated patterns with Tm, Yb and Lu below detection limit of the ionprobe. Figure 2.8 also includes patterns of a cpx from a spinel-peridotite xenolith which is distinct from megacryst cpx in its more depleted pattern, and a cpx from a pyroxenite xenolith which is similar in shape but overall more enriched for a given $mg\#$ and has troughs in Ti and Nb concentrations. Both xenoliths were brought to the surface along with the recent Biu Plateau volcanism.

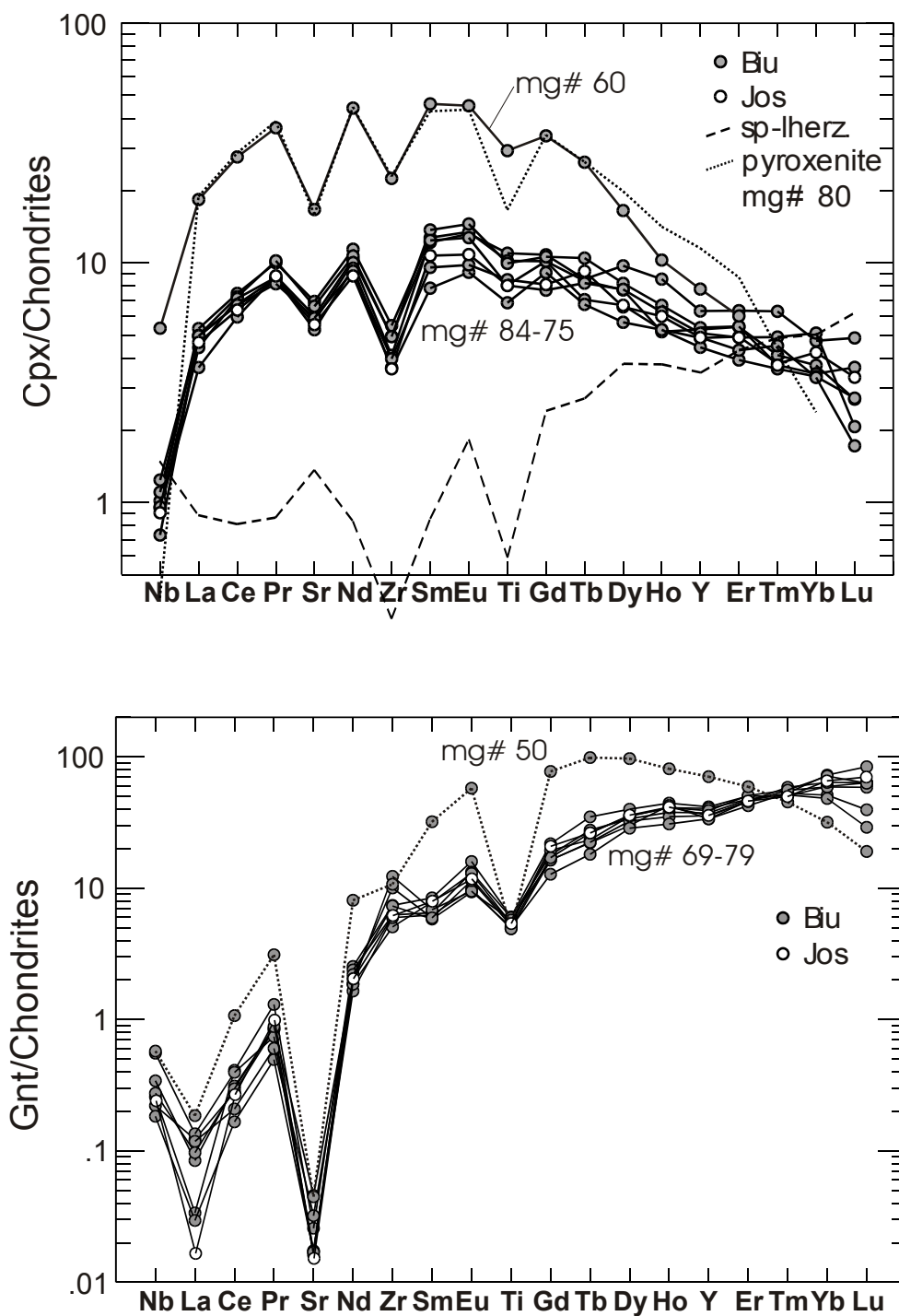


Fig. 2.8: Chondrite (McDonough & Sun, 1995) normalized trace element pattern of cpx (a) and gnt (b) megacrysts measured by SIMS. Evolved cpx and gnt compositions have fractionated HREE with Tm, Yb and Lu below DL for cpx. There is no detectable difference between the most primitive Biu and Jos Plateau megacrysts which points to a common source magma. Lherzolite-derived cpx is markedly different from megacryst cpx in its depleted pattern, pyroxenite-derived cpx shows higher trace element concentrations for a given mg# and relative depletions in niobium and titanium.

2.2.4. Megacrysts – moessbauer spectroscopy

Calculations of Fe^{3+} in e.g. cpx megacrysts based upon charge balance (Droop, 1987) should generally be handled with care because of the possible involvement of vacancies in the cpx structure and/or imprecision in the microprobe determination of SiO_2 (McGuire *et al.*, 1989). McGuire *et al.* (1989) found uniformly high $\text{Fe}^{3+}/\text{Fe}_{\text{tot}}$ of $30 \pm 3\%$ in cpx megacrysts from western Saudi Arabia, as opposed to what would be expected from low mantle oxygen fugacities. Because precise determinations of Fe^{3+} are crucial in the application of Fe^{2+} -Mg exchange thermometers (e.g. the one of Krogh (1988) which was used in this study), we analyzed a suite of cpx and garnet megacrysts using moessbauer spectroscopy. The results are given in tables B.9 and B.10. Figure 2.9 compares the results from moessbauer spectroscopy with those calculated by charge balance.

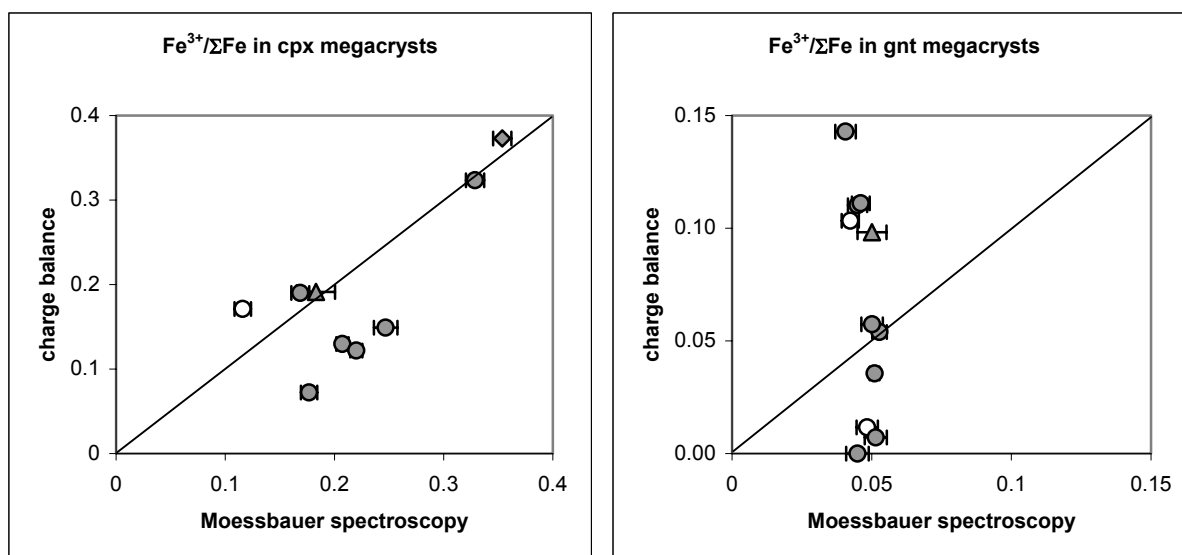


Fig. 2.9: Comparison of $\text{Fe}^{3+}/\text{Fe}_{\text{tot}}$ in cpx (a) and gnt (b) megacrysts measured by moessbauer spectroscopy with calculated values based on crystal charge balance (Droop, 1987). There is good agreement for evolved cpx megacrysts. However, there is considerable scatter in the calculated data for more primitive cpx compositions. There is practically no variation of $\text{Fe}^{3+}/\text{Fe}_{\text{tot}}$ in gnt megacrysts, in contrast to the results from charge balance calculations.

Indices of progressive fractionation such as e.g. decreasing mg# or increasing TiO_2 are correlated with increasing Fe^{3+} in cpx megacrysts, which may be used to calculate Fe^{3+} (and Fe^{2+}) for any given cpx megacryst from Biu and Jos Plateau. Together with the absence of significant variation of $\text{Fe}^{3+}/\text{Fe}_{\text{tot}}$ in gnt megacrysts, accurate input values for thermobarometric equations may be derived.

2.3. Discussion

2.3.1. Fe³⁺ and calculation of temperatures

The high pressure experimental data on which thermobarometric equations are calibrated are mostly derived from runs in graphite capsules. Fe³⁺/Fe²⁺ equilibrium of the experimental charge therefore is buffered on the GCO oxygen buffer. In their subsequent inversion of the data to thermobarometric expressions Putirka *et al.* (1996) and Krogh (1988) did not apply Fe³⁺-corrections based upon the reducing nature of the GCO buffer and hence low concentrations of Fe³⁺. Using the GCO calibration curve of Ulmer & Luth (1991), one calculates $\log(fO_2) = -6.8$ at $T = 1400^\circ\text{C}$ and $P = 20$ kbar. Off-craton peridotites record a range of oxygen fugacities during depletion of $\sim\text{NNO}$ to $\text{NNO}-3$ (Canil, 2002) (NNO = nickel-nickeloxide oxygen buffer). Assuming a mean of $\text{NNO}-1.5$, 1400°C and 20 kbar this translates to $\log(fO_2) = -6.7$ (O'Neill & Wall, 1987), which is very similar to the experimental conditions of Putirka *et al.* (1996) and Krogh (1988). It is concluded that the mentioned thermobarometric expressions give accurate results for the more primitive cpx and gnt compositions without correcting for Fe³⁺. However, this may not be true for the highly evolved cpx compositions with Fe³⁺/Fe_{tot} of as much as 35%. For example, taking the most evolved cpx/gnt intergrowth, one calculates an uncorrected temperature of 1387°C at $P = 20$ kbar, which is similar to most primitive cpx/gnt intergrowths. If correction for Fe³⁺ is applied, the calculated temperature decreases to 1097°C . Because we will show in a later section that the megacrysts are related by fractional crystallization (which requires decreasing temperature, cf. fig. 2.10), we conclude that the Fe³⁺-corrected results are more realistic for evolved megacrysts. However, no correction for primitive megacrysts is applied.

2.3.2. Origin of megacrysts - cogenetic or exotic to their host magma?

Different models for the genesis of megacrysts in alkaline basalts and kimberlites have been proposed and were summarized by e.g. Schulze (1987). Megacrysts could represent xenocrystic phases derived from disaggregated peridotite-, pyroxenite-, or gabbroic xenoliths (Irving, 1974), (Righter & Carmichael, 1993), or they could be magmatic phases from an earlier magmatic event unrelated to the volcanism, which brought them to the surface (Liotard *et al.*, 1988), (Capedri *et al.*, 1989), (Davies *et al.*, 2001), or they could be genetically related to their host lavas (Green & Ringwood, 1967), (Binns, 1969), (Binns *et al.*, 1970), (Frisch & Wright, 1971), (Wilkinson, 1975), (Irving & Frey, 1984), (Jones, 1987), (Moore, 1987),

(Geist *et al.*, 1988), (Wilkinson & Hensel, 1991), (Hops *et al.*, 1992), (Liu *et al.*, 1992a), (Liu *et al.*, 1992b), (Nasir, 1995), (Schulze *et al.*, 2001). Much of the discussion in literature was based upon comparison of isotope systematics or trace element concentrations of lavas and megacrysts. However, petrologic and petrographic evidence may be better suited to constrain the origin of some megacryst suites, because isotopic compositions and trace element budgets of the lavas may be modified subsequent to megacryst formation. In this section, these possibilities are evaluated for the megacrysts of the Biu and Jos Plateau.

Lavas from the Biu and Jos Plateau contain abundant upper mantle xenoliths, raising the possibility that associated megacrysts represent disaggregated phases of such peridotite and/or pyroxenite xenoliths. However, megacryst major element compositions and their systematic covariations (cf. fig. 2.4 and 2.5) are consistent with crystallization from an evolving magma (Putirka *et al.*, 1996), (Bultitude & Green, 1971), (Putirka, 1998), (Johnson, 1998), (Hart & Dunn, 1993), (Green *et al.*, 2000), (Rocholl *et al.*, 1996), (Hauri *et al.*, 1994), (Dunn, 1987), (Skulski *et al.*, 1994).

Temperatures calculated from primitive cpx-gnt megacryst intergrowths using the formulation of Krogh (1988) at an assumed pressure of 20 kbar, yield high temperatures of $1429 \pm 37^\circ\text{C}$. A change of ± 5 kbar in the pressure estimate translates into a shift of temperature of $+30^\circ/-56^\circ\text{C}$. The most evolved cpx-gnt megacryst intergrowth yields a Fe^{3+} -corrected temperature of only $\sim 1100^\circ\text{C}$ (cf. fig. 2.10). This is comparable to ambient lithospheric temperatures as recorded by spinel-lherzolite xenoliths from Biu Plateau (Lee *et al.*, 1996), which yield a mean temperature of $\sim 1000^\circ\text{C}$.

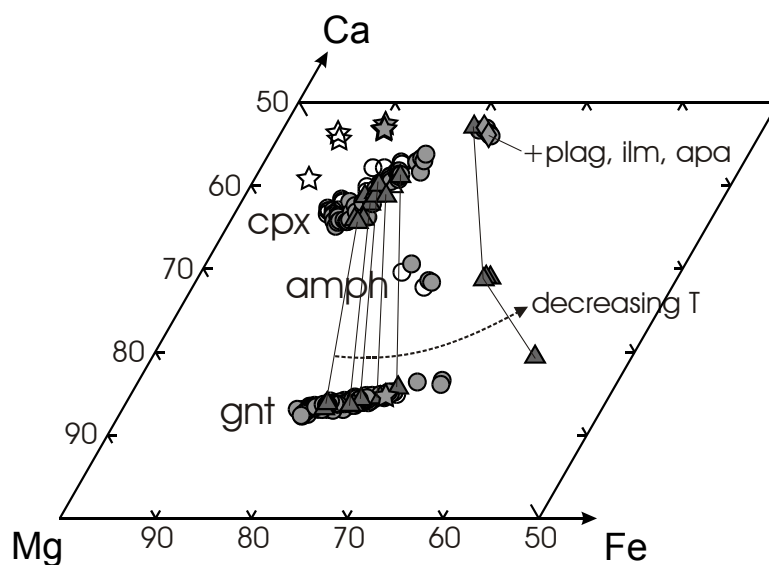


Fig. 2.10: Covariation of cpx, gnt and amphibole (potassian-titanian pargasites) megacrysts in the Ca-Mg-Fe quadrilateral. All Fe as FeO . Coding as before with intergrowths of megacrysts connected by tie-lines. The appearance of amphibole in the fractionating assemblage is consistent with an upper temperature limit of magmatic amphibole of $\sim 1250^\circ\text{C}$ (Huckenholtz *et al.*, 1992).

In summary, the compositional differences between pyroxenite- or peridotite-derived cpx/gnt and the megacrysts shown in fig. 2.4, 2.5, 2.6 and 2.8 and the range of magmatic temperatures recorded in cpx/gnt intergrowths (fig. 2.10) preclude formation of the megacrysts via simple xenolith disaggregation.

Because magmatism on both the Biu and Jos Plateau occurred in several time periods, we also have to evaluate the possibility that megacrysts could be cognate to an older magmatic event (the 147-106 Ma event in the northern Benue, cf. chapter 2.1.2) and were mechanically incorporated into the recent volcanism which brought them to the surface. The megacrysts preserve magmatic textures and temperatures and lack compositional zoning or exsolution lamellae. The pyroxenite xenolith on the other hand is similar to those studied by Sautter & Harte (1988), Sautter & Harte (1990), Sen & Jones (1988), Wilkinson & Stolz (1997), in that it shows (in contrast to any megacryst) exsolution lamellae of gnt and ilm in matrix cpx, strong diffusional gradients towards the lamellae, and a recrystallized metamorphic texture in parts of it (pic. 21,22). The temperature estimate for the cpx-gnt exsolution interface in the pyroxenite of $\sim 900^{\circ}\text{C}$ represents a freezing temperature, because further cooling to $\sim 630^{\circ}\text{C}$ is indicated by cpx-sp thermometry (Andersen *et al.*, 1993). The history of this pyroxenite xenolith is therefore interpreted as initial formation as cpx-sp-ilmenite accumulate from a basaltic liquid and subsequent isobaric cooling from high initial temperatures down to ambient lithospheric temperatures. Such cooling leads to decreasing subsolidus aluminium- and titanium-solubility in cpx (Herzberg, 1978), (Velz, 1999), (Sepp & Kunzmann, 2001), and ultimately exsolution of an Al- and/or Ti-rich phase such as garnet and ilmenite, respectively. Because recrystallization, diffusional gradients or exsolution are not observed in cpx megacrysts, it rules out the possibility that the megacrysts were precipitated by an earlier magmatic event and stored in cooler lithosphere before eruption to the surface with the recent volcanism.

Although it is difficult to give an upper time limit for the development of exsolution lamellae in cpx, similar Hawaiian xenoliths with a maximum age of the lithosphere of 90 Ma do show exsolution lamellae (Sen & Jones, 1988). More time constraints can be deduced from the length of diffusion profiles of magmatic cpx-gnt megacryst intergrowths (fig. 2.11 and pic. 23). The observed Fe-Mg concentration gradient in cpx adjacent to gnt would have been generated by keeping the assemblage at a lithospheric temperature of e.g. 1000°C (mean of xenolith data from Lee *et al.* (1996)) in only a few hundred years and thus the gnt-cpx assemblage cannot have been stored after precipitation at $\sim 1400^{\circ}\text{C}$ (defined by the plateau concen-

trations) for any significant amount of time in cooler lithosphere. A complete rehomogenisation of initially colder material on the other hand can be ruled out based on the magmatic texture and lack of zonation in very slow diffusing species such as Al in cpx.

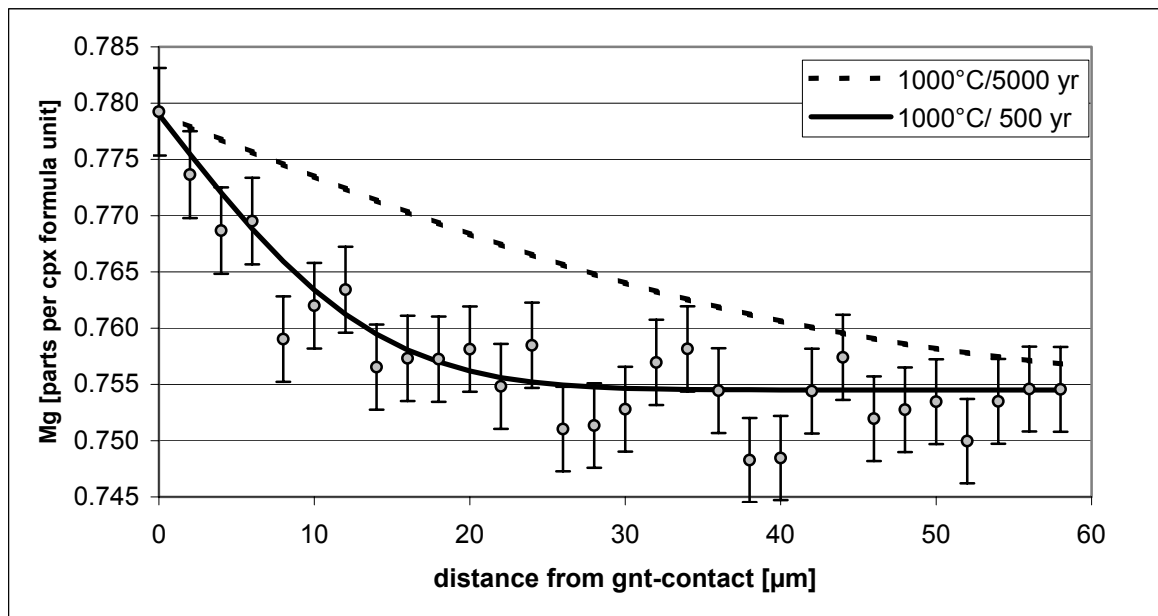
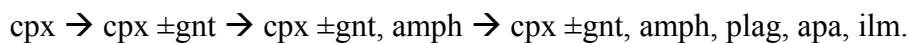


Fig. 2.11: Diffusion profile perpendicular to cpx-gnt interface. 2σ -error bars ($\sim 0.8\%$ rel.) calculated from counting statistics of EPMA. The fitted profile is a simple error function and is only dependant on time and the binary Mg-Fe interdiffusion coefficient D , which is itself a function of temperature. The observed gradient can be generated by keeping the assemblage at 1000°C in only 500 years, whereas a change of 100° of the ambient temperature translates into a time factor of ~ 10 . The plateau concentration is homogeneous throughout the crystal ($\sim 2\text{mm}$) and therefore was used to calculate the initial equilibration temperature of cpx-gnt. Since all relevant species have lower diffusivities in cpx than in gnt (Dimanov & Sautter, 2000), it is sufficient to look at cpx profiles for it is the rate limiting exchange partner.

In summary, it is concluded that the magmatic textures, temperatures and lack of zoning or exsolution lamellae indicate that the cpx and gnt megacrysts do not derive from an older period of CVL volcanism. Therefore, the megacrysts must be derived from magmas related to recent (~ 5 Ma to present) magmatism on Biu and Jos Plateau. The sequence of megacryst crystallization is deduced on the basis of major element covariations in fig. 2.4, 2.5, 2.7 and 2.10 and the systematics of mutual intergrowths shown in fig. 2.10 as



2.3.3. Where did the megacrysts grow – pressure estimates

Pressure estimates for crystallization of megacrysts are not easy to obtain because of the lack of a suitable barometer. However, results from high pressure experiments provide a matching sequence of crystallization with consistent major element compositions during fractionation of a basanitic/alkali-basaltic composition at upper mantle pressures. The pMelts code (Hirschmann *et al.*, 1998) can be considered a parameterization of such processes that is especially well calibrated in the pressure range between 10 and 20 kbar. Figure 2.12 shows a simplified calculated phase diagram for one of the most primitive lavas erupted on the Biu Plateau, which is similar to the experimental olivine nephelinite data of Bultitude & Green (1971).

With increasing pressure (above ~12 kbar) cpx replaces ol as the first liquidus phase for the liquid chosen. Based on the absence of olivine megacrysts and high Ni and Cr contents of most primitive cpx compositions, it is concluded that crystal fractionation started in the primary stability field of cpx which requires pressures greater than ~12 kbar. If fractionation took place at pressures corresponding to that at the base of the crust, we expect initial fractionation of olivine and consequently depletion of Ni in the liquid remaining (fig. 2.13). However, the observed high concentrations of Ni in most primitive cpx megacrysts in fig. 2.13 are not consistent with a low pressure fractionation history. Olivine present as small phenocrysts in the host lavas on the other hand crystallized most probably during and after eruption to the surface because of expansion of the olivine stability field at shallower pressure. This is consistent with calculated olivine/whole-rock temperatures of 1220 (–40/+20) °C (Putirka, 1997). (Equilibrium between olivine and whole-rock was assumed if calculated equilibrium olivine compositions (with $K_D^{ol/liq.}(Mg-Fe) = 0.30 \pm 0.03$ (Roeder & Emslie, 1970)) matched measured olivine phenocryst cores).

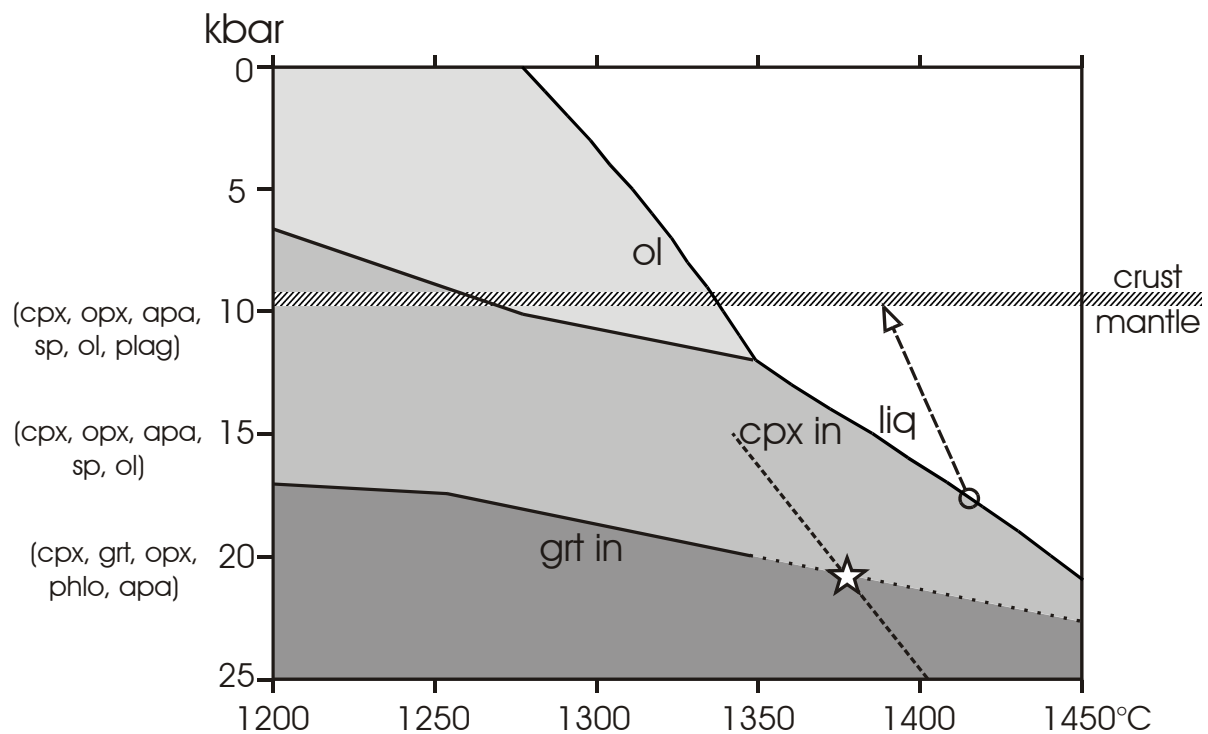


Fig. 2.12: Calculated phase diagram for a primitive Biu Plateau alkali basalt using the pMelts code (Hirschmann *et al.*, 1998). At pressures above ~12 kbar cpx replaces ol as the first liquidus phase. Dotted line marks locus of possible P,T-pairs for one cpx-gnt intergrowth. Phases in parenthesis (left side) are calculated near-solidus fractionation assemblages at 10, 15 and 20 kbar respectively. The crust-mantle boundary (Biu: 30 km, Jos: 28 km) is based upon gravity data (Poudjom-Djomani *et al.*, 1995). Note that for cpx and gnt to be near-liquidus phases they have to fractionate in the mantle. An adiabatic ascending path (arrow) will not saturate the magma in cpx or gnt. Addition of 0.5 wt% water will lower the solidus by ~40°K (Green, 1973), whereas addition of CO₂ will expand the liquidus phase volume of gnt against that of diopside and is therefore similar to increasing pressure (Adam, 1988).

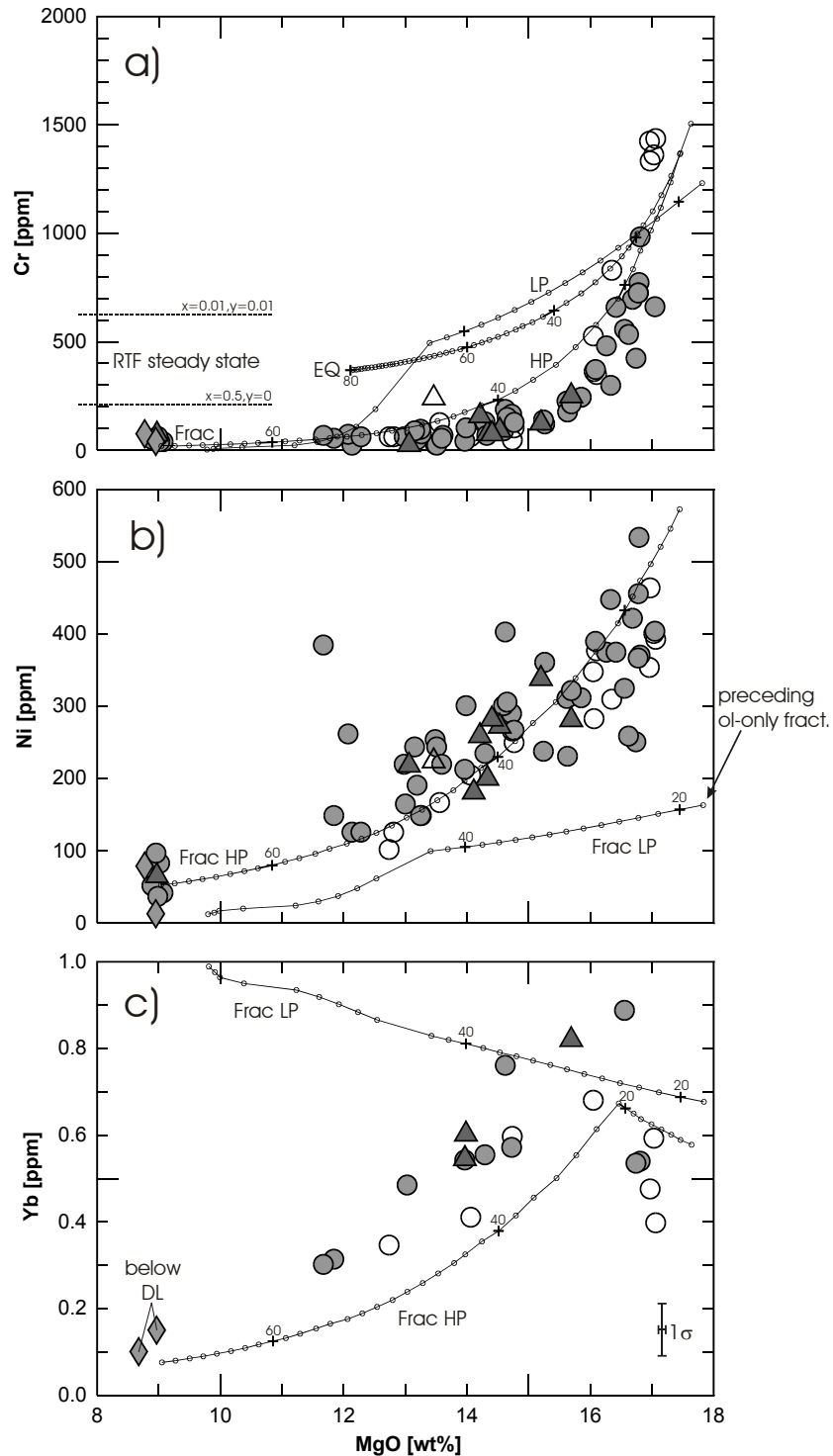


Fig. 2.13: MgO vs. Cr (a), Ni (b) and Yb (c) of cpx megacrysts. Symbols as fig. 2.4. The equilibrium and fractional crystallization models are calculated based on the phase proportions as predicted by the pMelts/Melts codes at 20 kbars (HP - pMelts) and 8 kbars (LP - Melts), respectively. Distribution coefficients were taken from Zack *et al.* (1997), Johnson (1998), McKenzie & O'Nions (1991), Nikogosian & Sobolev (1997) and Mysen (1978). Every point in the model curve represents 5° cooling while numbers refer to the percentage of solids crystallized. **a)** An equilibrium type crystallization will not yield the low concentrations of compatible elements (Cr and Mg) in the liquid and corresponding cpx. We also plotted the concentrations in a

steady state (RTF) magma chamber (O'Hara & Mathews, 1981), which for reasonable mass fractions of liquid crystallizing (x) and escaping (y) in each cycle also predicts too high Cr-concentrations. **b)** LP fractionation starts out with olivine (~18 wt%) and quickly depletes the liquids in Ni, which is inconsistent with high Ni concentrations in primitive cpx megacrysts. **c)** The sharp bend in the HP model curve of Yb marks onset of additional gnt-fractionation and therefore confirms the involvement of gnt in the fractionating assemblage (filled triangles). A low pressure fractionation path without involvement of gnt will not deplete liquids and cpx in HREE and therefore is inconsistent with the data.

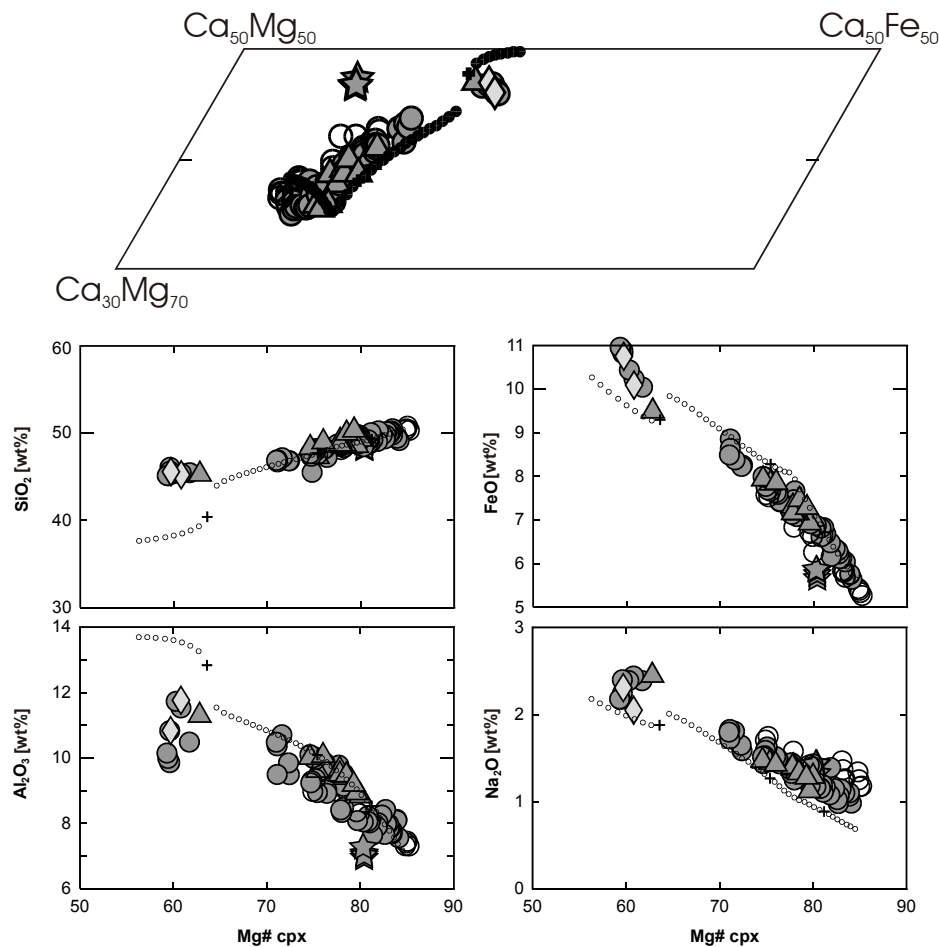


Fig. 2.14: Major element variations in cpx megacrysts versus cpx compositions predicted by the pMelts code (Hirschmann *et al.*, 1998) at 20 kbar assuming fractional crystallization. The trends predicted for mg# 85 – 70 are in good agreement with the variations observed in the megacrysts as a whole. The kink in CaO of cpx megacrysts in **a)** arises from onset of additional gnt fractionation (and not because of coexistence of opx), consistent with our data. However, the calculation assumes constant pressure, which may not be the case in nature. This may also be the reason for the poor fit of the highly evolved cpx megacrysts intergrown with plagioclase and apatite. Although there is no systematic experimental data for the stability of magmatic plagioclase in evolved liquids, available data suggests that these megacrysts have fractionated at shallower depths of <15 kbar.

Inspecting the phase diagram in fig. 2.12 further, we find that at higher pressures of ~17-20 kbar cpx is joined by garnet upon isobaric cooling. The depletion in heavy rare earths of evolved cpx (fig. 2.8a) is consistent with concurrent fractionation of garnet. In addition, major element compositions of more primitive cpx (and gnt, not shown) calculated by the pMelts code are consistent with those measured in the megacrysts (dotted curves in fig. 2.14). Combining the phase diagram with the locus of possible P,T-pairs of one cpx-gnt intergrowth calculated with the thermometer of Krogh (1988), we can further specify the formation pressure of that intergrowth to be greater than ~21 kbar (stippled line in fig. 2.12).

If we assume that most primitive cpx and basanitic melts found at the surface were in equilibrium at some point in their history, we can also use the cpx-liquid geothermometer of Putirka *et al.* (1996) and iteratively calculate a consistent P,T-estimate of 22 kbar and 1380°C from the most primitive cpx compositions from Biu Plateau and a slightly higher estimate of 23 kbar and 1390°C from the most primitive Jos Plateau cpx megacrysts. This result is rather insensitive to the exact melt composition as long as it is a primitive basanite or alkali basalt.

Although each of the above pressure estimates is dependant on certain model assumptions, the results are encouragingly mutually consistent. In each case, the pressure estimate for the primitive gnt and cpx megacrysts is ~17-23 kbar. Because the crust-mantle boundary underneath the Biu/Jos Plateaus is constrained from seismic data to depths of only 28/30 (± 6) km or 8/9 (± 2) kbar (Poudjom-Djomani *et al.*, 1995), this requires that the megacrysts grew well below the crust/mantle boundary, and we can therefore take the megacrysts as probes of melt evolution within the mantle.

Even though the liquid chosen in fig. 2.12 is not in equilibrium with mantle phases such as ol and opx at high pressure, it can be derived from a primary liquid such as the picritic basanite of Bultitude & Green (1971) by initial fractionation of ~10% olivine, which might be deposited in deep dunite channels leading from the area of magma formation to a magma chamber in the lithospheric mantle. This is consistent with slightly depleted Ni concentrations in the basanitic magmas of ~300 ppm as compared to 400-500 ppm in hypothetical primary liquids that are in equilibrium with typical mantle olivine with ~3000 ppm Ni. The origin of some rare large crystals of olivine that were collected on the Biu Plateau, with high forsterite contents ($f_{O_{91.6}}$), strong internal deformation textures and abundant melt and fluid inclusions, is as yet unclear. They may, however, represent fragments of dunite melt channels of the higher parts of the magma feeder system.

Since the majority of experimental data is obtained either from near liquidus conditions in basaltic systems or near solidus conditions in peridotitic systems there are few data published on evolved liquids which might shed some light on the genesis of ilmenite, albite-rich plagioclase, zircon and corundum (Guo *et al.*, 1996a), (Guo *et al.*, 1996b), (Sutherland *et al.*, 1998), (Sutherland & Fanning, 2001). Until a series of progressive experiments simulating fractional crystallization is available, the calculated near solidus fractionation assemblages in fig. 2.12 are relatively uncertain.

2.3.4. Further constraints on megacrysts growth

A liquid adiabatic ascending path with a typical dT/dz of $\sim 1^\circ\text{K km}^{-1}$ (McKenzie & Bickle, 1988) will not saturate the magma in any phase (arrow in fig. 2.12). We therefore conclude that cpx and garnet cannot be derived by flow differentiation of a rising magma unless significant heat is dissipated into the wall rock. However, the unzoned nature of the megacrysts suggests derivation from a slow evolving or quasi-steady state magma chamber (O'Hara & Mathews, 1981). For equilibrium or steady state RTF (periodically replenished, periodically tapped, continuously fractionated) type crystallization we expect buffering of compatible elements such as Mg, Cr and Ni at relatively high levels (e.g. Cr-concentrations >200 ppm in evolved cpx, see fig. 2.13a). However, what we observe is strong depletion in these elements in paths that are consistent with fractional crystallization.

Although pMelts modeling suggests that cpx precipitated by as much as 65% fractional crystallization from a basaltic liquid (fig. 2.13 and 2.14), the megacrysts have to grow homogeneously directly from the melt because of extremely long diffusional equilibration times. The diffusional relaxation of an initially growth-zoned cpx of 5 cm in diameter for example requires for the slow diffusing species aluminium ~ 220 Ma at 1350°C (after Chakraborty & Ganguly (1991)'s formulation $t_{\text{rel.}} \sim a^2/2D$, and $D(T)$ calculated with data from Jaoul *et al.* (1991)). Although the effects of pressure, oxygen fugacity and H_2O -activity on Al-diffusion are still uncertain, the time scale is definitively larger than 5-10 Ma of recent volcanism. The evidence for fractional crystallization (fig. 2.13) combined with the unzoned nature of the megacrysts, suggests that megacrysts derived from relatively large (and therefore slow cooling) magma chambers that formed within the subcontinental lithospheric mantle during CVL volcanism.

2.3.5. Contrasting crystallization/magma mixing histories deduced from megacrysts and lavas

In this section, we evaluate trace element budgets and distributions between melts and fractionated phases in order to constrain the evolution of the host magmas. As already pointed out, the megacrysts clearly follow high pressure fractionation trends. However, the lavas in fig. 2.15 plot closer to straight binary mixing lines rather than to the constantly evolving liquids modeled by high- or low-pressure fractionation. Possible evolved mixing endmember in fig. 2.15 might be the phonolite or a melt similar to that found as inclusions in ilmenite megacrysts.

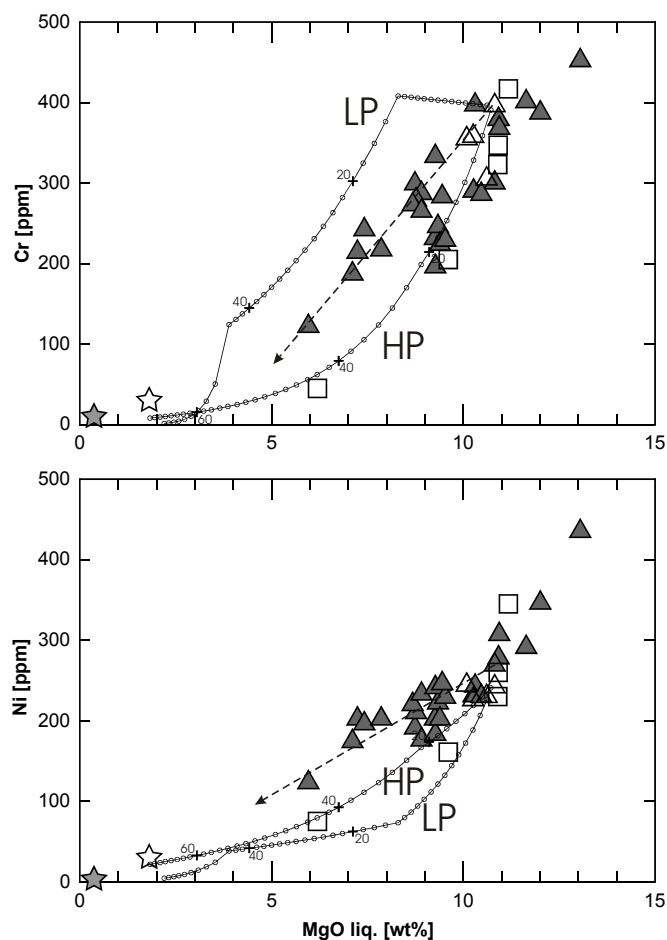


Fig. 2.15: Variation of Cr (a) and Ni (b) vs. MgO of basalts from Biu and Jos Plateau. HP (20 kbar) fractionation model involving phase proportions of cpx+gnt from pMelts, and LP (8 kbar) fractionation model involving ol+cpx+sp from Melts. Symbols for lavas and distribution coefficients as before, gray star marks phonolitic melt, open star marks melt inclusion in ilmenite megacryst. Liquids should quickly be depleted in compatible elements such as Cr and Ni in cpx and ol, respectively. However, the liquid lines of descent predicted from the fractionation models are not observed. Instead liquids more closely follow straight mixing trajectories from primitive melts to hypothetical evolved melts derived by fractional crystallization.

To account for both the evidence for magma mixing and the enriched trace elements in the host lavas, we propose a model in which magmas that carry megacrysts are mixtures of primitive magmas similar to those inverted from most primitive cpx megacrysts and thereof derived evolved melts, similar to the inclusions found in ilmenite megacrysts or those inverted from most evolved cpx megacrysts. Mixing of evolved and primitive magmas and entrainment of megacrysts may have occurred simultaneously as fresh batches of a deeply-sourced primitive magma entered mantle magma chambers in the feeder system, triggering ascent and eruption. Because all megacrysts are precipitating from a uniform magma they all lie on the same major element fractionation trends, consistent with the trends observed in fig. 2.4 – 2.7.

Figure 2.16 shows chondrite-normalized (McDonough & Sun, 1995) rare earth element patterns of Biu and Jos plateau lavas along with two calculated trace element patterns of melts in equilibrium with measured cpx trace element concentrations. For the primitive cpx composition, we minimized the effect of cpx major element composition on trace element distribution by using the D-set of Johnson (1998), where the experimental P,T-conditions (20-30 kbar, 1310°-1470°C) match the forming conditions of the megacrysts and more important, synthesized cpx major element compositions are indistinguishable from megacryst cpx. Because of the lack of a suitable set of distribution coefficients for the most evolved cpx, we used calculated $D^{\text{cpx}/\text{melt}}$ (REE) according to Wood & Blundy (1997)'s model c (which calculates $D^{\text{cpx}/\text{melt}}$ from cpx crystal composition, pressure and temperature). For an estimation of P_{eq} and T_{eq} , we assumed that the most evolved cpx is in equilibrium with melts similar to the ilmenite inclusions, and calculated 13.6 kbar and 1160°C using the model of Putirka *et al.* (1996). This estimate is consistent with the temperature calculated from the most evolved cpx/gnt intergrowth which yields ~1100°C. The resulting set of distribution coefficients for the most evolved cpx compositions is a factor of ~2.5 higher than the set of Johnson (1998) and is associated with errors of -40/+67% (Wood & Blundy, 1997). For the final inversion to melt concentrations, we have to consider the errors introduced by the uncertainty of P and T, and errors from SIMS measurements of cpx megacrysts. However, except for La and Ce the patterns of melt inclusion and inverted evolved cpx are similar and therefore consistent with the initial assumption of equilibrium between them. Moreover, the model suggests that the whole spectrum of cpx compositions may be derived from the spectrum of melt compositions observed.

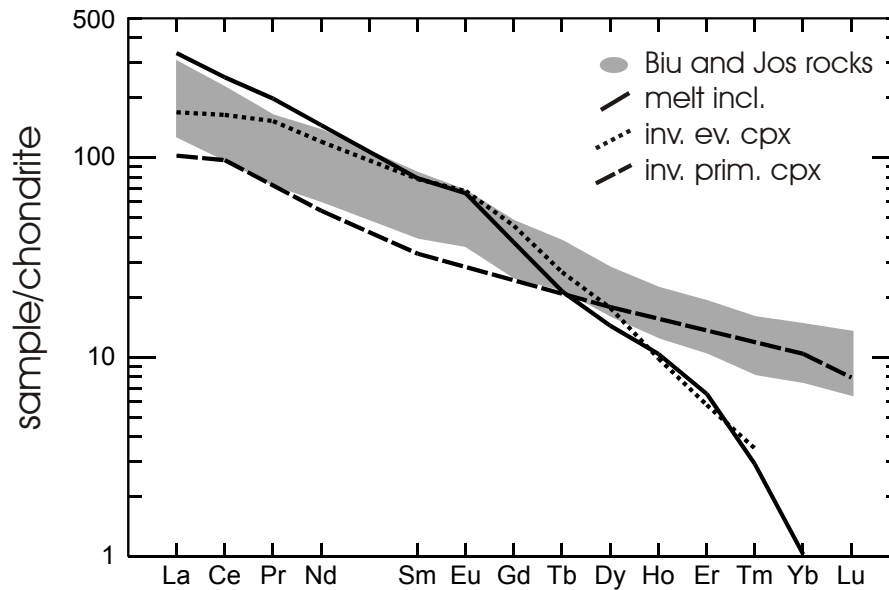


Fig. 2.16: Trace element patterns of Lavas from Biu and Jos Plateau, along with inversions of primitive and evolved cpx trace element concentrations to melt concentrations with appropriate sets of distribution coefficients. Stippled line: calculated melts from cpx mg# >80, dotted line: calculated melt from evolved cpx mg# ~60. The range of REE patterns of Biu and Jos Plateau rocks may be explained by mixing between primitive melts similar to those inverted from primitive cpx megacrysts and thereof derived evolved melts similar to the inclusions found in ilmenite megacrysts.

2.3.6. Constraints on the timing of magma mixing processes

Brearley & Scarfe (1986) conducted dry dissolution experiments on garnet in alkali basalts of similar compositions as samples reported here, and found a breakdown reaction rim ($\text{gnt} \rightarrow \text{ol} + \text{opx} + \text{sp} + \text{gl}$) with a dissolution rate of gnt of 1.67×10^{-5} cm/sec at 1300°C and 12 kbar. It follows that at conditions similar to a basaltic magma chamber at the base of the crust, a gnt of 5 cm in diameter is dissolved in only 3.5 days, whereby hydrous conditions enhance gnt melting even more (Canil & Fedortchouk, 1999). The same argument might be derived from dissolution experiments of plagioclase in a basaltic liquid (Donaldson, 1985). Therefore, storage of a mixed magma containing megacrysts at the base of the crust is unlikely. However, the model presented here allows magmas to show signs of crustal assimilation (via admixing of a portion of liquid that evolved at the base or in the crust) and to contain easily fusible components such as garnet and plagioclase megacrysts, if mixing of the differently evolved liquid components and their phenocrysts occurs directly prior to eruption to the surface.

2.3.7. Constraints on garnet/melt distribution coefficients

Calculated distribution coefficients ($D^{\text{cpx/gnt}}$) of cpx/gnt megacryst intergrowths from this work are shown in fig. 2.17 together with calculated distribution coefficients according to Harte & Kirkley (1997)'s scheme based on subsolidus equilibrated 'eclogite'-xenoliths from Roberts Victor kimberlite pipe in South Africa, which predicts $D^{\text{cpx/gnt}}$ for the REE, Ba, Sr, Y and Zr from the molar calcium distribution coefficient $D^{\text{cpx/gnt}}(\text{Ca}^*)$. Included is the set of distribution coefficients derived from Johnson (1998)'s experiment on 1921 Kilauea basalt at 1430°C and 30 kbar.

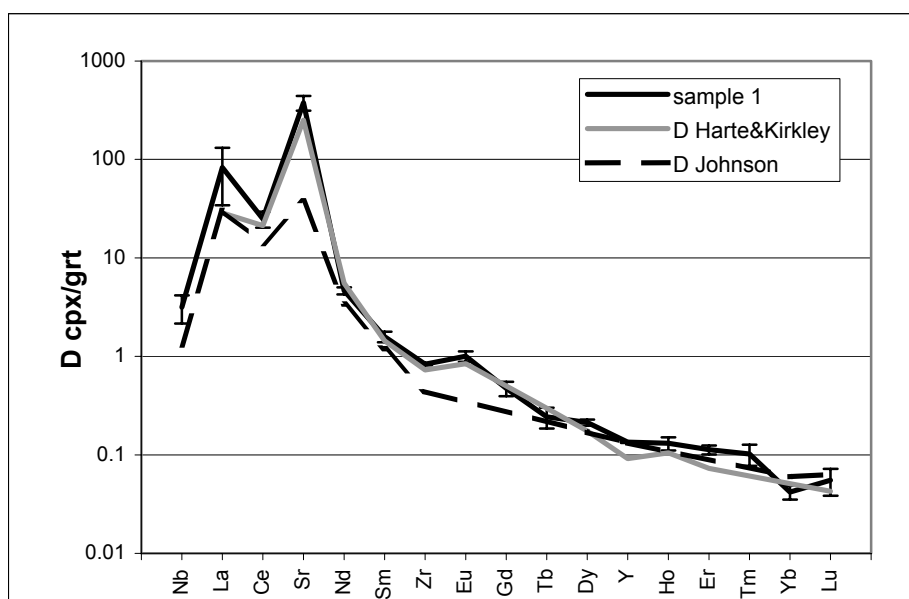


Fig. 2.17: Measured $D^{\text{cpx/gnt}}$ from intergrowths (black) compared to calculated D 's according to Harte & Kirkley (1997) (gray) and D 's from Johnson (1998) (black, stippled) experiment. Error bars are propagated 1σ -errors from SIMS analyses.

Harte & Kirkley (1997) and Green *et al.* (2000) pointed out that there is a discrepancy for some elements in mineral-mineral partitioning behavior between supersolidus experimental data sets (e.g. the set of Johnson (1998)) and subsolidus equilibrated natural rocks, in that there is a tendency for $D^{\text{cpx/gnt}}$ patterns to be 'flatter' in the presence of melt. Van Westrenen *et al.* (2000) suggested that the ideal ionic radius r_0 and Young's modulus E_x of gnt can be influenced by the presence and structure of a coexisting melt, and that therefore no model is available to predict $D^{\text{gnt/melt}}$ from crystal composition alone. Although the calculated equilibration temperatures of megacryst intergrowths are $\sim 300^\circ\text{C}$ higher than those of the xenoliths studied

by Harte & Kirkley (1997), we calculate a similar $D^{\text{cpx}/\text{gnt}}(\text{Ca}^*)$ leading to similar patterns of $D^{\text{cpx}/\text{gnt}}$. This is consistent with the suggestion that the temperature dependency of $D^{\text{cpx}/\text{gnt}}$ is insignificant (Harte & Kirkley, 1997), (Rocholl *et al.*, 1996). If the flatter $D^{\text{cpx}/\text{gnt}}$ pattern was caused by the presence of melt, as suggested by Van Westrenen *et al.* (2000), it is concluded that the assemblage has to reequilibrate after complete crystallization or withdrawal of the remaining melt. However, our megacryst assemblage shows no sign for reequilibration as e.g. chemical zonation or metamorphic textures. An alternative explanation for 'flat' $D^{\text{cpx}/\text{gnt}}$ patterns are microscopic melt inclusions in experimentally produced garnet which lead to elevated $D^{\text{gnt}/\text{melt}}$ for the very incompatible elements in garnet. Given that $D^{\text{cpx}/\text{melt}}$ does not differ significantly between published data sets (Hart & Dunn, 1993), (Hauri *et al.*, 1994), (Johnson, 1998), (Velz, 1999), this in turn leads to lower $D^{\text{cpx}/\text{gnt}}$.

However, a possible test for the accuracy of $D^{\text{min}/\text{melt}}$ data sets is to compare the concentrations of incompatible elements in a series of progressively fractionating megacrysts with those modeled by the phase proportions predicted by the pMelts code (fig. 2.18) and the different sets of $D^{\text{min}/\text{melt}}$. Figure 2.19 shows measured trace element concentrations of cpx megacrysts along with those modeled using the $D^{\text{cpx}/\text{melt}}$ data of Johnson (1998) and $D^{\text{gnt}/\text{melt}}$ data of Zack *et al.* (1997).

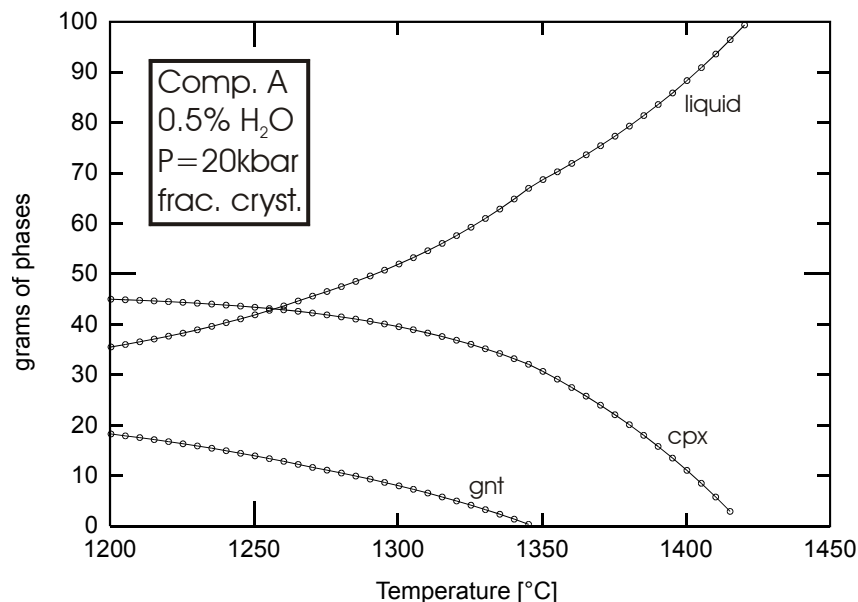


Fig. 2.18: Phase proportions fractionating from a primitive Biu Plateau basalt predicted by the pMelts code for the conditions given (Comp. A is a mean of the basalts 'Jigu Maar', 'Wiga', 'Etum', 'Tila Strom' and 'Biu 4'. The significance of Comp. A will be discussed in chapter 3 based upon isotope systematics). The amount of water added mainly controls the liquidus temperature, but does not change the proportion of cpx/gnt significantly. Each point represents 5°C cooling. At each step, trace element concentrations for the phases in equilib-

rium with the remaining liquid are calculated and subtracted from the liquid (stepwise fractionation). Major element variations of cpx calculated from this model and cpx found as megacrysts have been compared in fig. 2.14. Modeled major element compositions of garnet are also consistent with those found in the megacrysts.

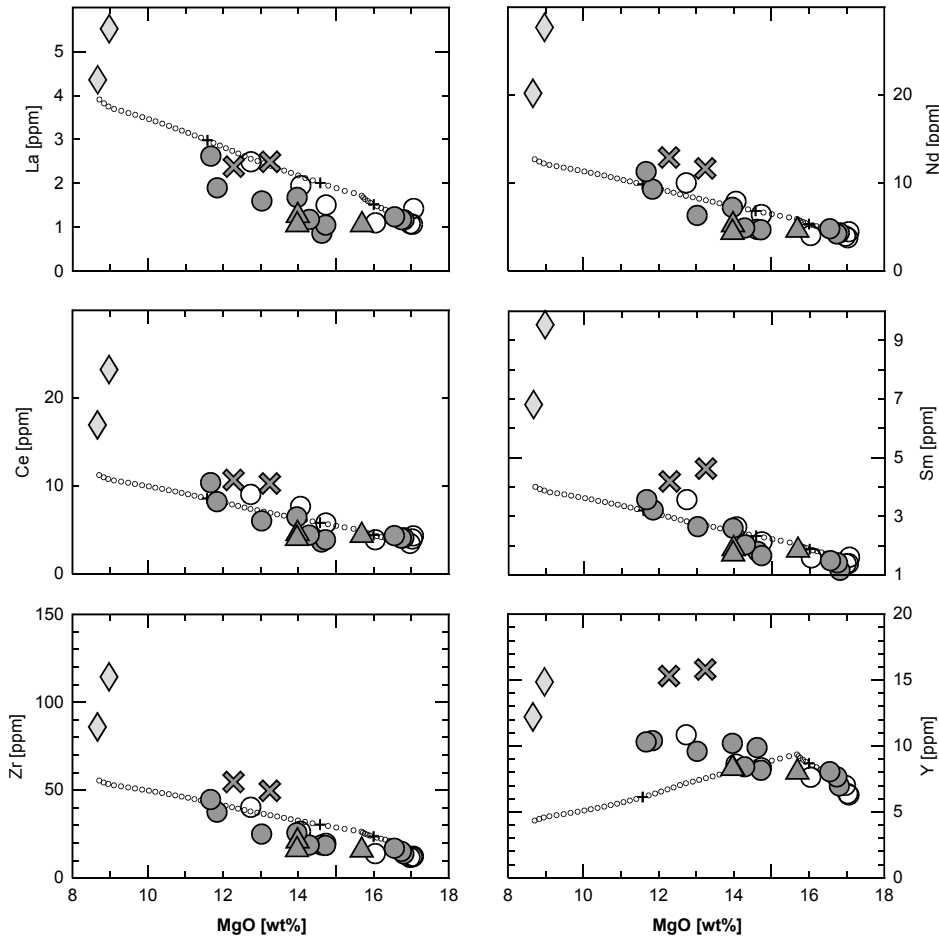


Fig. 2.19: Comparison of trace element concentrations in cpx megacrysts (coding as before) and concentrations calculated using $D^{\text{cpx}}_{\text{melt}}$ of Johnson (1998). Additional models for Cr, Ni and Yb are given in fig. 2.13. There is good agreement for cpx with 17 – 11.5 wt% MgO (i.e. mg# 85 – 70). The bad fit for the highly incompatible elements in evolved megacrysts with ~9 wt% MgO may have several reasons. Partition coefficients may be higher for cpx in equilibrium with evolved liquids, or the system gained incompatible elements during progressive crystallization (e.g. through assimilation of enriched wall-rock derived liquids, which will be discussed in the next chapter). Although the model predicts a kink in the yttrium fractionation path, this is not observed in the megacrysts, which suggests that the bulk distribution coefficient for Y was always <1 . This may be because of the modeled fraction of garnet is too high, or a too high $D^{\text{gnt}}_{\text{melt}}$ (Y). Megacrysts also suggest a slightly higher $D^{\text{cpx}}_{\text{melt}}$ (Cr) (see fig. 2.13a) compared to values published in literature. Cpx megacrysts from the 'Gumja' volcano (gray crosses), are more enriched in the heavy REE, possibly indicating fractionation at a higher level without involvement of garnet. This assumption is consistent with the lack of gnt in the 'Gumja' megacryst suite (cf. table A.1).

In summary, the trace element systematics (except for yttrium) of more primitive cpx with mg# 85 – 70 are consistent with the distribution coefficients and phase proportions used. Figure 2.20 applies the same scheme for gnt megacrysts to check for consistency of two different sets of $D^{\text{gnt}}/\text{melt}$, one calculated based upon equilibrated garnet pyroxenites from Kakanui, New Zealand (Zack *et al.*, 1997), and the other experimentally derived (Johnson, 1998).

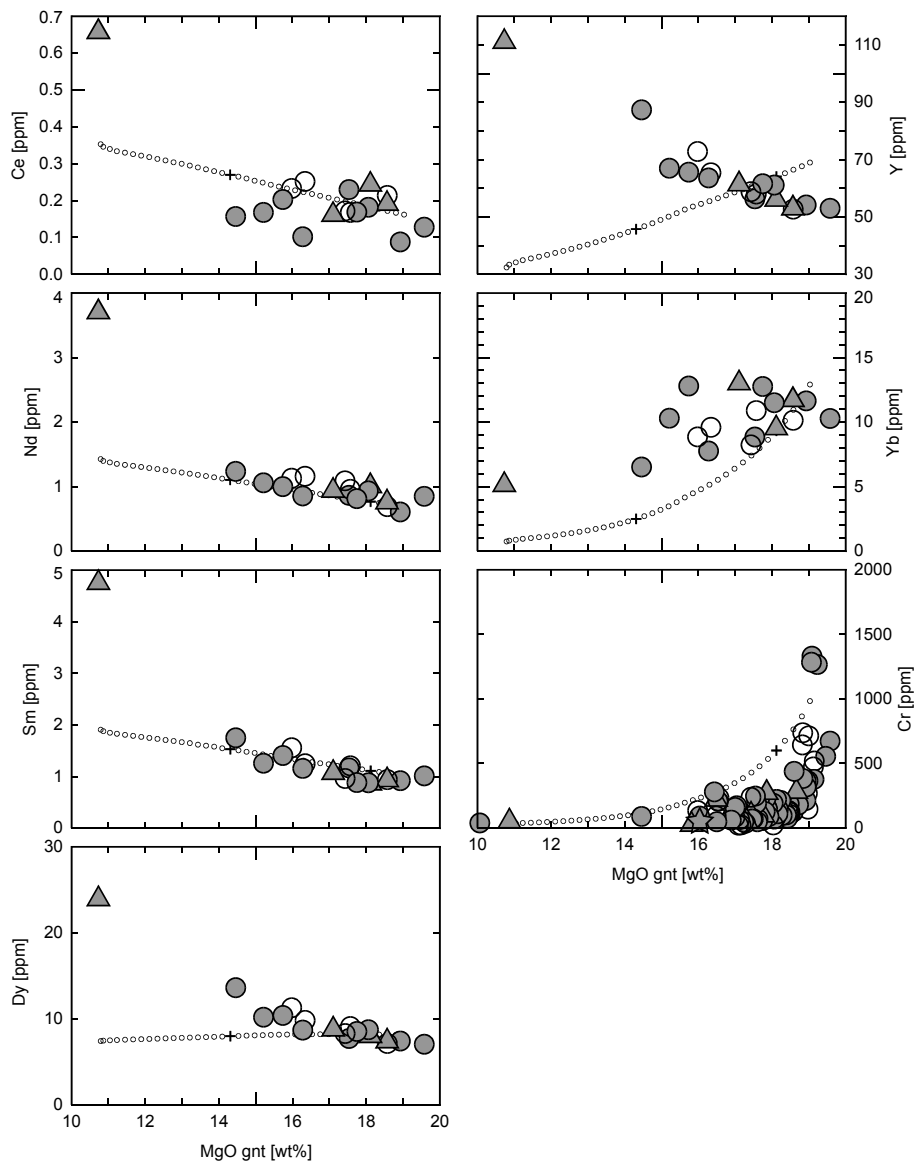


Fig. 2.20a: Comparison of measured trace element concentrations in gnt megacrysts (coding as before) and concentrations calculated using $D^{\text{gnt}}/\text{melt}$ of Zack *et al.* (1997). There is general good agreement between observed and predicted concentrations. Cerium concentrations in gnt are close to detection limit of SIMS and therefore introduce more scatter in the calculation. The yttrium distribution coefficient (3.08) is too high, leading to calculated excess concentrations in most primitive gnt megacrysts and a decreasing fractionation pattern. Our data suggests a lower $D^{\text{gnt}}/\text{melt}$ (Y) coefficient of ~ 2 .

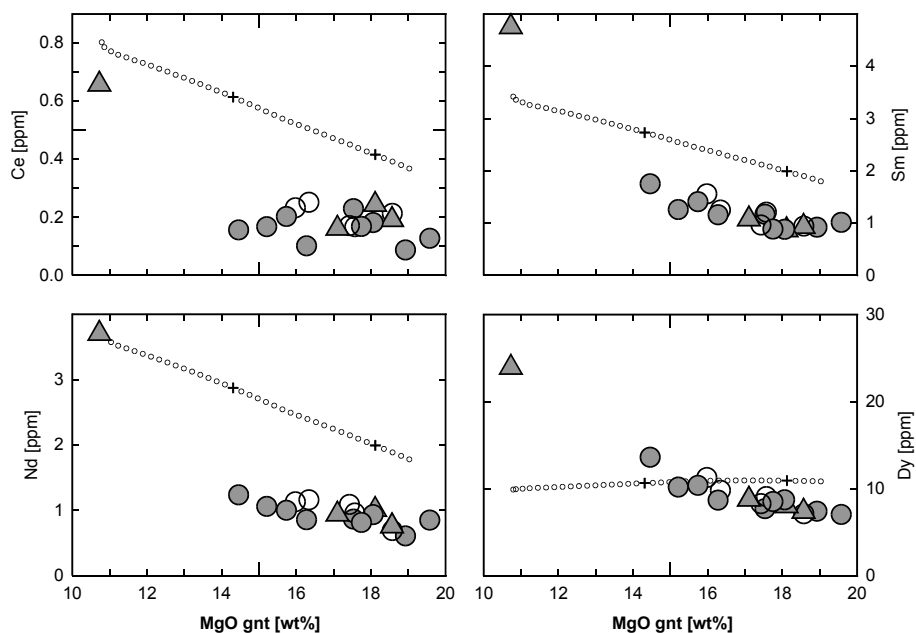


Fig. 2.20b: Comparison of trace element concentrations in gnt megacrysts and concentrations calculated using $D^{\text{gnt}/\text{melt}}$ of Johnson (1998). Distribution coefficients for the heavy REE are similar in both sets (cf. fig. 2.17). However, distribution coefficients for highly incompatible elements are too high and inconsistent with our data.

In summary, our data suggests that experimentally derived $D^{\text{gnt}/\text{melt}}$ tend to give too high values for the highly incompatible elements. This leads to overestimations in concentrations of these elements in most primitive megacrysts and steeper fractionation patterns. A change in the ratio of cpx/gnt in the fractionating assemblage will only change the slope of the pattern, however, it will not change its starting point. We therefore propose that the use of $D^{\text{cpx}/\text{gnt}}$ derived from subsolidus equilibrated gnt-pyroxenites (e.g. Zack *et al.* (1997), Harte & Kirkley (1997) or the set derived from this study) provides more realistic results in trace element modeling of highly incompatible elements, provided that the temperature dependence of partitioning may be neglected.

2.4. Conclusions

We have shown based on chemical and diffusional constraints that primitive cpx and gnt megacrysts are genetically related to recent CVL lavas that brought them to the surface, though they may not be directly cognate to their host lava. Lavas do not reflect simple frac-

tionation or equilibrium crystallization products, but instead reflect mixing of primitive and evolved batches of magma shortly before eruption. An especially interesting result of such mixing is that magmas with near 'primary' features (i.e. high mg#, Ni, Cr, containment of peridotitic xenoliths) can be significantly enriched in trace elements without significantly changing their major element compositions. Such mixing complicates efforts to infer the degree of partial melting or source enrichment by inversion of lava trace element compositions.

Garnet-melt distribution coefficients derived from equilibrated cpx/gnt intergrowths and a set of $D^{\text{cpx/melt}}$ may be more reliable than experimentally derived $D^{\text{gnt/melt}}$ data. However, the model presented here is based upon the cpx/gnt phase proportions predicted by the pMelts code of Hirschmann *et al.* (1998). It is clear that such a model cannot replace the insights from a series of high-pressure experiments simulating fractional crystallization, because thermodynamic data of the phases and their mixing properties involved in the pMelts code (especially minor phases such as plagioclase, spinel, ilmenite, apatite, etc.) are insufficiently constrained. Although such experiments have been accomplished (Kunzmann, pers. comm.), the results are as yet not published.

2.5. References

- Adam, J. (1988). Dry, hydrous, and CO₂-bearing liquidus phase-relationships in the CMAS system at 28 kb, and their bearing on the origin of alkali basalts. *Journal of Geology* **96** (6), 709-719.
- Andersen, D. J., Lindsley, D. H. & Davidson, P. M. (1993). Quilf - a Pascal program to assess equilibria among Fe-Mg-Mn-Ti oxides, pyroxenes, olivine and quartz. *Computers & Geosciences* **19** (9), 1333-1350.
- Binns, R. A. (1969). High-Pressure Megacrysts in Basanitic Lavas near Armidale New South Wales. *American Journal of Science* **267**, 33-49.
- Binns, R. A., Duggan, M. B. & Wilkinson, J. F. G. (1970). High Pressure Megacrysts in Alkaline Lavas from Northeastern New-South-Wales. *American Journal of Science* **269** (2), 132-168.
- Brearley, M. & Scarfe, C. M. (1986). Dissolution rates of upper mantle minerals in an alkali basalt melt at high-pressure: an experimental study and implications for ultramafic xenolith survival. *Journal of Petrology* **27** (5), 1157-1182.
- Bultitude, R. J. & Green, D. H. (1971). Experimental Study of Crystal-Liquid Relationships at High Pressures in Olivine Nephelinite and Basanite Compositions. *Journal of Petrology* **12** (1), 121-147.
- Canil, D. (2002). Vanadium in peridotites, mantle redox and tectonic environments: Archaean to present. *Earth and Planetary Science Letters* **195** (1-2), 75-90.

- Canil, D. & Fedortchouk, Y. (1999). Garnet dissolution and the emplacement of kimberlites. *Earth and Planetary Science Letters* **167** (3-4), 227-237.
- Capedri, S., Venturelli, G., Salviolimarini, E., Crawford, A. J., et al. (1989). Upper-Mantle Xenoliths and Megacrysts in an Alkali Basalt from Tallante, Southeastern Spain. *European Journal of Mineralogy* **1** (5), 685-699.
- Chakraborty, S. & Ganguly, J. (1991). Compositional Zoning and Cation Diffusion in Garnets. In: Ganguly, J. (ed) *Advances in Physical Geochemistry, Diffusion, Atomic Ordering, and Mass Transport: Selected Problems in Geochemistry*. Berlin: Springer Verlag, 120-175.
- Davies, G. R., Spriggs, A. J. & Nixon, P. H. (2001). A non-cognate origin for the Gibeon kimberlite megacryst suite, Namibia: Implications for the origin of Namibian kimberlites. *Journal of Petrology* **42** (1), 159-172.
- Dimanov, A. & Sautter, V. (2000). "Average" interdiffusion of (Fe,Mn)-Mg in natural diopside. *European Journal of Mineralogy* **12** (4), 749-760.
- Donaldson, C. H. (1985). The Rates of Dissolution of Olivine, Plagioclase, and Quartz in a Basalt Melt. *Mineralogical Magazine* **49** (354), 683-693.
- Droop, G. T. R. (1987). A general equation for estimating Fe³⁺ concentrations in ferromagnesian silicates and oxides from microprobe analyses, using stoichiometric criteria. *Mineralogical Magazine* **51** (361), 431-435.
- Dunn, T. (1987). Partitioning of Hf, Lu, Ti, and Mn between Olivine, Clinopyroxene and Basaltic Liquid. *Contributions to Mineralogy and Petrology* **96** (4), 476-484.
- Frisch, T. & Wright, J. B. (1971). Chemical composition of high-pressure megacrysts from Nigerian Cenozoic lavas. *Neues Jahrbuch für Mineralogie-Monatshefte* **7**, 289-304.
- Geist, D. J., Myers, J. D. & Frost, C. D. (1988). Megacryst-Bulk Rock Isotopic Disequilibrium as an Indicator of Contamination Processes - the Edgecumbe Volcanic Field, Se Alaska. *Contributions to Mineralogy and Petrology* **99** (1), 105-112.
- Green, D. H. (1973). Experimental Melting Studies on a Model Upper Mantle Composition at High-Pressure under Water-Saturated and Water- Undersaturated Conditions. *Earth and Planetary Science Letters* **19** (1), 37-53.
- Green, D. H. & Ringwood, A. E. (1967). The genesis of basaltic magmas. *Contributions to Mineralogy and Petrology* **15**, 103-190.
- Green, T. H., Blundy, J. D., Adam, J. & Yaxley, G. M. (2000). SIMS determination of trace element partition coefficients between garnet, clinopyroxene and hydrous basaltic liquids at 2-7.5 GPa and 1080-1200 degrees C. *Lithos* **53** (3-4), 165-187.
- Guo, J. F., Griffin, W. L. & O'Reilly, S. Y. (1999). Geochemistry and origin of sulphide minerals in mantle xenoliths: Qilin, southeastern China. *Journal of Petrology* **40** (7), 1125-1149.
- Guo, J. F., Oreilly, S. Y. & Griffin, W. L. (1996a). Corundum from basaltic terrains: A mineral inclusion approach to the enigma. *Contributions to Mineralogy and Petrology* **122** (4), 368-386.

- Guo, J. F., Oreilly, S. Y. & Griffin, W. L. (1996b). Zircon inclusions in corundum megacrysts I. Trace element geochemistry and clues to the origin of corundum megacrysts in alkali basalts. *Geochimica Et Cosmochimica Acta* **60** (13), 2347-2363.
- Hart, S. R. & Dunn, T. (1993). Experimental Cpx/Melt Partitioning of 24 Trace-Elements. *Contributions to Mineralogy and Petrology* **113** (1), 1-8.
- Harte, B. & Kirkley, M. B. (1997). Partitioning of trace elements between clinopyroxene and garnet: Data from mantle eclogites. *Chemical Geology* **136** (1-2), 1-24.
- Hauri, E. H., Wagner, T. P. & Grove, T. L. (1994). Experimental and Natural Partitioning of Th, U, Pb and Other Trace-Elements between Garnet, Clinopyroxene and Basaltic Melts. *Chemical Geology* **117** (1-4), 149-166.
- Herzberg, C. T. (1978). Bearing of Phase-Equilibria in Simple and Complex Systems on Origin and Evolution of Some Well-Documented Garnet-Websterites. *Contributions to Mineralogy and Petrology* **66** (4), 375-382.
- Hirschmann, M. M., Ghiorso, M. S., Wasylenki, L. E., Asimow, P. D., et al. (1998). Calculation of peridotite partial melting from thermodynamic models of minerals and melts I. Review of methods and comparison with experiments. *Journal of Petrology* **39** (6), 1091-1115.
- Hops, J. J., Gurney, J. J. & Harte, B. (1992). The Jagersfontein Cr-Poor Megacryst Suite - Towards a Model for Megacryst Petrogenesis. *Journal of Volcanology and Geothermal Research* **50** (1-2), 143-160.
- Huckenholz, H. G., Gilbert, M. C. & Kunzmann, T. (1992). Stability and Phase-Relations of Calcic Amphiboles Crystallized from Magnesio-Hastingsite Compositions in the 1 to 45 Kbar Pressure Range. *Neues Jahrbuch für Mineralogie-Abhandlungen* **164** (2-3), 229-268.
- Irving, A. J. (1974). Megacrysts from Newer Basalts and Other Basaltic Rocks of Southeastern Australia. *Geological Society of America Bulletin* **85** (10), 1503-1514.
- Irving, A. J. & Frey, F. A. (1984). Trace-Element Abundances in Megacrysts and Their Host Basalts - Constraints on Partition Coefficients and Megacryst Genesis. *Geochimica Et Cosmochimica Acta* **48** (6), 1201-1221.
- Irving, A. J. & Price, R. C. (1981). Geochemistry and Evolution of Lherzolite-Bearing Phonolitic Lavas from Nigeria, Australia, East-Germany and New-Zealand. *Geochimica Et Cosmochimica Acta* **45** (8), 1309-1320.
- Jaoul, O., Sautter, V. & Abel, F. (1991). Nuclear microanalysis: A powerful tool for measuring low atomic diffusivity with mineralogic applications. In: Ganguly, J. (ed) *Advances in Physical Geochemistry, Diffusion, Atomic Ordering, and Mass Transport: Selected Problems in Geochemistry*. Berlin: Springer Verlag, 198-220.
- Johnson, K. T. M. (1998). Experimental determination of partition coefficients for rare earth and high-field-strength elements between clinopyroxene, garnet, and basaltic melt at high pressures. *Contributions to Mineralogy and Petrology* **133** (1-2), 60-68.

- Jones, R. A. (1987). Strontium and neodymium isotopic and rare earth element evidence for the genesis of megacrysts in kimberlites of southern Africa. In: Nixon, P. H. (ed) *Mantle Xenoliths*. Chichester: John Wiley and Sons Ltd, 711-724.
- Krogh, E. J. (1988). The garnet-clinopyroxene Fe-Mg geothermometer: a reinterpretation of existing experimental data. *Contributions to Mineralogy and Petrology* **99** (1), 44-48.
- Le Bas, M. J., Le Maitre, R. W., Streckeisen, A. & Zanettin, B. (1986). A chemical classification of volcanic rocks based on the total alkali-silica diagram. *Journal of Petrology* **27** (3), 745-750.
- Lee, D. C., Halliday, A. N., Davies, G. R., Essene, E. J., et al. (1996). Melt enrichment of shallow depleted mantle: A detailed petrological, trace element and isotopic study of mantle-derived xenoliths and megacrysts from the Cameroon line. *Journal of Petrology* **37** (2), 415-441.
- Lee, D. C., Halliday, A. N., Fitton, J. G. & Poli, G. (1994). Isotopic Variations with Distance and Time in the Volcanic Islands of the Cameroon Line - Evidence for a Mantle Plume Origin. *Earth and Planetary Science Letters* **123** (1-4), 119-138.
- Liotard, J. M., Briot, D. & Boivin, P. (1988). Petrological and Geochemical Relationships between Pyroxene Megacrysts and Associated Alkali-Basalts from Massif Central (France). *Contributions to Mineralogy and Petrology* **98** (1), 81-90.
- Liu, C. Q., Masuda, A., Shimizu, H., Takahashi, K., et al. (1992a). Evidence for Pressure-Dependence of the Peak Position in the REE Mineral-Melt Partition Patterns of Clinopyroxene. *Geochimica Et Cosmochimica Acta* **56** (4), 1523-1530.
- Liu, C. Q., Masuda, A. & Xie, G. H. (1992b). Isotope and Trace-Element Geochemistry of Alkali Basalts and Associated Megacrysts from the Huangyishan Volcano, Kuandian, Liaoning, NE China. *Chemical Geology* **97** (3-4), 219-231.
- McDonough, W. F. & Sun, S. S. (1995). The Composition of the Earth. *Chemical Geology* **120** (3-4), 223-253.
- McGuire, A. V., Dyar, M. D. & Ward, K. A. (1989). Neglected $\text{Fe}^{3+}/\text{Fe}^{2+}$ Ratios: a Study of Fe^{3+} Content of Megacrysts from Alkali Basalts. *Geology* **17** (8), 687-690.
- McKenzie, D. & Bickle, M. J. (1988). The Volume and Composition of Melt Generated by Extension of the Lithosphere. *Journal of Petrology* **29** (3), 625-679.
- McKenzie, D. & O'Nions, R. K. (1991). Partial Melt Distributions from Inversion of Rare-Earth Element Concentrations. *Journal of Petrology* **32** (5), 1021-1091.
- Moore, A. E. (1987). A model for the origin of ilmenite in kimberlite and diamond: implications for the genesis of the discrete nodule (megacryst) suite. *Contributions to Mineralogy and Petrology* **95** (2), 245-253.
- Mysen, B. O. (1978). Experimental Determination of Nickel Partition-Coefficients between Liquid, Pargasite, and Garnet Peridotite Minerals and Concentration Limits of Behavior According to Henry's Law at High-Pressure and Temperature. *American Journal of Science* **278** (2), 217-243.
- Nasir, S. (1995). Cr-Poor Megacrysts from the Shamah Volcanic Field, Northwestern Part of the Arabian Plate. *Journal of African Earth Sciences* **21** (3), 349-357.

- Nikogosian, I. K. & Sobolev, A. V. (1997). Ion-microprobe analysis of melt inclusions in olivine: Experience in estimating the melt-olivine partitioning coefficients of elements. *Geokhimiya* (2), 149-157.
- O'Hara, M. J. & Mathews, R. E. (1981). Geochemical Evolution in an Advancing, Periodically Replenished, Periodically Tapped, Continuously Fractionated Magma Chamber. *Journal of the Geological Society* **138** (MAY), 237-277.
- O'Neill, H. S. & Wall, V. J. (1987). The Olivine-Orthopyroxene-Spinel-Oxygen Geobarometer, the Nickel Precipitation Curve, and the Oxygen Fugacity of the Earths Upper Mantle. *Journal of Petrology* **28** (6), 1169-1191.
- Poudjom-Djomani, Y. H., Nnange, J. M., Diament, M., Ebinger, C. J., et al. (1995). Effective Elastic Thickness and Crustal Thickness Variations in West Central-Africa Inferred from Gravity Data. *Journal of Geophysical Research-Solid Earth* **100** (B11), 22047-22070.
- Putirka, K. (1997). Magma transport at Hawaii: Inferences based on igneous thermobarometry. *Geology* **25** (1), 69-72.
- Putirka, K. (1998). Garnet plus liquid equilibrium. *Contributions to Mineralogy and Petrology* **131** (2-3), 273-288.
- Putirka, K., Johnson, M., Kinzler, R., Longhi, J., et al. (1996). Thermobarometry of mafic igneous rocks based on clinopyroxene-liquid equilibria, 0-30 kbar. *Contributions to Mineralogy and Petrology* **123** (1), 92-108.
- Righter, K. & Carmichael, I. S. E. (1993). Mega-Xenocrysts in Alkali Olivine Basalts - Fragments of Disrupted Mantle Assemblages. *American Mineralogist* **78** (11-12), 1230-1245.
- Rocholl, A., Ludwig, T., Altherr, R., Meyer, H.-P., et al. (1996). Experimental partitioning of trace elements between clinopyroxene, garnet and basanitic melt studied by ion microprobe. *Journal of Conference Abstracts* **1**, 517-518.
- Roeder, P. L. & Emslie, R. F. (1970). Olivine-liquid equilibrium. *Contributions to Mineralogy and Petrology* **29**, 275-289.
- Sautter, V. & Harte, B. (1988). Diffusion Gradients in an Eclogite Xenolith from the Roberts Victor Kimberlite Pipe - 1. Mechanism and Evolution of Garnet Exsolution in Al₂O₃-Rich Clinopyroxene. *Journal of Petrology* **29** (6), 1325-1352.
- Sautter, V. & Harte, B. (1990). Diffusion Gradients in an Eclogite Xenolith from the Roberts Victor Kimberlite Pipe - 2. Kinetics and Implications for Petrogenesis. *Contributions to Mineralogy and Petrology* **105** (6), 637-649.
- Schulze, D. J. (1987). Megacrysts from alkaline volcanic rocks. In: Nixon, P. H. (ed) *Mantle Xenoliths*. Chichester: John Wiley and Sons Ltd, 433-452.
- Schulze, D. J., Valley, J. R., Bell, D. R. & Spicuzza, M. J. (2001). Oxygen isotope variations in Cr-poor megacrysts from kimberlite. *Geochimica Et Cosmochimica Acta* **65** (23), 4375-4384.
- Sen, G. & Jones, R. E. (1988). Exsolved Silicate and Oxide Phases from Clinopyroxenes in a Single Hawaiian Xenolith - Implications for Oxidation-State of the Hawaiian Upper Mantle. *Geology* **16** (1), 69-72.

- Sepp, B. & Kunzmann, T. (2001). The stability of clinopyroxene in the system CaO-MgO-SiO₂-TiO₂ (CMST). *American Mineralogist* **86** (3), 265-270.
- Skulski, T., Minarik, W. & Watson, E. B. (1994). High-Pressure Experimental Trace-Element Partitioning between Clinopyroxene and Basaltic Melts. *Chemical Geology* **117** (1-4), 127-147.
- Sun, S. S. & McDonough, W. F. (1989). Chemical and isotopic systematics of oceanic basalts: implications for mantle composition and processes. In: D., S. A. & J., N. M. (eds) *Magmatism in the Ocean Basins* Geological Society Special Publication, 313-345.
- Sutherland, F. L. & Fanning, C. M. (2001). Gem-bearing basaltic volcanism, Barrington, New South Wales: Cenozoic evolution, based on basalt K-Ar ages and zircon fission track and U-Pb isotope dating. *Australian Journal of Earth Sciences* **48** (2), 221-237.
- Sutherland, F. L., Hoskin, P. W. O., Fanning, C. M. & Coenraads, R. R. (1998). Models of corundum origin from alkali basaltic terrains: a reappraisal. *Contributions to Mineralogy and Petrology* **133** (4), 356-372.
- Thirlwall, M. F. (1997). Pb isotopic and elemental evidence for OIB derivation from young HIMU mantle. *Chemical Geology* **139** (1-4), 51-74.
- Turner, D. C. (1978). Volcanoes of the Biu Basalt Plateau, Northeastern Nigeria. *Journal of Mining and Geology* **15** (2), 49-63.
- Ulmer, P. & Luth, R. W. (1991). The Graphite-COH Fluid Equilibrium in P, T, fO₂ Space - an Experimental Determination to 30 Kbar and 1600°C. *Contributions to Mineralogy and Petrology* **106** (3), 265-272.
- van Westrenen, W., Allan, N. L., Blundy, J. D., Purton, J. A., et al. (2000). Atomistic simulation of trace element incorporation into garnets - comparison with experimental garnet-melt partitioning data. *Geochimica Et Cosmochimica Acta* **64** (9), 1629-1639.
- Velz, S. (1999). Die Verteilung von Spurenelementen zwischen Klinopyroxen, Granat, Orthopyroxen, Olivin und silikatischen Schmelzen im Druckbereich 1.5 GPa bis 3.0 GPa und bei Temperaturen von 1150°C bis 1380°C. *unpublished Ph.D. Thesis, University of Köln*, 172 p.
- Weaver, B. L. (1991). The Origin of Ocean Island Basalt End-Member Compositions - Trace-Element and Isotopic Constraints. *Earth and Planetary Science Letters* **104** (2-4), 381-397.
- Wilkinson, J. F. G. (1975). Ultramafic Inclusions and High-Pressure Megacrysts from a Nephelinite Sill, Nandewar Mountains, Northeastern New-South- Wales, and Their Bearing on Origin of Certain Ultramafic Inclusions in Alkaline Volcanic Rocks. *Contributions to Mineralogy and Petrology* **51** (4), 235-262.
- Wilkinson, J. F. G. & Hensel, H. D. (1991). An Analcime Mugarite - Megacryst Association from Northeastern New-South-Wales: Implications for High-Pressure Amphibole-Dominated Fractionation of Alkaline Magmas. *Contributions to Mineralogy and Petrology* **109** (2), 240-251.
- Wilkinson, J. F. G. & Stolz, A. J. (1997). Subcalcic clinopyroxenites and associated ultramafic xenoliths in alkali basalt near Glen Innes, northeastern New South Wales, Australia. *Contributions to Mineralogy and Petrology* **127** (3), 272-290.

- Wood, B. J. & Blundy, J. D. (1997). A predictive model for rare earth element partitioning between clinopyroxene and anhydrous silicate melt. *Contributions to Mineralogy and Petrology* **129** (2-3), 166-181.
- Wright, J. B. (1970). High pressure phases in Nigerian Cenozoic lavas: Distribution and tectonic setting. *Bulletin of Volcanology* **34**, 833-847.
- Zack, T., Foley, S. F. & Jenner, G. A. (1997). A consistent partition coefficient set for clinopyroxene, amphibole and garnet from laser ablation microprobe analysis of garnet pyroxenites from Kakanui, New Zealand. *Neues Jahrbuch Fur Mineralogie-Abhandlungen* **172** (1), 23-41.

CHAPTER 3: THE ROLE OF CONTINENTAL CRUST AND LITHOSPHERIC MANTLE IN THE GENESIS OF CAMEROON VOLCANIC LINE LAVAS: CONSTRAINTS FROM ISOTOPIC VARIATIONS IN LAVAS AND MEGACRYSTS FROM THE BIU AND JOS PLATEAU

3.1. Introduction

Figure 3.1 shows a collection of published Sr-Nd isotopic compositions of the more primitive rocks of the CVL along with our own analyses of rocks from Biu and Jos Plateau, northern Nigeria (tables B.19 and B.22). Marzoli *et al.* (1999) pointed out that there is isotopic evidence for the involvement of continental crust in the most evolved silicic volcanoes of Oku, Bambouto and Ngaoundéré, which have $^{87}\text{Sr}/^{86}\text{Sr}$ as high as 0.705-0.714. We therefore restricted the compilation in fig. 3.1 to lavas with MgO >5 wt%. The magmas are isotopically heterogeneous in Sr-Nd isotope space with $^{87}\text{Sr}/^{86}\text{Sr}$ ranging from 0.7028 to 0.7038 and ϵ_{Nd} ranging from 7.5 to 2.5. Evidently, there is considerable overlap between compositions of continental and oceanic sector lavas, although the continental sector extends to somewhat lower ϵ_{Nd} . It is unclear whether the heterogeneity observed in the more primitive magmas is related primarily to heterogeneity in the asthenospheric source region of the lavas and represents mixing of a depleted and a more enriched endmember, or if part of this heterogeneity is due to melt interaction with continental lithospheric mantle, or melt interaction with continental crust. One way of constraining the role of crustal contamination in a suite of lavas is to compare the isotopic composition of the lavas with cogenetic phenocrystic or xenocrystic phases that precipitated in the mantle. We have argued in chapter 2 that the megacrysts from the Biu and Jos Plateau are genetically related to recent CVL volcanism. Given that the megacrysts record the isotopic composition of the magma from which they formed, comparison of the isotopic compositions of magmas and megacrysts allows us to evaluate subsequent modifications of the magmas after formation of the megacrysts.

Only six megacrysts from lavas of the CVL (three of cpx, two feldspars and one garnet) have been previously analyzed (Halliday *et al.*, 1990), (Lee *et al.*, 1996). Lee *et al.* (1996) suggested that these megacrysts were derived through fractional crystallization from earlier underplated CVL lavas that had assimilated lower continental crust. This conclusion was mainly drawn from the isotopic composition of a single gnt megacryst. However, as discussed in chapter 2, this conclusion is inconsistent with estimates of the pressure of formation

of the gnt megacrysts, which indicates that the megacrysts grew well below the crust/mantle boundary.

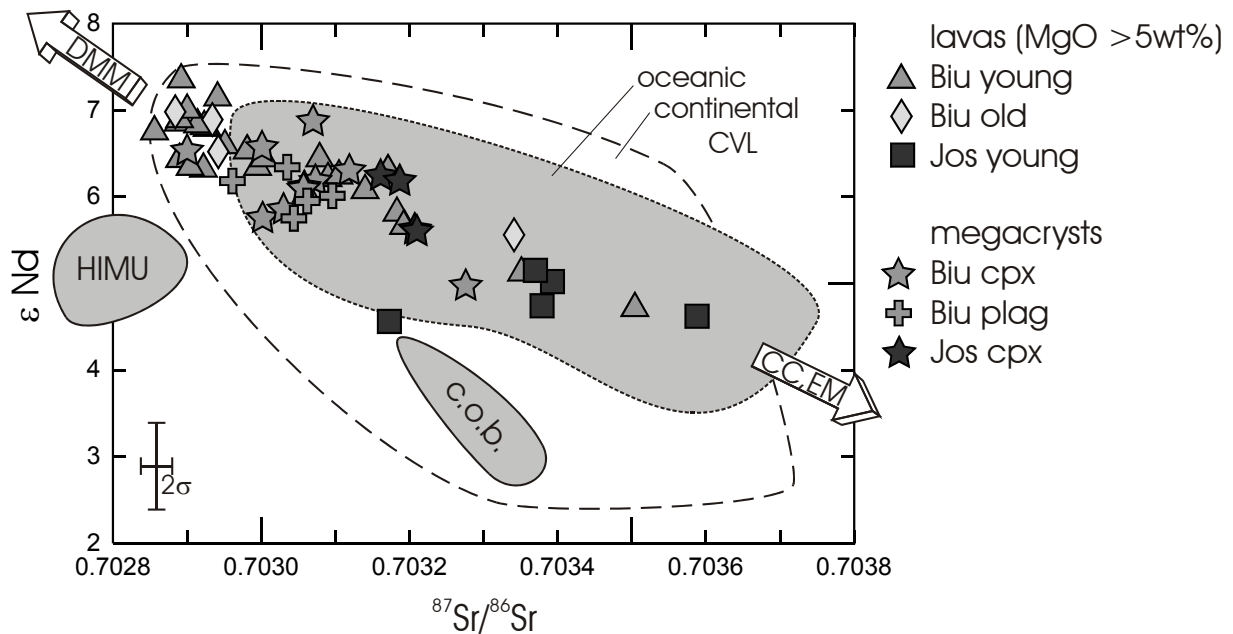


Fig. 3.1: Collection of Sr-Nd isotopic compositions of the more primitive rocks ($\text{MgO} > 5\text{ wt}\%$) from the oceanic and continental CVL along with data for megacrysts. Data compiled from Halliday *et al.* (1988), Halliday *et al.* (1990), Lee *et al.* (1994), Marzoli *et al.* (1999), Marzoli *et al.* (2000) and this work. Triangles: Biu young lavas, diamonds: Biu old lavas, squares: Jos lavas. Grey stars: Biu cpx megacrysts, crosses: Biu plag megacrysts, black stars: Jos cpx megacrysts. Most lavas from St. Helena, Tubuai and Mangaia plot in the field labeled 'HIMU'. Isotope systematics may be explained by mixing between a DMM (depleted MORB mantle) component and a CC (continental crust) and/or EM (enriched mantle) component.

In the following section, the respective contributions of crustal contamination and assimilation of subcontinental lithospheric mantle (SCLM) to the isotopic and trace element variations of Biu and Jos Plateau lavas (and, by inference, in the CVL as a whole) are examined by means of the megacrysts. However, in order to distinguish and quantify the particular contributions of continental crust and enriched SCLM to the genesis of lavas from Biu and Jos Plateau, it is insufficient to consider Sr-Nd isotopes alone, because both contamination vectors may be collinear in isotope space (cf. fig. 3.1). We therefore analyzed lead isotopes of whole rocks and megacrysts, as well as osmium isotopes of a subset of 17 rock samples (table B.19 and B.22). The Re-Os isotopic system provides an excellent tool for discrimination between continental crust and the SCLM. Unlike Sr, Nd and Pb isotopic compositions, which

may overlap in continental crust and the SCLM, there is a strong contrast in Osmium isotopes between the continental crust and the SCLM as a result of the compatible behavior of Os during mantle melting. Whereas continental crust generally has developed variable, but high $^{187}\text{Os}/^{188}\text{Os}$ ratios over time, the SCLM generally has complementary unradiogenic $^{187}\text{Os}/^{188}\text{Os}$ ratios. Thus, if a melt is contaminated by old crust-derived material, it should have an unusually radiogenic Os isotopic signature. In contrast, contaminants derived from the SCLM should have unradiogenic Os isotopic compositions.

3.2. Results

3.2.1. Sr, Nd, Pb and Os isotopes of lavas and megacrysts

$^{87}\text{Sr}/^{86}\text{Sr}$ ratios in lavas from the younger Biu Plateau range from 0.70286 to 0.70350, lavas from the older Biu suite span a similar range from 0.70288 to 0.70334, while Jos Plateau lavas are more radiogenic and range from 0.70317 to 0.70359. ϵ_{Nd} for Biu and Jos lavas range from 4.7 to 7.4 and 4.6 to 5.2 respectively. Cpx and plagioclase megacrysts from the younger Biu Plateau volcanics span a similar range in Sr-Nd isotopic composition to their host lavas, with $^{87}\text{Sr}/^{86}\text{Sr}$ ranging from 0.70290 to 0.70328 and ϵ_{Nd} ranging from 5.0 to 6.9 (n=14). Cpx megacrysts from the Jos Plateau are less enriched than their host lavas, but similar to Biu megacrysts with $^{87}\text{Sr}/^{86}\text{Sr}$ ranging from 0.70316 to 0.70321 and ϵ_{Nd} ranging from 5.6 to 6.2 (n=4).

$^{206}\text{Pb}/^{204}\text{Pb}$ ratios in lavas from the younger and older Biu Plateau overlap and range from 19.03 to 20.33. $^{206}\text{Pb}/^{204}\text{Pb}$ in lavas from the Jos Plateau are more restricted and range from 19.26 to 19.68. $^{207}\text{Pb}/^{204}\text{Pb}$ ratios in lavas from the younger and older Biu Plateau range from 15.62 to 15.69. $^{207}\text{Pb}/^{204}\text{Pb}$ in lavas from the Jos Plateau are higher for a given $^{206}\text{Pb}/^{204}\text{Pb}$ and range from 15.65 to 19.67. $^{208}\text{Pb}/^{204}\text{Pb}$ ratios in lavas from the younger and older Biu Plateau range from 39.18 to 40.35, while lavas from the Jos Plateau range from 39.30 to 39.64. In contrast, megacrysts from both the Biu and the Jos Plateau range to more radiogenic lead compositions than their associated host lavas. Biu megacrysts range from 20.05 to 20.90 in $^{206}\text{Pb}/^{204}\text{Pb}$, 15.71 to 15.76 in $^{207}\text{Pb}/^{204}\text{Pb}$ and 39.77 to 41.07 in $^{208}\text{Pb}/^{204}\text{Pb}$ (n=10). Jos megacrysts range from 19.82 to 20.04 in $^{206}\text{Pb}/^{204}\text{Pb}$, 15.67 to 15.70 in $^{207}\text{Pb}/^{204}\text{Pb}$ and 39.56 to 39.79 in $^{208}\text{Pb}/^{204}\text{Pb}$ (n=3).

Osmium concentrations in the lavas vary from 9 to 133 pg/g (table B.19), and are typical of those found in OIBs (Shirey & Walker, 1998). Rhenium concentrations on the other

hand vary from 17.5 to 146 ppt and are low when compared to average MORB (926 ppt) or OIB (377 ppt) (Richter & Hauri, 1998). Cu/Re ratios are significantly higher than the primitive mantle value of 1.07×10^5 (McDonough & Sun, 1995). Low Re concentrations and high Cu/Re ratios might be related to degassing of subaerial erupted lavas, as suggested by Bennett *et al.* (2000) for Hawaiian tholeiites. Re and Os concentrations do not correlate with silicate-compatible elements such as Mg or Ni, or with chalcophile elements such as Co or Cu. This indicates that there is no direct relationship between Os abundance and the degree of sample differentiation. However, Re and Os concentrations are quite well correlated ($r^2=0.6$).

The measured $^{187}\text{Os}/^{188}\text{Os}$ ratios of the lavas range from 0.1232 to 0.2449. $^{187}\text{Re}/^{188}\text{Os}$ ranges from 3.2 to 25.4. Given the young age of the rocks (5.35-0.84 Ma for older Biu Plateau lavas, other samples <50,000 a), age corrections are generally small and within analytical reproducibility. In $^{187}\text{Os}/^{188}\text{Os}$ versus $1/[\text{Os}]$ space (fig. 3.2a), the volcanics do not form a significant correlation. However, low concentrations (<30 ppt) are generally associated with the highest $^{187}\text{Os}/^{188}\text{Os}$ ratios (from 0.1351 to 0.2449).

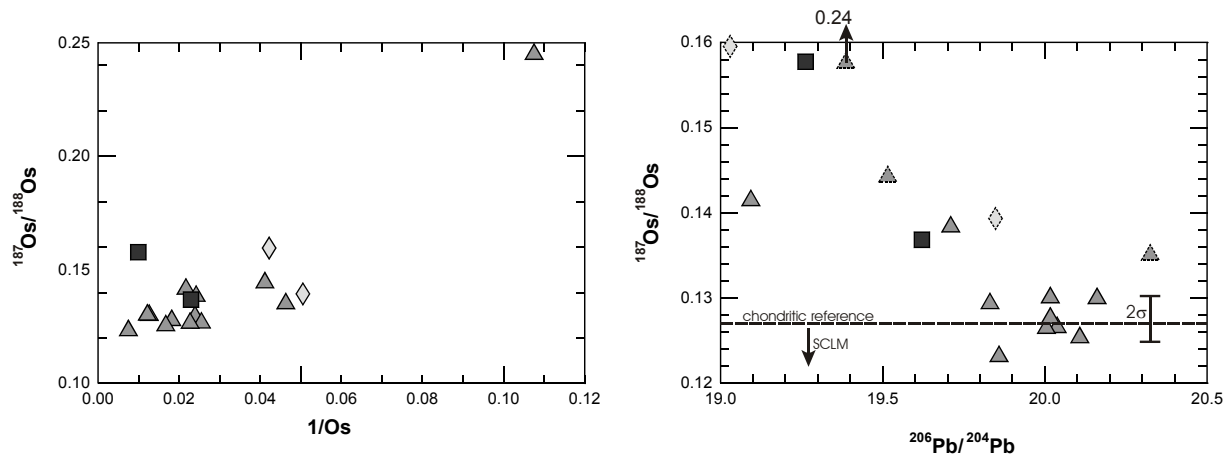


Fig. 3.2: Results from Os analyses. **a)** shows the well-known broad trend to radiogenic Os with decreasing Os concentration in the sample, commonly attributed to crustal contamination. **b)** shows the samples in Os-Pb isotope space. Samples with very low Os concentrations (<30ppt) are coded in dashed symbols. Considering the error range, samples with $^{206}\text{Pb}/^{204}\text{Pb} < 19.8$ are negatively correlated with $^{187}\text{Os}/^{188}\text{Os}$, whereas samples with $^{206}\text{Pb}/^{204}\text{Pb} > 19.8$ do not show a significant trend.

There is a broad correlation between $^{187}\text{Os}/^{188}\text{Os}$ ratios and $^{206}\text{Pb}/^{204}\text{Pb}$ (fig. 3.2b), with radiogenic Os associated with unradiogenic Pb compositions. There is no detectable trend in Os isotope composition in lavas with $^{206}\text{Pb}/^{204}\text{Pb} > 19.8$. They range between 0.1254 and 0.1301 with a mean value of 0.1280, similar to typical mantle values.

Figures 3.3a-f show our results for lavas and megacrysts in plots of $^{207}\text{Pb}/^{204}\text{Pb}$, $^{208}\text{Pb}/^{204}\text{Pb}$, $\Delta 7/4$, $\Delta 8/4$, ϵ_{Nd} and $^{87}\text{Sr}/^{86}\text{Sr}$ versus $^{206}\text{Pb}/^{204}\text{Pb}$. Rock samples from the Biu and Jos Plateau fall within the fields for oceanic and continental CVL rocks previously reported by Halliday *et al.* (1988), Halliday *et al.* (1990), Lee *et al.* (1994), Marzoli *et al.* (1999) and Marzoli *et al.* (2000). Samples with $^{206}\text{Pb}/^{204}\text{Pb} > 19.8$ lie close to the northern hemisphere reference line (NHRL) as defined by Hart (1984). As far as can be concluded from the restricted data set, megacrysts from a single location seem to form cluster on a general trend towards enriched compositions. For example, all four cpx and three plag megacrysts analyzed from the 'Miringa' volcano plot within a narrow range only slightly greater than analytical uncertainty. The isotope trends defined by the megacrysts as a whole overlap with basalt isotope data but extend to considerably more long-term enriched compositions. However, megacrysts are different from typical 'HIMU' compositions like St. Helena (SH), Tubuai (T) or Mangaia (M), because of their higher $^{208}\text{Pb}/^{204}\text{Pb}$ (fig. 3.3b, d) and $^{87}\text{Sr}/^{86}\text{Sr}$ (fig. 3.3f) ratios for a given $^{206}\text{Pb}/^{204}\text{Pb}$.

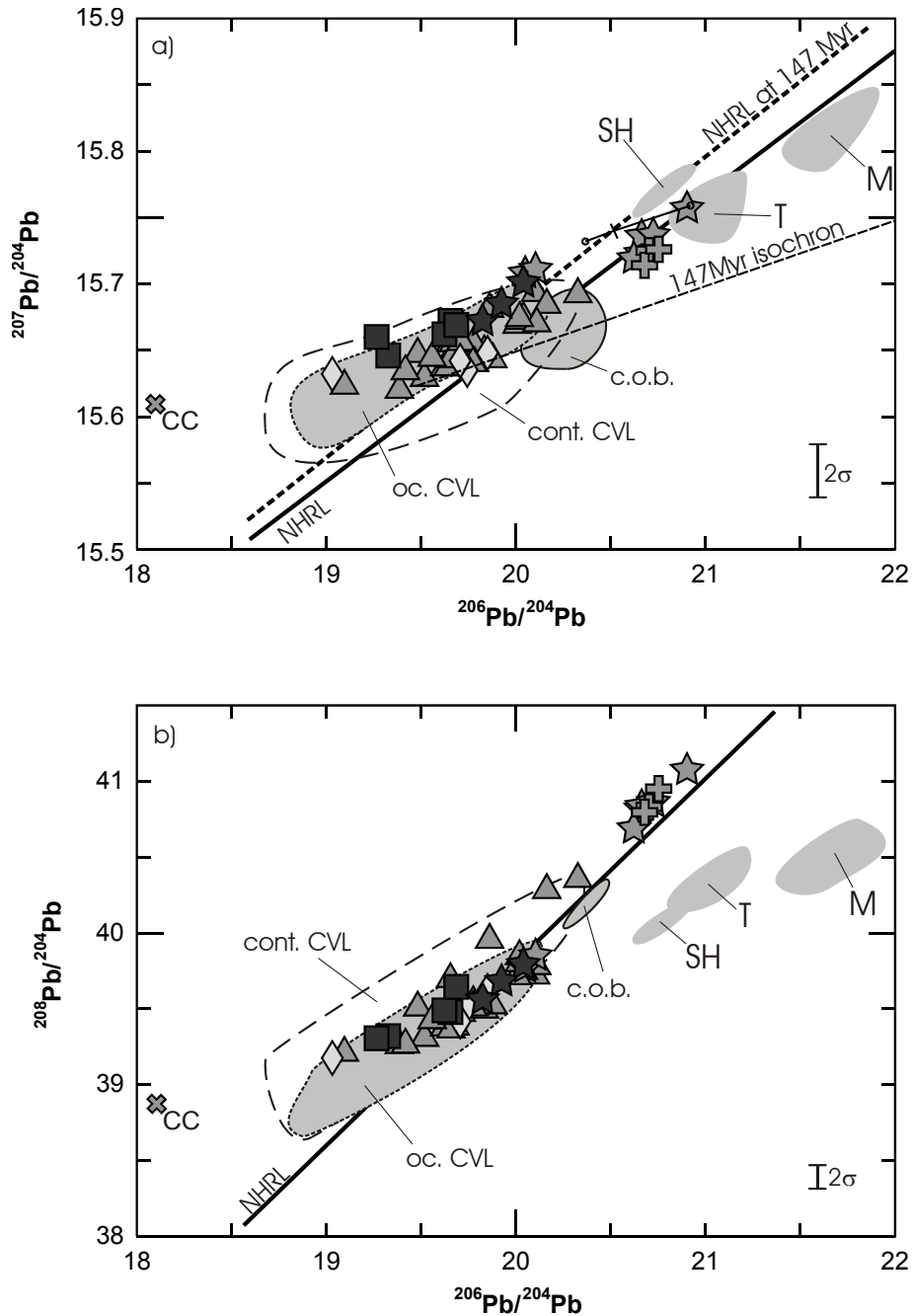


Fig. 3.3: Results in combined isotope spaces along with literature data for oceanic and continental CVL rocks with $\text{MgO} > 5\text{wt}\%$. Also shown are compositions of typical 'HIMU' basalts from St. Helena (SH), Tubuai (T) and Mangaia (M); and a mean of literature data for local continental crust (gray cross labeled CC). **a)** Megacrysts (cpx: stars, plag: crosses) extend to more radiogenic Pb isotopic compositions than associated host lavas (squares: Jos, triangles: Biu young, diamonds: Biu old) and lie close to the present-day NHRL. The heavy dashed line gives location of the NHRL at 147 Ma, calculated using a simple two-stage model starting 4.43 Ga ago with Canyon Diablo lead and $\mu' = 9.26$. Internal differentiation at ~ 1.77 Ga accounts for the NHRL. Thin dashed line represents an isochron of 147 Ma age. **b)** Source of megacrysts evolved with similar κ ($=^{232}\text{Th}/^{238}\text{U}$) than NHRL, and therefore is different from typical 'HIMU' compositions like St. Helena, Tubuai or Mangaia.

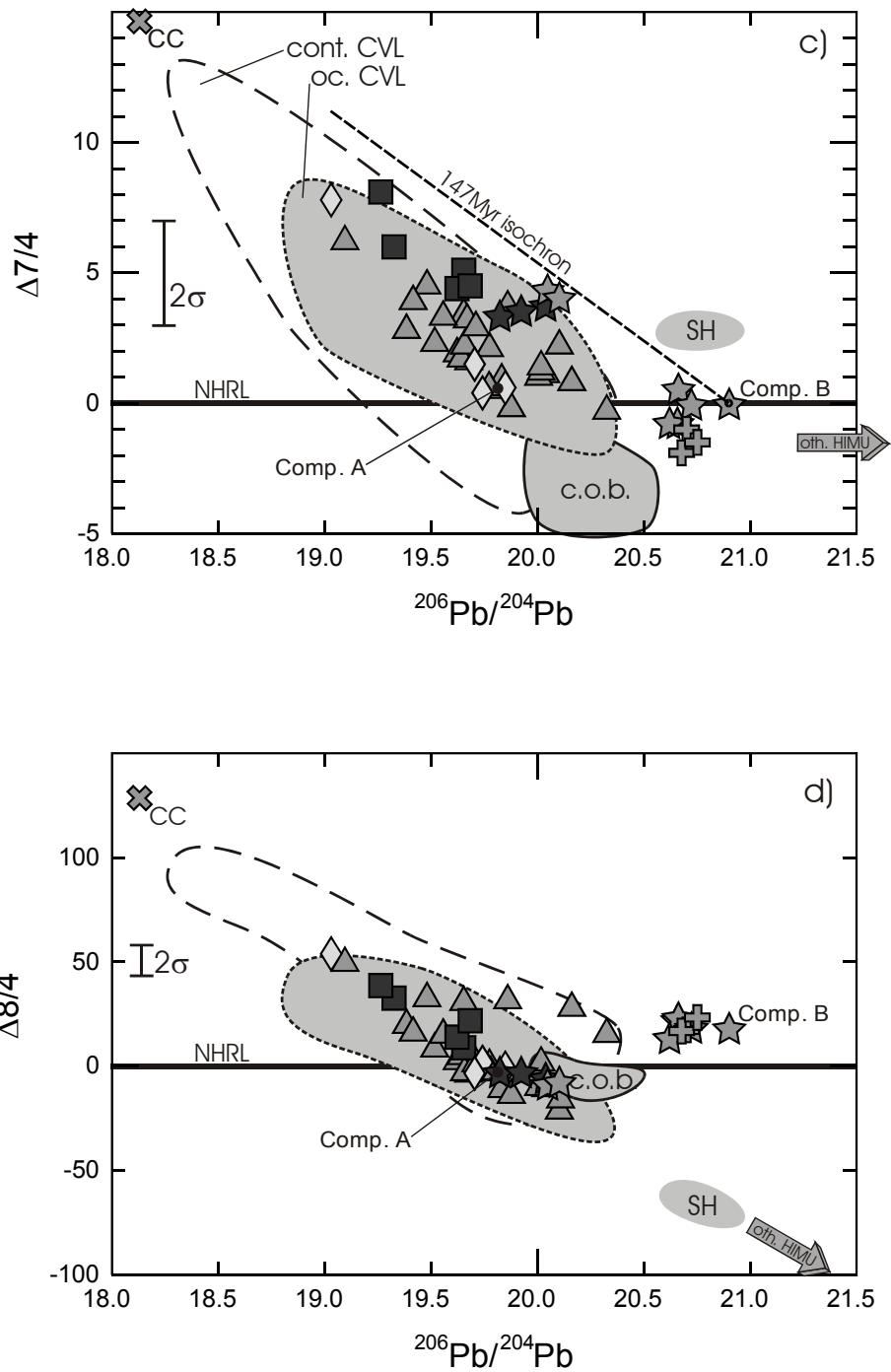


Fig. 3.3 cont.: Same data as in a and b, but in the delta notation of Hart (1984), which represents the vertical deviation of a given data point in $^{207}\text{Pb}/^{204}\text{Pb}$ (c) and $^{208}\text{Pb}/^{204}\text{Pb}$ (d) from the NHRL multiplied by a factor of 100.

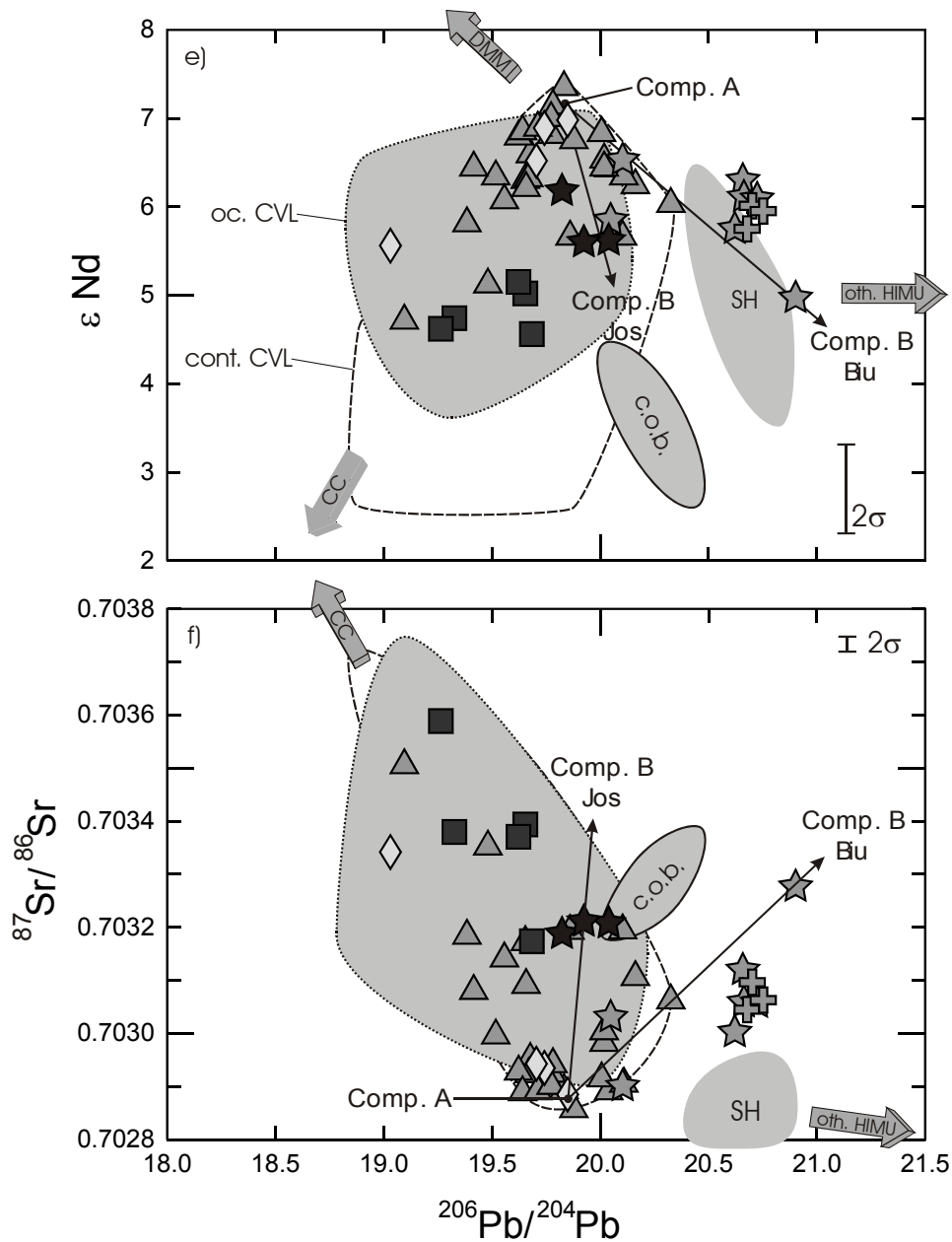


Fig. 3.3 cont.: In Pb-Sr (e) and Pb-Nd (f) isotope space, the megacrysts extend the trend formed by the magmas with $^{206}Pb/^{204}Pb > 19.8$. Other lavas are displaced towards the composition of Pan-African continental crust. We have used the megacryst data in figures 3.3 a-f to divide Biu and Jos Plateau rocks into two sets with different coding in the following discussion. Lavas that lie on a mixing trajectory from 'A' to 'B' are coded in open symbols, whereas lavas that do not overlap with megacryst compositions have solid symbols.

3.3. Discussion

3.3.1. Data arrays in Sr-Nd-Pb isotope space

In principle, the data in figures 3.3a-f can be divided into two linear arrays defined by three mixing endmember. The junction of both arrays is defined by a cluster of lavas with $^{206}\text{Pb}/^{204}\text{Pb} \sim 19.82$, $^{207}\text{Pb}/^{204}\text{Pb} \sim 15.64$, $^{208}\text{Pb}/^{204}\text{Pb} \sim 39.53$, $\epsilon_{\text{Nd}} \sim 7.0$ and $^{87}\text{Sr}/^{86}\text{Sr} \sim 0.70290$. We will refer to this composition in the following discussion as component 'A'. CVL lavas with similar composition have mantle-like $\delta^{18}\text{O}$ values of $\sim 5.5\%$ (Halliday *et al.*, 1988). The second endmember (component 'B') is best represented by the most radiogenic cpx megacryst of each plateau. An important observation from fig. 3.3a-f is that the megacrysts extend the array defined by the lavas to considerably higher $^{206}\text{Pb}/^{204}\text{Pb}$, $^{207}\text{Pb}/^{204}\text{Pb}$, $^{208}\text{Pb}/^{204}\text{Pb}$, $^{87}\text{Sr}/^{86}\text{Sr}$ and lower ϵ_{Nd} . Another observation is that cpx megacrysts from Biu and Jos Plateau do not overlap in all isotope systems. Jos cpx megacrysts are characterized by a lower $^{206}\text{Pb}/^{204}\text{Pb}$ for a given ϵ_{Nd} and $^{87}\text{Sr}/^{86}\text{Sr}$ when compared to Biu megacrysts (fig. 3.3e and f).

All Biu and Jos Plateau rocks with $^{206}\text{Pb}/^{204}\text{Pb} < 19.8$ seem to fan out to a composition which lies within literature data for Nigerian basement rocks (granulites, gneisses, migmatites and granites analyzed by Halliday *et al.* (1988), Dickin *et al.* (1991) and Dada *et al.* (1995)). Megacrysts do not plot on this trend. Interestingly, this third endmember (component 'C'), which is best represented by Pan-African continental crust, also seems to have affected CVL ocean islands with ages of oldest exposed rocks as little as 4.8 Ma (Pagalu). In the following section, we evaluate the nature of these three components.

3.3.2. Evidence for SCLM involvement in the genesis of Biu and Jos Plateau lavas

As pointed out above, the megacrysts extend to more radiogenic lead compositions than their host. In principle, this might be related to radiogenic ingrowth after formation of the megacrysts. However, cpx and plagioclase megacrysts from a single volcano are indistinguishable in lead isotope composition. Because of their very low U/Pb-ratios, radiogenic ingrowth of ^{207}Pb and ^{206}Pb is negligible in plagioclase megacrysts. Therefore, the lead isotope compositions of cpx and plagioclase reflect the source composition of the magma from which they grew. As a result, we conclude that either the megacrysts grew from melts that had been contaminated by a radiogenic component, or the lavas were contaminated with an unradiogenic component after megacryst crystallization.

There is evidence for an AFC (combined assimilation-fractional crystallization) process in the lavas lying along the trend from component 'A' to 'B', i.e. in lavas with $^{206}\text{Pb}/^{204}\text{Pb} > 19.8$. Correcting the MgO concentrations (as index of fractionation) of two samples for ol-accumulation (fig. 3.4a), the magmas show good correlations between decreasing MgO and increasing $^{206}\text{Pb}/^{204}\text{Pb}$ (fig. 3.4b) and decreasing ϵ_{Nd} respectively (fig. 3.4c). This suggests the temporal AFC progression proceeded from 'A' to 'B' and not vice versa.

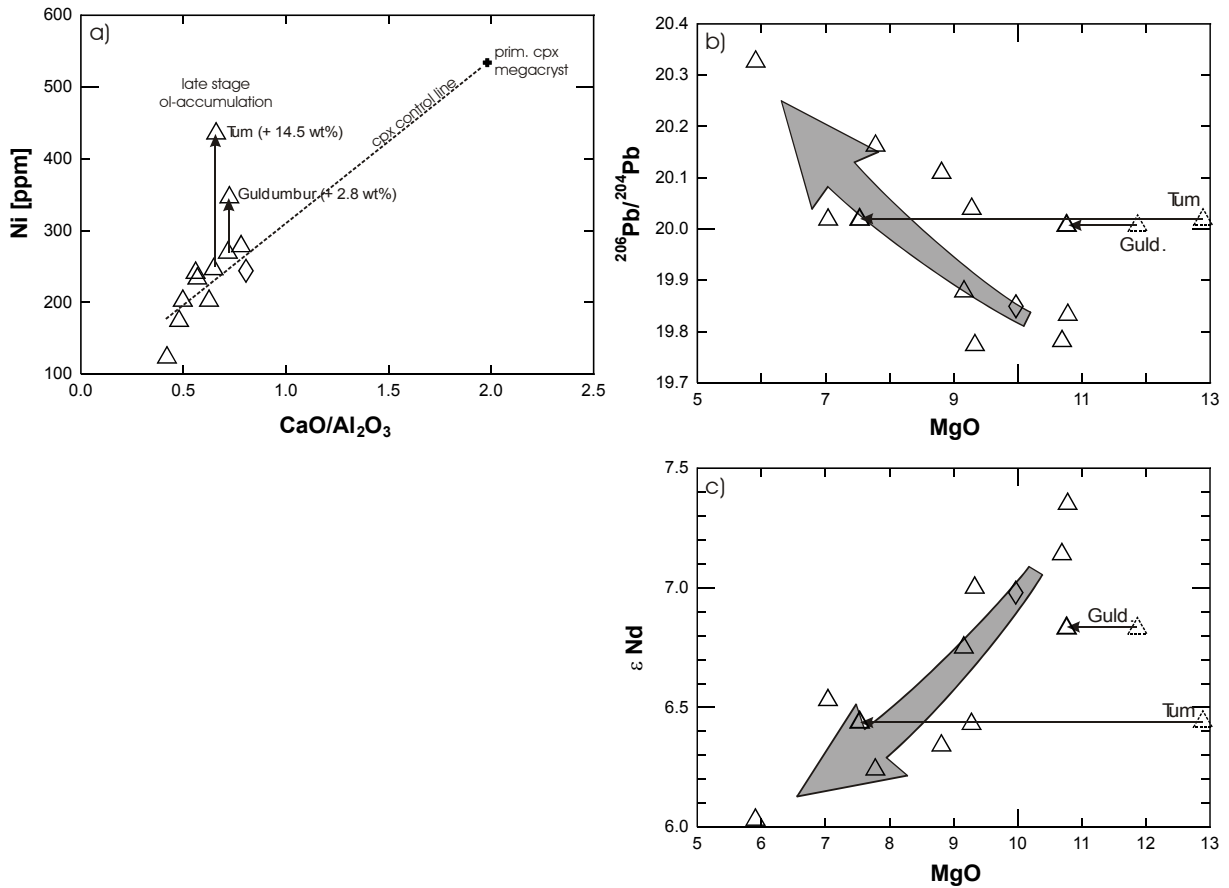


Fig. 3.4: Evidence for AFC in the basalts with $^{206}\text{Pb}/^{204}\text{Pb} > 19.8$. **a)** While most samples lie on a high-pressure cpx control line, two samples have elevated Ni concentrations, consistent with late-stage olivine accumulation. Assuming that cumulus olivine has 3000 ppm Ni and 49.8 wt% MgO, we calculate 14.5 and 2.8 wt% accumulation, which will not change the isotopic composition of the magmas. The MgO-corrected correlations are consistent with assimilation of a high $^{206}\text{Pb}/^{204}\text{Pb}$ **(b)** and low ϵ_{Nd} **(c)** component, while MgO decreases due to fractionation of cpx.

We therefore suggest that the isotopic trends observed for lavas with $^{206}\text{Pb}/^{204}\text{Pb} > 19.8$ reflect a mixing process between a 'primary' melt with lower $^{206}\text{Pb}/^{204}\text{Pb}$ of ~ 19.8 (component 'A') and liquids parental to the megacrysts (component 'B'), which had higher $^{206}\text{Pb}/^{204}\text{Pb}$, but which are not sampled at the surface in their original composition. Below, we evaluate whether this component derived from the SCLM, from assimilated continental crust, or from mixing with plume-derived 'HIMU' melts.

To determine the origin of component 'B', it is instructive to study Os isotope systematics of the lavas. Whereas the SCLM and thereof derived melts on average should have subchondritic to chondritic $^{187}\text{Os}/^{188}\text{Os}$ ratios, mantle plumes may have more radiogenic Os isotopes due to long-term recycling of Re-enriched oceanic crust. For example, typical 'HIMU' basalts from Mangaia have mean initial $^{187}\text{Os}/^{188}\text{Os}$ of 0.1492 (Hauri & Hart, 1993). Average continental crust on the other hand is highly radiogenic (e.g. 16 loess samples as proxy for eroded upper continental crust from China, Europe and South America have $^{187}\text{Os}/^{188}\text{Os}$ of ~ 1.05 (Peucker-Ehrenbrink & Jahn, 2001)). Assimilation of either SCLM, 'HIMU' or continental crust therefore should lead to different trends in $^{187}\text{Os}/^{188}\text{Os}$ when plotted versus indices of magma differentiation. Figure 3.2b shows that $^{187}\text{Os}/^{188}\text{Os}$ ratios of lavas with $^{206}\text{Pb}/^{204}\text{Pb} > 19.8$ scatter around typical mantle values of 0.125-0.129. Because we observe no trend towards high $^{187}\text{Os}/^{188}\text{Os}$, we rule out the possibility that component 'B' is crustally derived. This is also consistent with P,T-estimates for the crystallization of the megacrysts (chapter 2), which are well below the crust-mantle boundary.

Component 'B' also does not appear to be a typical 'HIMU' liquid, because megacryst compositions are significantly different from the latter in their higher $^{208}\text{Pb}/^{204}\text{Pb}$ and $^{87}\text{Sr}/^{86}\text{Sr}$ for a given $^{206}\text{Pb}/^{204}\text{Pb}$ (fig. 3.3b, 3.3f). Therefore, we propose that the trend observed between component 'A' and 'B' is due to assimilation of isotopically enriched SCLM or a SCLM-derived melt or fluid. To explain the isotopic offset between lavas and megacrysts, we propose that batches of a deep-sourced magma of composition 'A' emplaced in different depths of the SCLM, and concurrently assimilated enriched SCLM-derived liquids or fluids while fractionating the megacrysts. Megacrysts and evolved melts were subsequently mixed back in a fresh batch of magma of composition 'A' and finally erupted at the surface. This model is fully consistent with the model derived from major and trace element systematics in chapter 2. Although the process envisaged is an AFC-type process, we do not see correlations between isotopic composition of megacrysts of a single location and fractionation indices such as mg# of cpx megacrysts. Rather, megacrysts of a single location seem to be buffered at

a specific isotopic composition (cf. table B.22), implying isotopic homogenization within the magma chambers.

We have shown above that cpx megacrysts from Biu and Jos Plateau do not overlap in all isotope systems. However, the fact that primitive megacryst cpx compositions of Biu and Jos Plateau have similar trace element patterns, strongly suggests a common source magma for both areas. Therefore, the three Jos Plateau cpx megacrysts seem to define a different contamination vector in combined Nd-Sr-Pb isotope space than Biu megacrysts. Assuming that the process of megacryst genesis is similar in both areas, we propose that the lithospheric mantle underlying the Biu Plateau is more radiogenic in Pb isotopes compared to Jos Plateau, but similar in Sr-Nd isotopes. Additional analyses of peridotite xenoliths from Biu and Jos Plateau should better constrain the regional variations in lithospheric composition beneath the continental sector of the CVL.

3.3.3. Evidence for enriched lithosphere beneath the CVL

Evidence for a Mesozoic trace element enrichment of CVL mantle xenoliths was presented by Lee *et al.* (1996). However, the spatial pattern of enrichment displayed by CVL xenoliths does not correspond to the pattern of CVL lavas shown in fig. 1.3. For example, the xenoliths sampled from the c.o.b., which are supposed to show the highest enrichment (because of high $^{206}\text{Pb}/^{204}\text{Pb}$ of associated lavas), actually have the lowest $^{206}\text{Pb}/^{204}\text{Pb}$ (<18). Moreover, the most enriched xenolith with $^{206}\text{Pb}/^{204}\text{Pb}$ as high as 21.0 is a harzburgite xenolith from the Biu Plateau, which defines the northern end of the CVL. In principle, this might be related to disequilibrium between xenolith and thereof derived melt. However, diffusional constraints for equilibration of Sr, Nd and Pb isotopes are such that Sr and Pb should be well equilibrated in cpx of the xenoliths after ~150 Ma, while Nd might not be in equilibrium with its enriched environment (Van Orman *et al.*, 2001). Taking the data of Van Orman *et al.* (2002) along with P,T-estimates of the xenoliths of 1000°C and 15 kbar, and spherical cpx grain sizes of ~1 mm radius, we calculate that only 25.6% of the Nd in cpx has reached equilibrium concentrations (Crank, 1975). However, the cpx analyzed by Lee *et al.* (1996) has Nd concentrations equal to megacryst cpx and therefore represents a new grown or recrystallized grain, most probably representative of the ambient isotopic composition. In summary, the available xenolith data supports long-term metasomatic enrichment, but does not support the spatial pattern proposed by Halliday *et al.* (1990).

3.3.4. Models for the origin of enriched SCLM

Models for enrichment of SCLM as a result of underplated plumes or through metasomatism by asthenosphere-derived melts have been previously proposed (e.g. Ringwood (1982), Hawkesworth *et al.* (1984), Stein & Hofmann (1992), Halliday *et al.* (1995)). Halliday *et al.* (1990) suggested that the high $^{206}\text{Pb}/^{204}\text{Pb}$ -anomaly focused at the CVL continent/ocean-boundary was derived from radiogenic ingrowth in the lithospheric mantle with variable but high U/Pb over a time of ~ 125 Ma. A better estimate of the timing of enrichment of the lithosphere underlying the Biu Plateau might be 147 Ma, based upon the earliest period of magmatic activity in the northern Benue Trough (Coulon *et al.*, 1996).

If the radiogenic Pb signature of the CVL was derived from a homogeneous lithospheric source that was variably fractionated in U/Pb at ~ 150 Ma, we would expect the present-day samples to lie along a corresponding isochron in $^{206}\text{Pb}/^{204}\text{Pb}$ - $^{207}\text{Pb}/^{204}\text{Pb}$ isotope space. The 147 Ma isochron indicated in fig. 3.3a has a considerably shallower slope than the NHRL which yields an apparent 'age' of ~ 1.77 Ga. The signature of low $^{207}\text{Pb}/^{204}\text{Pb}$ for a given $^{206}\text{Pb}/^{204}\text{Pb}$ is best expressed by the parameter $\Delta 7/4$ defined by Hart (1984) as the vertical deviation in $^{207}\text{Pb}/^{204}\text{Pb}$ from the NHRL multiplied by a factor of 100. The model of Halliday *et al.* (1990) predicts a trend towards lower $\Delta 7/4$ with increasing $^{206}\text{Pb}/^{204}\text{Pb}$.

Component 'A' and the enriched lithospheric component 'B', as represented by megacryst compositions both cluster close to the NHRL, as seen on a plot of $\Delta 7/4$ versus $^{206}\text{Pb}/^{204}\text{Pb}$ (fig. 3.3c). If component 'B' were derived by 'young' fractionation from a starting composition such as component 'A', we would expect for the most radiogenic megacryst a $\Delta 7/4$ value of -6.0 . However, this is not observed. Component 'B' might also be derived from a starting composition with high $\Delta 7/4$, lying along the isochron specified in fig. 3.3c. However, no source rock with such composition has yet been recorded in CVL rocks. In summary, we conclude that generation of the radiogenic lead isotope signature in the modern CVL lithosphere due to 'young' U/Pb fractionation is unlikely.

Another possibility is impregnation of the preexisting lithosphere with 'HIMU'-type magmas derived from the fossil St. Helena hotspot, which at the time of opening of the South Atlantic was located in the region occupied by the present continent/ocean boundary (c.o.b.). However, as already pointed out by Halliday *et al.* (1990), there is a discrepancy between the isotope data for typical 'HIMU' and other CVL lavas, in that the former have lower $^{208}\text{Pb}/^{204}\text{Pb}$ and $^{87}\text{Sr}/^{86}\text{Sr}$ for a given $^{206}\text{Pb}/^{204}\text{Pb}$ and do not form an appropriate mixing end-

member for formation of the megacryst source magmas. We propose that impregnation by a different type of 'HIMU' melt is responsible for the elevated isotopic signatures of the lithosphere. This metasomatizing agent is distinct from typical 'HIMU' in its higher $\Delta 8/4$ and higher $^{87}\text{Sr}/^{86}\text{Sr}$, requiring higher time-integrated Th/U and Rb/Sr ratios in the source. This implies that 'HIMU' is more variable than previously suggested, and not a single 'component'.

3.3.5. Constraints on mixing relations from isotope systematics

The Pb and Os isotope systematics in the lavas with $^{206}\text{Pb}/^{204}\text{Pb} > 19.8$ also place constraints on the type of mixing. Due to much higher Os concentrations in mantle xenoliths (~ 3000 ppt) than in the lavas, the Os isotope composition of contaminated lavas will rapidly be controlled by the Os isotope composition of ambient SCLM. In contrast, assimilation of a SCLM-derived liquid that has lower Os concentrations does not produce such rapid changes in $^{187}\text{Os}/^{188}\text{Os}$. Figure 3.5a shows calculated mixing trajectories for both mixing scenarios along with our measured data, assuming that average SCLM has $^{187}\text{Os}/^{188}\text{Os} = 0.113$ (Shirey & Walker, 1998). Whatever the Os isotope composition of the ambient SCLM may be, bulk assimilation requires unreasonable large amounts of assimilation to account for the variation in Pb isotopes, and is energetically unfavorable. We therefore propose that the mixing process shown in fig. 3.5a is determined mainly by melt-melt mixing.

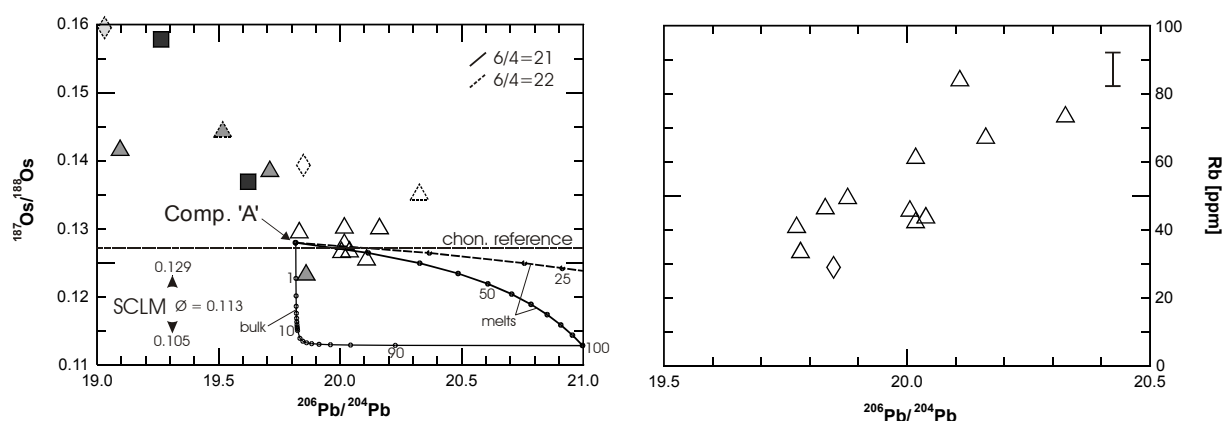


Fig. 3.5: a) Plot showing possible mixing scenarios in Os-Pb isotope space for lavas with $^{206}\text{Pb}/^{204}\text{Pb} > 19.8$. *Melt-melt mixing:* Comp. 'A': Mean of lavas with $[\text{Pb}] = 2.71$ ppm, $[\text{Os}] = 57.3$ ppt, $^{206}\text{Pb}/^{204}\text{Pb} = 19.82$, $^{187}\text{Os}/^{188}\text{Os} = 0.1281$. SCLM-derived melts: $[\text{Pb}] = 8.25$ ppm from highly enriched glasses found in spinel-peridotites as proxy for enriched SCLM melts (Yaxley *et al.*, 1997), $[\text{Os}] = 57.3$ ppt, $^{187}\text{Os}/^{188}\text{Os} = 0.113$, $^{206}\text{Pb}/^{204}\text{Pb} = 21.0$ (solid line) and 22.0 (dashed line). *Bulk SCLM assimilation:* $[\text{Pb}] = 0.16$

ppm, [Os]=3 ppb, isotopic composition as before. Dashed symbols mark samples with [Os] <30 ppt. Small numbers refer to percentage of liquid assimilated. **b)** Plot of $^{206}\text{Pb}/^{204}\text{Pb}$ versus rubidium of crustally uncontaminated lavas.

Looking at trace element systematics of lithospheric contaminated lavas, we find positive correlations between isotopic composition and concentrations of large ion lithophile elements (LILE) such as e.g. rubidium (fig. 3.5b). The variations in Rb content could in principle be related to passive enrichment due to megacryst fractionation, or to assimilation of a trace element enriched liquid. Unless the concentration of a trace element in bulk assimilated wall-rock is greater or equal to the concentration in the liquid, crystallization models limit the maximum enrichment of that trace element in the liquid to $1/F$. Major element modeling suggests ~65% fractional crystallization of cpx, gnt \pm apatite, plagioclase to form the most evolved cpx in the mantle (cf. fig. 2.13). This translates to a maximum enrichment in the liquid (assuming $D=0$ in all phases) of 2.86. However, looking only at cpx megacrysts from a single location (Miringa volcano), we find higher enrichment factors for Nb, La and Ce of 6.2, 4.7 and 5.7. Whereas bulk SCLM is characterized by low concentrations of incompatible elements when compared to the basalts, lithospheric-derived melts or fluids, similar to the melts commonly present as glasses in metasomatized mantle xenoliths (e.g. Chazot *et al.* (1996), Yaxley *et al.* (1997), Yaxley & Kemenetsky (1999), Schiano & Bourdon (1999), Coltorti *et al.* (2000)), may be highly enriched. A likely origin for the liquids parental to evolved cpx megacrysts therefore is assimilation of an enriched lithospheric-derived liquid.

3.3.6. A quantitative model of SCLM assimilation?

Any quantitative approach to model assimilation of SCLM-derived liquids requires input parameters for the concentration of trace elements in that liquid. Unfortunately the concentrations of Pb, Sr, Nd in bulk xenoliths and thereof derived liquid are largely unconstrained. Median Pb, Sr, Nd concentrations of 545 spinel lherzolite xenoliths reported in literature are Pb=0.16 ppm, Sr=17 ppm and Nd=1.11 ppm, similar to those commonly assumed for 'pyrolite' (McDonough & Sun, 1995). The most enriched reconstructed CVL xenolith P3 of Lee *et al.* (1996) yet has lower concentrations. This might be related to trace elements that are hosted in unrecognized interstitial glass films, or trace element-rich phases such as apatite and phlogopite that have not been analyzed. However, the inversion to melt concentrations is largely dependent on the initial xenolith mineralogy. Lamproites are thought to represent di-

rect partial melts of old refractory mantle peridotite that was formerly enriched in incompatible element bearing phases in the course of metasomatic processes (Bergmann, 1987). Although lamproites have highly enriched trace element concentrations with Sr and Nd reaching 6600 and 500 ppm, they have variable but unradiogenic $^{206}\text{Pb}/^{204}\text{Pb}$ ratios ranging from 16 to 18 (Bergmann, 1987). Such lamproite sources therefore evolved with low U/Pb, and provide no suitable model for the CVL lithosphere. However, they call attention to the possibly extreme trace element enrichment in lithospheric derived melts. Given these large uncertainties, any quantitative model of assimilation of a SCLM-derived liquid seems questionable and is therefore not attempted here.

3.3.7. Evidence for crustal contamination of Biu and Jos Plateau lavas

Removing the lavas that lie on a mantle mixing trend between primary composition 'A' and the inferred lithospheric mantle contaminant 'B', the remaining samples form broad trends pointing towards a third endmember characterized by high $^{87}\text{Sr}/^{86}\text{Sr}$, low ϵ_{Nd} , low $^{206}\text{Pb}/^{204}\text{Pb}$, high $\Delta 7/4$, high $\Delta 8/4$ and high $^{187}\text{Os}/^{188}\text{Os}$ (fig. 3.2, 3.3). Megacrysts with these compositions have not been observed. We therefore suggest that the trend towards component 'C' observed in the lavas was imposed on the magmas at shallower depths, after formation of the megacrysts. This may be due to assimilation of very shallow SCLM or the continental crust. Os isotopes provide a means for distinguishing the two possibilities. If the SCLM is responsible for the trends observed, we expect a trend towards lower or constant $^{187}\text{Os}/^{188}\text{Os}$ with increasing $^{87}\text{Sr}/^{86}\text{Sr}$ or decreasing $^{206}\text{Pb}/^{204}\text{Pb}$, respectively. Contamination with continental crust on the other hand should lead to significantly higher $^{187}\text{Os}/^{188}\text{Os}$. In fact, the latter observation is made in fig. 3.2b, indicating the involvement of crustal material. This is consistent with the trend towards high $\Delta 7/4$ observed in fig. 3.3c.

Lead as a trace element is also a powerful indicator for crustal contamination due to its high concentration in typical crustal rocks. Figure 3.6 shows a correlation in Ce/Pb vs. ϵ_{Nd} , consistent with assimilation of continental crust. Mass balancing, assuming 7% crustal assimilation, leads to changes of 26.7% in Ce/Pb, consistent with the data in fig. 3.6. Because of the high niobium concentrations in Biu and Jos Plateau basalts, Nb/U or Nb/Th change by only ~7%, and therefore are no significant indicators for crustal contamination. Although the occurrence of small felsic fragments in thin sections of some lavas from both the Biu and Jos Plateau also points to assimilation of continental crust, this cannot account for the isotopic

trends towards component 'C' alone. Firstly, the felsic fragments constitute less than $\sim 0.5\%$ by area in thin section, and secondly such contaminated rocks also fall on the crustally uncontaminated A-B trends in isotope space.

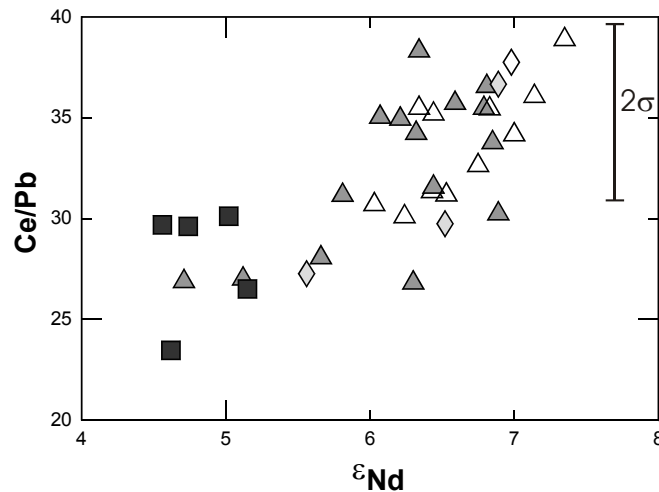


Fig. 3.6: Sensitive indicators for crustal contamination such as Ce/Pb ratios versus ϵ_{Nd} of Biu and Jos Plateau lavas are consistent with assimilation of continental crust.

To quantify the amount of crustal contamination in the lavas, we used the mean composition of Nigerian basement rocks found in literature (Halliday *et al.*, 1988), (Dickin *et al.*, 1991), (Dada *et al.*, 1995), which is similar to mean upper continental crust (Taylor & McLennan, 1995), but significantly more enriched in the REE. Sr, Nd, Pb and Os concentrations of the uncontaminated endmember were taken as mean of type 'A' lavas. Mixing can successfully be modeled via bulk rock assimilation. The results for Pb, Sr and Nd isotopes given in fig. 3.7a-d are encouragingly consistent, with maximum mass of assimilated crust on the order of $\sim 7\%$. Nigerian basement rocks have not been analyzed for $^{187}\text{Os}/^{188}\text{Os}$. However, depending on the mean age of the basement rocks which range from 0.6 to 3.5 Ga (Dada, 1998), we expect considerably higher crustal $^{187}\text{Os}/^{188}\text{Os}$ ratios than typical mantle values. A matching trend consistent with the results presented in fig. 3.7a-d may be achieved assuming $^{187}\text{Os}/^{188}\text{Os}$ of the crustal assimilant of ~ 0.6 (fig. 3.7e).

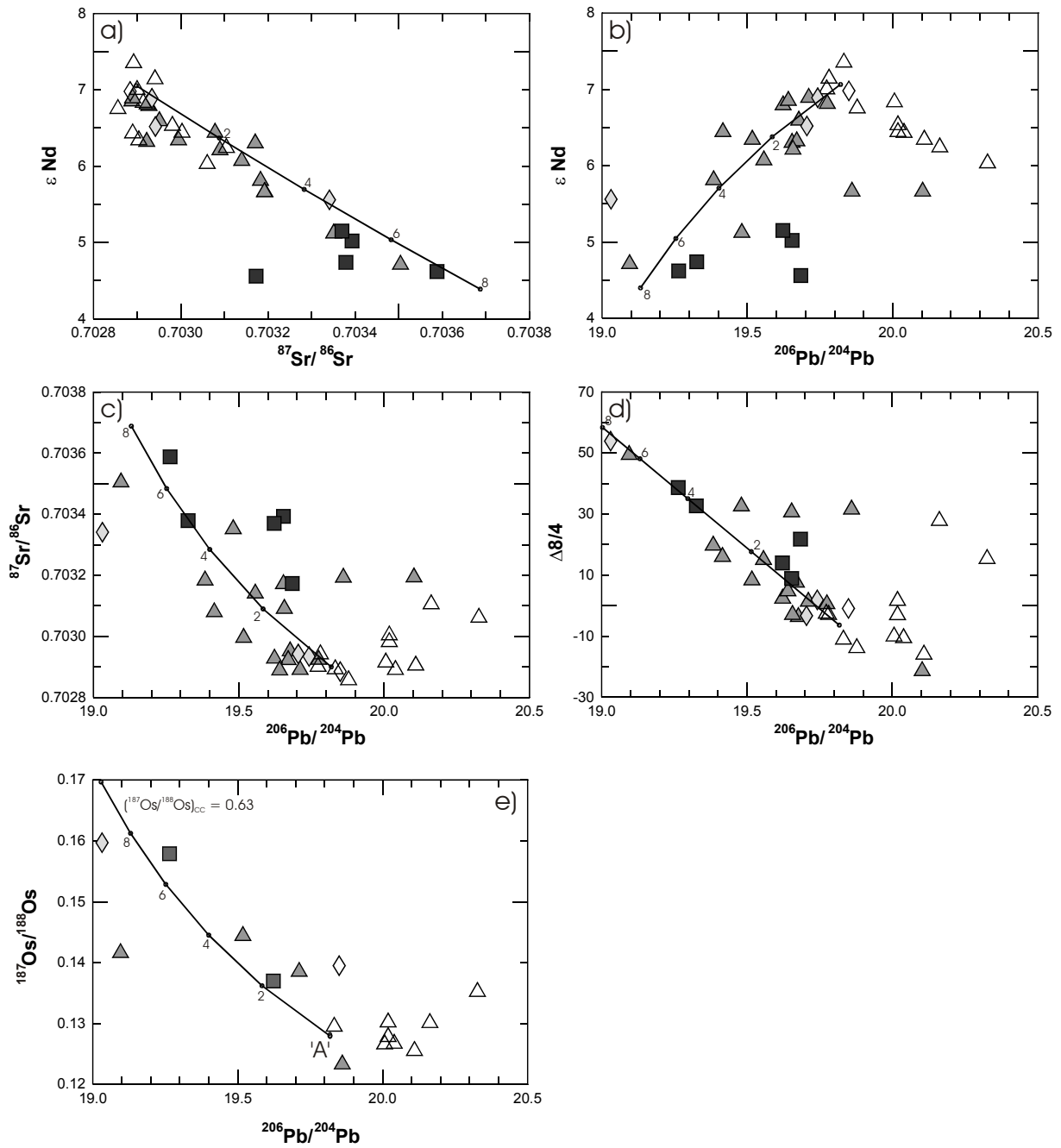


Fig. 3.7: a-d) Quantitative model of crustal contamination of composition 'A' using a mean literature dataset for the composition of the local crust with [Sr]=351 ppm, [Nd]=66.7 ppm, [Pb]=21.4 ppm, $^{87}Sr/^{86}Sr=0.7256$, $\epsilon_{Nd}=-16.2$, $^{206}Pb/^{204}Pb=18.13$, $\Delta 7/4=15.1$, $\Delta 8/4=128$. The results are mutually consistent in combined Sr, Nd, Pb isotopic systems, with maximum amounts of ~7% assimilation. e) Assuming [Os]=50 ppt for average continental crust (Esser & Turekian, 1993), the Os data is best explained by assimilation of material with $^{187}Os/^{188}Os \sim 0.6$.

3.3.8. Implications for crustal contamination in the oceanic CVL

Interestingly, the trends displayed by our isotope data from samples of the continental CVL towards high $\Delta 7/4$, $\Delta 8/4$, $^{87}\text{Sr}/^{86}\text{Sr}$ and low ϵ_{Nd} for a given $^{206}\text{Pb}/^{204}\text{Pb}$ are also existent in lavas from the oceanic part of the CVL (gray shaded fields in fig. 3.3a-f). If the trends in our data truly are generated by shallow contamination with Pan-African continental crust, then we have to raise the question whether shallow crustal contamination also was instrumental in formation of some CVL ocean island basalts.

Several investigators have suggested that crustal material was involved in the petrogenesis of anomalous oceanic tholeiites from the Kerguelen and Naturaliste Plateaux, Broken Ridge and Aphanasey Nikitin Rise in the Indian Ocean (for a summary see Borisova *et al.* (2001)). Studies of the Atlantic Ocean also have documented occurrences of ancient crust close to modern spreading ridges. Pilot *et al.* (1998) described Paleozoic and Proterozoic zircons in gabbros drilled from the Mid-Atlantic Ridge. Founded on diffusion coefficients of Lee *et al.* (1997), Pilot *et al.* (1998) emphasized that these zircons could not have resided in a shallow region of the upper convecting mantle for more than 1 my without totally losing their radiogenic lead, but could have been stored in cold detached slices of continental lithosphere. In addition, Precambrian gneiss has been dredged at the Mid-Atlantic Ridge at 26°N, a region believed to be outside the influence of ice-rafted debris (Belyatsky *et al.*, 1997). Bonatti *et al.* (1996) showed that lower cretaceous sedimentary rocks also occur close to the Mid-Atlantic Ridge. In this case, beneath the transform fracture there may be non-drifting segments where older material could remain for a long period. Thirlwall (1997) proposed that shield basalts of Gran Canaria may have been modified by assimilation of altered MORB-type crust or granitic bodies therein, and generally questions the quality of OIBs to reliably reflect the isotope and trace element compositions of their mantle source.

Assuming that the CVL as a whole shares a common and relatively homogeneous asthenospheric source (Fitton, 1987), (Ballentine *et al.*, 1997), (Barfod *et al.*, 1999), (Marzoli *et al.*, 2000) and that magma genesis in the continental and the oceanic sector of the CVL is similar, we propose that shallow contamination, either by rafted blocks of continental crust that became trapped in the ocean floor during breakup of Africa and South America, or alternatively assimilation of continental sediments is responsible for the similar isotopic trends in rocks from the continental and oceanic CVL. Os isotopes of samples from the oceanic CVL should help to identify continental contamination as both models predict a trend towards higher $^{187}\text{Os}/^{188}\text{Os}$ with lower $^{206}\text{Pb}/^{204}\text{Pb}$. Preliminary data of Gannoun *et al.* (2001) show

that basalts from the oceanic sector of the CVL extend to quite radiogenic Os isotopes ($^{187}\text{Os}/^{188}\text{Os}_{\text{ini}} = 0.1280\text{-}0.1876$). However, the covariation with $^{206}\text{Pb}/^{204}\text{Pb}$ seems to be the opposite of what we predict here.

Oxygen isotope variations may provide a means of distinguishing whether rafted continental crust or continent-derived sediments are responsible for the 'continental' signatures observed in oceanic CVL magmas. Seafloor sediments are characterized by very high $\delta^{18}\text{O}$ values (10-35‰, see Eiler *et al.* (2000) and references therein) and should therefore produce significant changes in $\delta^{18}\text{O}$, whereas granitic rocks have intermediate $\delta^{18}\text{O}$. For example, assuming 5% assimilation of crustal basement rocks ($\delta^{18}\text{O} = 10.6\text{‰}$ taken from Pan-African rocks from Yemen (Baker *et al.*, 2000)) in a magma with an initial $\delta^{18}\text{O}$ of 5.5‰ similar to most ultramafic rocks (Mattey *et al.*, 1994), we calculate a resultant shift in $\delta^{18}\text{O}$ of $\sim 0.25\text{‰}$. This may be too small to be easily resolved analytically. Assimilation of 5% average sediment (assuming $\delta^{18}\text{O} = 20\text{‰}$) on the other hand produces a shift in $\delta^{18}\text{O}$ of $\sim 0.9\text{‰}$. Available oxygen data presented by Halliday *et al.* (1988) do not provide a clear picture. Further study of Os and oxygen isotope trends in lava suites from individual CVL islands (e.g. Pagalu) are needed to determine the role of continental crust and sediments in the genesis of the lavas.

The geographic distribution of the continental signature in the oceanic CVL lavas suggests that assimilation of rafted continental crust rather than sediment is responsible for this signature. Islands closer to the continent should sit upon thicker sediment covers and therefore should be more easily affected by sediment assimilation than distant ones. However, the opposite relation is observed (Lee *et al.*, 1994). It is the island of Pagalu, which forms the most oceanward CVL extension, that shows the most pronounced continental signature. Therefore, shallow assimilation of rafted blocks of continental crust seems more likely.

Douglass *et al.* (1999) proposed a refractory 'LOMU' component as a characteristic source feature of Mid-Atlantic ridge basalts to produce trends towards low $^{206}\text{Pb}/^{204}\text{Pb}$ associated with high $^{87}\text{Sr}/^{86}\text{Sr}$, low ϵ_{Nd} and high $\Delta 7/4$. The lead isotope composition of 'LOMU' given in Douglass & Schilling (2000) plots on a straight extension from component 'A' through the composition of average Pan-African continental crust given in this paper. Douglass *et al.* (1999) assumed the 'LOMU' component to be delaminated subcontinental lithospheric mantle dispersed into the upper mantle during the breakup of Gondwana. However, the most pronounced 'LOMU' compositions sampled in oceanic basalts are found in the Aphanasey Nikitin Rise in the Indian Ocean (Douglass *et al.*, 1999), which were recently pro-

posed by Borisova *et al.* (2001) to be contaminated via shallow assimilation of lower continental crust. Based upon Os isotope systematics, we have shown above that the SCLM was not involved in generating the trends towards low $^{206}\text{Pb}/^{204}\text{Pb}$ and high $\Delta 7/4$ in our data (fig. 3.3a-f). We propose that the South Atlantic 'LOMU' signature in general does not correspond to refractory delaminated SCLM. It rather reflects shallow assimilation of rafted blocks of continental crust that became trapped in the oceanic lithosphere during continental breakup in the Mesozoic.

3.4 Conclusions

We have demonstrated that the isotopic compositions of megacrysts, which were argued to be genetically related to recent CVL volcanism, allow us to identify and distinguish the lithospheric modifications imprinted on two suites of CVL alkaline intraplate volcanics. Jos and Biu Plateau lavas are proposed to have a homogeneous asthenospheric source with $^{206}\text{Pb}/^{204}\text{Pb} \sim 19.8$, $\Delta 7/4$ and $\Delta 8/4 \sim 0$, $\epsilon_{\text{Nd}} \sim 7$, $^{87}\text{Sr}/^{86}\text{Sr} \sim 0.7029$, $^{187}\text{Os}/^{188}\text{Os} \sim 0.1280$ and $\delta^{18}\text{O}$ values of $\sim 5.5\%$. Magmas subsequently interacted with either enriched SCLM via melt-melt mixing, leading to increasing $^{206}\text{Pb}/^{204}\text{Pb}$, and/or continental crust, leading to decreasing $^{206}\text{Pb}/^{204}\text{Pb}$. The SCLM underlying the Biu Plateau is characterized by high $^{206}\text{Pb}/^{204}\text{Pb} \geq 21.0$, whereas the Jos Plateau SCLM probably has $^{206}\text{Pb}/^{204}\text{Pb} \approx 20$. While quantitative modeling of lithospheric contamination is hampered by too many unknown parameters, crustal contamination is well constrained and is on the order of 7% for the most contaminated lavas of both the Biu and Jos Plateau. Assuming that the continental and oceanic sector of the CVL are fed by a common and relatively homogeneous asthenospheric source, which is supported by hafnium and noble gas isotope studies (Ballentine *et al.*, 1997), (Barfod *et al.*, 1999), we conclude that the similar contamination trends seen in some oceanic CVL lavas are also caused by shallow assimilation of crustal material. Furthermore, we suggest that the South Atlantic 'LOMU' signature of Douglass *et al.* (1999) reflects assimilation of rafted blocks of continental crust rather than refractory delaminated SCLM.

3.5. Outlook

Subtracting the effects of lithospheric and crustal contamination on Biu and Jos Plateau magmas by means of associated megacrysts, we isolate an isotopically homogeneous source for continental CVL magmatism (composition 'A'), which is inferred to be derived

from asthenospheric depths. However, two problems remain incompletely understood. Firstly, primitive rocks of isotopic composition 'A' comprise both basanite with a negative K-anomaly and alkali basalt without K-anomaly (fig. 3.8). Given that both types of rocks should be derived from the same source by different degrees of melting, we would expect them to show the same kind of trace element pattern. Secondly, there is a discrepancy between the trace element concentrations deduced from the mean of lavas with composition 'A', and the concentrations inferred from inversion of most primitive cpx megacrysts (cf. fig. 2.16), in that the latter are lower by a factor of ~ 1.5 for the highly incompatible elements. Such a relation is commonly used to argue against a cogenetic relation between megacrysts and host magma. In part this may be explained by late-stage fractionation of olivine, as none of the liquids has mg# in equilibrium with typical mantle olivine. However, the amount of olivine that has to be added to the lavas does not exceed 10% and therefore does not explain the discrepancy alone. Alternatively the cpx/melt distribution coefficients may be too high. This cannot explain the difference either, as we have already utilized values from the low end of published data. However, these problems do not affect the conclusions drawn in this work, and leave space for further investigations.

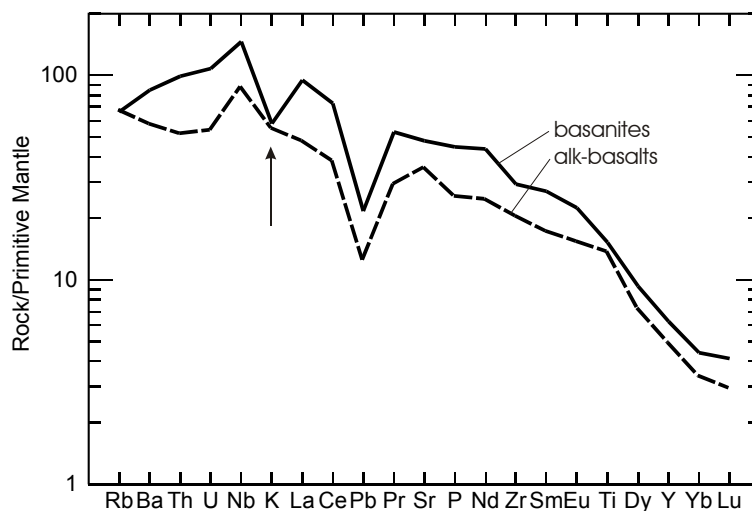


Fig. 3.8: Trace element patterns of rocks of composition 'A' comprise both basanites (solid line) showing a pronounced negative K-anomaly, and alkali basalts (broken line) without K-anomaly. Inverted melts from primitive cpx megacrysts also display a significant negative K-anomaly (literature $D(K)^{cpx/basalt}$ only varies between 0.0067-0.0081), implying derivation from melts similar to the basanites. The evolved melt inclusions, which are thought to be most affected by lithospheric contamination, do not show a significant K-anomaly (cf. fig. 2.3)

3.6. References

- Baker, J. A., MacPherson, C. G., Menzies, M. A., Thirlwall, M. F., et al. (2000). Resolving Crustal and Mantle Contributions to Continental Flood Volcanism, Yemen; Constraints from Mineral Oxygen Isotope Data. *Journal of Petrology* **41** (12), 1805-1820.
- Ballentine, C. J., Lee, D. C. & Halliday, A. N. (1997). Hafnium isotopic studies of the Cameroon line and new HIMU paradoxes. *Chemical Geology* **139** (1-4), 111-124.
- Barfod, D. N., Ballentine, C. J., Halliday, A. N. & Fitton, J. G. (1999). Noble gases in the Cameroon line and the He, Ne, and Ar isotopic compositions of high μ (HIMU) mantle. *Journal of Geophysical Research-Solid Earth* **104** (B12), 29509-29527.
- Belyatsky, B. V., Levsky, L. K., Trukhalev, A. I., Pogrebitsky, Y. E., et al. (1997). Precambrian granite-gneiss from the Mid-Atlantic Ridge (26°N): a U-Pb and Sm-Nd isotopic study. *Geochemistry International* **35** (8), 770-773.
- Bennett, V. C., Norman, M. D. & Garcia, M. O. (2000). Rhenium and platinum group element abundances correlated with mantle source components in Hawaiian picrites: sulphides in the plume. *Earth and Planetary Science Letters* **183** (3-4), 513-526.
- Bergmann, S. C. (1987). Lamproites and other potassium-rich igneous rocks: a review of their occurrence, mineralogy and geochemistry. In: Fitton, J. G. & Upton, B. G. J. (eds) *Alkaline Igneous Rocks*. Oxford: Geological Society Special Publication No. 30, 103-190.
- Bonatti, E., Ligi, M., Borsetti, A. M., Gasperini, L., et al. (1996). Lower Cretaceous deposits trapped near the equatorial Mid-Atlantic Ridge. *Nature* **380** (6574), 518-520.
- Borisova, A. Y., Belyatsky, B. V., Portnyagin, M. V. & Sushchevskaya, N. M. (2001). Petrogenesis of olivine-phyric basalts from the Aphanasey Nikitin Rise: Evidence for contamination by cratonic lower continental crust. *Journal of Petrology* **42** (2), 277-319.
- Chazot, G., Menzies, M. & Harte, B. (1996). Silicate glasses in spinel lherzolites from Yemen: Origin and chemical composition. *Chemical Geology* **134** (1-3), 159-179.
- Coltorti, M., Beccaluva, L., Bonadiman, C., Salvini, L., et al. (2000). Glasses in mantle xenoliths as geochemical indicators of metasomatic agents. *Earth and Planetary Science Letters* **183** (1-2), 303-320.
- Coulon, C., Vidal, P., Dupuy, C., Baudin, P., et al. (1996). The Mesozoic to Early Cenozoic magmatism of the Benue Trough (Nigeria): Geochemical evidence for the involvement of the St Helena plume. *Journal of Petrology* **37** (6), 1341-1358.
- Crank, J. (1975). *The mathematics of diffusion*. Oxford: Oxford University Press.
- Dada, S. S. (1998). Crust-forming ages and Proterozoic crustal evolution in Nigeria: a reappraisal of current interpretations. *Precambrian Research* **87** (1-2), 65-74.

- Dada, S. S., Briquieu, L., Harms, U., Lancelot, J. R., et al. (1995). Charnockitic and Monzonitic Pan-African Series from North-Central Nigeria: Trace-Element and Nd, Sr, Pb Isotope Constraints on Their Petrogenesis. *Chemical Geology* **124** (3-4), 233-252.
- Dickin, A. P., Halliday, A. N. & Bowden, P. (1991). A Pb, Sr and Nd Isotope Study of the Basement and Mesozoic Ring Complexes of the Jos Plateau, Nigeria. *Chemical Geology* **94** (1), 23-32.
- Dougllass, J. & Schilling, J. G. (2000). Systematics of three-component, pseudo-binary mixing lines in 2D isotope ratio space representations and implications for mantle plume-ridge interaction. *Chemical Geology* **163** (1-4), 1-23.
- Dougllass, J., Schilling, J. G. & Fontignie, D. (1999). Plume-ridge interactions of the Discovery and Shona mantle plumes with the southern mid-Atlantic ridge (40 degrees-55 degrees S). *Journal of Geophysical Research-Solid Earth* **104** (B2), 2941-2962.
- Eiler, J. M., Crawford, A., Elliott, T., Farley, K. A., et al. (2000). Oxygen isotope geochemistry of oceanic-arc lavas. *Journal of Petrology* **41** (2), 229-256.
- Esser, B. K. & Turekian, K. K. (1993). The Osmium Isotopic Composition of the Continental Crust. *Geochimica Et Cosmochimica Acta* **57** (13), 3093-3104.
- Fitton, J. G. (1987). The Cameroon Line, West-Africa: a comparison between oceanic and continental alkaline volcanism. In: Fitton, J. G. & Upton, B. G. J. (eds) *Alkaline Igneous Rocks* Geological Society Special Publication, 273-291.
- Gannoun, A., Burton, K. W., Barfod, D. N. & Halliday, A. (2001). Osmium-Isotope Variations in Cameroon Line Basalts: HIMU Mantle Versus Crustal Contamination. *Eos Trans. AGU*, 82(47), Fall Meet. Suppl., Abstract V21D-07
- Halliday, A. N., Davidson, J. P., Holden, P., Dewolf, C., et al. (1990). Trace-Element Fractionation in Plumes and the Origin of HIMU Mantle beneath the Cameroon Line. *Nature* **347** (6293), 523-528.
- Halliday, A. N., Dickin, A. P., Fallick, A. E. & Fitton, J. G. (1988). Mantle Dynamics - a Nd, Sr, Pb and O Isotopic Study of the Cameroon Line Volcanic Chain. *Journal of Petrology* **29** (1), 181-211.
- Halliday, A. N., Lee, D. C., Tommasini, S., Davies, G. R., et al. (1995). Incompatible Trace-Elements in OIB and MORB and Source Enrichment in the Sub-Oceanic Mantle. *Earth and Planetary Science Letters* **133** (3-4), 379-395.
- Hart, S. R. (1984). A Large-Scale Isotope Anomaly in the Southern-Hemisphere Mantle. *Nature* **309** (5971), 753-757.
- Hauri, E. H. & Hart, S. R. (1993). Re-Os Isotope Systematics of HIMU and EM-2 Oceanic Island Basalts from the South-Pacific Ocean. *Earth and Planetary Science Letters* **114** (2-3), 353-371.
- Hawkesworth, C. J., Rogers, N. W., Vancalsteren, P. W. C. & Menzies, M. A. (1984). Mantle Enrichment Processes. *Nature* **311** (5984), 331-335.

- Lee, D. C., Halliday, A. N., Davies, G. R., Essene, E. J., et al. (1996). Melt enrichment of shallow depleted mantle: A detailed petrological, trace element and isotopic study of mantle-derived xenoliths and megacrysts from the Cameroon line. *Journal of Petrology* **37** (2), 415-441.
- Lee, D. C., Halliday, A. N., Fitton, J. G. & Poli, G. (1994). Isotopic Variations with Distance and Time in the Volcanic Islands of the Cameroon Line - Evidence for a Mantle Plume Origin. *Earth and Planetary Science Letters* **123** (1-4), 119-138.
- Lee, J. K. W., Williams, I. S. & Ellis, D. J. (1997). Pb, U and Th diffusion in natural zircon. *Nature* **390** (6656), 159-162.
- Marzoli, A., Piccirillo, E. M., Renne, P. R., Bellieni, G., et al. (2000). The Cameroon Volcanic Line revisited: Petrogenesis of continental basaltic magmas from lithospheric and asthenospheric mantle sources. *Journal of Petrology* **41** (1), 87-109.
- Marzoli, A., Renne, P. R., Piccirillo, E. M., Francesca, C., et al. (1999). Silicic magmas from the continental Cameroon Volcanic Line (Oku, Bambouto and Ngaoundere): $^{40}\text{Ar}/^{39}\text{Ar}$ dates, petrology, Sr-Nd-O isotopes and their petrogenetic significance. *Contributions to Mineralogy and Petrology* **135** (2-3), 133-150.
- Mattey, D. P., Lowry, D. & Macpherson, C. G. (1994). Oxygen isotope composition of mantle peridotite. *Earth and Planetary Science Letters* **128**, 231-241.
- McDonough, W. F. & Sun, S. S. (1995). The Composition of the Earth. *Chemical Geology* **120** (3-4), 223-253.
- Peucker-Ehrenbrink, B. & Jahn, B.-m. (2001). Rhenium-osmium isotope systematics and platinum group element concentrations: Loess and the upper continental crust. *Geochemistry Geophysics Geosystems* **2**, U33-U59.
- Pilot, J., Werner, C. D., Haubrich, F. & Baumann, N. (1998). Palaeozoic and Proterozoic zircons from the Mid-Atlantic Ridge. *Nature* **393** (6686), 676-679.
- Righter, K. & Hauri, E. H. (1998). Compatibility of rhenium in garnet during mantle melting and magma genesis. *Science* **280** (5370), 1737-1741.
- Ringwood, A. E. (1982). Phase-Transformations and Differentiation in Subducted Lithosphere - Implications for Mantle Dynamics, Basalt Petrogenesis, and Crustal Evolution. *Journal of Geology* **90** (6), 611-643.
- Schiano, P. & Bourdon, B. (1999). On the preservation of mantle information in ultramafic nodules: glass inclusions within minerals versus interstitial glasses. *Earth and Planetary Science Letters* **169** (1-2), 173-188.
- Shirey, S. B. & Walker, R. J. (1998). The Re-Os isotope system in cosmochemistry and high-temperature geochemistry. *Annual Review of Earth and Planetary Sciences* **26**, 423-500.
- Stein, M. & Hofmann, A. W. (1992). Fossil Plume Head beneath the Arabian Lithosphere. *Earth and Planetary Science Letters* **114** (1), 193-209.
- Taylor, S. R. & McLennan, S. M. (1995). The Geochemical Evolution of the Continental Crust. *Reviews of Geophysics* **33** (2), 241-265.

- Thirlwall, M. F. (1997). Pb isotopic and elemental evidence for OIB derivation from young HIMU mantle. *Chemical Geology* **139** (1-4), 51-74.
- Van Orman, J. A., Grove, T. L. & Shimizu, N. (2001). Rare earth element diffusion in diopside: influence of temperature, pressure, and ionic radius, and an elastic model for diffusion in silicates. *Contributions to Mineralogy and Petrology* **141** (6), 687-703.
- Van Orman, J. A., Grove, T. L., Shimizu, N. & Layne, G. D. (2002). Rare earth element diffusion in a natural pyrope single crystal at 2.8 GPa. *Contributions to Mineralogy and Petrology* **142** (4), 416-424.
- Yaxley, G. M., Kamenetsky, V., Green, D. H. & Falloon, T. J. (1997). Glasses in mantle xenoliths from western Victoria, Australia, and their relevance to mantle processes. *Earth and Planetary Science Letters* **148** (3-4), 433-446.
- Yaxley, G. M. & Kamenetsky, V. (1999). In situ origin for glass in mantle xenoliths from southeastern Australia: insights from trace element compositions of glasses and metasomatic phases. *Earth and Planetary Science Letters* **172** (1-2), 97-109.

CHAPTER 4: APPENDICES

Appendix A: Sampling and analytical techniques

A.1.: Sampling locations

All samples (volcanic rocks, megacrysts and xenoliths) described in this work were collected during a field excursion to the Biu and Jos Plateau, northern Nigeria, in 1998. A summary of the sampling locations along with their geographic coordinates as determined by GPS is given in tables A.1 (Biu Plateau) and A.2 (Jos Plateau). Samples were wrapped in paper and labeled plastic bags and shipped to the University of Frankfurt in steel boxes. Only the volcanic rocks and the megacrysts were studied extensively so far, whereas the xenoliths (peridotites and pyroxenites) remain mainly unprocessed. Only two xenolith-derived cpx have been studied in detail by EMP and ionprobe to enlighten the significant differences between cpx megacrysts and cpx derived from disaggregated peridotites or pyroxenites.

Sample Location	Petrography	Megacrysts
Zagu Hill 10°56'85 N 12°05'11 E	trachybasalt some xenoliths	rare cpx
Jigu Hill 10°55'22 N 12°00'55 E	Jigu Maar: basanite Jigu 1: alk. basalt some xenoliths	no
Ohne Namen (X) 10°54'40 N 12°01'21 E	alk. basalt no xenoliths	no
Pelamabelu Hill (Pela jung) 10°50'55 N 12°06'15 E	trachybasalt some xenoliths (~1cm)	no
Koroko 10°50'22 N 11°56'70 E	phonolite small xenoliths	amphibole, phlogopite
Krater SW Pelamabelu Hill (Pela alt) 10°50'14 N 12°05'65 E	basaltic trachyandesite strongly weathered, many xenoliths	numerous, cpx, plagioclase,
Dutsin Dam Hill 10°49'30 N 12°02'56 E	Dam: basanite Dam 2: trachybasalt numerous xenoliths	garnet, cpx, plagioclase, ilmenite, amphibole, apatite, olivine
Dutse Bugor Hill 10°49'24 N 12°05'98 E	alk. basalt xenoliths oxidized,	cpx, plagioclase
Nowa Hill (Krater) 10°48'87 N 12°01'30 E	scoria only	cpx, plagioclase, ilmenite, zircon, corundum, spinel
Hügel SE Bugor 10°48'54 N 12°06'64 E	alk. basalt some xenoliths, cpx cumu- lates	

Bos Hill 10°47'34 N 12°01'81 E	alk. basalt cpx-ilm cumulates	
Hilia Hill 10°47'32 N 12°05'22 E	Hilia 1+2: alk. basalt xenoliths up to 30 cm, cpx-cumulates, some felsic	cpx, garnet, plagioclase, ilmenite, spinel
Tamza Hill 10°46'42 N 12°03'57 E	trachybasalt many xenoliths (up to 10 cm)	surrounded by laterite containing cpx, garnet, ilmenite
Gufka Hill 10°44'18 N 12°04'78 E	alk. basalt xenoliths, also felsic	cpx, garnet, plagioclase
Dutsin Miringa Hill 10°44'04 N 12°07'30 E	basaltic trachyandesite numerous xenoliths (felsic, maf. cumulates, peridotites up to 50 cm)	very abundant: garnet, ilmenite, cpx, plagioclase, spinel, olivine, phlogopite, apatite
Dutsin Maldau Hill 10°42'83 N 12°06'04 E	alk. basalt xenoliths up to 10 cm	plagioclase, ilmenite, garnet, cpx
Ga-Guldumbur Hill 10°42'30 N 12°07'41 E	alk. basalt few xenoliths	no
Pelamabelu Hill 2 10°41'18 N 12°07'85 E	alk. basalt numerous xenoliths up to 10 cm	no
Wiga Hill 10°40'79 N 12°00'25 E	alk. basalt	
Gwaram Hill 10°39'89 N 12°07'96 E	basaltic trachyandesite few xenoliths	few plagioclase, cpx, amphibole
Ga-Zumta Hill 10°38'96 N 12°06'84 E	trachybasalt some xenoliths	plagioclase
Ga-Hizshi Hill 10°38'72 N 12°08'10 E	trachybasalt, altered "Sonnenbrenner" peridotites up to 40 cm, cpx cumulates	plagioclase up to 5 cm, cpx
Tum 10°36'85 N 12°06'62 E	Tum: alk. basalt E'Tum: trachybasalt small xenoliths	no
Kudangir Hill 10°34'91 N 12°02'30 E	alk. basalt, no sample "Sonnenbrenner" very few xenoliths	no
Gumja Hill 10°33'45 N 12°06'15 E	alk. basalt xenoliths oxidized, many felsic	cpx, plagioclase, spinel
Ga Tila Hill 10°32'68 N 12°08'56 E	Tila 1: alk. basalt, maar Tila Str.: alk. basalt, flow	cpx, plagioclase

Table A.1: Volcanoes of the Biu-Plateau from N to S.

Dai 9°24'20 N 9°10'63 E	alk. basalt	
Kerang 9°20'65 N 9°11'49 E	basanite numerous xenoliths up to 25 cm, some felsic	cpx, gnt, plag, ilm, amph, ol
Ampang 9°19'07 N 9°11'99 E	trachybasalt small xenoliths	cpx, plag
Pidong 9°17'34 N 9°12'24 E	chain of 5 volcanoes Pidong S: trachybasalt, xenolithic? Pidong M: basanite, maar alternating layers of granite and lapilli	cpx, plag

Table A.2: Volcanoes of the Jos-Plateaus from N to S.

A.2.: Major and trace element analyses of volcanic rocks

Rocks were first coarsely crushed in steel mortars. Selected chips free of obvious xenocrysts or alteration were then powdered in an agate ring-disc mill. The powders were analyzed for major elements by X-ray fluorescence spectroscopy with a Philips PW 1404 instrument at the University of Frankfurt using Li-borate melt discs (table B.1) and for trace elements at the University of Mainz using pressed powder pellets (table B.2). A subset of 20 samples was analyzed by ICP-AES for REE concentrations following sinter dissolution at the GeoForschungsZentrum in Potsdam (table B.3, for analytical details see Zuleger & Erzinger (1988)). A subset of 17 samples was commercially analyzed by ICP-MS following HF-HNO₃ acid dissolution (table B.4) at the Department of Earth Science, Memorial University of Newfoundland, St. John's, Canada (MUN). The analytical package also includes XRF analyses for quality control (table B.5). Analytical details are found in Jenner *et al.* (1990). In addition, all samples were commercially analyzed by ICP-MS for trace elements at the University of Goettingen, Germany (table B.6).

Comparison of the 6 data sets revealed problems of the Goettingen ICP-MS lab to accurately determine HFSE concentrations (fig. A.1). Especially niobium, zirconium and strontium concentrations tend to be low when compared to consistent XRF and MUN ICP-MS data sets. The low results of the Goettingen lab are most easily explained by precipitation of insoluble fluorides from the sample solution (Yokoyama *et al.*, 1999). Therefore, the major and trace element analyses reported in table B.7, which is the basis for the discussions in chapter 2 and 3, are compiled by using the most accurate data set for each element (see table B.8). Major element concentrations were taken from XRF melt disc data from Frankfurt, which

showed excellent agreement with MUN XRF data. Ba, Nb, Sr, Zr, V, Cr, Ni and Zn concentrations with errors of <5%, and Sc, Co, Cu and Ga concentrations with errors of <15% were taken from XRF pressed powder pellet data (Mainz), whereas S and Cl concentrations with errors <5% are from MUN. Other data in table B.7 is compiled from ICP-MS and ICP-AES analyses with errors on Cs, Rb, Th, U, Pb, Ta, REE, Pb <10%, Hf <20%, and Mo <25% respectively.

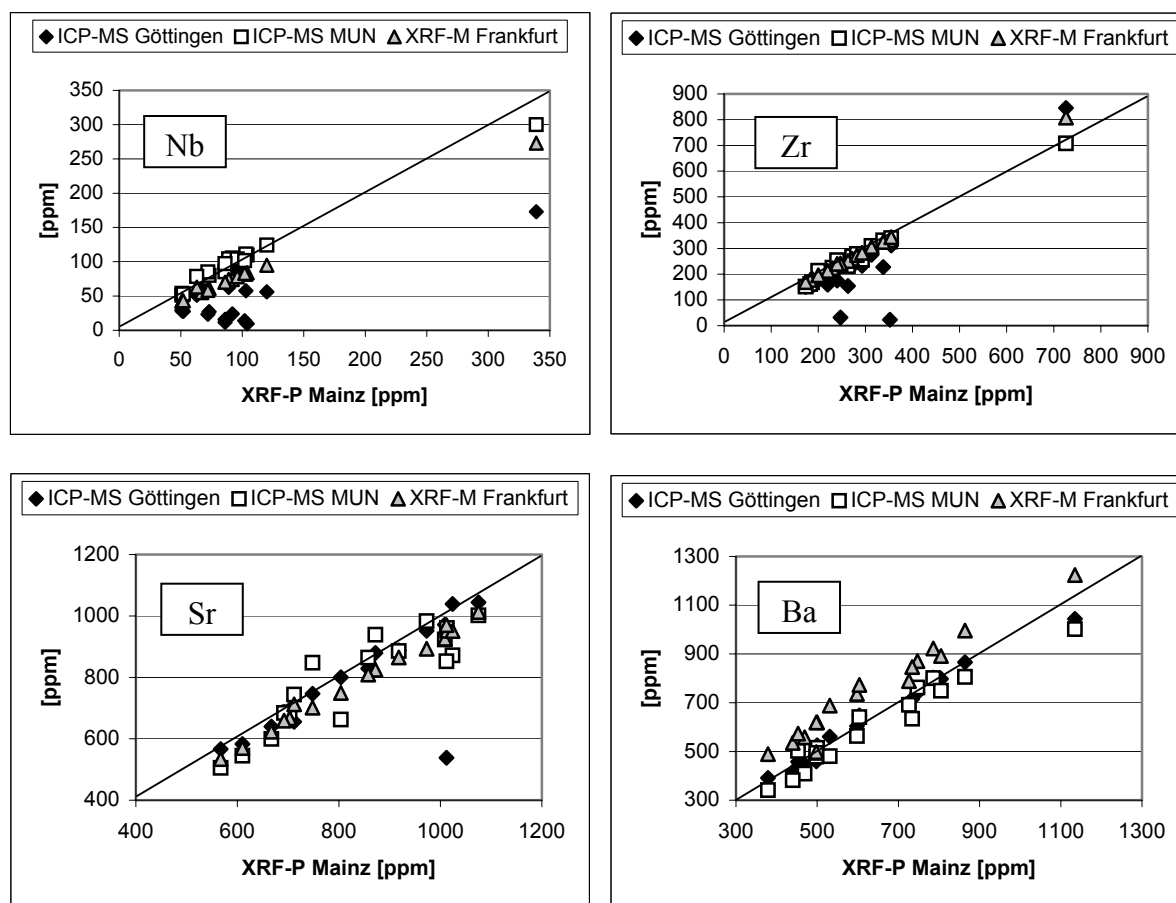


Fig. A.1 a-d: Comparison of 4 different determinations of trace element concentrations in volcanic rocks from the Bui and Jos Plateau. Because HFSE such as Nb and Zr are often hosted in phases which are difficult to attack such as spinel and zircon, HFSE determination methods like XRF of pressed powder pellets (XRF-P) that circumvent the problem of sample disintegration are advantageous. Therefore XRF-P analyses from the University of Mainz were taken as reference on the abscissa on each graph. Precision and accuracy of each method is reported in table B.8). All graphs show a 1:1 equiline for comparison. The highest Nb concentration in a) is outside the calibration limit of the powder pellets and therefore explains the inconsistency with other data. In general, there is good agreement between XRF-P, XRF-M and ICP-MS data from MUN. However, XRF data overall shows less scatter when compared to ICP-MS data. This is especially true for the poor data quality from

the Goettingen ICP-MS lab, which tends to give too low values for Nb, Zr and one Sr concentrations. The responsible scientist at Goettingen argued that sample inhomogeneity or high XRF detection limits are responsible for the poor agreement. However, sample inhomogeneity is rarely observed in basaltic rocks because of their fine-grained nature and should lead to results that are equally either too high or too low. Sample inhomogeneity also contradicts the consistency of the other data sets. Instead, the low results are most easily explained by precipitation of insoluble fluorides from the sample solution, which may act as a host for HFSE (Yokoyama *et al.*, 1999). Although the Frankfurt Ba data are highly correlated with the Mainz Ba data, there is an offset of the former to higher values. This is most easily explained by a different calibration of the Frankfurt XRF machine, leading to a high precision but low accuracy of the data.

Li concentrations were obtained only from the Goettingen lab, with standard reproducibility <5%. However, when plotted against other geochemical similar alkali metals like K, Rb and Cs, the samples show overall good correlations but also reveal 4 outliers with very low Li concentrations. In the light of the obvious problems with the Goettingen data, it is not clear if these low concentrations are real geochemical signatures. Until an independent cross-check of the Li data is available, I consider the data as suspect and do not include them into discussion. On the other hand, based upon the good correlations between different HFSE and relatively constant Zr/Hf and Nb/Ta ratios in the MUN ICP-MS data, I consider the poor Hf and Ta accuracies reported for their BR-688 standard as outliers.

A.3.: Major and trace element analyses of megacrysts

Megacrysts were coarsely crushed, sieved and washed in 1N HCl and distilled water to improve surface quality. Handpicked megacrysts were then mounted in epoxy and studied in detail by electron microprobe (Jeol JXA-8900 RL) at the University of Frankfurt. Major and minor element concentrations of clinopyroxene, garnet, plagioclase, ilmenite, amphibole, spinel, olivine, phlogopite and apatite megacrysts were obtained at 20 kV gun potential and 20 nA beam current using silicate, oxide and metal standards. The results are reported in tables B.9 – B.17. Count times ranged between 30 and 90 seconds to ensure detection limits of 100 ppm or better for all oxides except SrO and Na₂O (200 ppm). Accuracy of major element analyses was checked against secondary standards and is better than 1% (relative). Analytical precision is mainly controlled by counting statistics (which, for a given oxide species, depend on the concentration of that oxide in the phase being analyzed) and therefore strongly declines for minor and trace elements. At an oxide concentration of 0.10 wt%, 2 σ -errors range between 4-8% (relative), except for P₂O₅, Na₂O and SrO (12-18%). At the detection limit (0.01-

0.02 wt%), errors increase up to about 20% for the majority of oxides, but range between 27-45% for the latter group. Analytical accuracy also depends on the count rate on the standard used for calibration, sample and standard homogeneity and is limited at high concentrations through mechanical reproducibility of the spectrometer position (~0.5% relative).

A subset of cpx, gnt, plag and amphibole grains was further analyzed for trace elements (REE, Ba, K, Sr, Y, Zr and Nb) by secondary ion mass spectrometry (SIMS) on a recently upgraded Cameca IMS-3f at the MPI für Geochemie in Mainz. Results are included in tables B.9 – B.17. Negative oxygen ions were used as a primary source, using an accelerating potential of 12.5 kV and 20 nA beam current, and a high-energy offset of -80 eV for most analyses. The spot size for these conditions was 15-20 μm . Each measurement consisted of six cycles, where in each cycle ^{16}O , ^{30}Si , ^{39}K , ^{88}Sr , ^{89}Y , ^{90}Zr , ^{93}Nb , ^{133}Cs and all masses from 134 to 180 were analyzed in this order. ^{30}Si (3.1% isotopic abundance) was used as a reference mass, as determined by electron microprobe analysis. For each cycle, time-corrected mass-to- ^{30}Si ratios were formed after dead time and background corrections. To correct for isobaric interferences a matrix scheme was applied (Zinner & Crozaz, 1986). Every analysis reported represents a mean of two shots per grain. The well-studied glasses GOR132-G (komatiite) and KI-2G (basalt) (Jochum *et al.*, 2000) were used as external standards. Relative deviations from the standards are reported in table B.18 and are <15% for all elements except for Eu, Gd, Yb and Lu with errors <20%. Nb, which is present in the komatiite standard in the ppb range, revealed the largest error of 234%.

As outlined for EMP analyses, analytical precision of the ionprobe is also mainly controlled by counting statistics. Because the HREE-concentrations in some evolved cpx megacrysts reach the detection limit of the ionprobe, results show considerably more scatter as compared to the standard glass. Moreover, detection limits are dependent on MREE concentrations due to peak overlapping and therefore are individual for each sample (Zinner & Crozaz, 1986).

A.4.: Isotope (Sr, Nd, Pb, Os) analyses of volcanic rocks

Sr, Nd and Pb isotope analyses were carried out on all (n=36) rock samples at the Max-Planck-Institut in Mainz. Sieved and handpicked rock chips (~100mg of .75 to 1.5 mm fraction) were leached in hot 6N HCl for 1h and washed ultrasonically in deionized water before dissolution in HF-HNO₃. After sample digestion, Pb was extracted from the sample

solution by anion exchange in mixed HBr-HNO₃ media (Abouchami *et al.*, 2000). Every sample was run twice on the primary lead columns to ensure clean final elutes. The residual sample solution from the first step was dried down and retained for later Sr and Nd chemical separations. Samples were loaded together with a silica gel/phosphoric acid activator on rhenium filaments and run on a Finnigan MAT 261 TIMS instrument in static multicollection mode. All samples compiled in table B.19 are reported after fractionation correction of typically 0.116% a.m.u.⁻¹ as determined by alongside runs of the NBS981 standard (table B.20 and fig. A.2). External two-sigma reproducibility (n=29) of the standard was 392 ppm, 614 ppm and 860 ppm for 6/4, 7/4 and 8/4 ratios. Total procedural blanks were <50 pg and are considered negligible.

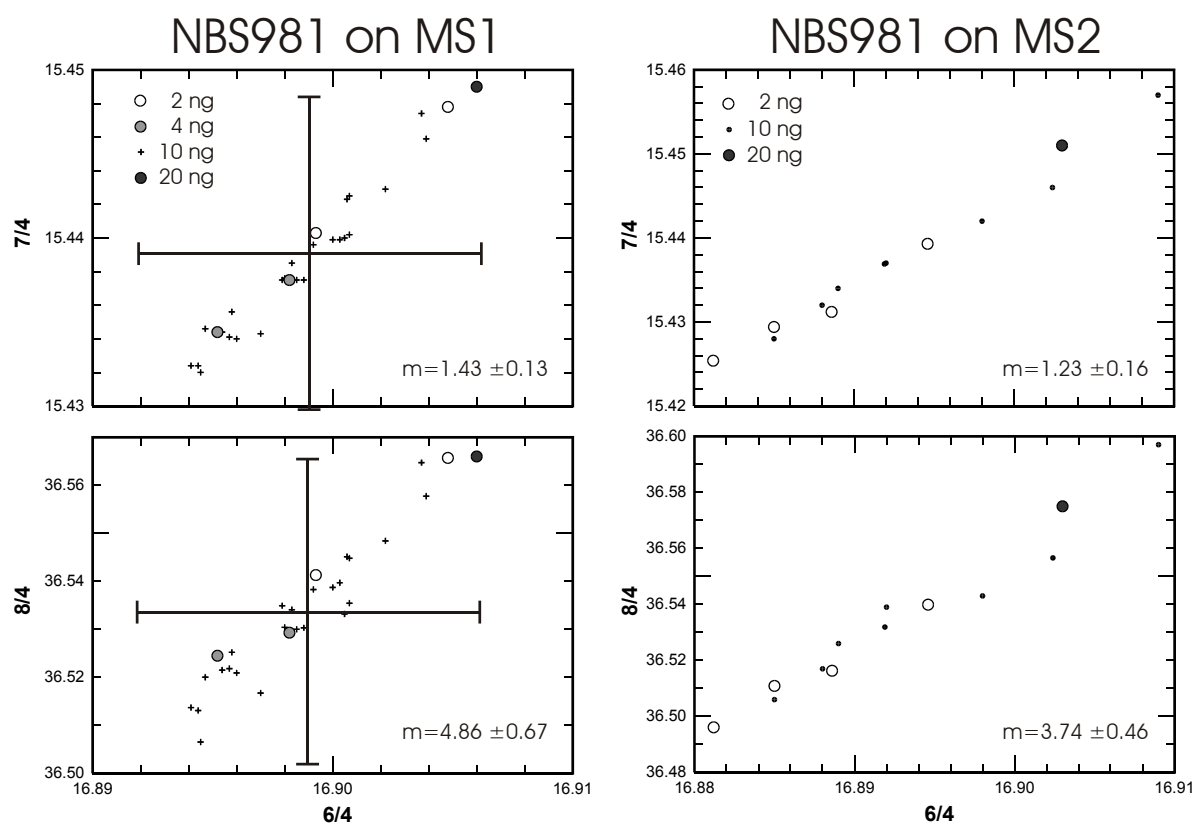


Fig. A.2: Instrumental fractionation vectors in Pb-Pb isotope space of two TIMS machines at the MPI in Mainz. MS1 shows an overall smaller range of fractionation and was therefore chosen for analyses of small sample masses. Standard samples from 2 to 4 ng Pb do not show significant over- or underfractionation when compared to 'normal' 10 ng standards. Using the NBS981 reference values of Todt *et al.* (1996), a mean fractionation per atomic mass unit of 0.116% is calculated and used for correction of all samples. The number in the lower right corner gives the slope of the fractionation vector calculated using the method of York (1969). They translate to steep inclinations to e.g. the NHRL in 7/4-6/4 and 8/4-6/4 space.

Sr and Nd were separated on conventional cation exchange columns following the procedures outlined by White & Patchett (1984). Sr was loaded with TaF₅ on single tungsten filaments, whereas Nd was measured as metal on double rhenium filaments. ⁸⁷Sr/⁸⁶Sr and ¹⁴³Nd/¹⁴⁴Nd ratios reported in table B.19 were normalized to ⁸⁶Sr/⁸⁸Sr = 0.1194 and ¹⁴⁶Nd/¹⁴⁴Nd = 0.7219, respectively. Over the course of this study, samples were run on two separate Finnigan MAT 261 TIMS instruments (MS 1 and MS 2). Repeated analyses of the NBS987 standard provided a mean ⁸⁷Sr/⁸⁶Sr of 0.71023 ± 0.00004 (2σ) on MS 1, and 0.71025 ± 0.00009 (2σ) on MS 2, respectively (table B.21, fig. A.3). Nd results were calibrated against the La Jolla standard which gave ¹⁴³Nd/¹⁴⁴Nd = 0.51187 ± 0.00004 (2σ) on MS 1 and 0.51186 ± 0.00005 (2σ) on MS 2 (table B.21, fig. A.4). Because samples were run on two separate instruments, all data from a specific machine have been normalized to reference values for standards: ⁸⁷Sr/⁸⁶Sr = 0.710250 for NBS987 and ¹⁴³Nd/¹⁴⁴Nd = 0.511850 for the La Jolla standard. Blanks are <120pg and <13pg for Sr and Nd, respectively, and are considered negligible.

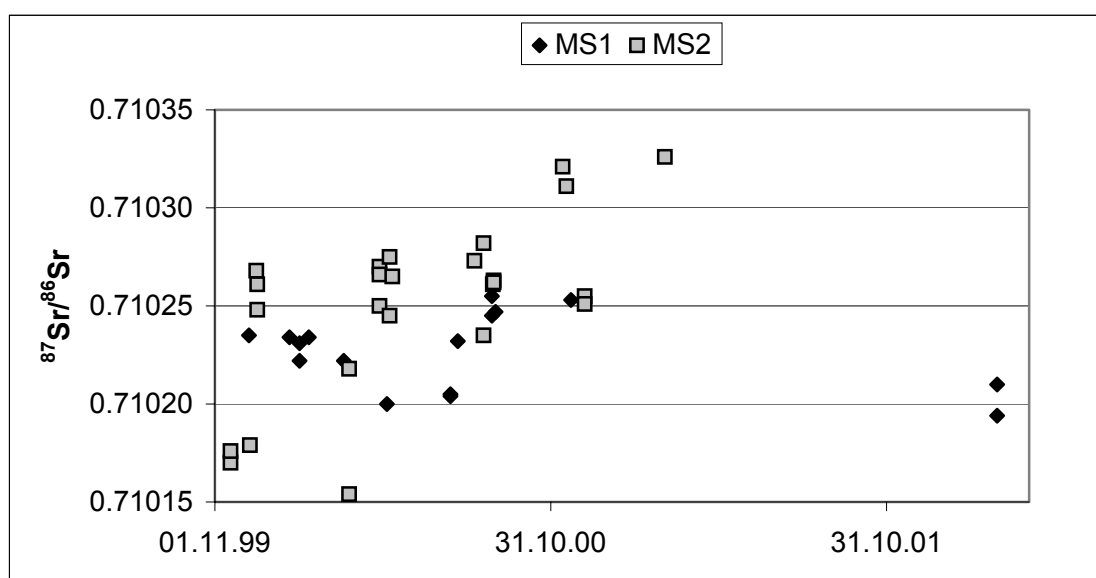


Fig. A.3: ⁸⁷Sr/⁸⁶Sr ratio of NBS987 standard on two TIMS machines during the course of this study. MS2 shows a significant trend towards high values over time. Considering all values, the mean is 0.710242 ± 0.000076 (2σ).

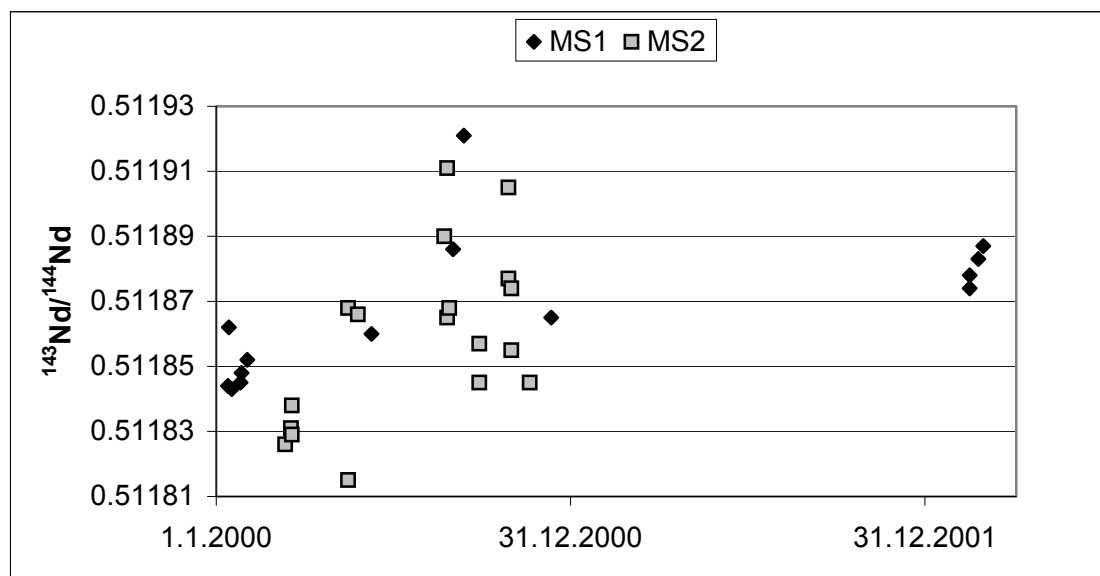


Fig. A.4: $^{143}\text{Nd}/^{144}\text{Nd}$ ratio of the La Jolla standard on two TIMS machines during the course of this study. Considering all values, the mean is 0.511863 ± 0.000050 (2σ).

For Re-Os analysis of a subset of 17 samples, ~ 2 g of rock powder were digested in a sealed quartz vessel together with a mixed $^{185}\text{Re}/^{190}\text{Os}$ isotope tracer and conc. HCl/HNO₃ (2:3) for 16 h in a Perkin Elmer high-pressure asher operating at 100 bar N₂ overpressure and 300°C (Brügman *et al.*, 1999). Osmium was extracted into liquid bromine and purified through micro distillation following the method of Birck *et al.* (1997). Rhenium was separated and purified from the residue using ion exchange extraction (Morgan & Walker, 1989). Os and Re were subsequently loaded onto Pt filaments with a mixed Na(OH) - Ba(OH)₂ emitter. The concentrations and isotopic compositions reported in table B.7 and B.19 were measured at MPI in Mainz using a Finnigan MAT-262 operating in negative ion mode (N-TIMS). The effects of fractionation during Os runs were eliminated by normalizing the Os isotope ratios to $^{192}\text{Os}/^{188}\text{Os} = 3.0827$ (Luck & Allègre, 1983). Five procedural blanks for Os ranged from 0.36 pg to 1.45 pg with $^{187}\text{Os}/^{188}\text{Os}$ between 0.23 and 0.39, resulting in corrections on sample $^{187}\text{Os}/^{188}\text{Os}$ of 1 to 4%, and corrections on sample Os concentrations of <1 to 5.5%. Measured Re procedural blanks were 11 to 47 pg Re, resulting in corrections to Re sample concentrations of up to 50%. The Mainz in-house Os standard yielded $^{187}\text{Os}/^{188}\text{Os}$ of 0.10703 ± 0.00020 (2σ , $n=5$). $^{187}\text{Os}/^{188}\text{Os}$ ratios based upon duplicate sample dissolutions were reproducible within <4.3%, significantly worse than the standard reproducibility. This may have several reasons. Osmium is a strongly chalcophile element and the Os budget in a sample may be dominated by Os contained in small sulfide globules (Roy-Barman *et al.*, 1998), which

may have heterogeneous isotopic composition. The specific distribution of sulfide globules within aliquots of the sample powder therefore may account for the poor sample reproducibility observed. The same effect may also be responsible for the poor reproducibility of Os and Re concentrations, which were within 11% and 5% of the mean. Similar variability in Os concentrations and isotopic compositions in individual flows has previously been reported by e.g. Alves *et al.* (1999). Minor sample contamination by disaggregated xenoliths may also contribute to sample heterogeneity.

An age correction was calculated assuming maximum ages for older Biu Plateau rocks of 5.35 Ma, and 50.000 a for younger Biu and Jos Plateau rocks, according to the equation:

$$\left({}^{187}\text{Os}/{}^{188}\text{Os}\right)_{\text{initial}} = \left({}^{187}\text{Os}/{}^{188}\text{Os}\right)_{\text{measured}} - \left({}^{187}\text{Re}/{}^{188}\text{Os}\right)_{\text{measured}} \times \left(e^{\lambda t} - 1\right) \quad (\text{eq.1})$$

with $\lambda = 1.666 \times 10^{-11} \text{ year}^{-1}$ (Shen *et al.*, 1996), (Smoliar *et al.*, 1996).

However, all age corrections given in table B.19 lie within the external sample reproducibility, and therefore are insignificant.

A.5.: Isotope analyses of megacrysts

Mineral separates for isotope analysis were prepared following the procedure of Zindler & Jagoutz (1988). For Sr and Nd isotope analyses, ~150 mg concentrates of cpx (n=14), gnt (n=4) and plag megacrysts (n=5) were handpicked under a binocular microscope in dark and bright field. Grains were then leached twice in hot 2.5N HCl for 20 minutes, then in cold 5% HF for 15 minutes in an ultrasonic bath, then rinsed with cold 2.5N HCl to remove fluoride complexes and finally rinsed in deionized water. In a second microscopic reexamination all grains with visible reaction rims were removed to insure 100% optically pure separates. Grains were then dissolved in Teflon beakers using HF-HNO₃. Sr and Nd extraction from the sample solution and conditions of TIMS measurement were the same as outlined for rock samples in chapter A.3. Results are summarized in table B.22. Whereas analyses of leached and unleached pure megacryst separates revealed no significant differences, cpx megacrysts with thick alteration crusts (Ker A) had significantly more radiogenic ⁸⁷Sr/⁸⁶Sr.

The assumption that cpx alteration rims are purely breakdown products and therefore unaffected by isotopic contamination therefore does not hold.

Reliable isotope analyses of garnet megacrysts were difficult to obtain because of their high resistance to acid attacks. A study of garnet attack using HF/HNO₃ mixtures in a microwave oven under 20 bars overpressure and 170-200°C resulted in mechanical failure of some Teflon beakers after 6 hours and cross-contamination of the samples. Successful dissolution attempts always left large amounts of a white residue, most probably insoluble aluminium compounds due to the high aluminium contents of the garnet. Subsequent Nd isotope analyses of the sample solutions were in the same range ($\epsilon_{Nd} = 5.4-6.6$) as associated cpx and plag megacrysts (5.0-6.9). One composite cpx-gnt megacryst (Mir+gnt) had similar Nd isotopic composition within error (ϵ_{Nd} cpx: 6.3, gnt: 5.5), thus suggesting isotopic equilibrium between the phases. Sr isotope analyses of garnet megacrysts were rejected in the discussion because of too large analytical uncertainties due to exceedingly low Sr concentrations in garnet (see table B.10) and significant reagent blanks.

Compared to Sr and Nd, cpx megacrysts have much lower Pb concentrations, too low to be determined by SIMS analysis. However, assuming a parental liquid similar to primitive basalts from this study with ~3 ppm Pb and a $D^{cpx/melt}(\text{Pb})$ of ~0.01 (Hauri *et al.*, 1994), one calculates a resulting Pb concentration in primitive cpx megacrysts of ~0.03 ppm. In order to gather enough lead for successful TIMS analysis, each individual Pb isotope analysis consisted of two batches of 100-150 mg pure cpx concentrate, that were run on separate Pb-columns in the first pass and then merged for the second. Given a total sample weight of 200-300 mg and a measured chemistry yield of ~75%, total yields are 4.5-6.75 ng Pb left for TIMS analysis. To study the effects of low sample loads on TIMS analyses, several standards in the range from 2-20 ng were run (table B.20). As evident from fig. A.2, there is no sign for significant over- or underfractionation of 2-4 ng samples, therefore justifying the use of the same fractionation correction scheme for the cpx megacrysts.

No attempt to analyze Pb isotopes of the garnets was made. Given a distribution coefficient $D^{gnt/melt}(\text{Pb})$ of 0.00012 (Hauri *et al.*, 1994), one calculates Pb concentrations in primitive gnt megacrysts of ~0.00036 ppm. In order to accumulate enough Pb for TIMS analyses, this requires an initial sample weight before dissolution of ~7.5 g. Such large quantities of pure garnet separates were impossible to obtain from a single specimen. Moreover, sample/blank ratios would be in the order of 1:1, and thus making the quality of the analysis questionable. The single ICP-MS garnet megacryst analysis provided by Lee *et al.* (1996) has a

typical crustal composition with e.g. $^{87}\text{Sr}/^{86}\text{Sr}$ of 0.709848 ± 26 and $^{206}\text{Pb}/^{204}\text{Pb}$ of 17.81. Lee *et al.* (1996) interpreted the data as contamination of the garnet megacryst (and not the cpx megacrysts!) with lower crustal material. In the light of the foregoing discussion, and the fact that P,T-estimates for the crystallization of garnet megacrysts are well below the crust/mantle boundary (see chapter 2), I doubt that this interpretation remains valid. It rather emphasizes the responsibility of the researcher to carefully evaluate his data before interpretations are made.

A.6.: Data analysis

Figure 2.12, the major element compositions of cpx shown in fig. 2.14 and the phase proportions shown in fig. 2.18 were calculated using the pMelts code of Hirschmann *et al.* (1998) available at <ftp://ftp.geology.washington.edu/pub/Melts/>.

Regression lines in Pb isotope space

For a slope m_{76} of a regression line in $^{207}\text{Pb}/^{204}\text{Pb}$ - $^{206}\text{Pb}/^{204}\text{Pb}$ space (fig. 3.3a), an age relating to this slope can be found by an iterative solution to the equation

$$m_{76} = \frac{\left(\frac{^{207}\text{Pb}}{^{204}\text{Pb}}\right)_{\text{sample}} - \left(\frac{^{207}\text{Pb}}{^{204}\text{Pb}}\right)_{\text{initial}}}{\left(\frac{^{206}\text{Pb}}{^{204}\text{Pb}}\right)_{\text{sample}} - \left(\frac{^{206}\text{Pb}}{^{204}\text{Pb}}\right)_{\text{initial}}} = \frac{1}{137.88} \cdot \frac{(e^{\lambda_{235}t} - 1)}{(e^{\lambda_{238}t} - 1)} \quad (\text{eq.2})$$

where λ are the decay constants of the uranium isotopes and t is age. This equation is independent on the U/Pb ratio of the samples. The interpretation of a linear array in $^{207}\text{Pb}/^{204}\text{Pb}$ - $^{206}\text{Pb}/^{204}\text{Pb}$ space as an isochron is, however, only applicable if the samples had the same Pb isotope initial ratios and had undisturbed U/Pb ratios since time t . Using a calculated age t from the $^{207}\text{Pb}/^{204}\text{Pb}$ - $^{206}\text{Pb}/^{204}\text{Pb}$ regression line, the present-day effective κ (= $^{232}\text{Th}/^{238}\text{U}$) can be calculated from the slope of a linear array in $^{208}\text{Pb}/^{204}\text{Pb}$ - $^{206}\text{Pb}/^{204}\text{Pb}$ space (fig. 3.3b) as

$$\kappa = m_{86} \cdot \frac{e^{\lambda_{238}t} - 1}{e^{\lambda_{232}t} - 1} \quad (\text{eq.3})$$

with m_{86} being the slope in $^{208}\text{Pb}/^{204}\text{Pb}$ - $^{206}\text{Pb}/^{204}\text{Pb}$ space and λ_{232} the decay constant of ^{232}Th . Because the elemental ratio Th/U is not fractionated appreciably during melting (Beattie, 1993), the measured κ^* should yield a value similar to the calculated κ , if the line in Pb-Pb isotope space truly represents an isochron (see Abouchami *et al.* (2000)). Alternative interpretations of linear arrays in Pb isotope space are a) interpretation as mixing lines, or b) as relaxation time of the different reservoirs with respect to the different isotopes (Albarède, 2001). In these cases the slope does not have any age significance.

Mixing calculations

The isotope ratios for two component mixing lines in chapter 3 were calculated using the mass-balance equation (e. g. Albarède (1995))

$$\alpha = \frac{\alpha_{\text{endmember1}} \cdot C_{\text{endmember1}}^i \cdot (1-f) + \alpha_{\text{endmember2}} \cdot C_{\text{endmember2}}^i \cdot f}{C_{\text{endmember1}}^i \cdot (1-f) + C_{\text{endmember2}}^i \cdot f} \quad (\text{eq.4})$$

where α is an isotope ratio, C_j^i is the concentration of element i in j and f is the mass fraction of endmember two. The trace element ratios of a mixture were determined with

$$\left(\frac{C_{\text{mix}}^a}{C_{\text{mix}}^b} \right) = \frac{C_{\text{endmember1}}^a \cdot (1-f) + C_{\text{endmember2}}^a \cdot f}{C_{\text{endmember1}}^b \cdot (1-f) + C_{\text{endmember2}}^b \cdot f} \quad (\text{eq.5}).$$

Diffusion Calculations

The Fe-Mg diffusion profile in fig. 2.11 was fitted using an error function given in Crank (1975) as

$$c(x) = \operatorname{erf}\left(\frac{x}{2\sqrt{Dt}}\right) \times (c_{core} - c_{rim}) + c_{rim} \quad (\text{eq.6})$$

with x = distance to rim, t = time, and the binary Fe-Mg interdiffusion coefficient D , which is itself is a function of pressure P and temperature T according to

$$D(T, P) = D_0 e^{\frac{-(E_A + PV_0)}{RT}} \quad (\text{eq.7}).$$

Data for activation energy $E_A = 406 \pm 64$ kJ/mol and $\log D_0 = -0.02 \pm 0.32$ cm²/s was taken from Dimanov & Sautter (2000). No activation volume data is available, and therefore the pressure dependence on D is neglected. Because diffusion of Fe and Mg is slower in cpx than in gnt, cpx exerts the primary control on the rate of equilibration.

The diffusional relaxation time of an initially zoned crystal may be calculated according to Fig. 12 of Chakraborty & Ganguly (1991)

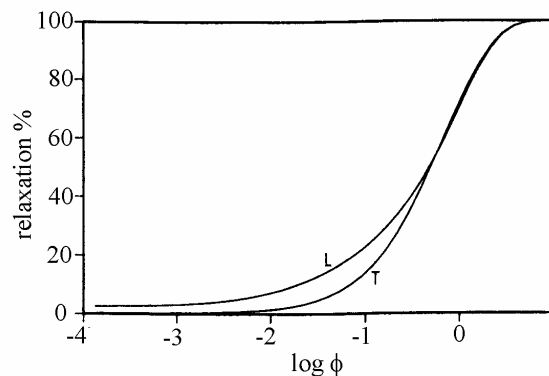


Fig. 12 of Chakraborty & Ganguly (1991): Extent of relaxation of growth zoning profile as a function of the dimensionless variable $\phi = \pi^2 Dt/a^2$. It is assumed that the initial growth profiles can be approximated by either a trigonometric (T) or a linear (L) function, and that the edge composition of the crystal has remained fixed.

From the diagram it is assumed that the crystal is reasonably homogenized at $\log \phi \sim 0.7$. With a given crystal radius a it follows

$$t \cong \frac{a^2}{2D} \quad (\text{eq.8}).$$

For an assumed temperature $T = 1350^\circ\text{C}$ the diffusion coefficient of aluminium in the biggest piece of cpx with 5 cm diameter is calculated according to eq.7 with $E_A = 272$ kJ/mol and $\log D_0 = -6.65 \pm 30\%$ cm²/s (Jaoul *et al.*, 1991) to 4.4×10^{-16} cm²/s. Putting the numbers in eq.8 gives a relaxation time t of $\sim 7.1 \times 10^{15}$ s or ~ 220 Ma.

Calculation of Nd-diffusion in a spherical cpx grain

The calculation in chapter 3.3.3. was made assuming $T = 1000^\circ\text{C}$, $P = 15$ kbar and $t = 150$ Ma using diffusion data of Van Orman *et al.* (2001) with $E_A = 496 \pm 77$ kJ/mol, $\log D_0 = -2.95 \pm 2.64$ m²/s, $V_0 = 9$ cm³/mol. $D(T,P)$ is calculated according to eq.7 to 1.4×10^{-24} m²/s. The total amount of diffusing substance entering or leaving the sphere is calculated according to Crank (1975) as

$$\frac{m_t}{m_\infty} = 1 - \frac{6}{\pi^2} \sum_{n=1}^{\infty} \frac{1}{n^2} e^{-\frac{Dt\pi^2 n^2}{a^2}} \quad (\text{eq.9})$$

with radius $a = 1$ mm one calculates a mass fraction of 25.6% that has reached equilibrium concentrations. Because of the higher diffusivities of Sr and Pb in cpx (Sneeringer *et al.*, 1984), (Cherniak, 2001), these elements should be well equilibrated after 150 Ma.

A.7.: References

Abouchami, W., Galer, S. J. G. & Hofmann, A. W. (2000). High precision lead isotope systematics of lavas from the Hawaiian Scientific Drilling Project. *Chemical Geology* **169** (1-2), 187-209.

Albarède, F. (1995). *Introduction to geochemical modeling*. Cambridge: Cambridge University Press, U.K.

- Albarède, F. (2001). Radiogenic ingrowth in systems with multiple reservoirs: applications to the differentiation of the mantle-crust system. *Earth and Planetary Science Letters* **189**, 59-73.
- Alves, S., Schiano, P. & Allegre, C. J. (1999). Rhenium-osmium isotopic investigation of Java subduction zone lavas. *Earth and Planetary Science Letters* **168** (1-2), 65-77.
- Beattie, P. (1993). Uranium Thorium Disequilibria and Partitioning on Melting of Garnet Peridotite. *Nature* **363** (6424), 63-65.
- Birck, J. L., Roy-Barman, M. & Capmas, F. (1997). Re-Os isotopic measurements at the femtomole level in natural samples. *Geostandards Newsletter-the Journal of Geostandards and Geoanalysis* **21** (1), 19-27.
- Brügman, G. E., Yang, J. H., Snow, J. E., Rehkämper, M., et al. (1999). Gemeinsame Bestimmung der Os-Isotopie und der Edelmetallkonzentrationen in Peridotiten, Basalten, Sulfiden und Eisenmeteoriten. *Kolloquium des DFG-Schwerpunktprogramms "Ocean drilling Programm and Deep Sea Drilling Project", Tagungsprogramm und Abstracts* 21-22.
- Chakraborty, S. & Ganguly, J. (1991). Compositional Zoning and Cation Diffusion in Garnets. In: Ganguly, J. (ed) *Advances in Physical Geochemistry, Diffusion, Atomic Ordering, and Mass Transport: Selected Problems in Geochemistry*. Berlin: Springer Verlag, 120-175.
- Cherniak, D. J. (2001). Pb diffusion in Cr diopside, augite, and enstatite, and consideration of the dependence of cation diffusion in pyroxene on oxygen fugacity. *Chemical Geology* **177** (3-4), 381-397.
- Crank, J. (1975). *The mathematics of diffusion*. Oxford: Oxford University Press.
- Dimanov, A. & Sautter, V. (2000). "Average" interdiffusion of (Fe,Mn)-Mg in natural diopside. *European Journal of Mineralogy* **12** (4), 749-760.
- Hauri, E. H., Wagner, T. P. & Grove, T. L. (1994). Experimental and Natural Partitioning of Th, U, Pb and Other Trace-Elements between Garnet, Clinopyroxene and Basaltic Melts. *Chemical Geology* **117** (1-4), 149-166.
- Hirschmann, M. M., Ghiorso, M. S., Wasylenki, L. E., Asimow, P. D., et al. (1998). Calculation of peridotite partial melting from thermodynamic models of minerals and melts I. Review of methods and comparison with experiments. *Journal of Petrology* **39** (6), 1091-1115.
- Jaoul, O., Sautter, V. & Abel, F. (1991). Nuclear microanalysis: A powerful tool for measuring low atomic diffusivity with mineralogic applications. In: Ganguly, J. (ed) *Advances in Physical Geochemistry, Diffusion, Atomic Ordering, and Mass Transport: Selected Problems in Geochemistry*. Berlin: Springer Verlag, 198-220.
- Jenner, G. A., Longerich, H. P., Jackson, S. E. & Fryer, B. J. (1990). ICP-MS: a Powerful Tool for High-Precision Trace-Element Analysis in Earth Sciences - Evidence from Analysis of Selected USGS Reference Samples. *Chemical Geology* **83** (1-2), 133-148.
- Jochum, K. P., Dingwell, D. B., Rocholl, A., Stoll, B., et al. (2000). The preparation and preliminary characterisation of eight geological MPI-DING reference glasses for in-site microanalysis. *Geostandards Newsletter-the Journal of Geostandards and Geoanalysis* **24** (1), 87-133.

- Lee, D. C., Halliday, A. N., Davies, G. R., Essene, E. J., et al. (1996). Melt enrichment of shallow depleted mantle: A detailed petrological, trace element and isotopic study of mantle-derived xenoliths and megacrysts from the Cameroon line. *Journal of Petrology* **37** (2), 415-441.
- Luck, J. M. & Allègre, C. J. (1983). $^{187}\text{Re} - ^{187}\text{Os}$ Systematics in Meteorites and Cosmochemical Consequences. *Nature* **302** (5904), 130-132.
- Morgan, J. W. & Walker, R. J. (1989). Isotopic Determinations of Rhenium and Osmium in Meteorites by Using Fusion, Distillation and Ion-Exchange Separations. *Analytica Chimica Acta* **222** (2), 291-300.
- Roy-Barman, M., Wasserburg, G. J., Papanastassiou, D. A. & Chaussidon, M. (1998). Osmium isotopic compositions and Re-Os concentrations in sulfide globules from basaltic glasses. *Earth and Planetary Science Letters* **154** (1-4), 331-347.
- Shen, J. J., Papanastassiou, D. A. & Wasserburg, G. J. (1996). Precise Re-Os determinations and systematics of iron meteorites. *Geochimica Et Cosmochimica Acta* **60** (15), 2887-2900.
- Smoliar, M. I., Walker, R. J. & Morgan, J. W. (1996). Re-Os Ages of Group IIA, IIIA, IVA, and IVB Iron Meteorites. *Science* **271** (5252), 1099-1102.
- Sneeringer, M., Hart, S. R. & Shimizu, N. (1984). Strontium and Samarium Diffusion in Diopside. *Geochimica Et Cosmochimica Acta* **48** (8), 1589-1608.
- Todt, W., Cliff, R. A., Hanser, A. & Hofmann, A. W. (1996). $^{202}\text{Pb} + ^{205}\text{Pb}$ double spike for lead isotopic analyses. In: Basu, A. & Hart, S. (eds) *Earth Processes: Reading the Isotopic Code* Geophysical Monograph Vol. 95
- Van Orman, J. A., Grove, T. L. & Shimizu, N. (2001). Rare earth element diffusion in diopside: influence of temperature, pressure, and ionic radius, and an elastic model for diffusion in silicates. *Contributions to Mineralogy and Petrology* **141** (6), 687-703.
- White, W. M. & Patchett, J. (1984). Hf-Nd-Sr Isotopes and Incompatible Element Abundances in Island Arcs - Implications for Magma Origins and Crust-Mantle Evolution. *Earth and Planetary Science Letters* **67** (2), 167-185.
- Yokoyama, T., Makishima, A. & Nakamura, E. (1999). Evaluation of the coprecipitation of incompatible trace elements with fluoride during silicate rock dissolution by acid digestion. *Chemical Geology* **157** (3-4), 175-187.
- York, D. (1969). Least-squares fitting of a straight line with correlated errors. *Earth and Planetary Science Letters* **5**, 320-324.
- Zindler, A. & Jagoutz, E. (1988). Mantle Cryptology. *Geochimica Et Cosmochimica Acta* **52** (2), 319-333.
- Zinner, E. & Crozaz, G. (1986). A Method for the Quantitative Measurement of Rare-Earth Elements in the Ion Microprobe. *International Journal of Mass Spectrometry and Ion Processes* **69** (1), 17-38.
- Zuleger, E. & Erzinger, J. (1988). Determination of the REE and Y in Silicate Materials with ICP-AES. *Fresenius Zeitschrift Fur Analytische Chemie* **332** (2), 140-143.

Appendix B: Data tables

Table B.1.: Major and trace element analyses of volcanic rocks by XRF melt discs (Frankfurt). *All Fe as Fe₂O₃

Sample	TUM	GULDUMBUR	BUGOR	TAMZA	ZAGU	HIZSHI	DAM	WIGA	SE BUGOR	JIGU-M	GUMJA	TILA 1	PELA 2	DAM 2	ETUM	PELA JUNG
SiO ₂ [wt%]	45.26	45.16	46.20	45.58	45.59	46.95	43.54	44.22	45.10	43.27	46.65	45.10	44.86	46.53	47.12	48.69
TiO ₂	2.36	2.54	2.39	3.00	2.56	2.62	2.94	2.94	2.38	3.01	2.64	3.01	2.84	2.53	2.51	2.16
Al ₂ O ₃	12.97	12.68	13.72	13.89	14.13	14.01	12.28	13.12	13.78	12.36	14.20	13.13	13.03	13.75	14.00	14.52
Fe ₂ O ₃ *	11.55	11.63	11.37	11.57	11.45	11.16	12.53	11.71	11.27	12.24	10.94	11.94	12.02	11.04	11.02	10.63
MnO	0.16	0.17	0.16	0.17	0.17	0.17	0.19	0.17	0.16	0.19	0.15	0.16	0.18	0.16	0.18	0.15
MgO	12.67	11.66	10.64	9.09	8.99	8.66	11.29	10.35	9.88	10.52	9.26	10.07	10.03	8.99	8.94	8.54
CaO	8.56	9.18	8.79	8.68	9.09	7.96	9.90	9.40	9.31	9.65	9.40	9.57	9.90	8.48	7.84	8.28
Na ₂ O	2.78	2.88	3.08	3.29	3.64	4.40	3.22	2.59	3.34	3.66	3.07	2.48	3.30	3.08	3.46	3.37
K ₂ O	1.39	1.58	1.44	1.96	1.79	1.56	1.53	1.54	1.49	1.73	1.35	1.37	1.60	2.09	1.83	1.60
P ₂ O ₅	0.56	0.74	0.57	0.77	0.79	0.80	0.79	0.82	0.60	0.97	0.57	0.57	0.74	0.70	0.70	0.55
Sum	98.26	98.22	98.36	98.00	98.20	98.29	98.21	96.86	97.31	97.60	98.23	97.40	98.50	97.35	97.60	98.49
V [ppm]	200	193	183	203	176	174	226	212	190	207	198	222	217	181	154	169
Cr	452	387	368	224	231	265	401	300	290	379	229	286	397	246	333	279
Ni	435	346	307	202	202	233	291	269	231	278	229	230	243	222	241	210
Rb	39	44	36	42	48	80	40	36	37	49	31	34	41	53	50	37
Sr	659	749	627	952	893	961	779	858	670	926	701	618	760	825	854	667
Y	21	25	24	27	28	29	28	25	24	31	22	26	30	25	29	22
Zr	213	251	203	325	260	373	288	260	198	332	196	240	268	306	350	223
Nb	61	70	52	82	74	91	71	72	60	84	58	51	69	74	79	55
Ba	619	688	601	773	922	893	848	696	572	736	573	536	714	870	637	619
La	34	50	50	66	46	62	54	33	29	54	41	31	49	49	45	32
Ce	80	100	37	120	107	128	127	106	91	143	85	73	109	116	125	79

Sample	JIGU	ZUMTA	HILIA 1	HILIA 2	X	TILA STR	GUFKA	MIR	PELA ALT	GWARAM	KOROKO	DAI	KERANG	AMPANG	PIDONG-M	PIDONG-S	stdev [wt%]
SiO ₂ [wt%]	48.31	48.75	45.55	48.65	46.54	45.88	50.89	51.59	49.88	48.91	56.80	45.02	43.94	45.41	45.02	46.19	0.45
TiO ₂	2.13	2.14	2.54	2.16	2.27	2.68	1.92	1.86	2.21	2.32	0.33	2.37	2.61	2.24	2.40	2.58	0.01
Al ₂ O ₃	14.48	15.02	14.29	14.51	14.04	13.76	15.26	15.69	14.90	14.81	19.44	13.41	13.40	12.80	13.28	15.75	0.14
Fe ₂ O ₃ *	10.60	9.63	11.43	10.93	11.25	11.98	9.98	8.09	10.07	10.07	3.27	11.30	12.29	11.33	11.71	11.41	0.06
MnO	0.15	0.13	0.17	0.15	0.16	0.15	0.13	0.12	0.14	0.15	0.17	0.16	0.19	0.17	0.17	0.17	0.004
MgO	8.49	7.58	8.99	8.48	8.57	9.03	7.31	5.73	7.00	6.87	0.35	10.48	9.30	10.75	10.64	5.92	0.046
CaO	9.02	7.47	9.06	9.16	9.63	8.91	8.85	6.59	7.02	7.10	1.92	9.51	9.71	8.87	9.41	8.35	0.08
Na ₂ O	3.26	3.67	3.65	3.13	3.08	2.34	3.47	3.82	3.52	4.44	7.90	2.84	3.91	3.24	3.55	3.35	0.07
K ₂ O	1.36	2.39	1.74	1.15	1.26	1.55	1.13	2.84	2.39	2.27	4.56	1.64	1.77	1.75	1.77	2.24	0.02
P ₂ O ₅	0.46	0.65	0.73	0.45	0.53	0.51	0.52	0.57	0.58	0.68	0.11	0.58	0.87	0.70	0.70	0.64	0.004
Sum	98.26	97.43	98.15	98.77	97.33	96.79	99.46	96.90	97.71	97.62	94.85	97.31	97.99	97.26	98.65	96.60	[ppm]
V [ppm]	170	144	189	180	196	200	146	121	176	157	<5	169	175	163	165	155	5.6
Cr	299	217	196	273	287	283	242	122	214	187	<10	323	205	417	347	45	18
Ni	191	202	183	220	176	246	196	123	202	174	<5	230	161	345	260	75	7
Rb	32	62	46	29	34	41	25	72	65	58	187	40	53	51	51	58	2.1
Sr	570	865	778	534	625	667	623	1013	766	972	970	761	951	809	791	1042	4.2
Y	22	20	27	20	24	22	18	18	22	26	39	23	27	23	23	23	1.5
Zr	183	274	247	178	180	211	169	344	332	420	808	223	283	242	248	320	2.7
Nb	43	78	68	43	52	50	43	95	77	92	273	60	83	70	70	78	1.2
Ba	558	891	719	489	529	517	535	996	965	957	1224	650	846	789	750	960	35
La	29	41	40	24	36	20	25	55	54	60	116	35	62	53	43	60	6.5
Ce	61	109	106	64	85	70	53	91	84	133	177	100	127	132	106	102	14.3

Table B.2.: Trace element analyses of volcanic rocks by XRF pressed powder pellets (Mainz)
 b.d.: below detection limit, numbers in brackets are outside calibration range
 Reproducibility taken from <http://www.uni-mainz.de/FB/Geo/Geologie/EMSRFA/RFA.html>

Sample	Zagu	Jigu	Jigu M	X	Pela jung	Koroko	Pela alt	Dam	Gumja
Pb [ppm]	3.4	2.7	4.5	3.9	5.4	21.7	4.6	4.2	3.1
Th	7.3	3.6	6.3	5.9	4.2	43.9	8	5.7	5.1
U	2.3		1.6	1.8	1.2	12.6	1.4	2.3	1.7
Sc	17	22	20	21	20	b.d.	17	22	20
V	155	164	201	183	166	9	184	192	197
Cr	214	289	359	266	269	b.d.	209	348	235
Ni	193	182	277	173	200	4	202	278	222
Co	45	43	52	47	40	3	40	49	49
Cu	37	57	43	45	46	7	26	51	62
Zn	104	91	125	96	109	137	124	109	92
Ga	22	20	21	20	21	35	23	22	20
Rb	53	35	50	37	39	196	68	45	34
Sr	973	610	1009	668	703	1012	805	858	748
Y	30	24	32	25	23	38	22	31	23
Zr	272	187	352	183	230	[726]	346	305	200
Nb	92	51	104	62	67	[339]	93	85	72
Ba	786	469	598	432	500	1135	830	736	453

Sample	Dam 2	Bugor	SE Bugor	Hilia 1	Hilia 2	Tamza	Gufka	Mir	Tila 1
Pb [ppm]	4	3.4	4.6	4.6	2.4	4.7	2.8	5	3.8
Th	6.3	4.4	5	6.2	3.1	8.1	3.6	10	4.4
U	<1.6	<1.6	<1.6	<1.6	<1.6	<1.6	<1.6	2.5	<1.6
Sc	20	21	23	19	22	17	17	11	22
V	183	184	181	160	171	197	141	122	210
Cr	248	360	289	162	252	230	225	125	267
Ni	221	300	239	169	215	199	187	117	208
Co	40	53	45	38	49	41	42	30	49
Cu	36	47	42	36	51	24	57	26	37
Zn	116	102	102	101	99	123	95	123	96
Ga	21	18	20	24	21	23	20	24	21
Rb	57	37	42	52	28	46	27	78	38
Sr	872	668	714	860	567	1013	667	1075	671
Y	26	26	26	28	23	28	20	18	27
Zr	313	211	206	259	183	338	173	355	252
Nb	89	65	73	83	51	103	52	120	61
Ba	747	441	438	628	379	604	440	864	384

Sample	Guldumbur	Pela 2	Wiga	Gwaram	Zumta	Hizshi	Tum	ETum	Tila Str
Pb [ppm]	4.1	3	4	4.9	3.9	5.2	4.2	4.2	3
Th	6.1	5.4	5.6	10.4	6.8	9.3	5.5	5.5	3.9
U	2.1	<1.6	<1.6	1.8	<1.6	2.5	<1.6	<1.6	<1.6
Sc	23	22	20	14	17	17	22	17	19
V	190	195	205	145	153	162	195	149	185
Cr	374	382	315	170	213	258	453	302	270
Ni	350	249	264	172	202	230	430	222	233
Co	52	49	51	38	40	46	58	38	48
Cu	40	46	52	22	57	27	78	31	41
Zn	106	107	109	134	115	132	105	109	108
Ga	20	21	19	25	23	24	18	23	21
Rb	47	47	35	63	70	89	43	52	45
Sr	804	824	895	1044	918	1017	692	918	708
Y	26	30	27	28	20	30	23	32	24
Zr	263	279	264	429	282	386	220	367	216
Nb	86	82	88	115	96	109	73	94	58
Ba	531	579	519	858	805	723	498	518	383

Sample	Dai	Kerang	Ampang	Pidong M	Pidong S	Biu 4	Biu 5	Biu 8	Biu 9	stdev [ppm]
Pb [ppm]	2.9	5.6	4.9	4.2	4	3.4	3.7	2.5	4.1	0.6
Th	5	8.4	7.8	6.2	7.8	3.7	4.7	2.1	6.4	0.4
U	1.9	1.8	2.8	<1.6	<1.6	<1.6	<1.6	<1.6	<1.6	0.3
Sc	20	18	19	21	16	16	19	21	18	not given
V	175	167	156	157	145	206	211	174	179	1.8
Cr	337	194	401	337	40	328	269	365	318	5.1
Ni	223	169	349	251	64	240	211	242	204	2.9
Co	53	50	51	52	34	46	50	51	43	2.3
Cu	38	28	57	32	27	50	46	35	50	2.2
Zn	105	128	116	120	107	102	100	90	99	1.5
Ga	20	21	20	19	21	22	21	19	20	0.7
Rb	45	57	56	55	63	32	45	28	46	1.0
Sr	803	1024	858	841	1128	712	635	497	888	2.5
Y	24	28	24	25	23	28	27	20	31	0.6
Zr	231	293	247	257	331	240	257	164	297	1.5
Nb	72	102	86	86	97	63	63	43	88	0.3
Ba	554	734	726	615	795	498	390	351	535	3.6

Table B.3.: Trace element analyses of volcanic rocks by ICP-AES (Potsdam) following sinter dissolution
*Govindaraju (1994)

Sample	Miringa	Bugor	Dam	Dam 2	Gufka	Gwaram	Hilia 1	Hilia 2	Hizshi	Jigu-M	Pela alt	Pela jung
La [ppm]	66	39	62	55	33	72	52	31	70	66	57	41
Ce	118	74	118	104	61	134	96	59	128	127	103	75
Pr	13	8.6	13	12	7.2	15	11	6.8	15	15	11	9.1
Nd	48	35	55	47	29	58	44	29	58	59	44	35
Sm	9	7.2	11	9.2	6.4	12	8.9	6.2	11	12	8.7	7.2
Eu	2.8	2.5	3.3	3	2.1	3.5	2.9	2.1	3.5	3.6	2.7	2.3
Gd	7.2	6.9	9.2	7.9	5.7	9.3	8.1	6	9.5	9.8	7.3	6.4
Tb	0.95	1	1.3	1.1	0.83	1.3	1.2	0.82	1.4	1.4	0.9	0.9
Dy	4.3	5.5	6.6	5.7	4.3	6.5	6	4.6	6.7	7	4.9	4.8
Ho	0.67	0.94	1.1	0.98	0.72	1	1	0.81	1.1	1.2	0.84	0.79
Er	1.4	2.4	2.8	2.3	1.9	2.4	2.5	1.9	2.5	2.9	1.9	2.1
Tm	0.16	0.31	0.34	0.3	0.23	0.28	0.32	0.27	0.3	0.39	0.24	0.26
Yb	1	1.8	2.1	1.7	1.3	1.7	2	1.6	1.9	2.1	1.4	1.5
Lu	0.14	0.27	0.3	0.25	0.18	0.23	0.28	0.22	0.26	0.3	0.2	0.21
Y	16	24	28	24	19	26	26	20	27	29	20	21
Sc	12	22	23	18	18	14	22	22	17	20	16	18

Sample	Tamza	Tila	Wiga	Koroko	Kerang	Ampang	Pidong M	Pidong S	JB-2	JB-2 ref.*	accuracy
La [ppm]	59	36	57	120	70	59	55	64	2.4	2.37	101.3%
Ce	110	73	105	206	128	107	102	124	6.9	6.77	101.9%
Pr	13	9.3	12	20	14	12	11	13	1.3	0.96	135.4%
Nd	50	37	48	64	56	46	46	54	6.6	6.7	98.5%
Sm	9.9	8.1	9.4	11	11	8.9	9.3	9.8	2.3	2.25	102.2%
Eu	3.2	2.6	3	3.1	3.5	2.9	2.9	3.1	0.83	0.86	96.5%
Gd	8.6	7.4	8.4	8.5	9.2	7.7	7.9	8	3.2	3.28	97.6%
Tb	1.2	1.1	1.2	1.2	1.3	0.97	1.2	1.2	0.58	0.62	93.5%
Dy	6.3	5.7	6	7	6.4	5.5	5.9	5.7	4.2	3.66	114.8%
Ho	1	0.97	1	1.3	1.1	0.88	0.92	0.95	0.82	0.81	101.2%
Er	2.6	2.4	2.4	3.7	2.6	2.1	2.4	2.3	2.8	2.63	106.5%
Tm	0.33	0.31	0.32	0.48	0.32	0.28	0.31	0.27	0.41	0.45	91.1%
Yb	1.9	1.8	1.8	3.5	1.8	1.6	1.7	1.7	2.6	2.51	103.6%
Lu	0.26	0.25	0.26	0.51	0.25	0.23	0.23	0.23	0.4	0.39	102.6%
Y	26	24	25	34	27	23	24	23	23	24.9	92.4%
Sc	19	22	20	0.53	19	19	20	15	56	53.5	104.7%

Table B.4.: Trace element analyses of volcanic rocks by ICP-MS (MUN)

*Govindaraju (1994), **internal MUN values.

Sample	ZUMTA	HILIA 2	JIGU 1	KOROKO	GUFKA	DAM 2	MIR	MIR	MIR	JIGU-M	GULDUMBUR	PELA JUNG	PELA JUNG	GUMJA	TUM	ZAGU
Comment	Biu young	Biu young	Biu young	Biu young	Biu young	Biu young	Biu young	Biu young	Biu young	Biu young	Biu young	Biu young	Biu young	Biu young	Biu young	Biu young
								dupl.	dupl.				dupl.			
Mo [ppm]	2.85	1.00	1.95	7.61	2.32	5.19	3.22	3.62	3.52	5.02	3.60	2.76	2.82	3.59	3.39	4.35
Hf	8.16	5.20	5.27	17.84	4.10	7.28	8.61	9.58	8.72	8.66	6.03	5.92	5.64	5.15	6.06	6.93
Ta	6.47	3.40	3.43	19.25	2.87	5.46	6.86	8.05	7.52	6.19	4.51	4.05	3.87	3.95	4.40	5.34
Rb	63.0	23.5	28.6	159.0	21.5	58.2	68.8	80.6	71.1	43.2	36.8	35.3	35.6	35.6	38.9	48.5
Sr	886	505	545	853	600	939	986	1175	1017	923	663	685	687	848	684	983
Y	17.7	18.2	19.0	30.3	16.3	25.7	15.0	17.7	15.7	28.1	20.3	20.2	20.3	24.4	20.1	26.9
Zr	278	162	169	708	152	310	339	363	342	326	232	225	226	213	206	268
Nb	104.2	51.1	53.9	300.0	52.9	104.4	122.9	137.0	125.7	109.8	85.2	75.8	76.4	85.1	80.0	105.5
Cs	0.74	0.25	0.24	0.47	0.09	0.72	0.56	0.65	0.58	0.59	0.48	0.38	0.36	0.45	0.57	0.59
Ba	750	341	409	1002	382	763	800	896	812	563	480	524	507	503	479	800
La	51.6	27.6	29.0	102.6	28.6	54.9	58.4	64.8	60.3	64.5	43.7	41.0	39.8	45.7	38.4	57.7
Ce	92.0	51.2	53.3	181.4	54.0	106.0	107.2	116.7	104.9	124.1	82.7	77.5	75.6	85.9	71.6	105.4
Pr	10.69	6.35	6.50	17.82	6.34	11.84	11.65	13.23	11.94	14.59	9.43	8.76	8.53	9.06	8.37	12.05
Nd	40.5	25.5	26.2	55.7	25.1	46.2	43.2	48.1	43.8	57.2	36.8	34.5	33.7	35.4	32.3	46.5
Sm	7.69	5.60	5.70	9.12	5.46	9.09	7.87	8.66	8.05	11.16	7.32	7.05	6.91	7.21	6.47	9.18
Eu	2.48	1.88	1.89	2.71	1.85	2.88	2.47	2.77	2.54	3.46	2.35	2.32	2.26	2.35	2.12	3.00
Gd	6.58	5.48	5.55	6.55	4.86	7.47	6.07	6.97	6.32	9.34	6.29	6.25	6.06	6.16	5.87	8.20
Tb	0.79	0.72	0.74	1.03	0.69	1.03	0.76	0.82	0.77	1.23	0.86	0.87	0.84	0.94	0.77	1.05
Dy	4.11	4.07	4.23	6.10	3.73	5.54	3.76	4.13	3.87	6.68	4.74	4.77	4.65	5.10	4.30	5.89
Ho	0.68	0.73	0.76	1.15	0.64	0.94	0.58	0.64	0.60	1.14	0.83	0.83	0.81	0.90	0.75	1.02
Er	1.58	1.85	1.96	3.26	1.60	2.35	1.35	1.49	1.39	2.85	2.08	2.10	2.03	2.28	1.95	2.61
Tm	0.19	0.25	0.27	0.48	0.22	0.33	0.16	0.21	0.19	0.37	0.27	0.29	0.28	0.31	0.25	0.35
Yb	1.09	1.38	1.52	3.12	1.14	1.69	0.88	0.98	0.91	2.06	1.60	1.56	1.48	1.70	1.51	1.89
Lu	0.14	0.17	0.19	0.36	0.12	0.19	0.10	0.11	0.10	0.24	0.18	0.17	0.17	0.18	0.18	0.23
Pb	3.07	1.58	2.05	16.90	1.73	3.68	3.60	4.23	3.65	3.31	2.25	2.87	2.66	2.57	1.96	3.00
Th	7.82	3.73	4.17	36.75	4.03	7.95	9.62	10.93	10.08	8.40	6.04	5.90	5.74	6.87	5.48	7.72
U	1.85	0.60	1.01	10.04	0.98	1.94	2.42	2.77	2.53	2.25	1.70	1.52	1.45	1.74	1.35	1.92

Table B.4.: Trace element analyses of volcanic rocks by ICP-MS (MUN)

*Govindaraju (1994), **internal MUN values.

Sample Comment	TAMZA	Biu4	Biu4	KERANG AMPANG		det. limit	MRG-1-67	MRG-1	MRG-1	MRG-1	BR-688-67	BR-688	BR-688	BR-688
	Biu young	Biu old	Biu old dupl.	Jos young	Jos young		std	ref.*	ref.**	accuracy	std	ref.*	ref.**	accuracy
Mo [ppm]	4.26	3.24	3.00	4.12	4.81	0.058	1.57	0.87	1.26	124.9%	0.636		0.52	122.3%
Hf	8.29	7.57	7.01	6.58	5.55	0.009	4.41	3.76	3.76	117.2%	2.52	1.6	1.56	161.5%
Ta	6.19	4.33	3.99	5.43	4.57	0.001	0.910	0.8	0.83	109.6%	0.406	0.31	0.27	150.2%
Rb	41.3	33.1	28.4	44.9	52.7	0.131	6.87	8.5	7.65	89.9%	2.13	1.91	2.07	102.7%
Sr	961	795	693	872	864	0.72	258	266	274	94.3%	179	169.2	168.01	106.8%
Y	25.1	28.0	24.8	22.6	22.4	0.004	11.2	14	11.6	96.2%	19.8	17	17.94	110.1%
Zr	331	275	234	256	238	0.065	90.7	108	93.7	96.8%	61.1	60.6	53.25	114.7%
Nb	111.3	83.7	73.3	101.5	97.2	0.005	21.9	19.2	22.3	98.1%	5.09		4.43	114.8%
Cs	1.50	0.25	0.23	0.98	1.11	0.031	0.583	0.57	0.60	97.1%	0.054	0.24	0.03	180.2%
Ba	641	512	475	634	691	0.93	44.2	61	47.5	93.1%	191	200	171.89	111.0%
La	58.0	38.3	35.8	60.1	56.4	0.013	8.61	9.8	9.07	95.0%	5.44	5.3	5.12	106.3%
Ce	106.9	73.0	70.5	112.0	108.2	0.012	24.0	26	26.2	91.6%	12.5	13.3	12.04	103.5%
Pr	12.18	8.96	8.61	12.72	11.59	0.013	3.62	3.4	3.79	95.5%	1.82		1.71	106.6%
Nd	48.5	37.6	35.4	48.4	43.7	0.023	17.3	19.2	18.3	94.6%	8.75	9.6	8.33	105.0%
Sm	9.41	8.17	7.63	9.36	8.40	0.015	4.28	4.5	4.51	94.8%	2.48	2.79	2.38	104.2%
Eu	3.01	2.71	2.49	2.98	2.69	0.010	1.36	1.39	1.46	93.1%	1.02	1.07	1.00	101.8%
Gd	8.14	7.73	7.01	7.75	6.60	0.010	3.96	4	4.11	96.3%	3.17	3.2	3.02	104.8%
Tb	1.05	1.02	0.95	1.01	0.97	0.002	0.516	0.51	0.55	93.9%	0.519	0.45	0.50	103.9%
Dy	5.73	5.63	5.37	5.44	5.19	0.005	2.81	2.9	3.01	93.4%	3.53	3.4	3.38	104.4%
Ho	0.99	0.99	0.92	0.93	0.88	0.002	0.482	0.49	0.51	94.6%	0.761	0.81	0.73	104.2%
Er	2.45	2.40	2.24	2.27	2.15	0.008	1.15	1.12	1.21	95.1%	2.27	2.11	2.18	103.9%
Tm	0.34	0.29	0.28	0.31	0.31	0.007	0.147	0.11	0.15	97.9%	0.354	0.29	0.32	110.7%
Yb	1.78	1.70	1.59	1.57	1.51	0.003	0.765	0.6	0.81	94.5%	2.15	2.09	2.08	103.6%
Lu	0.21	0.20	0.18	0.18	0.15	0.006	0.085	0.12	0.11	76.8%	0.282	0.34	0.31	90.9%
Pb	3.30	1.90	1.72	4.24	4.45	0.862	8.61	10	5.20	165.5%	3.18	3.3	3.39	93.8%
Th	8.27	4.43	4.31	8.19	7.90	0.002	0.750	0.93	0.78	96.1%	0.359	0.33	0.32	112.0%
U	2.21	1.18	1.09	1.99	1.84	0.011	0.232	0.24	0.25	92.6%	0.331	0.37	0.28	118.3%

Table B.5.: Major and trace element analyses of volcanic rocks by XRF (MUN)*all Fe as Fe₂O₃

Sample	Zumta	Hilia 2	Jigu 1	Koroko	Gufka	Dam 2	Mir	Mir	Jigu M	Guldumbur	Pela jung	Gumja	Tum	Zagu	Tamza	Biu 4	Kerang	Ampang
Comment	Biu young	Biu young	Biu young	Biu young	Biu young	Biu young	Biu young	Biu young	Biu young	Biu young	Biu young	Biu young	Biu young	Biu young	Biu young	Biu old	Jos young	Jos young
SiO₂ [wt%]	51.96	49.96	51.18	59.27	52.29	48.14	53.99	54.42	44.81	45.16	49.71	48.63	46.39	45.71	46.35	45.75	45.54	46.98
TiO₂	2.30	2.18	2.06	0.33	1.93	2.65	1.98	1.98	2.95	2.55	2.28	2.76	2.51	2.43	3.06	2.57	2.70	2.37
Al₂O₃	17.07	16.28	17.47	21.03	17.18	14.77	16.87	17.07	13.53	13.35	15.65	15.67	14.28	15.31	14.28	14.28	14.71	14.00
Fe₂O₃*	9.80	11.00	10.17	3.33	9.83	11.39	8.39	8.38	11.94	11.69	10.87	11.02	12.01	10.88	11.78	11.35	12.55	11.76
MnO	0.13	0.15	0.14	0.17	0.13	0.17	0.11	0.11	0.18	0.17	0.15	0.15	0.16	0.16	0.17	0.16	0.19	0.17
MgO	6.93	7.35	7.01	0.31	6.62	8.38	5.43	5.56	10.11	11.03	7.63	8.54	11.52	7.83	9.00	8.99	8.31	10.25
CaO	7.77	9.28	9.24	1.94	8.90	8.69	6.76	6.80	9.55	9.01	8.39	9.50	8.99	9.01	8.68	10.37	9.86	9.04
Na₂O	4.36	3.81	4.24	8.22	4.18	3.51	4.16	4.22	4.39	3.33	3.93	3.67	3.28	4.31	3.66	3.06	4.89	3.69
K₂O	2.55	1.21	1.53	4.61	1.22	2.15	2.87	2.92	1.80	1.61	1.62	1.43	1.46	1.88	1.96	1.33	1.90	1.85
P₂O₅	0.54	0.39	0.46	0.08	0.49	0.57	0.43	0.44	1.01	0.59	0.44	0.50	0.47	0.79	0.58	0.59	0.79	0.56
Sum	103.96	101.89	103.89	100.26	103.08	101.02	101.47	102.38	100.92	99.03	101.04	102.30	101.63	98.92	100.08	98.92	102.13	101.38
S [ppm]	36	46	8	44	45	126	37	31	68	29	30	32	77	49	65	56	298	377
Cl	1382	40	810	4466	248	1820	657	684	1955	1329	443	997	1379	1898	1525	1203	2341	2000
Sc	19	22	22	<5	14	17	12	18	27	22	22	23	29	19	25	25	16	19
V	154	167	178	<5	147	182	129	118	217	195	176	195	208	159	189	204	172	168
Cr	246	274	323	<5	257	283	137	143	392	466	309	258	500	245	255	423	222	452
Ni	180	199	166	<5	180	207	103	97	266	340	181	210	420	182	184	223	150	334
Cu	60	59	54	3	64	39	32	29	54	47	49	63	83	42	31	57	40	60
Zn	62	52	46	81	45	61	69	67	67	55	59	45	55	57	66	51	73	60
Ga	23	20	21	36	20	21	25	25	22	18	19	19	17	19	21	20	22	21
Rb	66	27	33	195	24	55	76	75	47	45	37	31	40	51	43	28	53	53
Sr	944	573	618	1042	677	885	1104	1099	1025	824	712	766	711	1032	1027	714	1039	880
Y	18	21	21	37	18	24	16	16	31	25	22	22	21	29	27	25	27	23
Zr	320	199	201	978	187	355	406	405	394	294	254	222	241	314	379	259	330	278
Nb	107	57	58	365	58	99	129	129	116	97	76	80	83	105	112	71	113	96
Ba	836	423	514	1193	441	794	883	887	674	601	571	480	556	898	658	543	762	752
Ce	115	14	55	229	16	125	139	116	119	86	57	88	79	102	91	48	121	105

Table B.6.: Trace element analyses of volcanic rocks by ICP-MS (Göttingen)*Imai et. al (1995), **Raczek et al. (2001), Chen et al. (2000). Precision denotes 1 σ st.dev.

Sample		Koroko	Gwaram	Hizshi	Jigu-M	Mir	Dam	Tamza	Wiga	Pela alt	Dam 2	Hilia 1	Guldumbur	Pela 2	Zagu	Etum
Comment	nuclide	Biu young	Biu young	Biu young	Biu young	Biu young	Biu young	Biu young	Biu young	Biu young	Biu young	Biu young	Biu young	Biu young	Biu young	Biu young
Li [ppm]	7	4.47	9.78	8.94	7.88	10.4	7.48	2.82	2.73	0.80	7.54	6.99	3.17	6.80	7.37	8.65
Sc	45	0.75	14.3	17.3	20.4	12.0	22.0	18.3	20.0	16.0	18.6	22.2	21.4	24.2	20.8	17.2
Co	59	1.77	36.3	43.1	49.9	29.6	53.4	45.3	50.5	43.0	44.3	49.2	51.9	54.5	46.8	40.3
Ni	60	2.86	160	214	256	116	260	182	245	198	213	185	324	247	194	221
Zn	66	121	133	129	126	120	124	124	118	130	119	122	115	125	118	118
Rb	85	157	61.0	83.8	46.2	73.9	40.7	43.5	33.3	66.8	55.8	50.2	45.5	45.1	50.4	49.2
Sr	88	538	1063	1000	972	1065	815	962	894	807	880	848	800	833	952	878
Y	89	10.3	26.2	27.4	29.5	16.3	27.1	25.4	24.4	20.2	24.2	26.7	25.1	29.3	27.3	28.2
Zr	90	845	396	358	23.3	327	56.9	227	53.1	281	276	205	154	125	231	335
Nb	93	173	76.7	63.9	9.74	78.9	20.8	57.6	23.1	60.1	62.6	33.3	11.8	19.9	24.0	42.3
Cs	133	0.52	0.99	0.82	0.60	0.63	0.51	1.60	0.71	0.50	0.71	0.59	0.57	0.49	0.63	0.67
Ba	137	1044	879	758	604	888	731	648	545	813	741	593	561	581	802	539
La	139	13.5	72.0	67.9	67.8	63.8	55.2	58.2	54.9	53.8	52.7	50.0	50.6	51.0	58.8	54.7
Ce	140	72.9	139	133	138	123	113	115	106	101	104	96.5	97.8	99.2	110	108
Pr	141	2.78	15.1	14.4	15.3	12.6	12.6	12.3	11.5	10.7	11.2	10.2	10.6	10.9	11.7	12.1
Nd	143	9.52	59.7	56.7	62.4	48.1	51.3	49.7	46.7	42.8	45.4	42.1	44.4	46.5	48.7	48.8
Sm	147	1.94	11.5	11.3	12.4	8.8	10.6	10.0	9.57	8.05	9.19	8.49	8.72	9.16	9.38	9.55
Eu	151	0.78	3.67	3.49	3.90	2.86	3.32	3.20	3.02	2.67	2.93	2.72	2.87	3.01	3.18	3.09
Gd	157	2.01	8.79	8.68	9.67	6.88	8.30	7.82	7.49	6.44	7.28	6.87	6.78	7.20	7.72	7.90
Tb	159	0.32	1.30	1.26	1.41	0.91	1.25	1.20	1.15	0.94	1.11	1.05	1.08	1.09	1.19	1.24
Dy	163	1.92	6.10	6.09	6.96	3.97	6.25	5.75	5.61	4.36	5.39	5.39	5.50	5.64	6.07	6.70
Ho	165	0.39	1.01	1.03	1.22	0.63	1.11	1.01	0.94	0.76	0.95	0.95	0.98	0.99	1.11	1.22
Er	166	1.20	2.55	2.67	3.10	1.57	2.93	2.60	2.44	1.86	2.36	2.48	2.54	2.54	2.71	2.94
Tm	169	0.18	0.29	0.30	0.37	0.17	0.36	0.32	0.31	0.23	0.30	0.32	0.33	0.33	0.36	0.39
Yb	172	1.23	1.64	1.73	2.20	0.98	2.07	1.86	1.67	1.22	1.69	1.82	1.90	1.84	2.03	2.38
Lu	175	0.18	0.22	0.25	0.31	0.14	0.31	0.27	0.24	0.18	0.23	0.26	0.27	0.28	0.29	0.33
Hf	178	16.0	8.9	7.72	0.58	7.26	1.10	4.13	1.00	5.86	6.30	3.21	2.11	1.88	4.73	8.1
Ta	181	1.06	2.68	2.76	0.70	3.65	1.50	4.07	1.53	3.66	1.62	2.16	1.00	1.41	1.93	3.14
W	182	1.11	1.10	1.15	0.38	0.80	0.40	1.01	0.39	0.93	0.93	0.68	0.37	0.33	0.56	0.71
Pb	208	17.84	4.46	3.75	3.55	3.95	2.95	3.67	2.94	3.60	3.88	2.64	2.76	2.84	3.08	3.31
Th	232	8.46	10.5	8.98	8.38	10.35	7.06	8.69	7.36	7.57	7.86	6.49	7.37	6.39	7.93	7.83
U	238	3.14	2.73	2.39	2.43	2.69	1.89	2.36	1.96	1.98	1.94	1.67	2.12	1.52	1.99	2.08

Table B.6.: Trace element analyses of volcanic rocks by ICP-MS (Göttingen)*Imai et. al (1995), **Raczek et al. (2001), Chen et al. (2000). Precision denotes 1 σ st.dev.

Sample	Gumja	Pela jung	Zumta	Bugor	Tila 1	X	Tum	Gufka	Hilia 2	SE Bugor	Jigu 1	Tila Str	Mir	Gufka	Biu 4	Biu 5
Comment	Biu young	Biu young	Biu young	Biu young	Biu young	Biu young	Biu young	Biu young	Biu young	Biu young	Biu young	Biu young	Biu young	Biu young	Biu old	Biu old
Li [ppm]	6.20	6.34	6.77	5.68	6.31	6.15	6.01	5.22	5.46	5.70	5.85	6.12	9.31	4.76	5.42	6.02
Sc	20.4	19.4	15.7	22.1	23.8	24.2	23.7	18.3	21.1	21.6	21.3	16.7	11.4	16.4	21.2	21.8
Co	48.9	45.8	40.4	52.7	53.6	49.3	61.2	44.5	48.7	48.2	44.9	49.7	28.7	38.5	52.4	55.8
Ni	222	207	200	299	231	181	427	201	214	217	182	229	111	173	236	233
Zn	105	114	122	117	124	113	115	105	111	108	104	127	117	92.8	120	129
Rb	32.7	39.0	66.9	37.9	35.8	36.1	42.1	25.1	28.3	38.3	32.4	40.7	72.6	23.5	29.0	41.8
Sr	747	695	888	673	675	698	686	667	566	692	583	689	1023	612	655	617
Y	21.7	21.8	18.1	23.9	25.7	23.3	20.9	18.8	20.3	23.0	20.4	21.3	15.7	16.9	24.1	24.0
Zr	176	213	263	199	207	176	159	158	157	103	153	176	297	142	175	225
Nb	23.4	64.8	88.0	37.7	47.1	46.4	27.1	34.8	30.3	13.5	28.2	46.0	33.1	20.4	51.2	51.2
Cs	0.43	0.39	0.80	0.46	0.36	0.53	0.65	0.09	0.29	0.49	0.26	0.30	0.61	0.09	0.29	0.43
Ba	457	525	798	451	397	435	506	431	391	472	447	382	843	404	460	393
La	42.7	40.6	54.5	38.1	36.6	37.5	40.2	31.8	30.2	39.5	30.2	31.1	62.0	29.4	34.4	36.8
Ce	78.6	77.5	102	72.9	76.7	72.9	78.1	61.4	60.1	76.6	59.4	64.2	118	56.0	70.6	78.1
Pr	8.43	8.57	11.0	8.34	9.01	8.10	8.55	6.99	6.85	8.67	6.74	7.49	12.4	6.35	8.37	8.97
Nd	34.5	35.0	42.8	33.9	38.9	33.2	34.2	28.6	28.2	34.5	28.1	31.1	46.3	26.3	35.1	38.3
Sm	6.77	7.02	8.04	7.03	8.48	7.01	6.89	6.00	6.17	7.01	6.00	7.04	8.60	5.62	7.59	8.11
Eu	2.31	2.37	2.63	2.37	2.71	2.32	2.29	2.13	2.20	2.43	2.08	2.38	2.81	1.93	2.53	2.75
Gd	5.80	5.94	6.33	6.02	6.93	5.95	5.94	5.16	5.33	6.11	5.36	5.88	6.62	4.74	6.50	6.96
Tb	0.92	0.97	0.95	0.99	1.09	0.93	0.89	0.80	0.86	0.95	0.86	0.95	0.93	0.76	1.07	1.08
Dy	4.88	4.87	4.33	5.12	5.51	4.88	4.64	4.02	4.49	4.93	4.48	4.91	4.09	3.84	5.27	5.20
Ho	0.86	0.87	0.70	0.93	0.96	0.87	0.82	0.71	0.82	0.89	0.84	0.85	0.65	0.67	0.91	0.93
Er	2.18	2.17	1.78	2.39	2.41	2.26	2.09	1.74	2.04	2.33	2.11	2.13	1.53	1.60	2.32	2.34
Tm	0.29	0.26	0.20	0.30	0.30	0.29	0.27	0.23	0.27	0.31	0.27	0.25	0.17	0.21	0.29	0.28
Yb	1.70	1.61	1.21	1.74	1.76	1.74	1.61	1.27	1.53	1.76	1.57	1.50	0.99	1.20	1.65	1.54
Lu	0.24	0.21	0.16	0.25	0.25	0.25	0.24	0.18	0.22	0.26	0.23	0.20	0.14	0.16	0.23	0.22
Hf	4.03	5.30	5.98	4.71	4.39	4.12	2.78	3.87	4.05	1.60	3.80	4.26	6.36	3.29	4.29	5.40
Ta	1.80	4.69	4.69	2.60	3.44	3.02	2.04	1.55	2.47	1.22	2.20	3.68	3.10	1.41	4.13	3.74
W	0.57	0.90	0.79	0.69	0.40	0.67	0.58	0.46	0.25	0.24	0.24	0.43	0.40	0.34	0.74	0.41
Pb	2.60	2.87	3.39	2.13	2.19	2.34	2.22	1.92	1.78	2.16	2.21	1.88	3.87	1.80	1.87	2.13
Th	6.57	6.06	8.22	5.20	4.54	5.30	5.78	4.35	4.07	5.65	4.36	4.14	10.2	4.14	4.21	4.66
U	1.72	1.54	2.00	1.39	1.11	1.28	1.43	1.05	0.65	1.51	1.06	1.10	2.64	0.97	1.12	1.16

Table B.6.: Trace element analyses of volcanic rocks by ICP-MS (Göttingen)*Imai et. al (1995), **Raczek et al. (2001), Chen et al. (2000). Precision denotes 1 σ st.dev.

Sample Comment	Biu 8 Biu old	Biu 9 Biu old	Dai Jos young	Kerang Jos young	Ampang Jos young	Pidong-M Jos young	Pidong-S Jos young	JG-2 std	JG-2 std	precision	JG-2 ref.*	accuracy	BCR-2 std	BCR-2 ref.**	accuracy
Li [ppm]	4.99	7.82	5.96	7.76	8.99	8.13	8.13	43.96	39.95	4.8%	42.2	99.4%	8.28		
Sc	20.8	22.9	22.8	20.2	18.6	20.7	13.7	2.8	2.64	3.8%	2.42	113.2%	31.6	33	95.7%
Co	49.2	50.2	53.1	48.8	50.2	51.2	36.0	3.8	3.41	5.5%	3.62	99.5%	35.5	37	96.0%
Ni	230	227	234	157	332	251	64	3.65	3.08	8.6%	4.35	77.3%	13.1		
Zn	102	128	116	129	116	124	116	13	12.39	3.6%	13.6	94.6%	133	127	104.9%
Rb	24.6	44.9	45.1	54.5	53.0	54.5	56.7	315.5	303.36	2.0%	301	102.8%	46.1	46.9	98.3%
Sr	472	881	827	1039	829	867	1057	20	19.08	3.3%	17.9	110.2%	325	340	95.5%
Y	18.6	29.1	23.3	27.7	22.0	24.7	21.4	80.0	78.25	1.1%	86.5	91.5%	31.6	37	85.3%
Zr	100	272	105	232	31.7	228	284	104	100.79	1.7%	97.6	105.0%	149	188	79.4%
Nb	29.0	23.4	14.3	13.8	15.8	23.2	68.2	16.6	16.60	0.1%	14.7	113.1%	8.17	12.9	63.4%
Cs	0.23	0.49	0.72	1.07	1.11	0.97	0.67	7.74	7.75	0.1%	6.79	114.1%	1.12	1.1	102.1%
Ba	346	519	564	715	685	627	824	66	66.27	0.4%	81	81.5%	632	677	93.4%
La	25.3	53.1	42.5	67.5	56.5	52.4	62.4	18.6	18.69	0.3%	19.9	93.6%	23.5	24.9	94.2%
Ce	51.8	105	84.1	128	107	101	125	47	47.26	0.7%	48.3	97.2%	51.5	52.9	97.4%
Pr	6.14	11.4	9.24	13.6	11.3	10.8	13.4	5.8	6.01	2.0%	6.2	95.1%	6.44	6.57	98.0%
Nd	25.1	47.5	37.9	53.5	44.2	43.7	52.2	24.5	25.30	1.5%	26.4	94.4%	27.6	28.7	96.1%
Sm	5.52	9.61	7.74	10.3	8.5	8.90	9.6	7.85	8.21	2.3%	7.78	103.2%	6.43	6.57	97.9%
Eu	1.84	2.99	2.57	3.51	2.83	2.93	3.15	0.11	0.11	1.0%	0.1	112.3%	2.04	1.96	104.3%
Gd	4.63	7.61	6.44	8.58	6.81	6.96	7.47	7.62	8.18	3.5%	8.01	98.6%	5.59	6.75	82.8%
Tb	0.74	1.16	0.99	1.24	1.00	1.07	1.08	1.74	1.89	3.9%	1.62	112.0%	1.04	1.07	97.0%
Dy	3.97	5.98	4.98	5.91	4.92	5.23	5.21	11.68	12.80	4.6%	10.5	116.6%	6.15	6.41	95.9%
Ho	0.72	1.06	0.89	0.98	0.84	0.92	0.91	2.54	2.80	4.9%	1.67	159.9%	1.21	1.3	93.3%
Er	1.78	2.68	2.27	2.54	2.13	2.35	2.33	7.79	8.44	4.0%	6.04	134.3%	3.46	3.66	94.6%
Tm	0.23	0.35	0.28	0.30	0.26	0.29	0.29	1.21	1.34	5.0%	1.16	109.9%	0.48	0.564	85.6%
Yb	1.44	2.04	1.64	1.67	1.49	1.57	1.62	7.74	8.72	6.0%	6.85	120.2%	3.23	3.38	95.6%
Lu	0.21	0.30	0.24	0.23	0.22	0.24	0.24	1.16	1.30	5.8%	1.22	101.0%	0.48	0.519	93.3%
Hf	2.51	5.40	1.39	3.10	0.63	4.29	7.27	5.06	5.74	6.3%	4.73	114.3%	4.35	4.8	90.7%
Ta	2.25	1.45	1.12	0.74	1.04	1.59	4.94	2.39	3.72	21.7%	2.76	110.7%	0.74		
W	0.34	0.48	0.28	0.29	0.38	0.66	0.60	18.27	20.50	5.7%	23	84.3%	0.38		
Pb	1.90	3.53	2.84	4.25	4.56	3.81	4.21	30.93	33.54	4.0%	31.5	102.3%	9.98	11	90.7%
Th	3.08	6.49	6.08	8.31	7.46	7.21	7.74	29.49	33.13	5.8%	31.6	99.1%	5.72	6.2	92.3%
U	0.76	1.73	1.47	2.01	1.79	1.80	1.95	10.23	11.24	4.7%	11.3	95.0%	1.61	1.69	95.5%

Table B.7.: Compilation of major and trace element data for Biu and Jos Plateau lavas and melt inclusions used for discussion
 b.d.: below detection limit of ionprobe, empty fields: not measured, accuracy of measurement reported in Table B.8. and B.18.

Sample Comment	ZAGU Biu young	JIGU 1 Biu young	JIGU-M Biu young	X Biu young	PELA JUNG Biu young	KOROKO Biu young	PELA ALT Biu young	DAM Biu young	DAM 2 Biu young	BUGOR Biu young	SE BUGOR Biu young
SiO₂ [wt%]	46.42	49.17	44.34	47.82	49.44	59.88	51.05	44.33	47.80	46.97	46.35
TiO₂	2.61	2.17	3.08	2.33	2.19	0.35	2.26	2.99	2.60	2.43	2.45
Al₂O₃	14.39	14.74	12.66	14.43	14.74	20.50	15.25	12.50	14.12	13.95	14.16
FeO_t	10.49	9.71	11.28	10.40	9.71	3.10	9.27	11.48	10.20	10.40	10.42
MnO	0.18	0.15	0.19	0.16	0.15	0.18	0.14	0.20	0.16	0.16	0.17
MgO	9.15	8.64	10.78	8.81	8.67	0.37	7.16	11.50	9.23	10.82	10.15
CaO	9.26	9.18	9.89	9.89	8.41	2.02	7.18	10.08	8.71	8.94	9.57
Na₂O	3.71	3.32	3.75	3.16	3.42	8.33	3.60	3.28	3.16	3.13	3.43
K₂O	1.82	1.38	1.77	1.29	1.62	4.81	2.45	1.56	2.15	1.46	1.53
P₂O₅	0.80	0.47	0.99	0.54	0.56	0.12	0.59	0.80	0.72	0.58	0.62
Sum	98.83	98.92	98.74	98.84	98.92	99.65	98.97	98.72	98.86	98.84	98.84
mg#	60.9	61.3	63.0	60.1	61.4	17.5	57.9	64.1	61.7	65.0	63.5
S [ppm]	49.0	7.7	68.0		29.5	43.5			125.5		
Cl	1898	810	1955		443	4466			1820		
Li	7.37	5.85	7.88	6.15	6.34		0.80	7.48	7.54	5.68	5.70
Cs	0.63	0.26	0.60	0.53	0.39		0.50	0.51	0.71	0.46	0.49
Rb	50.4	32.4	46.2	36.1	39.0	196	66.8	40.7	55.8	37.9	38.3
Ba	786	469	598	432	500	1135	830	736	747	441	438
Th	7.93	4.36	8.38	5.30	6.06	36.7	7.57	7.06	7.86	5.20	5.65
U	1.99	1.06	2.43	1.28	1.54	10.0	1.98	1.89	1.94	1.39	1.51
Nb	92	51	104	62	67	339	93	85	89	65	73
Ta	5.34	3.43	6.19		3.96	19.2			5.46		
La	58.8	30.2	67.8	37.5	40.6	120	53.8	55.2	52.7	38.1	39.5
Ce	110	59.4	138	72.9	77.5	206	101	113	104	72.9	76.6
Pb	3.08	2.21	3.55	2.34	2.87	16.9	3.60	2.95	3.88	2.13	2.16
Pr	11.7	6.74	15.3	8.10	8.57	20	10.7	12.6	11.2	8.34	8.67
Sr	973	610	1009	668	703	1012	805	858	872	668	714
Nd	48.7	28.1	62.4	33.2	35.0	64	42.8	51.3	45.4	33.9	34.5
Zr	272	187	352	183	230	808	346	305	313	211	206
Hf	6.93	5.27	8.66		5.78	17.8			7.28		
Sm	9.38	6.00	12.4	7.01	7.02	11	8.05	10.6	9.19	7.03	7.01
Eu	3.18	2.08	3.90	2.32	2.37	3.1	2.67	3.32	2.93	2.37	2.43
Gd	7.72	5.36	9.67	5.95	5.94	8.5	6.44	8.30	7.28	6.02	6.11
Tb	1.19	0.86	1.41	0.93	0.97	1.2	0.94	1.25	1.11	0.99	0.95
Dy	6.07	4.48	6.96	4.88	4.87	7.0	4.36	6.25	5.39	5.12	4.93
Ho	1.11	0.84	1.22	0.87	0.87	1.3	0.76	1.11	0.95	0.93	0.89
Y	27.3	20.4	29.5	23.3	21.8	34	20.2	27.1	24.2	23.9	23.0
Er	2.71	2.11	3.10	2.26	2.17	3.7	1.86	2.93	2.36	2.39	2.33
Tm	0.36	0.27	0.37	0.29	0.26	0.48	0.23	0.36	0.30	0.30	0.31
Yb	2.03	1.57	2.20	1.74	1.61	3.5	1.22	2.07	1.69	1.74	1.76
Lu	0.29	0.23	0.31	0.25	0.21	0.51	0.18	0.31	0.23	0.25	0.26
Sc	20.8	21.3	20.4	24.2	19.4	0.75	16.0	22.0	18.6	22.1	21.6
V	155	164	201	183	166	9	184	192	183	184	181
Cr	231	299	379	287	279	10	214	401	246	368	290
Ni	202	191	278	176	210	3	202	291	222	307	231
Co	45	43	52	47	40	3	40	49	40	53	45
Cu	37	57	43	45	46	7	26	51	36	47	42
Zn	104	91	125	96	109	137	124	109	116	102	102
Ga	22	20	21	20	21	35	23	22	21	18	20
Mo	4.35	1.95	5.02		2.79	7.61			5.19		
Re [ppt]		65.2	48.9	50.1			90.4	17.5			
Os [ppt]		46.1	41.8	9.3			133.5	24.3			
La/Yb	28.91	19.17	30.81	21.62	25.20	34.29	44.10	26.63	31.12	21.88	22.43
Zr/Nb	2.96	3.67	3.38	2.95	3.43	2.38	3.72	3.59	3.52	3.25	2.82
Ce/Pb	35.7	26.9	38.8	31.2	27.0	12.2	28.2	38.2	26.8	34.3	35.4
K/U	7612	10792	6061	8400	8737	3974	10263	6838	9208	8736	8416
Nb/Ta	17.2	14.9	16.8		16.9	17.6			16.3		

Table B.7.: Compilation of major and trace element data for Biu and Jos Plateau lavas and melt inclusions used for discussion
 b.d.: below detection limit of ionprobe, empty fields: not measured, accuracy of measurement reported in Table B.8. and B.18.

Sample	HILIA 1	HILIA 2	TAMZA	GUFKA	MIR	syn. glas	MIR	GULDUMBUR	PELA 2	WIGA	GWARAM
Comment	Biu young	Biu young	Biu young	Biu young	Biu young	Biu young	Biu young	Biu young	Biu young	Biu young	Biu young
					Qz in thin sec. ionprobe check						
SiO ₂ [wt%]	46.41	49.26	46.51	51.17	53.24	52.76		45.98	45.54	45.66	50.10
TiO ₂	2.59	2.19	3.06	1.93	1.92	1.91		2.59	2.88	3.04	2.38
Al ₂ O ₃	14.56	14.69	14.17	15.34	16.19	16.30		12.91	13.23	13.55	15.17
FeO _i	10.48	9.96	10.62	9.03	7.51	7.28		10.65	10.98	10.88	9.28
MnO	0.17	0.15	0.17	0.13	0.12	0.12		0.18	0.18	0.17	0.15
MgO	9.16	8.59	9.28	7.35	5.91	5.96		11.87	10.18	10.69	7.04
CaO	9.23	9.27	8.86	8.90	6.80	6.64		9.35	10.05	9.71	7.27
Na ₂ O	3.72	3.17	3.36	3.49	3.94	3.97		2.93	3.35	2.67	4.55
K ₂ O	1.77	1.16	2.00	1.14	2.93	2.87		1.61	1.62	1.59	2.33
P ₂ O ₅	0.74	0.46	0.79	0.52	0.59	0.57		0.75	0.75	0.85	0.70
Sum	98.83	98.89	98.82	98.99	99.16	98.36		98.81	98.78	98.79	98.97
mg#	60.9	60.6	60.9	59.2	58.4	59.4		66.5	62.3	63.6	57.5
S [ppm]		46.0	65.1	44.6	34.0			29.1			
Cl		40	1525	248	670			1329			
Li	6.99	5.46	2.82	4.99	9.85			3.17	6.80	2.73	9.78
Cs	0.59	0.29	1.60	0.09	0.62			0.57	0.49	0.71	0.99
Rb	50.2	28.3	43.5	24.3	73.2			45.5	45.1	33.3	61.0
Ba	628	379	604	440	864		1083	531	579	519	858
Th	6.49	4.07	8.69	4.24	10.29			7.37	6.39	7.36	10.5
U	1.67	0.65	2.36	1.01	2.67			2.12	1.52	1.96	2.73
Nb	83	51	103	52	120		149	86	82	88	115
Ta		3.40	6.19	2.87	7.48			4.51			
La	50.0	30.2	58.2	30.6	62.9		68.9	50.6	51.0	54.9	72.0
Ce	96.5	60.1	115	58.7	120		130	97.8	99.2	106	139
Pb	2.64	1.78	3.67	1.86	3.91			2.76	2.84	2.94	4.46
Pr	10.2	6.85	12.3	6.67	12.5		14.8	10.6	10.9	11.5	15.1
Sr	860	567	1013	667	1075		1205	804	824	895	1044
Nd	42.1	28.2	49.7	27.4	47.2		52.3	44.4	46.5	46.7	59.7
Zr	259	183	338	173	355		382	263	279	264	429
Hf		5.20	8.29	4.10	8.97		9.43	6.03			
Sm	8.49	6.17	10.0	5.81	8.7		9.49	8.72	9.16	9.57	11.5
Eu	2.72	2.20	3.20	2.03	2.83		2.94	2.87	3.01	3.02	3.67
Gd	6.87	5.33	7.82	4.95	6.75		6.21	6.78	7.20	7.49	8.79
Tb	1.05	0.86	1.20	0.78	0.92		0.815	1.08	1.09	1.15	1.30
Dy	5.39	4.49	5.75	3.93	4.03		4.49	5.50	5.64	5.61	6.10
Ho	0.95	0.82	1.01	0.69	0.64		0.831	0.98	0.99	0.94	1.01
Y	26.7	20.3	25.4	17.8	16.0		17.2	25.1	29.3	24.4	26.2
Er	2.48	2.04	2.60	1.67	1.55		1.98	2.54	2.54	2.44	2.55
Tm	0.32	0.27	0.32	0.22	0.17		0.225	0.33	0.33	0.31	0.29
Yb	1.82	1.53	1.86	1.23	0.99		1.18	1.90	1.84	1.67	1.64
Lu	0.26	0.22	0.27	0.17	0.14		0.211	0.27	0.28	0.24	0.22
Sc	22.2	21.1	18.3	17.4	11.7			21.4	24.2	20.0	14.3
V	160	171	197	141	122			190	195	205	145
Cr	196	273	224	242	122		110	387	397	300	187
Ni	183	220	202	196	123		128	346	243	269	174
Co	38	49	41	42	30			52	49	51	38
Cu	36	51	24	57	26			40	46	52	22
Zn	101	99	123	95	123			106	107	109	134
Ga	24	21	23	20	24			20	21	19	25
Mo		1.00	4.26	2.32	3.46			3.60			
Re [ppt]			40.5		27.5			56.1			48.3
Os [ppt]			39.2		21.6			44.0			55.0
La/Yb	27.52	19.78	31.35	24.77	63.83			26.66	27.68	32.79	43.86
Zr/Nb	3.12	3.59	3.28	3.33	2.96			3.06	3.40	3.00	3.73
Ce/Pb	36.6	33.7	31.3	31.5	30.8			35.5	34.9	36.2	31.3
K/U	8814	14900	7038	9324	9120			6295	8845	6742	7065
Nb/Ta		15.0	16.6	18.1	16.1			19.1			

Table B.7.: Compilation of major and trace element data for Biu and Jos Plateau lavas and melt inclusions used for discussion
 b.d.: below detection limit of ionprobe, empty fields: not measured, accuracy of measurement reported in Table B.8. and B.18.

Sample Comment	ZUMTA Biu young	HIZSHI Biu young	TUM Biu young	ETUM Biu young	GUMJA Biu young	TILA 1 Biu young	TILA STR Biu young	30-1 MW Biu young melt incl.	35e4 MW Biu young melt incl.	ilm a1 Biu young melt incl.	ilm a2 Biu young melt incl.
SiO₂ [wt%]	50.03	47.77	46.06	48.28	47.49	46.30	47.40	53.19	52.01	54.33	53.35
TiO ₂	2.20	2.67	2.40	2.57	2.69	3.09	2.77	2.38	2.68	2.33	2.31
Al ₂ O ₃	15.42	14.25	13.20	14.34	14.46	13.48	14.22	18.10	17.61	17.66	16.86
FeO _t	8.89	10.22	10.58	10.16	10.02	11.03	11.14	6.63	7.56	4.40	6.37
MnO	0.14	0.17	0.16	0.18	0.15	0.16	0.15	0.07	0.09	0.066	0.076
MgO	7.78	8.81	12.89	9.16	9.43	10.34	9.33	1.55	1.737	1.2	1.485
CaO	7.67	8.10	8.71	8.03	9.57	9.83	9.21	4.23	4.545	4.62	4.6
Na ₂ O	3.77	4.48	2.83	3.55	3.13	2.55	2.42	6.01	5.81	5.94	5.95
K ₂ O	2.45	1.59	1.41	1.88	1.37	1.41	1.60	3.25	3.13	3.08	3.06
P ₂ O ₅	0.67	0.81	0.57	0.72	0.58	0.59	0.53	0.92	0.985	1.016	1.041
Sum	99.01	98.86	98.82	98.87	98.88	98.77	98.76	96.34	96.16	94.64	95.10
mg#	60.9	60.6	68.5	61.6	62.6	62.6	59.9	29.4	29.1	32.7	29.4
S [ppm]	36.0		77.0		31.6						
Cl	1382		1379		997						
Li	6.77	8.94	6.01	8.65	6.20	6.31	6.12				
Cs	0.80	0.82	0.65	0.67	0.43	0.36	0.30	1.05	1.87	0.77	0.85
Rb	66.9	83.8	42.1	49.2	32.7	35.8	40.7				
Ba	805	723	498	518	453	384	383	1165	1135	1230	1185
Th	8.22	8.98	5.78	7.83	6.57	4.54	4.14				
U	2.00	2.39	1.43	2.08	1.72	1.11	1.10				
Nb	96	109	73	94	72	61	58	183	166	209	200
Ta	6.47		4.40		3.95						
La	54.5	67.9	40.2	54.7	42.7	36.6	31.1	78.5	75.1	83.2	81.1
Ce	102	133	78.1	108	78.6	76.7	64.2	154	145	163	160
Pb	3.39	3.75	2.22	3.31	2.60	2.19	1.88				
Pr	11.0	14.4	8.55	12.1	8.43	9.01	7.49	18.2	17.4	19.0	19.0
Sr	918	1017	692	918	748	671	708	1605	1495	1690	1600
Nd	42.8	56.7	34.2	48.8	34.5	38.9	31.1	65.2	62.9	69.5	68.7
Zr	282	386	220	367	200	252	216	346	356	377	364
Hf	8.16		6.06		5.15			7.61	8.77	8.04	8.39
Sm	8.04	11.3	6.89	9.55	6.77	8.48	7.04	11.3	11.5	11.9	12.3
Eu	2.63	3.49	2.29	3.09	2.31	2.71	2.38	3.92	3.51	3.68	3.87
Gd	6.33	8.68	5.94	7.90	5.80	6.93	5.88	7.24	7.23	7.32	8.14
Tb	0.95	1.26	0.89	1.24	0.92	1.09	0.95	0.73	0.65	0.82	0.90
Dy	4.33	6.09	4.64	6.70	4.88	5.51	4.91	3.24	3.56	3.41	3.96
Ho	0.70	1.03	0.82	1.22	0.86	0.96	0.85	0.49	0.55	0.58	0.65
Y	18.1	27.4	20.9	28.2	21.7	25.7	21.3	11.0	12.0	10.9	13.6
Er	1.78	2.67	2.09	2.94	2.18	2.41	2.13	0.90	1.00	0.98	1.31
Tm	0.20	0.30	0.27	0.39	0.29	0.30	0.25	0.06	0.06	0.03	0.07
Yb	1.21	1.73	1.61	2.38	1.70	1.76	1.50	0.18	0.02	0.07	0.08
Lu	0.16	0.25	0.24	0.33	0.24	0.25	0.20	0.09	0.08	b.d.	0.01
Sc	15.7	17.3	23.7	17.2	20.4	23.8	16.7				
V	153	162	195	149	197	210	185				
Cr	217	265	452	333	229	286	283				
Ni	202	233	435	241	229	230	246				
Co	40	46	58	38	49	49	48				
Cu	57	27	78	31	62	37	41				
Zn	115	132	105	109	92	96	108				
Ga	23	24	18	23	20	21	21				
Mo	2.85		3.39		3.59						
Re [ppt]	93.4	56.4	145.7		43.1						
Os [ppt]	79.1	59.8	82.1		41.3						
La/Yb	45.01	39.29	24.94	22.99	25.09	20.78	20.71	436.11	3755.00	1188.57	1013.75
Zr/Nb	2.94	3.54	3.01	3.90	2.78	4.13	3.72	1.89	2.14	1.80	1.82
Ce/Pb	30.1	35.3	35.1	32.6	30.2	35.1	34.1				
K/U	10167	5523	8237	7476	6638	10499	12093				
Nb/Ta	14.8		16.6		18.2						

Table B.7.: Compilation of major and trace element data for Biu and Jos Plateau lavas and melt inclusions used for discussion
 b.d.: below detection limit of ionprobe, empty fields: not measured, accuracy of measurement reported in Table B.8. and B.18.

Sample Comment	113 Biu young melt incl.	melt incl. Biu young mean of 5	Biu4 Biu old	Biu5 Biu old	Biu8 Biu old	Biu9 Biu old	DAI Jos young	KERANG Jos young	AMPANG Jos young Qz in thin sec.	PIDONG-M Jos young Qz in thin sec.	PIDONG-S Jos young
SiO₂ [wt%]	52.58	53.09	46.18	45.93	48.01	46.63	46.26	44.84	46.69	45.63	47.82
TiO ₂	2.46	2.43	2.96	3.15	2.21	2.77	2.44	2.66	2.30	2.43	2.67
Al ₂ O ₃	16.96	17.44	13.30	13.13	13.95	13.84	13.78	13.68	13.16	13.46	16.30
FeO _t	7.08	6.41	10.89	11.13	10.21	10.54	10.45	11.29	10.48	10.68	10.63
MnO	0.065	0.07	0.16	0.17	0.17	0.19	0.17	0.19	0.18	0.18	0.17
MgO	1.629	1.52	9.97	10.48	10.70	10.14	10.77	9.49	11.05	10.79	6.13
CaO	4.21	4.44	10.71	10.31	9.68	9.74	9.77	9.91	9.12	9.54	8.64
Na ₂ O	5.93	5.93	2.69	2.38	2.41	2.63	2.92	3.99	3.33	3.60	3.47
K ₂ O	3.17	3.14	1.32	1.50	1.13	1.62	1.69	1.81	1.80	1.79	2.32
P ₂ O ₅	0.904	0.97	0.61	0.58	0.40	0.73	0.60	0.89	0.72	0.71	0.66
Sum	94.99	95.45	98.79	98.76	98.86	98.83	98.84	98.74	98.83	98.81	98.82
mg#	29.1	29.7	62.0	62.7	65.1	63.2	64.8	60.0	65.3	64.3	50.7
S [ppm]			55.9					297.5	377.5		
Cl			1203					2341	2000		
Li			5.42	6.02	4.99	7.82	5.96	7.76	8.99	8.13	8.13
Cs		1.14	0.29	0.43	0.23	0.49	0.72	1.07	1.11	0.97	0.67
Rb			29.0	41.8	24.6	44.9	45.1	54.5	53.0	54.5	56.7
Ba		1179	498	390	351	535	554	734	726	615	795
Th			4.21	4.66	3.08	6.49	6.08	8.31	7.46	7.21	7.74
U			1.12	1.16	0.76	1.73	1.47	2.01	1.79	1.80	1.95
Nb		190	63	63	43	88	72	102	86	86	97
Ta			4.16					5.43	4.57		
La		79.5	34.4	36.8	25.3	53.1	42.5	67.5	56.5	52.4	62.4
Ce		156	70.6	78.1	51.8	105	84.1	128	107	101	125
Pb			1.87	2.13	1.90	3.53	2.84	4.25	4.56	3.81	4.21
Pr		18.4	8.37	8.97	6.14	11.4	9.24	13.6	11.3	10.8	13.4
Sr		1598	712	635	497	888	803	1024	858	841	1128
Nd		66.6	35.1	38.3	25.1	47.5	37.9	53.5	44.2	43.7	52.2
Zr		361	240	257	164	297	231	293	247	257	331
Hf		8.20	7.29					6.58	5.55		
Sm		11.8	7.59	8.11	5.52	9.61	7.74	10.3	8.5	8.90	9.6
Eu		3.75	2.53	2.75	1.84	2.99	2.57	3.51	2.83	2.93	3.15
Gd		7.48	6.50	6.96	4.63	7.61	6.44	8.58	6.81	6.96	7.47
Tb		0.78	1.07	1.08	0.74	1.16	0.99	1.24	1.00	1.07	1.08
Dy		3.54	5.27	5.20	3.97	5.98	4.98	5.91	4.92	5.23	5.21
Ho		0.57	0.91	0.93	0.72	1.06	0.89	0.98	0.84	0.92	0.91
Y		11.9	24.1	24.0	18.6	29.1	23.3	27.7	22.0	24.7	21.4
Er		1.05	2.32	2.34	1.78	2.68	2.27	2.54	2.13	2.35	2.33
Tm		0.06	0.29	0.28	0.23	0.35	0.28	0.30	0.26	0.29	0.29
Yb		0.09	1.65	1.54	1.44	2.04	1.64	1.67	1.49	1.57	1.62
Lu		0.06	0.23	0.22	0.21	0.30	0.24	0.23	0.22	0.24	0.24
Sc			21.2	21.8	20.8	22.9	22.8	20.2	18.6	20.7	13.7
V			206	211	174	179	175	167	156	157	145
Cr			355	305	396	358	323	205	417	347	45
Ni			244	230	242	226	230	161	345	260	75
Co			46	50	51	43	53	50	51	52	34
Cu			50	46	35	50	38	28	57	32	27
Zn			102	100	90	99	105	128	116	120	107
Ga			22	21	19	20	20	21	20	19	21
Mo			3.12					4.12	4.81		
Re [ppt]			44.7		23.0				136.1	55.2	
Os [ppt]			19.8		23.7				100.7	43.6	
La/Yb			20.86	23.95	17.62	26.08	25.87	40.47	37.82	33.32	38.61
Zr/Nb			3.81	4.08	3.81	3.38	3.21	2.87	2.87	2.99	3.41
Ce/Pb			37.8	36.7	27.2	29.8	29.6	30.2	23.5	26.6	29.7
K/U			9791	10697	12237	7755	9521	7445	8326	8276	9854
Nb/Ta			15.1					18.8	18.8		

Table B.8.: Analytical accuracy/precision of major and trace element data

Volcanic Rocks		
element	method	error on accuracy
SiO₂ [wt%]	XRF-M Frankfurt	<5%
TiO₂	XRF-M Frankfurt	<5%
Al₂O₃	XRF-M Frankfurt	<5%
FeO_t	XRF-M Frankfurt	<5%
MnO	XRF-M Frankfurt	<5%
MgO	XRF-M Frankfurt	<5%
CaO	XRF-M Frankfurt	<5%
Na₂O	XRF-M Frankfurt	<5%
K₂O	XRF-M Frankfurt	<5%
P₂O₅	XRF-M Frankfurt	<5%
S [ppm]	XRF-M MUN	<5%
Cl	XRF-M MUN	<5%
Li	ICP-MS Göttingen	<10% ?
Cs	ICP-MS MUN	<10%
Rb	ICP-MS MUN	<10%
Ba	XRF-P Mainz	<5%
Th	ICP-MS Göttingen	<10%
U	ICP-MS Göttingen	<10%
Nb	XRF-P Mainz	<5%
Ta	ICP-MS MUN	<10%
La	ICP-MS MUN	<10%
Ce	ICP-MS MUN	<10%
Pb	ICP-MS Göttingen	<10%
Pr	ICP-MS MUN	<10%
Sr	XRF-P Mainz	<5%
Nd	ICP-MS MUN	<10%
Zr	XRF-P Mainz	<5%
Hf	ICP-MS MUN	<20%
Sm	ICP-MS MUN	<10%
Eu	ICP-MS MUN	<10%
Gd	ICP-MS MUN	<10%
Tb	ICP-MS MUN	<10%
Dy	ICP-MS MUN	<10%
Ho	ICP-MS MUN	<10%
Y	ICP-MS MUN	<10%
Er	ICP-MS MUN	<10%
Tm	ICP-MS MUN	<10%
Yb	ICP-MS MUN	<10%
Lu	ICP-MS MUN	<10%
Sc	XRF-P Mainz	<15%
V	XRF-P Mainz	<5%
Cr	XRF-P Mainz	<5%
Ni	XRF-P Mainz	<5%
Co	XRF-P Mainz	<15%
Cu	XRF-P Mainz	<15%
Zn	XRF-P Mainz	<5%
Ga	XRF-P Mainz	<10%
Mo	ICP-MS MUN	<25%
error on precision		
Re [ppt]	ID-TIMS	11%
Os	ID-TIMS	5%

Accuracy defined as relative deviation of standard reference materials from recommended values.

Table B.9.: Major and trace element data of cpx
 b.d.: below detection limit, iso: isotope analysis available in Table B.22., empty fields: not measured, Fe³⁺ by moessbauer spectroscopy

Sample Comment	Kerang Jos	Ampang Jos	Kerang Jos	Mir 48-16 Biu	Ker Jos	Dam 45-20 Biu	Dam+ Biu	Ampang Jos	Mir 21 Biu	Ker 2 Jos	Dam 60-4 Biu	Dam++ Biu	Mir 60-1 Biu	Pela alt Biu	Mir+Grt Biu	Mir+Grt Biu	Mir 15 Biu	Pid M Jos	Gumja2 Biu	Mir 45-7 Biu	Gumja1 Biu	Pela alt b Biu	Damknolle Biu
					iso		iso	iso	+gnt, S iso	iso	iso	iso	iso	iso	+gnt iso	dupl.	iso	iso	+S iso				+gnt, ilm, plag, apa
SiO₂ [wt%]	50.33	50.49	50.37	49.16	49.82	49.92	50.17	49.36	49.26	49.85	48.94	49.05	48.38	48.57	48.75	49.12	48.38	48.09	47.36	47.19	46.96	46.89	46.17
TiO₂	0.51	0.52	0.50	0.50	0.59	0.62	0.61	1.04	0.59	0.82	0.81	0.74	0.73	0.95	0.75	0.69	1.03	1.46	1.68	1.33	1.96	1.55	2.02
Al₂O₃	7.31	7.40	7.32	7.56	7.78	7.99	7.98	8.49	8.83	8.36	9.03	9.18	9.52	9.56	9.58	9.57	10.02	8.98	9.24	10.71	9.49	10.48	11.69
Cr₂O₃	0.210	0.199	0.195	0.144	0.077	0.062	0.081	0.009	0.036	0.007	0.028	0.024	0.019	0.006	0.015	0.012	0.007	0.009	0.014	0.008	0.009	0.010	0.010
FeO	5.27	5.39	5.43	5.64	5.69	6.12	6.12	6.26	7.01	6.71	7.18	7.28	7.08	7.13	7.24	7.35	7.71	7.58	7.99	8.38	8.86	8.49	9.45
MnO	0.120	0.119	0.134	0.145	0.143	0.151	0.151	0.126	0.155	0.141	0.160	0.154	0.146	0.145	0.143	0.145	0.142	0.128	0.143	0.132	0.147	0.124	0.116
MgO	17.06	17.03	16.97	16.81	16.05	16.74	16.55	14.06	15.69	14.73	14.62	14.72	14.29	13.96	13.98	13.97	13.03	12.74	13.25	11.84	12.28	11.67	9.04
CaO	16.58	16.14	16.38	16.36	16.69	16.07	15.81	17.83	15.32	16.68	16.34	16.08	16.69	16.91	16.92	16.42	16.90	17.57	17.21	17.54	17.11	17.79	17.77
NiO	0.050	0.051	0.059	0.047	0.044	0.032	0.041	0.026	0.036	0.034	0.051	0.037	0.030	0.027	0.038	0.035	0.024	0.013	0.019	0.019	0.016	0.049	0.010
Na₂O	1.18	1.26	1.34	0.99	1.27	1.15	1.07	1.44	1.29	1.42	1.27	1.28	1.35	1.33	1.38	1.34	1.52	1.71	1.44	1.81	1.72	1.80	2.43
Sum	98.63	98.62	98.71	97.36	98.16	98.86	98.60	98.66	98.22	98.77	98.44	98.55	98.25	98.60	98.80	98.66	98.77	98.30	98.34	98.96	98.58	98.85	98.74
mg#	85.2	84.9	84.8	84.1	83.4	83.0	85.4	80.0	82.8	79.6	78.4	82.2	78.2	82.3	80.8	77.2	79.2	74.9	74.7	71.6	78.6	71.0	63.0
Cations to 4 oxygens																							
Si	1.847	1.851	1.848	1.831	1.841	1.832	1.842	1.827	1.823	1.838	1.815	1.815	1.800	1.801	1.804	1.817	1.796	1.801	1.776	1.762	1.766	1.757	1.742
Ti	0.014	0.014	0.014	0.014	0.016	0.017	0.017	0.029	0.016	0.023	0.022	0.020	0.020	0.027	0.021	0.019	0.029	0.041	0.047	0.037	0.055	0.044	0.057
Al	0.316	0.320	0.317	0.332	0.339	0.346	0.345	0.370	0.385	0.363	0.394	0.400	0.417	0.418	0.418	0.417	0.438	0.396	0.408	0.471	0.421	0.463	0.520
Fe²⁺	0.162	0.165	0.167	0.176	0.176	0.188	0.155	0.194	0.180	0.207	0.223	0.176	0.220	0.167	0.183	0.227	0.190	0.238	0.251	0.262	0.1871	0.266	0.298
Fe³⁺							0.033		0.037			0.050		0.055	0.041		0.050				0.0916		
Mn	0.004	0.004	0.004	0.005	0.004	0.005	0.005	0.004	0.005	0.004	0.005	0.005	0.005	0.005	0.004	0.005	0.004	0.004	0.005	0.004	0.005	0.004	0.004
Mg	0.933	0.931	0.928	0.933	0.884	0.915	0.906	0.775	0.865	0.810	0.808	0.812	0.792	0.772	0.771	0.770	0.721	0.711	0.74	0.659	0.688	0.652	0.508
Ca	0.652	0.634	0.644	0.653	0.661	0.632	0.622	0.707	0.607	0.659	0.649	0.637	0.665	0.672	0.671	0.651	0.672	0.705	0.691	0.702	0.689	0.714	0.718
Na	0.084	0.089	0.096	0.071	0.091	0.082	0.076	0.103	0.093	0.102	0.091	0.091	0.097	0.095	0.099	0.096	0.109	0.124	0.105	0.131	0.126	0.131	0.178
Sum	4.012	4.008	4.017	4.016	4.013	4.015	4.001	4.009	4.011	4.006	4.008	4.007	4.017	4.009	4.013	4.002	4.009	4.020	4.023	4.029	4.029	4.031	4.026
Ba [ppm]	b.d.	b.d.	0.066	0.107	b.d.	b.d.	0.079	0.114	0.074	0.045	b.d.	0.056	b.d.	0.042	b.d.	0.052	0.058	0.072	0.084	b.d.	0.058	0.066	0.056
Nb	0.230	0.205	0.222	0.298	0.218	0.176	0.167	0.425	0.230	0.255	0.228	0.190	0.265	0.339	0.244	0.194	0.349	0.548	0.674	0.532	0.572	0.634	2.32
K	43.1	41.1	35.3	37	26.2	28.9	44.8	37.5	30.7	36.5	17.8	30.8	23.1	36.4	25.0	32.4	27.4	33.3	30.5	30.4	25.5	35.8	19.7
La	1.43	1.07	1.08	1.17	1.10	1.18	1.24	1.95	1.05	1.51	0.867	1.05	1.18	1.68	1.26	1.05	1.6	2.49	2.49	1.9	2.38	2.62	7.41
Ce	4.35	3.98	3.48	4.11	3.90	4.09	4.37	7.69	4.36	5.80	3.65	3.90	4.43	6.50	4.57	4.01	6.04	9.06	10.3	8.23	10.7	10.4	28.9
Pr	0.974	0.8	0.747	0.8	0.790	0.759	0.78	1.55	0.806	1.07	0.818	0.837	0.946	1.39	0.928	0.767	1.2	1.91	2.06	1.64	2.15	1.86	6.05
Sr	49.1	43.7	43.1	38.1	40.1	42.7	45.5	71.3	41.5	63.4	43.5	44.6	47.8	60.8	50.1	44.1	61.1	90.7	84.5	75.3	97.1	94.9	184
Nd	4.45	3.77	3.96	4.34	4.03	4.22	4.8	7.91	4.58	6.42	4.74	4.69	4.88	7.23	5.21	4.33	6.31	10.01	11.65	9.3	12.9	11.3	32.6
Zr	12.4	12.1	11.8	13.8	13.95	15.2	17	26.6	15.7	19.8	18.85	18.6	18.8	25.8	20.9	16	25.1	40.3	49.6	37.5	54.6	44.7	133
Sm	1.61	1.39	1.38	1.16	1.59	1.42	1.49	2.64	1.84	2.13	1.8	1.66	2.03	2.6	1.89	1.7	2.65	3.57	4.63	3.22	4.19	3.57	10.15
Eu	0.711	0.535	0.504	0.514	0.610	0.552	0.619	0.851	0.717	0.731	0.745	0.672	0.818	1.02	0.758	0.697	1.07	1.28	1.70	1.1	1.66	1.23	3.65
Ti	3057	3123	2985	2999	3547	3741	3679	6255	3538	4921	4826	4407	4376	5720	4486	4136	6165	8776	10053	7949	11762	9274	13600
Gd	1.49	1.74	1.53	1.81	2.02	1.62	2.54	2.72	1.53	2.07	2.15	1.57	2.11	2.24	2.02	1.82	3	4.17	5.07	3.38	5.07	4.63	9.00
Tb	0.263	0.232	0.268	0.242	0.254	0.333	0.293	0.393	0.297	0.319	0.309	0.362	0.378	0.431	0.304	0.21	0.337	0.532	0.817	0.453	0.723	0.531	1.055
Dy	1.54	1.68	1.64	1.39	1.64	1.61	1.94	2.26	1.91	1.93	2.39	1.84	2.02	2.36	1.90	1.86	2.57	2.85	3.94	2.67	4	3.11	4.6
Ho	0.288	0.265	0.308	0.287	0.288	0.327	0.353	0.358	0.34	0.344	0.467	0.312	0.363	0.478	0.282	0.304	0.327	0.507	0.638	0.386	0.672	0.485	0.512
Y	6.29	6.38	7.01	6.97	7.63	7.66	8.05	8.62	7.99	8.34	9.88	8.15	8.42	10.2	8.29	8.26	9.59	10.9	15.8	10.4	15.3	10.3	12.8
Er	0.717	0.586	0.659	0.629	0.787	0.692	0.944	0.750	0.781	0.848	1.01	0.799	0.869	0.934	0.864	0.912	0.903	0.854	1.38	0.754	1.32	1.07	0.587
Tm	0.107	0.110	0.126	0.089	0.094	0.112	0.121	0.064	0.121	0.074	0.155	0.101	0.092	0.131	0.102	0.139	0.114	0.123	0.138	0.089	0.128	0.155	0.077
Yb	0.398	0.593	0.476	0.540	0.681	0.536	0.888	0.411	0.820	0.597	0.761	0.572	0.555	0.543	0.602	0.545	0.485	0.347	0.698	0.314	0.923	0.302	b.d.
Lu	0.032	0.028	0.028	0.067	0.082	0.042	0.083	0.022	0.051	0.111	0.120	0.060	0.090	0.011	0.066	0.128	0.151	b.d.	b.d.	b.d.	0.059	0.085	b.d.

Table B.9.: Major and trace element data of cpx
 b.d.: below detection limit, iso: isotope analysis available in Table B.22., empty fields: not measured, Fe³⁺ by moessbauer spectroscopy

Sample Comment	Bos Hill Biu ilm exsol.	Miringa Biu	Kerang Jos fluid incl.	Miringa Biu	Mir Biu +gnt	Mir Biu +gnt	Mir Biu +gnt	Mir Biu +gnt	Miringa Biu	Dam Biu	Mir Biu +gnt	Miringa Biu	Kerang Biu +S	Miringa Biu	Mir Biu +gnt	Mir Biu +gnt	Mir Biu +gnt	Gufka Biu	Miringa Biu	Miringa Biu	Gufka Biu	Mir Biu	Mir Biu +gnt
SiO₂ [wt%]	48.86	48.46	49.76	48.73	48.54	50.31	49.94	48.71	48.36	49.08	48.46	48.77	48.13	48.51	48.58	49.14	48.70	48.71	47.52	47.23	48.24	48.13	48.97
TiO₂	1.29	0.55	0.80	0.61	0.88	0.58	0.62	0.72	0.66	0.70	0.83	0.56	1.24	0.73	0.73	0.74	0.73	0.75	0.93	0.99	0.92	0.90	0.68
Al₂O₃	7.27	8.05	8.29	8.08	8.92	9.18	9.46	9.39	8.48	9.13	9.46	8.33	8.94	8.41	9.52	9.64	9.49	9.78	9.02	8.92	9.85	9.63	10.06
Cr₂O₃	0.028	0.031	0.015	0.018	0.018	0.036	0.042	0.013	0.013	0.022	0.011	0.020	0.019	0.019	0.023	0.011	b.d.	0.010	b.d.	b.d.	0.010	b.d.	b.d.
FeO	5.86	6.87	6.62	6.91	6.92	7.28	7.46	7.16	7.23	7.29	7.16	7.67	6.84	7.47	7.19	7.31	7.16	7.32	7.42	7.43	7.59	7.63	7.85
MnO	0.111	0.158	0.138	0.152	0.146	0.157	0.152	0.148	0.157	0.153	0.147	0.150	0.124	0.157	0.153	0.151	0.150	0.148	0.143	0.134	0.134	0.134	0.135
MgO	13.38	15.69	14.76	15.26	15.20	15.67	15.33	14.53	14.59	14.65	14.33	15.24	13.56	14.76	14.21	14.40	14.11	14.32	13.48	13.51	13.61	13.59	13.97
CaO	20.40	15.88	17.10	16.32	16.76	15.18	15.26	15.67	16.26	16.56	16.48	15.45	17.65	16.03	16.68	16.30	16.85	16.54	17.18	17.16	17.14	16.93	16.17
NiO	0.018	0.041	0.032	0.046	0.043	0.037	0.040	0.035	0.038	0.039	0.026	0.030	0.021	0.034	0.033	0.036	0.023	0.089	0.032	0.031	0.054	0.028	0.031
Na₂O	1.43	1.17	1.40	1.19	1.12	1.28	1.33	1.35	1.28	1.32	1.39	1.25	1.58	1.37	1.41	1.38	1.40	1.45	1.45	1.44	1.50	1.52	1.43
Sum	98.67	96.91	98.89	97.34	98.58	99.73	99.64	97.74	97.09	98.94	98.31	97.50	98.10	97.51	98.54	99.12	98.62	99.13	97.18	96.87	99.05	98.52	99.30
mg#	80.3	80.3	79.9	79.7	79.6	79.3	78.5	78.3	78.2	78.2	78.1	78.0	77.9	77.9	77.9	77.8	77.8	77.7	76.4	76.4	76.2	76.0	76.0
Cations to 4 oxygens																							
Si	1.823	1.823	1.834	1.827	1.799	1.831	1.822	1.815	1.820	1.812	1.801	1.826	1.800	1.820	1.802	1.809	1.805	1.797	1.797	1.793	1.788	1.793	1.803
Ti	0.036	0.015	0.022	0.017	0.025	0.016	0.017	0.020	0.019	0.019	0.023	0.016	0.035	0.020	0.020	0.020	0.020	0.021	0.026	0.028	0.026	0.025	0.019
Al	0.320	0.357	0.360	0.357	0.390	0.394	0.407	0.412	0.376	0.397	0.414	0.368	0.394	0.372	0.416	0.418	0.415	0.425	0.402	0.399	0.430	0.423	0.436
Fe²⁺	0.183	0.216	0.204	0.217	0.215	0.222	0.228	0.223	0.228	0.225	0.222	0.240	0.214	0.234	0.223	0.225	0.222	0.226	0.235	0.236	0.235	0.238	0.242
Fe³⁺																							
Mn	0.004	0.005	0.004	0.005	0.005	0.005	0.005	0.005	0.005	0.005	0.005	0.005	0.004	0.005	0.005	0.005	0.005	0.005	0.005	0.004	0.004	0.004	0.004
Mg	0.744	0.880	0.811	0.853	0.840	0.850	0.833	0.807	0.819	0.806	0.794	0.851	0.756	0.825	0.786	0.790	0.780	0.787	0.760	0.764	0.752	0.755	0.766
Ca	0.816	0.640	0.676	0.656	0.665	0.592	0.596	0.625	0.656	0.655	0.656	0.620	0.707	0.644	0.663	0.643	0.669	0.654	0.696	0.698	0.681	0.676	0.638
Na	0.104	0.086	0.100	0.086	0.081	0.090	0.094	0.098	0.093	0.095	0.100	0.091	0.115	0.100	0.101	0.099	0.101	0.104	0.106	0.106	0.108	0.110	0.102
Sum	4.029	4.023	4.013	4.017	4.018	3.998	4.001	4.005	4.016	4.015	4.016	4.016	4.024	4.020	4.017	4.009	4.017	4.018	4.027	4.029	4.023	4.023	4.009

Table B.9.: Major and trace element data of cpx
 b.d.: below detection limit, iso: isotope analysis available in Table B.22., empty fields: not measured, Fe³⁺ by moessbauer spectroscopy

Sample Comment	Miringa Biu	Kerang Jos +gnt, S	Pidong Jos	Mir Biu	Mir Biu	Gumya Biu	Mir Biu +gnt	Tila Biu	Miringa Biu	Miringa Biu	Wiga Biu	Miringa Biu	Mir Biu	Maldau Biu	Mir Biu +apa, S, plag, melt	Miringa Biu	Miringa Biu	Miringa Biu
SiO₂ [wt%]	47.58	47.27	47.99	47.95	48.03	45.52	48.30	47.66	46.85	46.83	46.71	45.47	45.40	45.39	45.57	45.65	45.13	45.15
TiO₂	1.00	1.04	1.43	0.98	0.99	1.64	1.00	1.22	1.29	1.24	2.02	1.79	1.89	2.00	1.77	1.65	1.74	1.78
Al₂O₃	8.94	9.61	9.36	10.03	10.00	9.30	10.00	10.10	9.49	9.85	10.37	10.48	11.53	11.73	10.83	9.86	9.98	10.15
Cr₂O₃	b.d.	0.035	b.d.	b.d.	b.d.	0.011	b.d.	0.013	b.d.	0.011	b.d.	b.d.	b.d.	b.d.	b.d.	b.d.	b.d.	b.d.
FeO	7.66	7.84	7.53	7.69	7.77	7.98	7.93	8.00	8.26	8.23	8.64	10.05	10.24	10.44	10.75	10.89	10.92	10.96
MnO	0.135	0.144	0.115	0.145	0.144	0.145	0.143	0.145	0.130	0.132	0.149	0.113	0.134	0.143	0.141	0.151	0.138	0.136
MgO	13.19	13.46	12.81	12.98	13.00	13.26	13.06	13.15	12.13	12.07	11.92	9.07	8.89	8.88	8.95	9.02	8.98	8.96
CaO	17.38	16.50	17.79	17.25	17.06	16.98	17.02	17.29	17.53	17.40	17.58	17.92	17.89	18.10	17.80	18.06	17.97	17.87
NiO	0.024	0.029	0.016	0.028	0.021	0.019	0.028	0.031	0.016	0.033	b.d.	b.d.	0.007	b.d.	b.d.	0.011	b.d.	0.012
Na₂O	1.46	1.45	1.75	1.63	1.59	1.53	1.47	1.52	1.59	1.65	1.83	2.39	2.44	2.39	2.31	2.24	2.18	2.18
Sum	97.40	97.37	98.81	98.71	98.62	96.39	98.99	99.15	97.30	97.47	99.24	97.33	98.46	99.10	98.16	97.55	97.08	97.21
mg#	75.4	75.4	75.2	75.1	74.9	74.8	74.6	74.6	72.4	72.3	71.1	61.7	60.8	60.3	59.7	59.6	59.4	59.3
Cations to 4 oxygens																		
Si	1.798	1.784	1.789	1.785	1.789	1.748	1.792	1.771	1.780	1.775	1.745	1.751	1.729	1.720	1.744	1.762	1.751	1.749
Ti	0.028	0.030	0.040	0.028	0.028	0.047	0.028	0.034	0.037	0.035	0.057	0.052	0.054	0.057	0.051	0.048	0.051	0.052
Al	0.398	0.427	0.411	0.440	0.439	0.421	0.437	0.442	0.425	0.440	0.457	0.476	0.517	0.524	0.489	0.448	0.457	0.463
Fe²⁺	0.242	0.247	0.235	0.239	0.242	0.256	0.246	0.249	0.262	0.261	0.270	0.324	0.326	0.331	0.344	0.351	0.354	0.355
Fe³⁺																		
Mn	0.004	0.005	0.004	0.005	0.005	0.005	0.005	0.005	0.004	0.004	0.005	0.004	0.004	0.005	0.005	0.005	0.005	0.004
Mg	0.743	0.757	0.712	0.720	0.722	0.759	0.722	0.728	0.687	0.682	0.664	0.521	0.505	0.501	0.511	0.519	0.520	0.517
Ca	0.704	0.667	0.710	0.688	0.681	0.699	0.676	0.688	0.714	0.707	0.704	0.740	0.730	0.735	0.730	0.747	0.747	0.742
Na	0.107	0.106	0.126	0.118	0.115	0.114	0.106	0.109	0.117	0.121	0.133	0.178	0.180	0.176	0.171	0.168	0.164	0.164
Sum	4.025	4.023	4.027	4.024	4.020	4.049	4.012	4.026	4.027	4.027	4.034	4.045	4.045	4.047	4.044	4.047	4.048	4.047

Table B.10.: Major and trace element analyses of garnet
 b.d.: below detection limit, iso: isotope analysis available in Table B.22., empty fields: not measured, Fe³⁺ by moessbauer spectroscopy

Sample Comment	Mir 37e Biu	Mir 37f Biu	Ker GB Jos	Mir 21 Biu +cpx	Mir 23 Biu +cpx	Mir 37h Biu	Mir 1 Biu	Ker GA Jos	Mir 37g Biu	Schliff 5 Biu	Mir+Grt Biu +cpx iso	Schliff 1 Biu	Mir 2 Biu	Schliff 2 Biu	Mir 13 Biu	Dam 45-14 Biu	Mir 37i Biu	Damknolle Biu +cpx	Mir Biu	Mir Biu	Mir Biu	Mir Biu	Kerang Jos	Kerang Jos
SiO₂ [wt%]	41.37	41.27	41.65	41.38	41.19	40.89	41.72	41.30	40.93	40.74	40.96	41.18	41.23	41.12	40.73	40.34	40.24	39.73	41.55	41.29	41.17	41.16	41.29	41.40
TiO₂	0.371	0.299	0.384	0.361	0.420	0.380	0.403	0.405	0.373	0.438	0.326	0.444	0.396	0.478	0.469	0.399	0.510	0.361	0.391	0.113	0.110	0.117	0.332	0.369
Al₂O₃	23.55	23.55	23.64	23.76	23.63	23.51	23.65	23.57	23.43	22.91	23.40	23.40	23.39	23.27	23.30	22.78	22.85	22.56	23.64	23.93	23.81	23.81	23.70	23.56
Cr₂O₃	0.098	0.098	0.098	0.098	0.098	0.098	0.098	0.098	0.098	0.098	0.098	0.098	0.098	0.098	0.098	0.098	0.098	0.098	0.081	0.195	0.185	0.188	0.076	0.069
FeO	9.26	10.32	10.16	10.23	10.62	11.25	11.06	11.34	11.71	11.91	12.13	12.82	12.86	13.09	13.66	14.45	15.65	19.34	9.47	9.39	9.55	9.53	9.72	9.76
MnO	0.312	0.324	0.318	0.330	0.338	0.327	0.353	0.342	0.349	0.353	0.359	0.373	0.370	0.393	0.375	0.387	0.409	0.552	0.32	0.29	0.30	0.30	0.31	0.32
MgO	19.58	18.93	18.57	18.57	18.12	18.06	17.54	17.57	17.75	17.43	17.11	16.34	16.28	15.98	15.74	15.21	14.46	10.73	19.46	19.09	19.23	19.07	19.15	19.12
CaO	5.21	5.21	5.15	5.20	5.38	5.43	5.52	5.59	5.47	5.27	5.76	5.76	5.76	5.72	6.02	6.36	6.19	7.31	5.19	4.79	4.82	4.90	5.05	5.17
Na₂O	0.030	0.030	0.026	0.021	0.025	0.021	0.027	0.033	0.022	0.036	0.031	0.035	0.034	0.036	0.034	0.036	0.047	0.056	0.022	0.031	0.026	0.019	0.031	0.032
Sum	99.81	100.00	100.03	99.92	99.77	99.90	100.30	100.16	100.06	99.14	100.12	100.37	100.33	100.11	100.36	100.00	100.41	100.71	100.16	99.14	99.22	99.12	99.68	99.82
mg#	79.0	76.6	77.4	76.4	76.2	74.1	74.7	73.4	73.0	72.3	72.6	69.4	70.4	68.5	68.4	65.2	62.2	51.0	78.5	78.4	78.2	78.1	77.8	77.7
Cations to 8 oxygens																								
Si	2.957	2.958	2.978	2.964	2.963	2.949	2.988	2.970	2.953	2.969	2.961	2.977	2.981	2.983	2.960	2.960	2.956	2.970	2.961	2.966	2.959	2.962	2.959	2.964
Ti	0.020	0.016	0.021	0.019	0.023	0.021	0.022	0.022	0.020	0.024	0.018	0.024	0.022	0.026	0.026	0.022	0.028	0.020	0.021	0.006	0.006	0.006	0.018	0.020
Al	1.984	1.990	1.992	2.006	2.003	1.998	1.997	1.997	1.992	1.968	1.993	1.993	1.993	1.990	1.996	1.970	1.978	1.987	1.986	2.026	2.017	2.019	2.001	1.987
Fe²⁺	0.553	0.619	0.578	0.613	0.605	0.678	0.633	0.682	0.706	0.726	0.697	0.775	0.738	0.794	0.789	0.887	0.961	1.148	0.564	0.564	0.574	0.573	0.582	0.584
Fe³⁺			0.029		0.034		0.030				0.037		0.040		0.042			0.062						
Mn	0.019	0.020	0.019	0.020	0.021	0.020	0.021	0.021	0.021	0.022	0.022	0.023	0.023	0.024	0.023	0.024	0.025	0.035	0.019	0.018	0.018	0.018	0.019	0.019
Mg	2.085	2.022	1.979	1.983	1.942	1.941	1.872	1.883	1.908	1.893	1.843	1.760	1.754	1.728	1.705	1.663	1.583	1.195	2.066	2.044	2.060	2.045	2.045	2.040
Ca	0.399	0.400	0.394	0.399	0.414	0.420	0.423	0.430	0.423	0.412	0.446	0.446	0.446	0.444	0.469	0.500	0.487	0.585	0.396	0.368	0.371	0.378	0.388	0.396
Na	0.004	0.004	0.004	0.003	0.004	0.003	0.004	0.005	0.003	0.005	0.004	0.005	0.005	0.005	0.005	0.005	0.007	0.008	0.003	0.004	0.004	0.003	0.004	0.004
Sum	8.021	8.029	7.995	8.007	8.009	8.030	7.989	8.009	8.026	8.019	8.021	8.002	8.001	7.994	8.014	8.031	8.025	8.010	8.016	7.997	8.009	8.005	8.016	8.016
Ba [ppm]	b.d.	b.d.	0.109	0.046	b.d.	b.d.	0.105	b.d.	b.d.	b.d.	0.076	b.d.	0.132	b.d.	0.012	b.d.	b.d.	0.014						
Nb	b.d.	0.058	0.067	0.082	0.133	0.066	0.163	0.059	0.094	0.053	0.061	0.062	0.044	0.047	0.134	0.096	0.079	0.138						
K	5.51	4.39	b.d.	b.d.	b.d.	5.00	b.d.	b.d.	3.35	b.d.	b.d.	b.d.	b.d.	b.d.	b.d.	b.d.	b.d.	b.d.						
La	0.028	0.029	0.010	0.020	0.032	0.023	0.035	b.d.	b.d.	0.029	0.013	b.d.	b.d.	b.d.	0.013	0.029	b.d.	0.044						
Ce	0.128	0.088	0.214	0.191	0.243	0.182	0.230	0.168	0.169	0.172	0.161	0.252	0.102	0.233	0.203	0.168	0.157	0.657						
Pr	0.056	0.049	0.042	0.079	0.069	0.082	0.105	0.094	0.079	0.078	0.081	0.121	0.046	0.087	0.117	0.179	0.120	0.289						
Sr	0.233	0.294	0.108	0.126	0.123	0.332	0.133	0.112	0.278	0.117	0.117	0.187	0.124	0.208	0.141	b.d.	0.408	0.325						
Nd	0.850	0.608	0.690	0.754	1.01	0.933	0.865	0.958	0.813	1.09	0.934	1.16	0.855	1.13	1.00	1.06	1.24	3.70						
Zr	47.1	30.7	21.2	22.8	28.0	38.4	25.8	24.3	38.2	23.9	19.2	28.3	19.4	27.7	27.4	25.6	57.3	41.0						
Sm	1.02	0.922	0.944	0.927	0.862	0.880	1.17	1.21	0.885	0.964	1.07	1.25	1.16	1.56	1.41	1.26	1.75	4.75						
Eu	0.535	0.515	0.557	0.553	0.528	0.643	0.707	0.682	0.708	0.746	0.695	0.900	0.729	1.01	0.874	0.747	1.16	3.25						
Ti	2224	1792	2303	2165	2519	2278	2417	2430	2236	2626	1956	2663	2377	2863	2812	2392	3057	2163						
Gd	2.54	2.86	2.81	3.27	3.26	3.40	3.20	4.27	3.52	3.57	3.85	4.34	3.86	4.90	5.08	4.69	5.40	15.4						
Tb	0.654	0.720	0.841	0.801	0.807	0.951	1.060	0.979	0.906	1.00	0.865	1.26	0.843	1.29	1.18	1.07	1.57	3.57						
Dy	7.06	7.44	7.14	7.37	7.99	8.74	7.73	9.12	8.54	8.30	8.75	9.83	8.70	11.3	10.4	10.2	13.6	23.9						
Ho	1.69	1.95	1.87	2.33	1.91	2.24	2.22	2.33	2.32	2.07	2.32	2.43	2.24	3.09	2.45	2.63	3.28	4.43						
Y	53.0	54.2	52.7	52.9	56.0	61.1	56.3	58.0	61.6	58.8	61.3	65.4	63.6	72.8	65.6	67.0	87.3	111.0						
Er	7.37	7.55	7.08	6.80	7.31	8.13	7.12	7.60	8.30	7.58	8.08	8.05	7.61	9.27	8.63	8.78	9.73	9.49						
Tm	1.45	1.37	1.28	1.31	1.38	1.38	1.14	1.27	1.46	1.30	1.36	1.24	1.27	1.44	1.38	1.38	1.39	1.12						
Yb	10.3	11.7	10.1	11.7	9.51	11.5	8.85	10.9	12.8	8.24	13.0	9.60	7.76	8.86	12.8	10.3	6.52	5.12						
Lu	1.57	1.87	1.79	2.07	1.45	1.55	1.25	1.78	1.98	0.974	2.32	1.56	0.716	1.22	2.33	1.60	0.746	0.469						

Table B.10.: Major and trace element analyses of garnetb.d.: below detection limit, iso: isotope analysis available in Table B.22., empty fields: not measured, Fe³⁺ by moessbauer spectroscopy

Sample	Mir	Kerang	Mir	Kerang	Kerang	Kerang	Kerang	Mir	Mir	Mir	Mir	Gufka	Mir	Kerang	Mir	Kerang	Kerang	Mir	Gufka	Kerang	Kerang	Mir	Mir	Kerang
Comment	Biu	Jos	Biu	Jos	Jos	Jos	Jos	Biu	Biu	Biu	Biu	Biu	Biu	Jos	Biu	Jos	Jos	Biu	Biu	Jos	Jos	Biu	Biu	Jos
															+cpx			+cpx, S						
SiO₂ [wt%]	41.61	41.15	41.42	41.34	41.43	41.17	41.66	41.28	41.33	41.55	40.81	41.41	41.31	41.15	41.07	41.33	41.00	41.20	41.35	40.98	41.24	41.55	41.34	41.52
TiO₂	0.314	0.389	0.323	0.336	0.326	0.400	0.352	0.384	0.349	0.341	0.385	0.343	0.417	0.323	0.349	0.328	0.400	0.427	0.381	0.394	0.327	0.340	0.350	0.322
Al₂O₃	23.68	23.52	23.35	23.66	23.77	23.57	23.41	23.44	23.37	23.63	23.58	23.40	23.36	23.46	23.13	23.48	23.09	23.37	23.46	23.17	23.34	23.52	23.40	23.52
Cr₂O₃	0.055	0.104	0.539	0.039	0.021	0.094	0.049	0.031	0.053	0.053	0.018	0.056	0.026	0.027	0.041	0.015	0.018	0.018		0.020	0.015	0.064	0.011	0.019
FeO	9.82	9.77	9.90	9.77	9.85	10.00	10.06	10.11	10.19	10.27	10.15	10.54	10.49	10.44	10.62	10.61	10.62	10.62	10.75	10.70	10.64	10.85	10.78	10.91
MnO	0.33	0.33	0.32	0.33	0.33	0.34	0.33	0.32	0.33	0.32	0.35	0.32	0.33	0.34	0.33	0.34	0.33	0.33	0.34	0.34	0.36	0.32	0.32	0.34
MgO	19.14	19.00	19.25	18.96	18.98	18.82	18.94	18.92	18.98	18.92	18.57	18.84	18.72	18.47	18.66	18.49	18.47	18.44	18.58	18.43	18.26	18.60	18.42	18.48
CaO	5.36	5.26	4.94	5.28	5.22	5.20	5.38	5.31	5.33	5.22	5.22	5.21	5.45	5.21	5.20	5.37	5.39	5.45	5.41	5.37	5.55	5.18	5.45	5.24
Na₂O	0.024	0.033	0.034	0.031	0.024	0.035	0.032	0.032	0.030	0.030	0.029	0.034	0.019	0.028	0.032	0.027	0.045	0.030	0.026	0.030	0.025	0.031	0.016	0.032
Sum	100.37	99.58	100.09	99.77	99.97	99.66	100.22	99.84	100.00	100.36	99.14	100.17	100.15	99.46	99.45	100.02	99.39	99.91	100.30	99.49	99.78	100.47	100.12	100.41
mg#	77.6	77.6	77.6	77.6	77.4	77.0	77.0	76.9	76.8	76.7	76.5	76.1	76.1	75.9	75.8	75.6	75.6	75.6	75.5	75.4	75.4	75.3	75.3	75.1
Cations to 8 oxygens																								
Si	2.964	2.956	2.961	2.962	2.962	2.957	2.975	2.961	2.962	2.965	2.949	2.965	2.961	2.966	2.965	2.966	2.964	2.961	2.961	2.960	2.969	2.969	2.966	2.970
Ti	0.017	0.021	0.017	0.018	0.018	0.022	0.019	0.021	0.019	0.018	0.021	0.018	0.022	0.018	0.019	0.018	0.022	0.023	0.021	0.021	0.018	0.018	0.019	0.017
Al	1.988	1.991	1.968	1.998	2.002	1.995	1.971	1.982	1.974	1.988	2.008	1.975	1.973	1.993	1.968	1.986	1.967	1.980	1.980	1.973	1.980	1.981	1.979	1.983
Fe²⁺	0.585	0.587	0.592	0.585	0.589	0.600	0.601	0.607	0.611	0.613	0.614	0.631	0.629	0.629	0.641	0.637	0.642	0.638	0.644	0.646	0.641	0.648	0.647	0.625
Fe³⁺																								0.028
Mn	0.020	0.020	0.020	0.020	0.020	0.020	0.020	0.019	0.020	0.019	0.021	0.019	0.020	0.020	0.020	0.020	0.020	0.020	0.020	0.021	0.022	0.019	0.019	0.021
Mg	2.032	2.034	2.051	2.025	2.022	2.015	2.016	2.023	2.027	2.013	2.001	2.011	2.000	1.984	2.008	1.978	1.990	1.976	1.983	1.984	1.959	1.981	1.970	1.971
Ca	0.409	0.405	0.378	0.406	0.399	0.400	0.411	0.408	0.409	0.399	0.404	0.400	0.419	0.402	0.402	0.413	0.417	0.420	0.415	0.416	0.428	0.397	0.419	0.401
Na	0.003	0.005	0.005	0.004	0.003	0.005	0.004	0.004	0.004	0.004	0.004	0.005	0.003	0.004	0.004	0.004	0.006	0.004	0.004	0.004	0.003	0.004	0.002	0.004
Sum	8.018	8.017	7.993	8.018	8.016	8.015	8.017	8.026	8.025	8.018	8.023	8.024	8.027	8.017	8.028	8.020	8.028	8.022	8.028	8.025	8.020	8.017	8.021	8.019

Table B.10.: Major and trace element analyses of garnetb.d.: below detection limit, iso: isotope analysis available in Table B.22., empty fields: not measured, Fe³⁺ by moessbauer spectroscopy

Sample	Mir	Kerang	Mir	Maldau	Mir	Mir	Kerang	Kerang	Kerang	Kerang	Mir	Mir	Mir	Dam	Mir	Kerang	Mir	Mir	Kerang	Kerang	Mir	Mir	Kerang	Mir
Comment	Biu	Jos	Biu	Biu	Biu	Biu	Jos	Jos	Jos	Jos	Biu	Biu	Biu	Biu	Biu	Jos	Biu	Biu	Jos	Jos	Biu	Biu	Jos	Biu
SiO₂ [wt%]	41.11	40.94	41.40	41.12	40.75	41.22	41.05	40.99	41.06	41.05	41.06	41.25	41.22	41.30	40.95	41.13	41.08	40.85	41.48	40.64	41.03	40.59	40.95	40.81
TiO₂	0.367	0.433	0.345	0.405	0.356	0.399	0.338	0.414	0.404	0.377	0.346	0.382	0.385	0.404	0.393	0.411	0.363	0.313	0.369	0.372	0.311	0.329	0.366	0.315
Al₂O₃	23.22	23.61	23.47	23.25	23.48	23.51	23.28	23.49	23.51	23.50	23.50	23.41	23.47	23.34	23.16	23.48	23.51	23.49	23.38	23.55	23.22	23.51	23.43	23.50
Cr₂O₃		0.025	0.015	0.014	0.017	0.014		0.015	0.011	0.012	0.031	0.021	0.011	0.032	0.023	0.012	0.016	0.028		0.023	0.021	0.034	0.011	0.014
FeO	10.86	10.85	11.04	10.95	10.93	11.03	10.96	10.97	11.01	11.03	11.18	11.19	11.17	11.20	11.16	11.17	11.32	11.37	11.46	11.38	11.42	11.45	11.50	11.51
MnO	0.34	0.34	0.34	0.34	0.34	0.33	0.34	0.34	0.34	0.34	0.33	0.37	0.34	0.34	0.37	0.35	0.35	0.33	0.35	0.35	0.34	0.33	0.35	0.34
MgO	18.30	18.21	18.39	18.24	18.14	18.27	18.14	18.12	18.03	18.05	18.24	18.17	18.09	18.12	18.02	17.98	18.16	18.03	18.03	17.86	17.88	17.84	17.81	17.66
CaO	5.43	5.33	5.25	5.47	5.05	5.49	5.42	5.45	5.40	5.36	5.30	5.42	5.45	5.40	5.52	5.35	5.37	5.29	5.36	5.57	5.39	5.09	5.40	5.22
Na₂O	0.026	0.031	0.029	0.035	0.031	0.029	0.043	0.030	0.031	0.039	0.030	0.034	0.027	0.029	0.030	0.035	0.032	0.032	0.031	0.032	0.025	0.033	0.028	0.024
Sum	99.70	99.80	100.31	99.88	99.11	100.33	99.59	99.83	99.80	99.77	100.06	100.27	100.20	100.19	99.67	99.94	100.23	99.77	100.50	99.81	99.68	99.23	99.88	99.42
mg#	75.0	74.9	74.8	74.8	74.7	74.7	74.7	74.6	74.5	74.5	74.4	74.3	74.3	74.3	74.2	74.2	74.1	73.9	73.7	73.7	73.6	73.5	73.4	73.2
Cations to 8 oxygens																								
Si	2.965	2.949	2.967	2.962	2.955	2.956	2.965	2.954	2.959	2.959	2.954	2.962	2.961	2.967	2.961	2.962	2.953	2.950	2.973	2.938	2.967	2.948	2.956	2.958
Ti	0.020	0.023	0.019	0.022	0.019	0.022	0.018	0.022	0.022	0.020	0.019	0.021	0.021	0.022	0.021	0.022	0.020	0.017	0.020	0.020	0.017	0.018	0.020	0.017
Al	1.974	2.004	1.982	1.974	2.006	1.987	1.982	1.995	1.997	1.997	1.993	1.981	1.987	1.976	1.973	1.993	1.992	2.000	1.975	2.007	1.979	2.012	1.994	2.008
Fe²⁺	0.655	0.654	0.632	0.660	0.663	0.662	0.662	0.661	0.663	0.665	0.672	0.672	0.671	0.673	0.675	0.673	0.680	0.687	0.687	0.688	0.691	0.695	0.694	0.698
Fe³⁺			0.030																					
Mn	0.021	0.021	0.021	0.021	0.021	0.020	0.021	0.021	0.021	0.021	0.020	0.022	0.021	0.021	0.023	0.021	0.021	0.020	0.021	0.022	0.021	0.021	0.022	0.021
Mg	1.967	1.955	1.964	1.959	1.960	1.953	1.953	1.946	1.937	1.940	1.956	1.945	1.937	1.941	1.942	1.930	1.946	1.941	1.926	1.925	1.927	1.931	1.916	1.908
Ca	0.420	0.411	0.403	0.422	0.392	0.422	0.419	0.420	0.417	0.414	0.409	0.417	0.419	0.415	0.428	0.413	0.414	0.409	0.412	0.431	0.418	0.396	0.418	0.405
Na	0.004	0.004	0.004	0.005	0.004	0.004	0.006	0.004	0.004	0.004	0.005	0.004	0.005	0.004	0.004	0.005	0.004	0.004	0.004	0.005	0.004	0.005	0.004	0.003
Sum	8.024	8.022	8.021	8.025	8.021	8.026	8.026	8.024	8.019	8.022	8.026	8.024	8.022	8.019	8.027	8.018	8.029	8.028	8.018	8.036	8.022	8.025	8.024	8.018

Table B.10.: Major and trace element analyses of garnet
 b.d.: below detection limit, iso: isotope analysis available in Table B.22., empty fields: not measured, Fe³⁺ by moessbauer spectroscopy

Sample	Mir	Mir	Kerang	Kerang	Mir	Mir	Mir	Mir	Maldau	Mir	Krater	Kerang	Dam	Mir	Hilia	Kerang	Mir	Kerang	Mir	Mir	Kerang	Kerang	Krater	Kerang
Comment	Biu	Biu	Jos	Jos	Biu	Biu	Biu	Biu	Biu	Biu	Biu	Jos	Biu	Biu	Biu	Jos	Biu	Jos	Biu	Biu	Jos	Jos	Biu	Jos
		+cpx												+cpx, opx					+cpx					
SiO₂ [wt%]	41.10	41.53	40.86	41.36	41.34	40.79	40.97	41.09	40.88	40.93	41.23	41.24	40.92	40.68	41.02	41.44	40.85	41.06	40.72	40.24	40.82	40.83	41.00	40.91
TiO₂	0.325	0.312	0.439	0.423	0.344	0.397	0.339	0.368	0.430	0.336	0.336	0.437	0.325	0.330	0.364	0.424	0.343	0.385	0.384	0.347	0.454	0.421	0.348	0.452
Al₂O₃	23.29	24.17	23.49	23.08	23.44	23.24	23.56	23.24	23.22	23.59	23.33	22.91	23.18	23.66	23.27	23.41	23.36	23.14	22.97	23.29	23.46	23.29	23.29	23.27
Cr₂O₃	0.010	0.040	0.011		0.013	0.019	0.018	0.010			0.028	0.010	0.036	0.015	0.010								0.025	
FeO	11.61	11.67	11.61	11.65	11.79	11.72	11.83	11.80	11.78	11.84	11.86	11.83	11.93	11.87	11.89	12.09	11.97	12.16	12.21	12.27	12.30	12.32	12.41	12.60
MnO	0.35	0.33	0.36	0.37	0.35	0.35	0.35	0.35	0.36	0.35	0.36	0.37	0.37	0.35	0.36	0.36	0.37	0.37	0.36	0.37	0.38	0.36	0.37	0.38
MgO	17.79	17.86	17.75	17.73	17.92	17.70	17.81	17.62	17.57	17.60	17.58	17.49	17.55	17.43	17.46	17.56	17.28	17.42	17.31	17.23	17.12	17.09	17.04	17.16
CaO	5.44	5.17	5.48	5.55	5.32	5.55	5.46	5.61	5.68	5.61	5.62	5.72	5.33	5.26	5.67	5.62	5.53	5.62	5.60	5.56	5.47	5.79	5.68	5.61
Na₂O	0.026	0.033	0.028	0.025	0.031	0.027	0.030	0.019	0.036	0.023	0.040	0.038	0.033	0.032	0.032	0.038	0.037	0.024	0.027	0.029	0.033	0.037	0.018	0.032
Sum	99.96	101.11	100.05	100.22	100.58	99.81	100.39	100.12	99.99	100.33	100.40	100.06	99.70	99.66	100.11	100.97	99.76	100.21	99.61	99.37	100.06	100.16	100.22	100.43
mg#	73.2	73.2	73.2	73.1	73.0	72.9	72.9	72.7	72.7	72.6	72.5	72.5	72.4	72.4	72.4	72.1	72.0	71.9	71.7	71.5	71.3	71.2	71.0	70.8
Cations to 8 oxygens																								
Si	2.966	2.957	2.948	2.978	2.966	2.953	2.948	2.965	2.956	2.948	2.967	2.979	2.965	2.948	2.962	2.967	2.960	2.965	2.961	2.936	2.953	2.955	2.964	2.955
Ti	0.018	0.017	0.024	0.023	0.019	0.022	0.018	0.020	0.023	0.018	0.018	0.024	0.018	0.018	0.020	0.023	0.019	0.021	0.021	0.019	0.025	0.023	0.019	0.025
Al	1.981	2.028	1.997	1.958	1.982	1.982	1.998	1.976	1.979	2.003	1.979	1.950	1.980	2.020	1.981	1.975	1.995	1.970	1.969	2.002	2.000	1.986	1.984	1.980
Fe²⁺	0.701	0.695	0.701	0.701	0.675	0.710	0.712	0.712	0.712	0.713	0.714	0.715	0.723	0.719	0.718	0.724	0.726	0.734	0.742	0.749	0.744	0.746	0.750	0.761
Fe³⁺					0.033																			
Mn	0.022	0.020	0.022	0.022	0.021	0.021	0.021	0.021	0.022	0.022	0.022	0.022	0.023	0.022	0.022	0.022	0.022	0.023	0.022	0.023	0.023	0.022	0.023	0.023
Mg	1.914	1.895	1.909	1.902	1.916	1.909	1.910	1.895	1.893	1.890	1.886	1.883	1.896	1.883	1.879	1.874	1.867	1.875	1.877	1.874	1.846	1.843	1.836	1.847
Ca	0.421	0.394	0.423	0.428	0.409	0.431	0.421	0.434	0.440	0.433	0.433	0.442	0.414	0.408	0.439	0.431	0.429	0.435	0.437	0.434	0.424	0.449	0.440	0.434
Na	0.004	0.005	0.004	0.003	0.004	0.004	0.004	0.003	0.005	0.003	0.006	0.005	0.005	0.004	0.004	0.005	0.005	0.003	0.004	0.004	0.005	0.005	0.003	0.004
Sum	8.025	8.009	8.028	8.017	8.023	8.031	8.032	8.025	8.030	8.029	8.025	8.021	8.023	8.022	8.026	8.022	8.024	8.027	8.032	8.041	8.020	8.028	8.019	8.029

Table B.10.: Major and trace element analyses of garnet
 b.d.: below detection limit, iso: isotope analysis available in Table B.22., empty fields: not measured, Fe³⁺ by moessbauer spectroscopy

Sample	Kerang	Mir	Dam	Mir	Mir	Kerang	Dam	Kerang	Kerang	Mir	Mir	Mir	Mir	Mir	Mir	Kerang	Mir	Mir	Mir
Comment	Jos	Biu +cpx	Biu	Biu	Biu +S	Jos	Biu	Jos	Jos	Biu	Biu	Biu	Biu	Biu	Biu	Jos	Biu	Biu +apa, ilm	Biu xenolith cpx exsol.
SiO₂ [wt%]	40.72	41.07	41.21	40.86	40.64	40.63	40.71	40.56	40.65	40.29	40.56	40.74	40.19	40.76	40.17	40.80	39.82	39.61	40.25
TiO₂	0.445	0.329	0.289	0.368	0.413	0.484	0.423	0.480	0.500	0.473	0.605	0.393	0.464	0.426	0.378	0.491	0.551	0.359	0.142
Al₂O₃	23.42	23.91	23.31	23.26	23.27	23.30	23.13	23.19	23.21	23.22	22.86	23.12	23.03	23.23	22.96	23.11	22.55	23.01	22.96
Cr₂O₃	0.012	0.011	0.023			0.034	0.030	0.014	0.031		0.041		0.013						
FeO	12.56	12.54	12.71	12.61	12.73	12.96	12.95	13.09	13.24	13.25	13.25	13.30	13.29	13.49	13.57	13.80	15.65	20.19	12.99
MnO	0.36	0.35	0.37	0.36	0.37	0.37	0.38	0.39	0.38	0.38	0.37	0.37	0.38	0.38	0.39	0.40	0.42	0.62	0.54
MgO	16.99	16.80	17.00	16.83	16.90	16.56	16.54	16.48	16.54	16.50	16.43	16.27	16.03	16.19	16.04	16.07	14.38	10.06	16.04
CaO	5.41	5.67	5.49	5.77	5.70	5.75	5.82	5.69	5.71	5.78	5.64	5.93	5.79	5.92	5.91	5.80	6.40	7.53	5.59
Na₂O	0.044	0.025	0.023	0.036	0.037	0.040	0.039	0.047	0.030	0.040	0.040	0.028	0.040	0.039	0.028	0.052	0.036	0.059	0.027
Sum	99.99	100.72	100.44	100.12	100.08	100.16	100.07	99.96	100.31	99.96	99.82	100.16	99.24	100.46	99.47	100.55	99.84	101.51	98.57
mg#	70.7	70.5	70.4	70.4	70.3	69.5	69.5	69.2	69.0	68.9	68.8	68.6	68.3	68.1	67.8	67.5	62.1	47.0	68.7
Cations to 8 oxygens																			
Si	2.951	2.953	2.974	2.961	2.949	2.949	2.958	2.952	2.950	2.937	2.958	2.962	2.951	2.957	2.948	2.961	2.946	2.950	2.970
Ti	0.024	0.018	0.016	0.020	0.023	0.026	0.023	0.026	0.027	0.026	0.033	0.021	0.026	0.023	0.021	0.027	0.031	0.020	0.008
Al	2.001	2.027	1.982	1.987	1.990	1.994	1.981	1.989	1.985	1.995	1.965	1.981	1.993	1.987	1.987	1.977	1.967	2.019	1.998
Fe²⁺	0.762	0.754	0.736	0.764	0.773	0.787	0.787	0.797	0.803	0.808	0.809	0.809	0.816	0.818	0.833	0.837	0.969	1.258	0.802
Fe³⁺			0.031																
Mn	0.022	0.021	0.022	0.022	0.023	0.023	0.023	0.024	0.023	0.023	0.023	0.023	0.023	0.023	0.024	0.025	0.026	0.039	0.034
Mg	1.836	1.801	1.828	1.818	1.827	1.792	1.791	1.788	1.789	1.793	1.787	1.763	1.755	1.751	1.755	1.738	1.586	1.117	1.764
Ca	0.420	0.437	0.424	0.448	0.443	0.448	0.453	0.444	0.444	0.451	0.441	0.462	0.455	0.460	0.465	0.451	0.507	0.601	0.442
Na	0.006	0.003	0.003	0.005	0.005	0.006	0.005	0.007	0.004	0.006	0.006	0.004	0.006	0.006	0.004	0.007	0.005	0.009	0.004
Sum	8.023	8.013	8.017	8.024	8.033	8.024	8.022	8.026	8.025	8.039	8.021	8.026	8.025	8.025	8.037	8.023	8.037	8.013	8.021

Table B.11.: Major and trace element analyses of plagioclase

b.d.: below detection limit, iso: isotope analysis available in Table B.22.

Sample Comment	Kerang Jos	Krater Biu	Hilia Biu	Mir Biu	Mir Biu	Krater Biu	Mir Biu	Mir Biu	Gwaram Biu	Gwaram Biu	Dam Biu	Mir Biu	Hizshi Biu	Krater Biu zircon incl.
									iso					
SiO₂ [wt%]	61.81	61.55	60.35	60.83	60.96	61.27	61.02	61.86	61.84	61.31	62.16	62.14	62.44	64.48
Al₂O₃	23.45	23.63	23.41	23.06	23.28	23.43	23.40	22.91	21.81	23.24	22.65	22.96	22.37	19.66
FeO	0.17	0.19	0.19	0.18	0.17	0.20	0.18	0.18	0.202	0.20	0.16	0.18	0.17	0.06
MgO	0.019	0.019	0.024	0.020	0.026	0.020	0.022	0.017	0.015	0.015	0.010	0.017	0.025	0.012
CaO	4.25	4.28	4.39	4.39	4.37	4.40	4.34	3.93	3.977	3.88	3.68	3.52	3.41	0.91
Na₂O	7.37	7.99	8.42	8.47	8.55	8.64	8.60	7.99	8.466	8.79	8.90	8.89	8.59	6.95
K₂O	1.37	1.18	1.21	1.18	1.19	1.19	1.14	1.22	1.199	1.26	1.22	1.40	1.95	6.53
Sum	98.47	98.91	98.09	98.20	98.61	99.23	98.76	98.15	97.549	98.72	98.81	99.17	98.98	98.62
Cations to 32 oxygens														
Si	11.120	11.050	10.970	11.037	11.016	11.007	11.007	11.171	11.262	11.059	11.181	11.145	11.234	11.745
Al	4.973	5.000	5.015	4.931	4.958	4.961	4.975	4.875	4.681	4.940	4.802	4.853	4.743	4.220
Fe²⁺	0.025	0.029	0.029	0.028	0.026	0.029	0.027	0.027	0.031	0.030	0.024	0.027	0.026	0.009
Mg	0.005	0.005	0.007	0.005	0.007	0.005	0.006	0.005	0.004	0.004	0.003	0.005	0.007	0.003
Ca	0.820	0.824	0.855	0.854	0.846	0.847	0.839	0.760	0.776	0.750	0.709	0.676	0.657	0.178
Na	2.570	2.780	2.968	2.980	2.996	3.009	3.008	2.799	2.989	3.074	3.104	3.092	2.997	2.455
K	0.314	0.271	0.281	0.274	0.273	0.273	0.262	0.280	0.278	0.290	0.280	0.320	0.448	1.518
Sum	19.832	19.967	20.138	20.116	20.131	20.143	20.131	19.926	20.027	20.150	20.106	20.127	20.115	20.131
Or	8.5	7.0	6.8	6.7	6.6	6.6	6.4	7.3	6.9	7.0	6.8	7.8	10.9	36.6
Ab	69.4	71.7	72.3	72.5	72.8	72.9	73.2	72.9	73.9	74.7	75.8	75.6	73.1	59.1
An	22.1	21.3	20.8	20.8	20.6	20.5	20.4	19.8	19.2	18.2	17.3	16.5	16.0	4.3

Table B.12.: Major element analyses of ilmenite
*Fe₂O₃ from stoichiometry

Sample	Mir	Mir	Mir	Bos Hill	Bos Hill	Miringa	Dam	Dam	Miringa	Mir	Mir	Miringa	Miringa	Damknolle	Mir	Miringa	Mir
Comment	Biu	Biu	Biu	Biu	Biu	Biu	Biu	Biu	Biu	Biu	Biu	Biu	Biu	Biu	Biu	Biu	Biu
		pyroxenite +sp	pyroxenite +cpx	exsol. in cpx	exsol. in cpx							+glas incl.	+glas incl.				
SiO₂ [wt%]	0.018	0.114	0.239	0.038	0.052	0.028	0.028	0.031	0.033	0.032	0.029	0.033	0.035	0.035	0.023	0.035	0.033
TiO₂	50.51	46.86	46.55	52.68	53.03	46.92	41.16	42.61	40.53	40.42	41.09	40.25	40.48	39.67	41.14	40.03	39.75
Al₂O₃	1.05	0.96	0.97	0.15	0.13	0.90	1.48	1.22	1.48	1.62	1.59	1.48	1.54	1.59	1.58	1.51	1.66
Cr₂O₃	0.041	0.038	0.031	0.047	0.055	0.031	0.040	0.036	0.042	0.014	0.033	0.029	0.025	0.030	0.025	0.023	0.038
FeO	27.92	26.52	26.67	32.57	33.20	29.96	29.64	31.08	29.82	29.82	30.51	29.75	30.04	29.42	30.69	29.69	29.75
MnO	0.315	0.282	0.281	0.570	0.758	0.300	0.171	0.153	0.160	0.157	0.156	0.155	0.149	0.162	0.159	0.159	0.146
MgO	9.54	8.56	8.17	7.85	7.02	6.64	4.03	3.93	3.57	3.56	3.50	3.48	3.50	3.38	3.44	3.41	3.26
Fe₂O₃*	11.28	14.25	13.97	6.12	5.14	14.68	23.98	21.04	23.57	23.52	22.90	24.06	24.07	23.56	23.01	24.70	24.66
Sum	100.79	97.68	97.34	100.22	99.79	99.52	100.56	100.14	99.26	99.18	99.85	99.28	99.85	97.89	100.09	99.60	99.33
Cations to 3 oxygens																	
Si	0.000	0.003	0.006	0.001	0.001	0.001	0.001	0.001	0.001	0.001	0.001	0.001	0.001	0.001	0.001	0.001	0.001
Ti	0.886	0.854	0.852	0.942	0.955	0.853	0.757	0.787	0.757	0.756	0.763	0.753	0.753	0.752	0.763	0.747	0.744
Al	0.029	0.027	0.028	0.004	0.004	0.026	0.043	0.035	0.043	0.047	0.046	0.043	0.045	0.047	0.046	0.044	0.049
Cr	0.001	0.001	0.001	0.001	0.001	0.001	0.001	0.001	0.001	0.000	0.001	0.001	0.000	0.001	0.000	0.000	0.001
Fe²⁺	0.545	0.537	0.543	0.648	0.665	0.606	0.606	0.639	0.620	0.620	0.630	0.619	0.621	0.620	0.633	0.616	0.619
Fe³⁺	0.198	0.260	0.256	0.109	0.093	0.267	0.441	0.389	0.441	0.440	0.426	0.450	0.448	0.447	0.427	0.461	0.462
Mn	0.006	0.006	0.006	0.011	0.015	0.006	0.004	0.003	0.003	0.003	0.003	0.003	0.003	0.003	0.003	0.003	0.003
Mg	0.332	0.309	0.296	0.278	0.251	0.239	0.147	0.144	0.132	0.132	0.129	0.129	0.129	0.127	0.126	0.126	0.121
Sum	1.997	1.997	1.988	1.995	1.985	1.998	1.999	1.998	1.998	1.999	1.999	1.999	1.999	1.998	1.999	1.998	1.999
Fe₂O₃	0.101	0.133	0.131	0.055	0.047	0.136	0.226	0.199	0.226	0.226	0.218	0.231	0.230	0.230	0.219	0.236	0.237
FeTiO₃	0.556	0.548	0.558	0.655	0.677	0.616	0.621	0.652	0.635	0.637	0.647	0.634	0.637	0.637	0.649	0.632	0.636
MgTiO₃	0.338	0.315	0.304	0.281	0.255	0.244	0.150	0.147	0.136	0.135	0.132	0.132	0.132	0.130	0.130	0.129	0.124

Table B.12.: Major element analyses of ilmenite
*Fe₂O₃ from stoichiometry

Sample Comment	Miringa Biu	Miringa Biu	Miringa Biu	Mir Biu +glas incl.	Miringa Biu	Miringa Biu	Mir Biu	Dam Biu polyphase	Miringa Biu	Mir Biu	Miringa Biu	Miringa Biu +glas incl.	Miringa Biu	Miringa Biu	Krater Biu	Mir Biu	Miringa Biu +S	Miringa Biu +S
SiO₂ [wt%]	0.026	0.031	0.028	0.032	0.037	0.034	0.034	0.031	0.033	0.028	0.032	0.026	0.031	0.034	0.038	0.042	0.023	0.030
TiO₂	39.36	39.44	38.87	39.23	38.64	38.51	40.59	39.52	37.98	38.50	38.26	38.24	38.12	37.48	38.67	38.52	37.09	38.42
Al₂O₃	1.53	1.57	1.50	1.72	1.63	1.55	1.67	1.42	1.57	1.69	1.57	1.65	1.64	1.59	1.64	1.62	1.77	1.52
Cr₂O₃	0.021	0.037	0.026	0.027	0.034	0.019	0.031	0.021	0.020	0.019	0.025	0.039	0.028	0.013	0.018	0.034	0.010	0.039
FeO	29.38	29.50	29.23	29.64	29.06	29.11	30.84	30.01	28.81	29.14	29.02	29.03	28.98	28.45	29.51	29.51	28.19	29.53
MnO	0.159	0.165	0.152	0.152	0.151	0.133	0.152	0.167	0.143	0.138	0.146	0.146	0.138	0.146	0.123	0.148	0.123	0.144
MgO	3.27	3.24	3.09	3.07	3.04	3.03	3.05	3.00	2.93	2.94	2.91	2.89	2.87	2.84	2.83	2.79	2.77	2.70
Fe₂O₃*	25.77	25.33	26.31	25.71	26.76	26.79	23.94	25.64	27.73	27.36	26.98	27.11	27.22	28.75	27.98	27.00	29.32	26.88
Sum	99.53	99.35	99.23	99.62	99.41	99.18	100.33	99.85	99.23	99.86	98.98	99.17	99.06	99.35	100.85	99.70	99.33	99.32
Cations to 3 oxygens																		
Si	0.001	0.001	0.001	0.001	0.001	0.001	0.001	0.001	0.001	0.001	0.001	0.001	0.001	0.001	0.001	0.001	0.001	0.001
Ti	0.736	0.739	0.730	0.733	0.724	0.724	0.753	0.738	0.715	0.719	0.722	0.720	0.718	0.705	0.716	0.722	0.698	0.723
Al	0.045	0.046	0.044	0.050	0.048	0.046	0.048	0.042	0.046	0.050	0.046	0.049	0.048	0.047	0.048	0.048	0.052	0.045
Cr	0.000	0.001	0.001	0.001	0.001	0.000	0.001	0.000	0.000	0.000	0.000	0.001	0.001	0.000	0.000	0.001	0.000	0.001
Fe²⁺	0.611	0.614	0.611	0.616	0.606	0.609	0.636	0.624	0.603	0.605	0.609	0.608	0.607	0.595	0.608	0.615	0.590	0.618
Fe³⁺	0.482	0.475	0.495	0.481	0.502	0.504	0.444	0.479	0.522	0.511	0.509	0.511	0.513	0.541	0.519	0.506	0.552	0.506
Mn	0.003	0.003	0.003	0.003	0.003	0.003	0.003	0.004	0.003	0.003	0.003	0.003	0.003	0.003	0.003	0.003	0.003	0.003
Mg	0.121	0.120	0.115	0.114	0.113	0.113	0.112	0.111	0.109	0.109	0.109	0.108	0.107	0.106	0.104	0.104	0.103	0.101
Sum	1.999	1.999	1.999	1.999	1.998	2.000	1.999	1.999	1.999	1.998	1.999	1.999	1.999	1.999	1.998	1.999	1.998	1.999
Fe₂O₃	0.247	0.244	0.254	0.247	0.258	0.259	0.228	0.246	0.268	0.263	0.261	0.262	0.264	0.278	0.266	0.260	0.284	0.260
FeTiO₃	0.627	0.631	0.626	0.634	0.623	0.625	0.654	0.639	0.619	0.623	0.625	0.624	0.624	0.611	0.625	0.632	0.607	0.635
MgTiO₃	0.124	0.123	0.118	0.117	0.116	0.116	0.115	0.114	0.112	0.112	0.112	0.111	0.110	0.109	0.107	0.106	0.106	0.104

Table B.12.: Major element analyses of ilmenite
*Fe₂O₃ from stoichiometry

Sample Comment	Mir Biu	Mir Biu +S	Mir Biu	Miringa Biu +S	Miringa Biu +S	Miringa Biu	Mir Biu	Miringa Biu	Mir Biu	Mir Biu	Mir Biu	Mir Biu	Mir Biu	Mir Biu +S	Mir Biu	Mir Biu
SiO₂ [wt%]	0.029	0.041	0.023	0.028	0.038	0.026	0.023	0.020	0.042	0.031	0.024	0.032	0.030	0.036	0.034	0.026
TiO₂	39.48	36.45	36.05	36.13	37.59	35.81	36.74	35.86	36.36	36.16	37.01	36.36	37.63	35.78	36.51	30.62
Al₂O₃	1.88	1.79	1.74	1.69	1.86	1.68	1.79	1.66	1.77	1.77	1.98	1.74	1.75	1.49	1.71	1.33
Cr₂O₃	0.021	0.019	0.020	0.009	0.022	0.023	0.021	0.018	0.024	0.012	0.018	0.020	0.025	0.022	0.013	0.014
FeO	30.56	27.94	27.69	27.70	29.08	27.46	28.28	27.51	28.16	27.94	28.79	28.23	29.34	27.91	28.53	24.83
MnO	0.141	0.133	0.121	0.124	0.122	0.131	0.135	0.124	0.132	0.131	0.130	0.137	0.128	0.124	0.135	0.153
MgO	2.66	2.62	2.58	2.57	2.55	2.55	2.55	2.51	2.48	2.46	2.44	2.41	2.40	2.34	2.33	1.43
Fe₂O₃*	25.56	30.80	31.10	30.97	27.68	31.43	30.21	31.42	30.99	30.85	29.21	31.04	28.56	32.20	30.42	41.12
Sum	100.36	99.82	99.35	99.26	98.99	99.13	99.78	99.17	99.98	99.39	99.61	99.98	99.93	99.91	99.70	99.54
Cations to 3 oxygens																
Si	0.001	0.001	0.001	0.001	0.001	0.001	0.001	0.001	0.001	0.001	0.001	0.001	0.001	0.001	0.001	0.001
Ti	0.734	0.684	0.680	0.682	0.710	0.677	0.690	0.678	0.682	0.682	0.696	0.682	0.706	0.674	0.687	0.586
Al	0.055	0.052	0.051	0.050	0.055	0.050	0.053	0.049	0.052	0.052	0.058	0.051	0.052	0.044	0.050	0.040
Cr	0.000	0.000	0.000	0.000	0.000	0.000	0.000	0.000	0.000	0.000	0.000	0.000	0.000	0.000	0.000	0.000
Fe²⁺	0.632	0.583	0.581	0.582	0.611	0.578	0.590	0.579	0.587	0.586	0.602	0.589	0.612	0.584	0.598	0.528
Fe³⁺	0.476	0.578	0.587	0.585	0.523	0.595	0.567	0.595	0.582	0.582	0.549	0.583	0.536	0.607	0.573	0.787
Mn	0.003	0.003	0.003	0.003	0.003	0.003	0.003	0.003	0.003	0.003	0.003	0.003	0.003	0.003	0.003	0.003
Mg	0.098	0.097	0.096	0.096	0.096	0.095	0.095	0.094	0.092	0.092	0.091	0.089	0.089	0.087	0.087	0.054
Sum	1.999	1.999	1.999	1.999	1.999	1.999	1.999	1.998	1.999	1.999	2.000	1.999	1.998	2.000	1.999	1.999
Fe₂O₃	0.245	0.298	0.302	0.301	0.270	0.306	0.292	0.306	0.299	0.300	0.284	0.300	0.276	0.311	0.295	0.403
FeTiO₃	0.652	0.600	0.597	0.598	0.630	0.594	0.608	0.595	0.605	0.603	0.621	0.606	0.630	0.599	0.614	0.540
MgTiO₃	0.101	0.100	0.099	0.099	0.099	0.098	0.098	0.097	0.095	0.095	0.094	0.092	0.092	0.089	0.089	0.055

Table B.13.: Major and trace element analyses of amphibole
b.d.: below detection limit

Sample Comment	Kerang Jos	Gwaram Biu	Kerang Jos	Koroko Biu in phonolite	Koroko Biu in phonolite	Damknolle Biu +grt, cpx, ilm, apa, plag	Damknolle Biu	Damknolle Biu	Mir Biu pyroxenit xenolith
SiO₂ [wt%]	40.20	40.27	40.05	39.62	39.77	39.16	38.55	38.36	40.39
TiO₂	4.58	4.40	4.47	4.31	4.27	4.87	4.69	4.70	3.65
Al₂O₃	15.01	15.03	14.60	14.04	14.08	15.61	15.35	15.49	14.48
Cr₂O₃	0.007	0.008	0.012	0.032	0.009	0.013	b.d.	0.009	b.d.
FeO	9.69	9.93	11.01	11.30	11.45	13.09	13.23	12.96	8.06
MnO	0.099	0.102	0.100	0.124	0.118	0.092	0.095	0.087	0.094
MgO	12.90	12.48	12.30	12.34	12.26	10.16	9.90	9.95	14.57
CaO	10.71	11.09	9.91	10.41	10.32	9.83	9.79	9.78	10.39
NiO	0.008	b.d.	0.012	0.011	b.d.	0.024	0.011	0.022	0.011
Na₂O	2.41	3.18	2.74	3.03	2.94	3.05	3.13	3.08	3.64
K₂O	2.36	1.32	2.11	1.84	1.89	1.44	1.37	1.42	0.30
P₂O₅	0.018	0.016	0.015	0.016	0.035	0.064	0.064	0.058	0.019
Sum	98.00	97.83	97.30	97.07	97.14	97.40	96.16	95.91	95.60
mg#	70.3	69.1	66.6	66.1	65.6	58.1	57.1	57.8	76.3
Cations to 23 oxygens									
Si	5.904	5.916	5.947	5.924	5.940	5.849	5.844	5.826	5.982
Ti	0.506	0.486	0.499	0.485	0.480	0.547	0.535	0.536	0.406
Al	2.597	2.602	2.554	2.474	2.478	2.747	2.742	2.772	2.527
Fe²⁺	1.191	1.220	1.367	1.413	1.430	1.635	1.677	1.646	0.998
Mn	0.012	0.013	0.013	0.016	0.015	0.012	0.012	0.011	0.012
Mg	2.823	2.733	2.722	2.750	2.729	2.263	2.236	2.253	3.216
Ca	1.685	1.745	1.576	1.668	1.651	1.573	1.589	1.592	1.649
Na	0.687	0.906	0.789	0.878	0.851	0.884	0.920	0.907	1.045
K	0.442	0.247	0.399	0.351	0.360	0.275	0.265	0.275	0.056
Sum	15.848	15.867	15.869	15.957	15.935	15.797	15.821	15.819	15.892
Ba [ppm]						488			
Nb						60.1			
La						9.5			
Ce						33.5			
Pr						6.67			
Sr						1030			
Nd						33.2			
Zr						78.7			
Sm						9.79			
Eu						3.84			
Gd						8.02			
Tb						0.851			
Dy						4.24			
Ho						0.639			
Y						13.7			
Er						0.905			
Tm						b.d.			
Yb						b.d.			
Lu						b.d.			

Table B.14.: Major element analyses of spinel
*Fe₂O₃ from stoichiometry

Sample Comment	Gumya Biu	Mir Biu	Hilia Biu	Mir Biu pyroxenite xenolith	Mir Biu pyroxenite xenolith	Mir Biu Iherzolite xenolith	Mir Biu Iherzolite xenolith	Mir Biu olivine incl. xenolith?
TiO ₂ [wt%]	0.342	0.498	0.529	0.454	0.433	0.335	0.049	0.690
Al ₂ O ₃	61.98	60.07	58.55	59.27	58.56	48.69	43.45	21.37
Cr ₂ O ₃	1.74	0.09	0.05	0.03	0.04	16.44	24.35	43.75
FeO	11.99	14.01	16.50	15.37	15.38	11.57	8.66	11.06
MgO	19.51	18.28	16.55	17.22	16.73	18.44	19.84	16.38
NiO	0.33	0.16	0.19	0.15	0.14	0.32	0.31	0.24
Fe ₂ O ₃ *	4.47	7.67	8.75	7.96	7.24	4.59	4.20	7.43
Sum	100.54	100.99	101.31	100.64	98.72	100.61	101.13	101.21
mg#	74.4	69.9	64.1	66.6	66.0	74.0	80.3	72.5
Cr#	1.8	0.1	0.1	0.0	0.0	18.5	27.3	57.9
Cations to 4 oxygens								
Ti	0.007	0.010	0.010	0.009	0.009	0.007	0.001	0.016
Al	1.864	1.826	1.803	1.822	1.834	1.541	1.384	0.755
Cr	0.035	0.002	0.001	0.001	0.001	0.349	0.520	1.038
Fe ²⁺	0.256	0.302	0.361	0.335	0.342	0.260	0.196	0.277
Mg	0.742	0.703	0.645	0.669	0.663	0.738	0.799	0.733
Ni	0.007	0.003	0.004	0.003	0.003	0.007	0.007	0.006
Fe ³⁺	0.086	0.149	0.172	0.156	0.145	0.093	0.086	0.168
Sum	2.996	2.995	2.995	2.995	2.995	2.995	2.993	2.992

Table B.15.: Major element analyses of olivine

Sample Comment	Dam Biu	Dam Biu	Dam Biu	Miringa Biu	Miringa Biu Iherzolite xenolith
SiO ₂ [wt%]	40.19	40.21	40.02	40.28	40.30
Al ₂ O ₃	0.041	0.046	0.044	0.057	0.073
Cr ₂ O ₃	0.018	0.066	0.009	0.064	0.069
FeO	8.97	8.43	10.41	8.43	8.49
MnO	0.131	0.134	0.153	0.099	0.145
MgO	49.53	49.86	48.47	49.56	49.80
CaO	0.088	0.152	0.084	0.176	0.142
NiO	0.376	0.384	0.374	0.394	0.398
Sum	99.40	99.30	99.62	99.09	99.42
mg#	90.8	91.3	89.2	91.3	91.3
Cations to 4 oxygens					
Si	0.990	0.989	0.990	0.993	0.991
Al	0.001	0.001	0.001	0.002	0.002
Cr	0.000	0.001	0.000	0.001	0.001
Fe ²⁺	0.185	0.173	0.215	0.174	0.175
Mn	0.003	0.003	0.003	0.002	0.003
Mg	1.819	1.829	1.787	1.821	1.824
Ca	0.002	0.004	0.002	0.005	0.004
Ni	0.007	0.008	0.007	0.008	0.008
Sum	3.007	3.009	3.007	3.005	3.008

Table B.16.: Major element analyses of phlogopite
b.d.: below detection limit

Sample Comment	Mir Biu	Koroko Biu in phonolite
SiO ₂ [wt%]	34.62	40.05
TiO ₂	5.16	1.43
Al ₂ O ₃	15.93	12.73
Cr ₂ O ₃	b.d.	0.301
FeO	18.60	4.11
MnO	0.127	0.057
MgO	10.61	23.45
CaO	0.010	0.019
NiO	0.017	0.124
Na ₂ O	0.862	1.187
K ₂ O	8.37	8.69
Sum	94.32	92.14
mg#	50.4	91.0
Cations to 22 oxygens		
Si	5.331	5.860
Ti	0.598	0.157
Al	2.891	2.195
Cr	b.d.	0.035
Fe ²⁺	2.395	0.503
Mn	0.017	0.007
Mg	2.435	5.114
Ca	0.002	0.003
Ni	0.002	0.015
Na	0.257	0.337
K	1.644	1.622
Sum	15.574	15.847

Table B.17.: Major element analyses of apatite

Sample Comment	Mir Biu	Mir Biu	Damknolle Biu	Damknolle Biu
SiO ₂ [wt%]	0.18	0.18	0.17	0.17
FeO	0.91	0.90	0.808	0.792
MnO	0.07	0.08	0.064	0.045
MgO	0.57	0.56	0.621	0.654
CaO	51.69	51.91	51.38	51.44
Na ₂ O	0.40	0.41	0.498	0.484
P ₂ O ₅	40.09	39.91	39.58	39.71
Sum	93.92	93.96	93.13	93.32

Table 18.: Analytical precision and accuracy of ionprobe analyses
*Jochum et al. (2000)

Sample								
Gor 132-G	22.08.00	24.11.00	12.03.01	12.06.01	mean	prec. (1 σ)	ref.*	acc.
Ba	0.879	1.000	0.954	0.772	0.901	11.0%	0.86	104.8%
La	0.105	0.070	0.075	0.0842	0.084	18.4%	0.0769	108.7%
Ce	0.398	0.407	0.361	0.511	0.419	15.3%	0.375	111.8%
Pr	0.128	0.088	0.092	0.0572	0.091	31.8%	0.1	91.3%
Nd	0.550	0.752	0.683	0.641	0.657	12.9%	0.685	95.8%
Sm	0.561	0.577	0.625	0.453	0.554	13.1%	0.509	108.8%
Eu	0.286	0.297	0.258	0.339	0.295	11.4%	0.254	116.1%
Gd	1.830	1.580	1.18	1.33	1.480	19.3%	1.25	118.4%
Tb	0.239	0.288	0.291	0.332	0.288	13.2%	0.27	106.5%
Dy	2.300	2.270	2.22	2.6	2.348	7.3%	2.2	106.7%
Ho	0.565	0.500	0.576	0.615	0.564	8.5%	0.55	102.5%
Er	1.520	1.790	1.5	1.55	1.590	8.5%	1.68	94.6%
Tm	0.266	0.273	0.207	0.237	0.246	12.3%	0.25	98.3%
Yb	2.270	2.030	1.65	2.17	2.030	13.4%	1.67	121.6%
Lu	0.342	0.244	0.134	0.311	0.258	35.7%	0.254	101.5%
K	272	278	289	n.m.	280	3.1%	260	107.6%
Sr	16.1	16	15.2	n.m.	15.77	3.1%	18	87.6%
Y	12.9	12.6	12.8	n.m.	12.77	1.2%	12	106.4%
Zr	9.81	10.3	11.7	n.m.	10.603	9.3%	10.5	101.0%
Nb	0.205	0.139	0.162	n.m.	0.169	19.9%	0.072	234.3%
KL2-G								
Ba	162	136			149	12.3%	124	120.2%
La	14.7	13.5			14.1	6.0%	13.3	106.0%
Ce	37.2	34.2			35.7	5.9%	33.2	107.5%
Pr	5.74	5.14			5.44	7.8%	4.8	113.3%
Nd	24.5	22.6			23.6	5.7%	22.2	106.1%
Sm	6.6	5.62			6.11	11.3%	5.72	106.8%
Eu	2.36	1.99			2.18	12.0%	1.99	109.3%
Gd	5.35	5.02			5.19	4.5%	6.07	85.4%
Tb	0.992	0.713			0.853	23.1%	0.93	91.7%
Dy	5.65	5.08			5.37	7.5%	5.37	99.9%
Ho	1.13	0.895			1.01	16.4%	1.01	100.2%
Er	2.65	2.91			2.78	6.6%	2.64	105.3%
Tm	0.364	0.338			0.351	5.2%	0.34	103.2%
Yb	2.8	2.1			2.45	20.2%	2.09	117.2%
Lu	0.323	0.395			0.359	14.2%	0.293	122.5%
K	4530	4390			4460	2.2%	4050	110.1%
Sr	426	396			411	5.2%	362	113.5%
Y	25.6	25.2			25.4	1.1%	27	94.1%
Zr	171	170			171	0.4%	160	106.6%
Nb	20.2	19.5			19.9	2.5%	17	116.8%

Table B.19.: TIMS isotope data for Biu and Jos Plateau lavas

Os and Re conc. and ¹⁸⁷Os/¹⁸⁸Os blank corrected. Duplicate Re and Os conc. in brackets. Δ7/4 and Δ8/4 notation from Hart (1984)

Sample Comment	ZAGU Biu young	JIGU 1 Biu young	JIGU-M Biu young	X Biu young	PELA JUNG Biu young	KOROKO Biu young	PELA ALT Biu young	DAM Biu young	DAM 2 Biu young	BUGOR Biu young	BUGOR Leachate	SE BUGOR Biu young	HILIA 1 Biu young
⁸⁷ Sr/ ⁸⁶ Sr	0.702951	0.703468	0.702892	0.703183	0.703347	0.703234	0.703192	0.702995	0.703178	0.702922		0.702927	0.702923
duplicate		0.703505			0.703355	0.703195			0.703151				
duplicate		0.703492				0.703174							
¹⁴³ Nd/ ¹⁴⁴ Nd	0.512976	0.512878	0.513015	0.512936	0.512897	0.512928	0.512928	0.512963	0.512951	0.512962		0.512986	0.512987
duplicate		0.512877			0.512903				0.512968				
duplicate		0.512862							0.512957				
εNd	6.6	4.7	7.4	5.8	5.1	5.7	5.7	6.3	6.3	6.3		6.8	6.8
²⁰⁶ Pb/ ²⁰⁴ Pb	19.677	19.096	19.832	19.384	19.481	20.103	19.851	19.518	19.654	19.670	19.641	19.623	19.775
duplicate							19.851		19.664				
duplicate							19.869						
duplicate							19.868						
²⁰⁷ Pb/ ²⁰⁴ Pb	15.640	15.623	15.649	15.620	15.647	15.693	15.677	15.629	15.655	15.655	15.652	15.637	15.655
duplicate							15.669		15.657				
duplicate							15.684						
duplicate							15.695						
²⁰⁸ Pb/ ²⁰⁴ Pb	39.380	39.208	39.493	39.259	39.505	39.717	39.939	39.307	39.694	39.484	39.452	39.374	39.541
duplicate							39.916		39.699				
duplicate							39.961						
duplicate							39.997						
Δ7/4	1.6	6.2	0.9	2.8	4.5	2.2	3.7	2.3	3.4	3.2		1.9	2.1
Δ8/4	-3.6	49.5	-11.1	19.7	32.5	-21.4	31.5	8.3	30.6	7.7		2.3	0.6
¹⁸⁷ Os/ ¹⁸⁸ Os		0.1415	0.1282	0.2449			0.1232	0.1488					
duplicate			0.1305					0.1443					
Os [ppt]		46	42 [42]	9			134	20 [24]					
Re [ppt]		65	49 [48]	50			90	19 [18]					
¹⁸⁷ Os/ ¹⁸⁸ Os _{ini}		0.1415	0.1294	0.2449			0.1232	0.1466					
²³⁸ U/ ²⁰⁴ Pb	42.27	31.18	44.86	35.62	35.10	39.29	36.36	41.84	32.80	42.84		45.63	41.58
²³² Th/ ²³⁸ U	4.12	4.23	3.57	4.28	4.06	3.78	3.95	3.86	4.20	3.86		3.87	4.02
¹⁴⁷ Sm/ ¹⁴⁴ Nd	0.116	0.128	0.120	0.127	0.121	0.103	0.113	0.124	0.122	0.125		0.122	0.121
⁸⁷ Rb/ ⁸⁶ Sr	0.150	0.154	0.132	0.156	0.161	0.560	0.240	0.137	0.185	0.164		0.155	0.169

Table B.19.: TIMS isotope data for Biu and Jos Plateau lavas
Os and Re conc. and $^{187}\text{Os}/^{188}\text{Os}$ blank corrected. Duplicate Re and Os conc. in brackets. $\Delta 7/4$ and $\Delta 8/4$ notation from Hart (1984)

Sample Comment	HILIA 2 Biu young	TAMZA Biu young	GUFKA Biu young	MIR Biu young	GULDUMBUR Biu young	PELA 2 Biu young	WIGA Biu young	GWARAM Biu young	ZUMTA Biu young	HIZSHI Biu young	TUM Biu young	ETUM Biu young	GUMJA Biu young
	Qz in thin sec.												
$^{87}\text{Sr}/^{86}\text{Sr}$ duplicate duplicate duplicate	0.702888	0.702890	0.703079	0.703092 0.703062 0.703087 0.703062	0.702914	0.703091 0.703095	0.702941	0.702981	0.703096 0.703110 0.703089	0.702904	0.703000 0.703017	0.702856	0.702890
$^{143}\text{Nd}/^{144}\text{Nd}$ duplicate duplicate	0.512989	0.512968 0.512967	0.512977 0.512971	0.512954 0.512930	0.512992 0.512984	0.512964 0.512957	0.513004	0.512973	0.512966 0.512943	0.512963	0.512968	0.512984	0.512991
ϵNd	6.8	6.4	6.4	6.0	6.8	6.2	7.1	6.5	6.2	6.3	6.4	6.7	6.9
$^{206}\text{Pb}/^{204}\text{Pb}$ duplicate duplicate duplicate	19.641	20.039	19.416	20.267 20.326	20.006	19.657	19.781	20.018	20.162	20.109	20.018	19.878	19.711
$^{207}\text{Pb}/^{204}\text{Pb}$ duplicate duplicate duplicate	15.637	15.675	15.634	15.699 15.692	15.669	15.643	15.640	15.673	15.685	15.670	15.675	15.643	15.656
$^{208}\text{Pb}/^{204}\text{Pb}$ duplicate duplicate duplicate	39.420	39.748	39.261	40.313 40.354	39.712	39.362	39.513	39.798	40.281	39.779	39.844	39.521	39.470
$\Delta 7/4$	1.7	1.1	3.9	-0.3	1.0	2.2	0.5	1.2	0.8	0.0	1.4	-0.2	2.9
$\Delta 8/4$	4.7	-10.6	16.0	15.3	-10.1	-3.0	-3.0	-3.0	27.8	-16.0	1.6	-13.9	1.3
$^{187}\text{Os}/^{188}\text{Os}$ duplicate		0.1266		0.1351	0.1265			0.1277	0.1300	0.1254	0.1301		0.1384
Os [ppt]		39		22	44			55	79	60	82		41
Re [ppt]		41		28	56			48	93	56	146		43
$^{187}\text{Os}/^{188}\text{Os}_{\text{ini}}$		0.1266		0.1351	0.1265			0.1277	0.1300	0.1254	0.1301		0.1384
$^{238}\text{U}/^{204}\text{Pb}$	23.78	42.53	35.32	45.65	50.80	35.06	43.73	40.51	39.40	42.07	42.41	41.40	43.28
$^{232}\text{Th}/^{238}\text{U}$	6.49	3.81	4.33	3.99	3.59	4.33	3.89	3.96	4.24	3.89	4.19	3.89	3.95
$^{147}\text{Sm}/^{144}\text{Nd}$	0.132	0.121	0.128	0.111	0.118	0.119	0.123	0.116	0.113	0.119	0.121	0.118	0.118
$^{87}\text{Rb}/^{86}\text{Sr}$	0.144	0.124	0.105	0.197	0.164	0.158	0.108	0.169	0.211	0.238	0.176	0.155	0.126

Table B.19.: TIMS isotope data for Biu and Jos Plateau lavas
Os and Re conc. and ¹⁸⁷Os/¹⁸⁸Os blank corrected. Duplicate Re and Os conc. in brackets. Δ7/4 and Δ8/4 notation from Hart (1984)

Sample Comment	TILA 1 Biu young	TILA STR Biu young	Biu4 Biu old	Biu4 Leachate	Biu5 Biu old	Biu8 Biu old	Biu9 Biu old	DAI Jos young	KERANG Jos young	AMPANG Jos young Qz in thin sec.	PIDONG-M Jos young Qz in thin sec.	PIDONG-S Jos young
⁸⁷ Sr/ ⁸⁶ Sr	0.703145	0.702900	0.702884	0.704116	0.702934	0.703337	0.702942	0.703379	0.703405	0.703588	0.703370	0.703175
duplicate	0.703150					0.703328			0.703436			0.703157
duplicate	0.703161											0.703197
¹⁴³ Nd/ ¹⁴⁴ Nd	0.512966	0.512997	0.512996	0.512978	0.512991	0.512923	0.512982	0.512881	0.512908	0.512875	0.512902	0.512872
duplicate	0.512949						0.512972		0.512886			0.512859
duplicate	0.512948											
εNd	6.1	7.0	7.0	6.6	6.9	5.6	6.5	4.7	5.0	4.6	5.1	4.6
²⁰⁶ Pb/ ²⁰⁴ Pb	19.558	19.773	19.849		19.742	19.031	19.705	19.326	19.654	19.264	19.622	19.684
duplicate						19.086				19.266		
duplicate												
duplicate												
²⁰⁷ Pb/ ²⁰⁴ Pb	15.644	15.640	15.648		15.635	15.632	15.642	15.646	15.673	15.660	15.662	15.669
duplicate						15.639				15.650		
duplicate												
duplicate												
²⁰⁸ Pb/ ²⁰⁴ Pb	39.422	39.506	39.616		39.515	39.175	39.417	39.320	39.477	39.305	39.489	39.643
duplicate						39.269				39.288		
duplicate												
duplicate												
Δ7/4	3.3	0.6	0.6		0.4	7.8	1.5	6.0	5.1	8.1	4.4	4.5
Δ8/4	15.0	-2.6	-0.9		1.9	53.9	-3.3	32.7	8.9	38.7	14.0	21.8
¹⁸⁷ Os/ ¹⁸⁸ Os			0.1394			0.1596				0.1578	0.1369	
duplicate												
Os [ppt]				20		24				101	44	
Re [ppt]				45		23				136	55	
¹⁸⁷ Os/ ¹⁸⁸ Os _{ini}			0.1385			0.1592				0.1578	0.1369	
²³⁸ U/ ²⁰⁴ Pb	33.24	38.36	39.30		35.81	26.00	32.15	33.66	31.07	25.56	30.90	30.48
²³² Th/ ²³⁸ U	4.21	3.89	3.90		4.15	4.17	3.87	4.27	4.26	4.30	4.14	4.09
¹⁴⁷ Sm/ ¹⁴⁴ Nd	0.131	0.136	0.130		0.128	0.133	0.122	0.123	0.116	0.116	0.122	0.111
⁸⁷ Rb/ ⁸⁶ Sr	0.154	0.166	0.118		0.190	0.143	0.146	0.162	0.154	0.179	0.187	0.145

Table B.20.: Reproducibility of SRM981 isotopic standard during the period of measurements
*Todd et al. (1996)

Date	Spectr.	²⁰⁶ Pb/ ²⁰⁴ Pb	2σ(m)%	²⁰⁷ Pb/ ²⁰⁴ Pb	2σ(m)%	²⁰⁸ Pb/ ²⁰⁴ Pb	2σ(m)%	load
28.07.00	MS 1	16.9006	0.006	15.4423	0.007	36.5451	0.010	10 ng
28.07.00	MS 1	16.8958	0.007	15.4356	0.008	36.5252	0.010	10 ng
28.07.00	MS 1	16.8957	0.012	15.4376	0.007	36.5320	0.010	10 ng
28.07.00	MS 1	16.8983	0.007	15.4385	0.009	36.5341	0.011	10 ng
07.08.00	MS 1	16.9003	0.006	15.4399	0.006	36.5397	0.007	10 ng
07.08.00	MS 1	16.8980	0.033	15.4376	0.007	36.5304	0.013	10 ng
07.08.00	MS 1	16.8941	0.005	15.4324	0.005	36.5137	0.006	10 ng
07.08.00	MS 1	16.9007	0.006	15.4425	0.006	36.5448	0.006	10 ng
08.08.00	MS 1	16.8957	0.008	15.4341	0.010	36.5218	0.012	10 ng
08.08.00	MS 1	16.8954	0.006	15.4344	0.007	36.5215	0.009	10 ng
08.08.00	MS 1	16.8944	0.009	15.4324	0.009	36.5131	0.009	10 ng
08.08.00	MS 1	16.9039	0.008	15.4459	0.011	36.5577	0.015	10 ng
08.08.00	MS 1	16.9022	0.007	15.4429	0.009	36.5484	0.011	10 ng
08.08.00	MS 1	16.8960	0.012	15.4340	0.012	36.5209	0.013	10 ng
18.09.00	MS 1	16.9005	0.006	15.4400	0.007	36.5332	0.009	10 ng
18.09.00	MS 1	16.8974	0.007	15.4343	0.007	36.5167	0.008	10 ng
06.10.00	MS 1	16.9007	0.006	15.4402	0.008	36.5354	0.011	10 ng
12.10.00	MS 1	16.8945	0.006	15.4320	0.007	36.5065	0.008	10 ng
28.10.00	MS 1	16.8988	0.013	15.4375	0.012	36.5303	0.013	10 ng
13.11.00	MS 1	16.8985	0.008	15.4375	0.009	36.5300	0.010	10 ng
23.11.00	MS 1	16.9037	0.009	15.4474	0.009	36.5647	0.012	10 ng
15.03.01	MS 1	16.9060	0.009	15.4490	0.011	36.5660	0.016	20 ng
18.09.01	MS 1	16.8979	0.008	15.4375	0.010	36.5349	0.011	10 ng
11.11.01	MS 1	16.8947	0.007	15.4346	0.007	36.5200	0.007	10 ng
11.11.01	MS 1	16.8993	0.068	15.4403	0.068	36.5413	0.067	2 ng
11.11.01	MS 1	16.9048	0.016	15.4478	0.016	36.5657	0.016	2 ng
17.11.01	MS 1	16.9000	0.007	15.4399	0.008	36.5387	0.009	10 ng
21.11.01	MS 1	16.8982	0.020	15.4375	0.020	36.5293	0.021	4 ng
22.11.01	MS 1	16.8952	0.012	15.4344	0.013	36.5245	0.013	4 ng
09.03.01	MS 2	16.8922	0.015	15.4369	0.016	36.5387	0.018	10 ng
09.03.01	MS 2	16.8979	0.015	15.4416	0.016	36.5434	0.018	10 ng
09.03.01	MS 2	16.9088	0.015	15.4567	0.017	36.5968	0.021	10 ng
09.03.01	MS 2	16.8889	0.014	15.4337	0.015	36.5256	0.015	10 ng
09.03.01	MS 2	16.8849	0.013	15.4282	0.014	36.5064	0.014	10 ng
10.03.01	MS 2	16.8912	0.017	15.4343	0.017	36.5227	0.017	10 ng
11.03.01	MS 2	16.9029	0.010	15.4515	0.011	36.5754	0.013	20 ng
21.04.01	MS 2	16.8919	0.012	15.4369	0.014	36.5319	0.018	10 ng
08.11.01	MS 2	16.9024	0.027	15.4460	0.027	36.5566	0.027	10 ng
08.11.01	MS 2	16.8850	0.049	15.4294	0.049	36.5109	0.048	2 ng
08.11.01	MS 2	16.8886	0.042	15.4312	0.042	36.5163	0.042	2 ng
08.11.01	MS 2	16.8812	0.035	15.4254	0.036	36.4961	0.036	2 ng
08.11.01	MS 2	16.8946	0.037	15.4393	0.036	36.5399	0.036	2 ng
Mean MS 1		16.8987		15.4386		36.5340		
2σ		0.0066		0.0095		0.0314		
2σ [ppm]		392		614		860		
Mean MS 2		16.8931		15.4378		36.5354		
2σ		0.0160		0.0184		0.0564		
2σ [ppm]		950		1194		1543		
ref.*		16.9373		15.4925		36.7054		
fract. corr.								
MS 1 [amu⁻¹]		0.1143%		0.1163%		0.1173%		
MS 2 [amu⁻¹]		0.1308%		0.1182%		0.1551%		

Lead isotope data are normalized to values specific for the machine on which they were measured.

Table B.21.: Reproducibility of SRM987 and La Jolla isotopic standards during the period of measurements

Date	Spectr.	⁸⁷ Sr/ ⁸⁶ Sr	±	Date	Spectr.	¹⁴³ Nd/ ¹⁴⁴ Nd	±
08.12.99	MS 1	0.710235	10	13.01.00	MS 1	0.511844	9
21.01.00	MS 1	0.710234	6	14.01.00	MS 1	0.511862	9
01.02.00	MS 1	0.710222	7	17.01.00	MS 1	0.511843	17
01.02.00	MS 1	0.710231	11	26.01.00	MS 1	0.511845	13
11.02.00	MS 1	0.710234	8	27.01.00	MS 1	0.511848	10
20.03.00	MS 1	0.710222	10	02.02.00	MS 1	0.511852	10
06.05.00	MS 1	0.710200	9	09.06.00	MS 1	0.511860	10
14.07.00	MS 1	0.710204	10	01.09.00	MS 1	0.511886	10
14.07.00	MS 1	0.710205	9	12.09.00	MS 1	0.511921	6
22.07.00	MS 1	0.710232	8	11.12.00	MS 1	0.511865	9
28.08.00	MS 1	0.710255	7	15.02.02	MS 1	0.511878	12
28.08.00	MS 1	0.710245	10	15.02.02	MS 1	0.511874	19
01.09.00	MS 1	0.710247	8	24.02.02	MS 1	0.511883	15
22.11.00	MS 1	0.710253	10	01.03.02	MS 1	0.511887	9
28.02.02	MS 1	0.710194	9	12.03.00	MS 2	0.511826	6
28.02.02	MS 1	0.710210	12	18.03.00	MS 2	0.511831	11
18.11.99	MS 2	0.710170	8	19.03.00	MS 2	0.511838	9
18.11.99	MS 2	0.710176	10	19.03.00	MS 2	0.511829	5
09.12.99	MS 2	0.710179	24	16.05.00	MS 2	0.511868	7
16.12.99	MS 2	0.710268	16	16.05.00	MS 2	0.511815	14
17.12.99	MS 2	0.710248	15	26.05.00	MS 2	0.511866	20
17.12.99	MS 2	0.710261	15	23.08.00	MS 2	0.511890	13
26.03.00	MS 2	0.710218	10	26.08.00	MS 2	0.511911	9
26.03.00	MS 2	0.710154	18	26.08.00	MS 2	0.511865	13
28.04.00	MS 2	0.710270	10	28.08.00	MS 2	0.511868	14
28.04.00	MS 2	0.710250	9	28.09.00	MS 2	0.511857	12
28.04.00	MS 2	0.710266	14	28.09.00	MS 2	0.511845	2
09.05.00	MS 2	0.710275	12	28.10.00	MS 2	0.511905	13
09.05.00	MS 2	0.710245	11	28.10.00	MS 2	0.511877	5
12.05.00	MS 2	0.710265	11	31.10.00	MS 2	0.511874	7
09.08.00	MS 2	0.710273	8	31.10.00	MS 2	0.511855	6
19.08.00	MS 2	0.710282	5	19.11.00	MS 2	0.511845	11
19.08.00	MS 2	0.710235	9				
29.08.00	MS 2	0.710261	6				
30.08.00	MS 2	0.710263	12				
30.08.00	MS 2	0.710262	9				
13.11.00	MS 2	0.710321	9				
17.11.00	MS 2	0.710311	11				
07.12.00	MS 2	0.710255	9				
07.12.00	MS 2	0.710251	12				
04.03.01	MS 2	0.710326	12				
Mean MS 1		0.710226				0.511868	
2σ		0.000038				0.000044	
Mean MS 2		0.710251				0.511859	
2σ		0.000087				0.000053	

Strontium and neodymium isotope data of each machine are normalized to reference values for standards NBS 987 (⁸⁷Sr/⁸⁶Sr=0.71025) and La Jolla (¹⁴³Nd/¹⁴⁴Nd=0.51185).

Table B.22.: TIMS isotope data for Biu and Jos Plateau megacrysts
 $\Delta 7/4$ and $\Delta 8/4$ notation from Hart (1984)

Sample Comment	Ker cpx Jos	Ker L leachate of Ker	Ker a same as Ker w. thick alt. crusts	Ker b same as Ker w. sulf. inclusions	Ker c same as Ker clean picked unleached	Dam+ cpx Biu	Ampang cpx Jos	Mir 21 cpx Biu	Ker 2 cpx Jos	Dam 60-4 cpx Biu	Dam++ cpx Biu	Mir 60-1 cpx Biu	Pela alt cpx Biu	Mir+Grt cpx Biu
⁸⁷ Sr/ ⁸⁶ Sr	0.703158	0.703197	0.703260	0.703208	0.703171	0.703030	0.703207	0.703057	0.703187	0.703095	0.702900	0.703090	0.703276	0.703112
dupl.	0.703161	0.703182								0.703058	0.702893	0.703073	0.703264	0.703126
dupl.										0.703056				
¹⁴³ Nd/ ¹⁴⁴ Nd	0.512955		0.512928	0.512975	0.512973	0.512938	0.512940	0.512957	0.512975	0.512990	0.512988	0.512963	0.512913	0.512952
dupl.	0.512946		0.512960	0.512926	0.512930		0.512926	0.512950	0.512955	0.513012	0.512957		0.512893	0.512961
ϵ_{Nd}	6.1		6.0	6.1	6.1	5.9	5.8	6.2	6.4	7.1	6.5	6.3	5.2	6.2
²⁰⁶ Pb/ ²⁰⁴ Pb						20.048	20.039	20.724	19.823		20.103		20.902	20.658
²⁰⁷ Pb/ ²⁰⁴ Pb						15.708	15.701	15.737	15.672		15.711		15.757	15.723
²⁰⁸ Pb/ ²⁰⁴ Pb						39.771	39.791	40.862	39.560		39.850		41.073	40.818
$\Delta 7/4$						4.3	3.7	-0.1	3.3		4.0		0.0	-0.8
$\Delta 8/4$						-9.3	-6.3	17.9	-3.4		-8.1		17.6	21.6

Table B.22.: TIMS isotope data for Biu and Jos Plateau megacrysts
 $\Delta 7/4$ and $\Delta 8/4$ notation from Hart (1984)

Sample Comment	Mir 15 cpx Biu	Pid M cpx Jos	Gumja2 cpx Biu	Mir+Pl. cpx Biu	Mir a plag Biu	Mir b plag Biu	Mir c plag Biu	Hilia2 plag Biu	Gwaram plag Biu	Mir+Grt gnt Biu	Damknolle gnt Biu	Ker GA gnt Jos	Schliff 1 gnt Jos
⁸⁷ Sr/ ⁸⁶ Sr dupl. dupl.	0.703037 0.703002	0.703210	#BEZUG! 0.703053	0.703053 0.703063	0.703096	0.703044	0.703062	0.703035 0.703036	0.702961	0.706229	0.704710	0.705490	0.705968
¹⁴³ Nd/ ¹⁴⁴ Nd dupl.	0.512959 0.512933	0.512939 0.512925	0.512975	0.512966 0.512951	0.512981 0.512946	0.512948 0.512933	0.512949 0.512943	0.512963	0.512955	0.512953	0.512960	0.512948	0.512982
ϵ_{Nd}	6.0	5.7	6.6	6.3	6.3	5.9	6.0	6.3	6.2	6.1	6.3	6.0	6.7
²⁰⁶ Pb/ ²⁰⁴ Pb	20.621	19.924		20.663	20.702	20.678	20.752						
²⁰⁷ Pb/ ²⁰⁴ Pb	15.719	15.685		15.736	15.725	15.714	15.726						
²⁰⁸ Pb/ ²⁰⁴ Pb	40.688	39.681		40.835	40.830	40.795	40.950						
$\Delta 7/4$	-0.8	3.5		0.5	-1.0	-1.9	-1.5						
$\Delta 8/4$	13.0	-3.4		22.7	17.5	16.9	23.4						

Appendix C: Picture tables



Pic.1: small cinder cone, Biu



Pic.2: Gwaram, Biu, base diameter ~2km



Pic.3: Lake Tila, Biu, maar



Pic.4: xenolith-bearing basalt, Dam, Biu



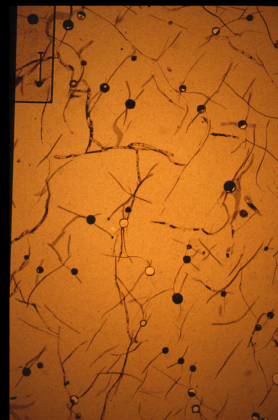
Pic.5: bomb containing sp-peridotite



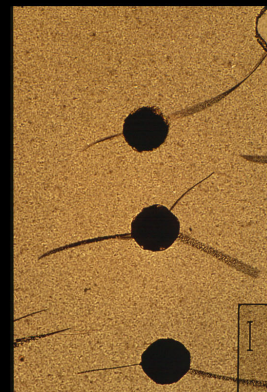
Pic.6: pyroxenite xenolith



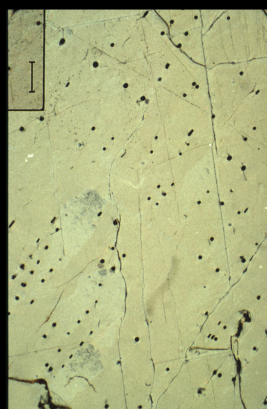
Pic.7: large cpx megacryst with ilmenite inclusion



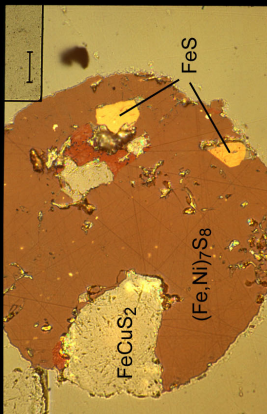
Pic.8: cpx thin section with sulfides and fluid inclusions along cracks



Pic.9: magnification of Pic. 8 sulfides lost in preparation scale bar ~50 μm



Pic.10: cpx thin section with sulfides orientated along crystal planes



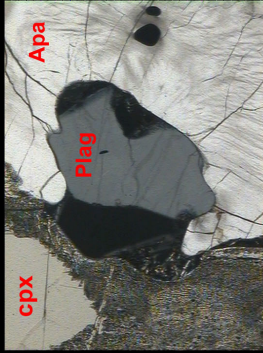
Pic.11: sulfide inclusion in reflected light with three separate S-phases



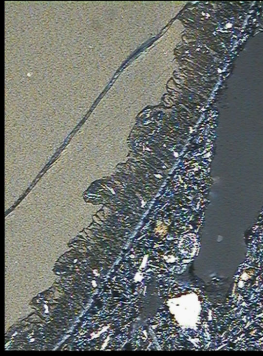
Pic.12: cpx-gnt intergrowth



Pic.13: cpx-gnt intergrowth in thin section



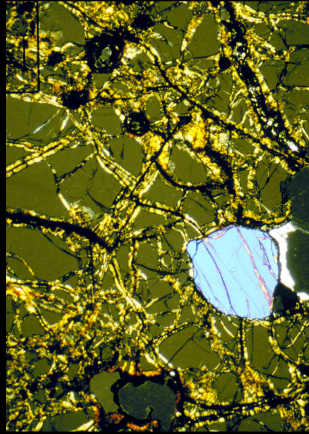
Pic.14: evolved cpx intergrowth with plagioclase and apatite



Pic.15: rim of evolved cpx with breakdown reaction



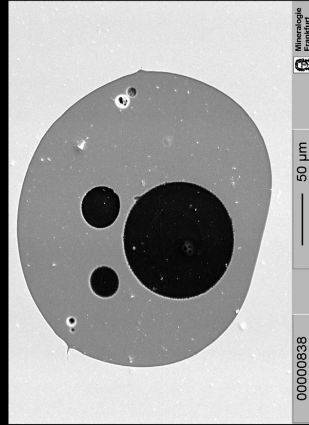
Pic.16: large gnt-megacryst



Pic.17: gnt-megacrysts with cracks and cpx inclusion



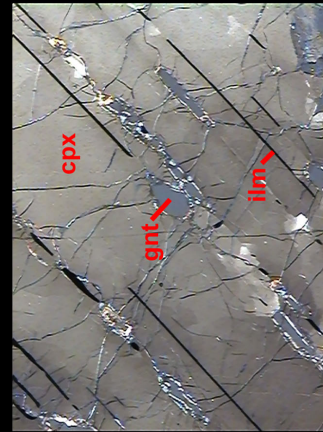
Pic.18: ilmenite megacrysts



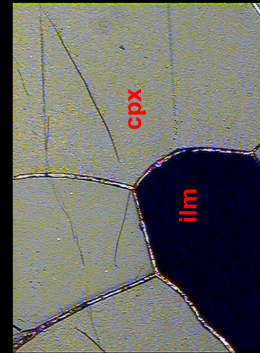
Pic.19: melt inclusion in ilmenite with three gas bubbles



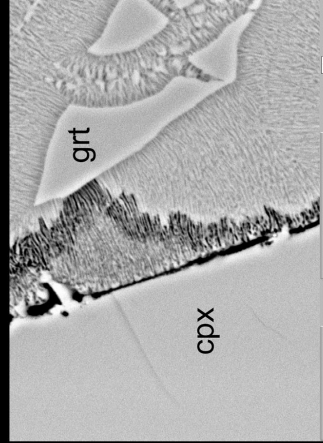
Pic.20: plagioclase megacrysts



Pic.21: pyroxenite xenolith in thin section with exsolution lamellae of ilm and gnt



Pic.22: same xenolith, showing recrystallized texture



Pic.23: EMP-image of cpx-gnt intergrowth showing breakdown of gnt

LEBENS LAUF

Kai Rankenburg
Nackenheim Str. 21
65428 Rüsselsheim

Geboren am 15.12.1966 in Frankfurt am Main

Berufserfahrung

- 11.2001- 05.2002 Wissenschaftlicher Mitarbeiter des Max-Planck Institutes für Chemie, Abteilung Geochemie.
- 1997 - 2000 Wissenschaftlicher Mitarbeiter der J.W.Goethe-Universität am Institut für Mineralogie, Petrologie und Geochemie.

Studium

- 1998 - 2002 Doktorand im Fach Mineralogie/Geochemie an der J.W.Goethe-Universität. Promotion am 29.11.2002 mit dem Gesamturteil 'magna cum laude'. Thema der Promotionsarbeit: *"Megacrysts in Volcanic Rocks of the Cameroon Volcanic Line - Constraints on Magma Genesis and Contamination"* betreut von Prof. Gerhard Brey (Frankfurt) und Dr. John C. Lassiter (MPI).
- 1991 - 1997 Studium der Geologie an der J.W.Goethe-Universität, Frankfurt am Main. Diplom am 29.09.1997 mit dem Gesamturteil 'sehr gut'. Thema der Diplomarbeit: *"Platingruppenelemente in Böden entlang der Autobahn"* betreut von Prof. Hans Urban und Dr. Fathi Zereini.

Wehrdienst

- 1986 - 1988 Abgeleistet als Zivildienst im Sozialamt der Stadt Rüsselsheim.

Schulausbildung

- 1979 - 1986 Immanuel-Kant-Gymnasium in Rüsselsheim, Leistungsfächer Mathematik und Chemie, Abitur mit der Gesamtnote 2,0.

Mainz, den 5. Dezember 2002